Ph.D Thesis

Alum-stabilized Pickering emulsion as the delivery platform for antigen spatiotemporal delivery

Sha Peng

Supervisor: Kenji Ogino

Guanghui Ma

Yufei Xia

Graduate School of Bio-Applications and Systems Engineering

Tokyo University of Agriculture and Technology

June, 2024

Abstract

To address the urgent needs of emerging epidemics and significant infectious diseases, designing safe, efficient vaccine adjuvants that enhance immune responses from existing materials is an ideal strategy. However, due to stringent safety requirements for vaccine adjuvants in clinical settings, aluminum adjuvants remain the only adjuvants approved for clinical use in China. The primary mechanism of aluminum adjuvants involves antigen attachment to cell membranes without entering the cells, limiting their involvement in intracellular antigen processing and presentation. Consequently, antigens are processed via the lysosomal pathway and presented by Major Histocompatibility Complex (MHC) II, primarily triggering a humoral immune response while providing less effective cellular immunity. This limitation has impeded the comprehensive protective capabilities of aluminum adjuvants alone, failing to meet the growing demands for vaccine adjuvants. In response, our preliminary research proposed a particulate emulsion strategy for aluminum adjuvants, enhancing both humoral and cellular immune responses. Advanced research has shown that simple mixtures of adjuvants and antigens do not induce efficient immune responses but can lead to immune cell dysfunction, depletion, and suppression. Repeated immunizations have unexpectedly induced exhausted, immunosuppressive T cell responses, significantly delaying the clinical application of tumor vaccines. Thus, our approach focuses on spatial-temporal delivery of multiple antigen components to maximize immune activation and induce strong immune responses through the interaction of Major Histocompatibility Complex (MHC) I and co-stimulatory molecules in a time- and space-dependent manner. Our findings also determine the optimal vaccination frequency for particulate aluminum adjuvant vaccines.

The dissertation studies were unfolded as follows

1. Development and Optimal Immune Strategy of an Alum-Stabilized Pickering emulsion for Cancer Vaccines. This study reports on the development and efficacy of an alum-stabilized Pickering emulsion (APE) designed for the sustained release of a high antigen load to facilitate extensive maturation and activation of antigen-presenting cells (APCs). Following two vaccination sessions, APE/OVA successfully stimulated the production of both IFN- γ -secreting T cells (Th1) and IL-4-secreting T cells (Th2), leading to the generation of effective $CD8^+$ T cells capable of inhibiting tumor growth. Despite enhanced cellular immune responses in the spleen, repeated vaccine administrations (three or four doses at three-day intervals) appeared to augment immunosuppression, characterized by an increased presence of $PD\text{-}1^+$ and $LAG\text{-}3^+$ $CD8^+$ T cells within the tumor environment, thus reducing the overall anti-tumor efficacy. However, the concomitant use of anti-PD-1 antibodies mitigated this suppressive effect and significantly increased tumor regression in B16-OVA-bearing mice. These findings emphasize the potential of integrating therapeutic cancer

vaccines with immune checkpoint inhibitors to overcome the challenges of immunosuppression and enhance cancer treatment outcomes.

2. Spatiotemporal Coordination of Antigen Presentation and Co-stimulatory Signal for Enhanced Anti-tumor Vaccination. This study developed a soft particle-stabilized emulsion (SPE) to deliver lipopeptides with varying release profiles by modifying hydrophobic chain lengths: C_6-SPE for fast release, C_{10}-SPE for medium release, and C_{16}-SPE for slow release. Upon administration, C_6-SPE rapidly releases antigens, prompting immediate antigen presentation, while C_{16}-SPE's delayed release causes late antigen presentation. Both miss the optimal timing to coordinate with CD86 expression, resulting in T-cell apoptosis or inadequate activation. In contrast, C_{10}-SPE ensures a synchronized effect between the MHC-I-peptide complex and the co-stimulatory signal CD86, leading to effective dendritic cell (DC) activation, robust T-cell response, and tumor regression in EG7-OVA-bearing mice. Additionally, co-delivering cytosine-phosphate-guanine (CpG) with SPE extends the expression window of CD86, enhancing DC activation and achieving anti-tumor responses with C_6-SPE comparable to those with C_{10}-SPE. This study underscores the importance of synchronizing the spatiotemporal dynamics of antigen presentation and APC activation for optimizing vaccine efficacy against tumors.

3. Inside-out assembly of viral antigens for the enhanced vaccination. This study introduces a novel vaccine delivery system, termed multi-layered aluminum hydroxide-stabilized emulsion (MASE), designed to optimize the delivery sequence of antigens and enhance immune responses against enveloped RNA viruses. Traditional vaccine strategies often mimic the natural dissemination patterns of live pathogens, which can inadvertently delay the exposure of core antigens like nucleocapsid protein (NP) to immune surveillance due to the evolutionary adaptations of pathogens aimed at evading the immune system. In our approach, the receptor-binding domain (RBD, a surface antigen) of the spike protein is encapsulated within the nanocavities of the emulsion, while NP is adsorbed on the exterior, facilitating an initial burst release of NP followed by the exposure of RBD. This inside-out antigen delivery strategy contrasts with the natural packaging of viruses and has been found to provoke potent type I interferon-mediated innate immune responses, creating an immune-potentiated environment that enhances $CD40^+$ dendritic cell activation and lymph node engagement. Empirical results from vaccine trials using this system against H1N1 influenza and SARS-CoV-2 demonstrated a significant increase in antigen-specific antibody production, memory T cell engagement, and a Th1-biased immune response, leading to reduced viral loads following lethal viral challenges. Our findings suggest that reversing the natural antigen delivery sequence can substantially improve the efficacy of vaccines against enveloped RNA viruses, offering a promising direction for future vaccine development.

Index

Chapter 1 General Introduction

Infectious diseases have been appeared as a major threat to public health, causing extensive loss of life and significant economic losses. With growing concern over the cost-effective and adverse reactions of vaccines, the safety risks associated with traditional vaccines are increasingly recognized.[1] Globally, vaccination has been proven to be a cost-effective public health intervention for the prevention of infectious diseases. Vaccination significantly reduces morbidity and mortality rates, enhances quality of life, and extends average life expectancy.[2-4] Vaccines play a crucial role in the prevention and control of diseases. According to statistics from the National Institutes of Health in 2010, vaccinations prevent approximately 2.5 million deaths annually and avert countless occurrences of diseases.[5,6]

Traditional vaccines primarily consist of attenuated or inactivated viruses or bacteria. These vaccines contain a variety of components, including multiple antigenic proteins, immune-agonists, targeting molecules, which can trigger strong and long-lasting immune responses.[7,8] Although these vaccines are often highly effective, increasing public concern over vaccine efficacy and adverse reactions has highlighted the safety risks associated with traditional vaccines, such as incomplete inactivation and reversion to virulence. This has led to the development of novel vaccine, such as recombinant protein vaccines, split vaccines, subunit vaccines, and synthetic peptide vaccines, which offer the advantages of well-defined components and enhanced safety and stability.[9,10] Particularly, recent advances in biochemical engineering have further propelled the development and application of these new types of vaccines. However, these vaccines alone may struggle to induce an effective immune response. Therefore, to enhance their immunogenicity and protective effects, adjuvants are often added to the vaccine formulations to boost the immune response.[11,12]

Adjuvants are substances that can be introduction to vaccines in enhancing the immune response and modulate the type of immune response. The primary functions of adjuvants include increasing the immunogenicity of antigens, reducing the amounts of antigens and the frequency of vaccinations, and altering the nature of the immune response. Adjuvants can be categorized into three distinct types based on their mode of action: (1) Pathogen-Associated Molecular Patterns (PAMPs) adjuvants, such as NOD-like Receptors (NLRs), Toll-like Receptors (TLRs), C-type Lectin Receptors (CLRs), and Retinoic Acid-inducible Gene I-like Receptors (RLRs), stimulating immune responses by interacting with pattern recognition receptors (PRRs) on Antigen-Presenting Cells (APCs); (2) Carrier delivery adjuvants, including aluminum salts, water-in-oil or oil-in-water emulsions, polymer particles, liposomes, and hydrogel particles, enhancing immune responses by improving the uptake efficiency of antigens by APCs, utilizing an antigen depot effect to extend the presentation time of antigens by APCs, preventing antigen degradation through hydrolysis or proteolysis, and promoting antigen accumulation in lymph nodes. Additionally, some of these adjuvants can induce a strong cytotoxic T lymphocyte (CTL) response through cross-presentation of antigen; (3) APCs independent adjuvants, as

exemplified by Type I Interferon (IFN), tumor necrosis factor, and CD28 antibodies, activating immune responses without the direct involvement of APCs.[13,14]

With ongoing advancements in immunology and vaccine adjuvants, modern vaccine adjuvants not only enhance antigen immunogenicity and reduce antigen dosage but also improve antigen delivery and presentation efficiency, as well as promote the activation of co-stimulatory signaling pathways.[15,16] In fact, immune activation is a series of orderly immune responses occurring in both spatial and temporal. This includes the synergistic interaction of innate and adaptive immunity, interplay among various immune cells, and cooperation across different parts of the body's immune system.[17] Thus, increasing the potency, quality and durability of the vaccine response (Figure 1-1). Thus, effective vaccines should be multicomponent systems that synergistically combine components to coordinate innate and adaptive immunity and interactions among immune cells, ensuring optimal prevention and treatment outcomes. However, rational design and synergistic delivery of multicomponent vaccines still pose significant challenges. This chapter will discuss the basic principles of vaccines, the composition of multicomponent vaccines, delivery vehicles, and the challenges faced, and will propose the research strategies and plans of this thesis.[18]

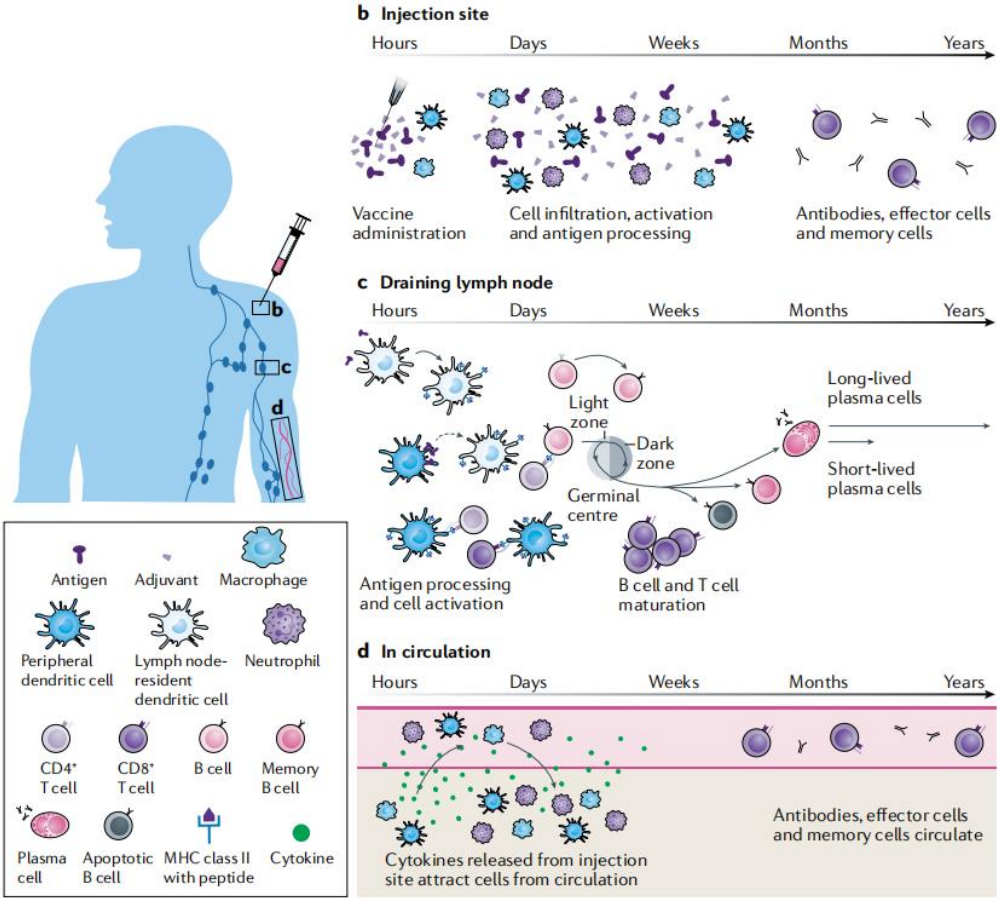

Figure 1-1 Timeline of vaccine advances and vaccine immune response.[18]

1.1 The basic principle of vaccine immunity.

In general, the body's immunity primarily comprises innate immunity and adaptive immunity. Innate immunity lacks specificity but has a broad scope of action and is also known as nonspecific immunity or inherent immunity. Adaptive immunity, on the other hand, is a specific immune response generated after antigen stimulation, also referred to as specific immunity or acquired immunity. The following discussion will elucidate the basic principles of vaccine function by introducing innate and adaptive immunity.[19-21]

1.1.1 Innate immune response

As the body's primary line of defense, innate immunity significantly influences the initiation and magnitude of the immune response. Innate immunity comprises tissue barriers, innate immune cells, and innate immune molecules.[22] Toll-like receptors (TLRs) are a class of crucial protein molecules involved in innate immunity and serve as a bridge linking innate and adaptive immune responses. TLRs are single, transmembrane, non-catalytic proteins capable of recognizing conserved structural motifs derived from microbes.[23] When microbes breach the body's physical barriers, such as the skin and mucous membranes, TLRs can identify these intruders and activate an immune cell response in the body. This dual role highlights TLRs as pivotal components in the immune system, mediating a critical link between the recognition of pathogens and the activation of immune responses, thus forming a fundamental aspect of research in the biomedical field (Figure 1-2).[24-26]

Innate immune molecules are primarily composed of cytokines, complement components, antimicrobial peptides, and enzymes. Cytokines are protein molecules produced by immune or tissue cells in response to pathogen infection or stimulation. They can induce inflammatory responses at the site of infection and also play roles in antiviral activities and immune modulation. The complement system plays a crucial role in early immune responses.[27] Pathogens invading the body can activate the complement system via the alternative pathway or through the mannose-binding lectin (MBL) pathway, leading to bacteriolysis. Additionally, once the body produces antibodies against specific pathogens, the antigen-antibody complexes can activate the complement system through the classical pathway to enhance the immune response. Antimicrobial peptides, often cationic peptides such as defensins and beta-lysin, are lethal to invading bacteria, fungi, or enveloped viruses. Lysozyme, a protease found extensively in body fluids and lysosomes, cleaves the β-1,4-glycosidic bonds between N-acetylglucosamine and N-acetylmuramic acid in the cell walls of Gram-positive bacteria, thereby disrupting the cell wall to eliminate pathogens.[28-30]

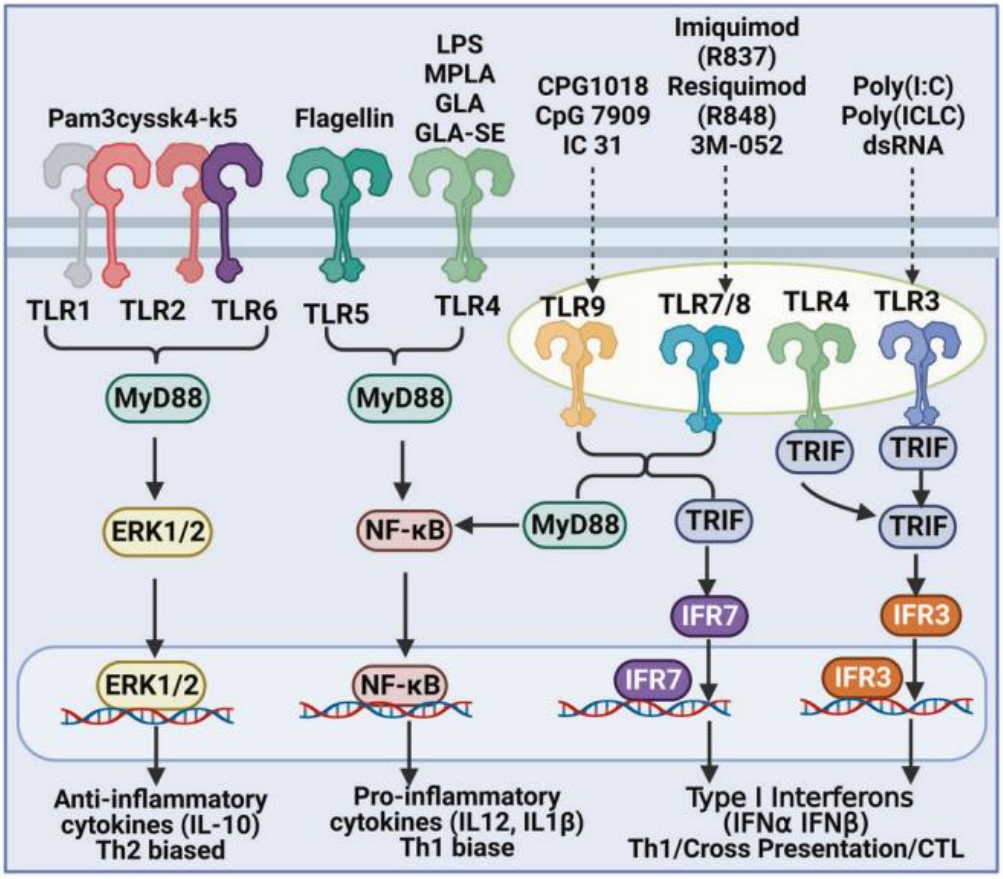

Figure 1-2 Innate immune receptors involved in virus recognition[26]

1.1.2 Adaptive immune response

Upon encountering pathogens or antigens, antigen-presenting cells (APCs) such as dendritic cells or macrophages rapidly accumulate at the site of infection and ingest the invading pathogens. These cells then migrate to the draining lymph nodes where they present antigenic peptide epitopes via Major Histocompatibility Complex (MHC) class I and/or II molecules to $CD4^+$ or $CD8^+$ T cells in the lymph nodes. Interaction of the T cell receptor (TCR) on the surface of T cells with the MHC-antigen peptide complex provides the primary stimulatory signal, while co-stimulatory factors such as CD80 and CD86 deliver a second signal essential for T cell activation.[31] Most pathogens contain pathogen-associated molecular patterns (PAMPs) such as lipopolysaccharide (LPS), viral-derived double-stranded RNA (dsRNA), and CpG, which play a crucial role in the expression of co-stimulatory factors by APCs and enhance the efficiency of antigen cross-presentation. Additionally, related immune cells produce cytokines or chemokines as a third signal, which, in conjunction with the first and second signals, influences the differentiation and function of T cells. Once activated, T cells rapidly proliferate and differentiate into effector T cells, which travel through the bloodstream to the site of infection to perform their immune functions.[32]

Many pathogenic infections do not occur inside cells but in the extracellular spaces, and these pathogens are primarily cleared through humoral immunity mediated by B cells. The response process mediated by B cells varies with the type of

antigen. Under the stimulation of thymus-dependent antigens (TD), B cells require the assistance of T helper (Th) cells, whereas for thymus-independent antigens (e.g., LPS, flagellin), B cells can directly recognize antigens and mount an immune response. In the case of TD antigens, the activation of B cells is similar to that of T cells, also requiring the involvement of related stimulatory signals and cytokines. The binding of the B cell receptor to an antigenic epitope initiates the first stimulatory signal. The second signal for activation is obtained through interaction with Th helper cells. Additionally, cytokines produced by macrophages play an essential role in the activation of B cells.[33-35]

Humoral immunity mediated by B cells can effectively clear extracellular pathogens; however, once pathogens enter cells, antibodies are unable to continue their function. In contrast, cell-mediated immunity, particularly through CTLs, can lyse target cells, thus capable of killing pathogens residing within cells or tumor cells.[36] Therefore, developing vaccines that can activate the cellular immune response is crucial for expanding the range and intensity of the body's immune response (Figure 1-3).

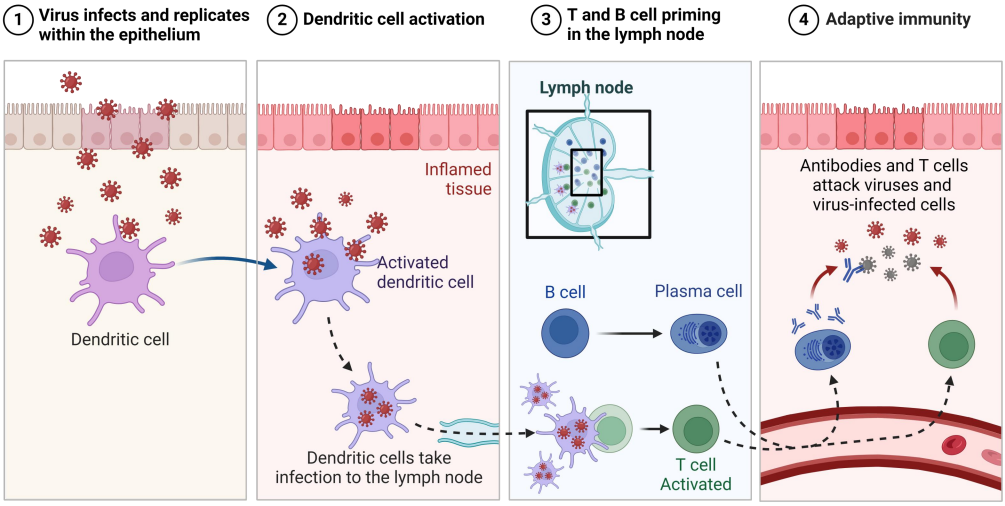

Figure 1-3 Viral infects and the corresponding adaptive immune response

1.2 The Vaccine composition.

Multicomponent vaccines comprise several crucial elements, including antigens, immune stimulants, specific targeting molecules, and efficient delivery vehicles (Figure 1-4).[37] Antigens are fundamental for eliciting specific immune responses that clear pathogens or kill tumor cells.[38] Immune stimulants, specific targeting molecules, and delivery systems play vital supportive and enhancing roles in the activation of the immune system.[39] Immune stimulants primarily act as nonspecific enhancers of immune activation pathways, triggering cascading reactions that amplify the immune effect. Specific targeting molecules are essential for multicomponent vaccines, not only efficiently targeting specific immune cells but also activating associated signaling pathway cascades, thereby strengthening the immune response of specific immune cells. Efficient delivery vehicles primarily facilitate the uptake and presentation of antigens by APCs and prevent antigen degradation, enhancing the

overall vaccine efficacy.[40]

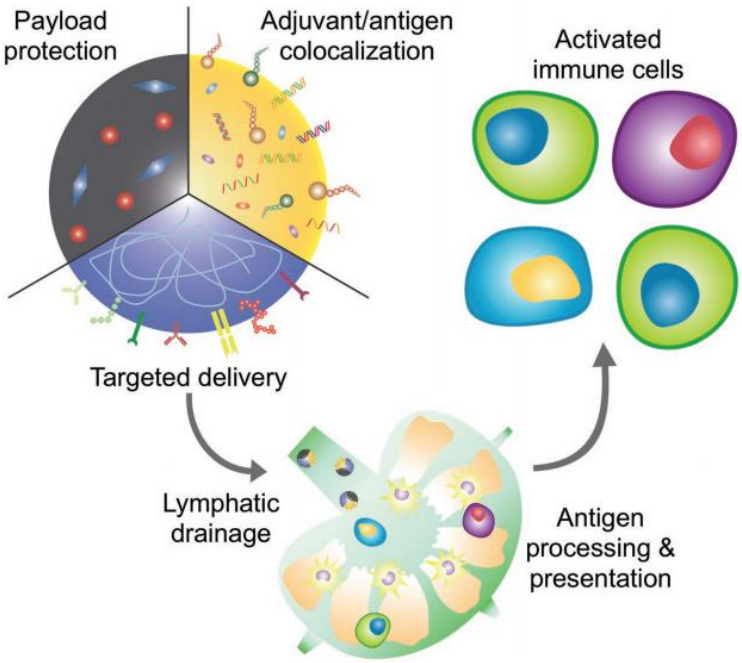

Figure 1-4 Multi components vaccine to achieve efficient immune response[37]

Toll-like receptors (TLRs) are a family of pattern recognition receptors with 10 identified TLRs in humans, TLR1 through TLR10, and 12 identified in mice, TLR1 through TLR9 and TLR11 through TLR13. TLRs are predominantly distributed on the cell surface (TLR1, TLR2, TLR4, TLR5, and TLR6) and within endosomal compartments (TLR3, TLR7, TLR8, and TLR9) (Figure 1-5). The cell surface TLRs primarily engage in the recognition of PAMPs from various pathogens, whereas the endosome-located TLRs are mainly involved in the recognition of nucleic acids from viruses or pathogenic bacteria. This distribution enables TLRs to play a crucial role in the innate immune response by detecting and responding to microbial and viral infections.[41,42]

The natural ligand for TLR3 is dsRNA. Upon recognition of dsRNA, TLR3 dimerizes and recruits the adaptor molecule TRIF, which subsequently activates transcription factors, leading to the upregulation of IFN-α and pro-inflammatory cytokines. Currently, two synthetic nucleic acid compounds, Polyinosinic-polycytidylic acid (Poly (I:C)) and Polyadenylic-polyuridylic acid (Poly (A:U)), have also been shown to effectively activate TLR3. Numerous studies indicate that activation of TLR3 can induce a CTL response, and the TRIF-dependent signaling pathway further enhances this response by upregulating IFN-γ expression. Mouse model studies have shown that Poly(I:C) can enhance the immune response to peptide-based cancer vaccines; however, this anti-tumor activity has not been observed in humans, possibly due to nucleolytic degradation of Poly(I:C). To improve the stability and safety of Poly(I:C), researchers have developed two other TLR3 ligands based on Poly(I:C): poly ICLC (a complex of Poly(I:C) with polylysine) and

poly I:C12U. These ligands retain immunomodulatory activity but exhibit lower toxicity compared to Poly(I:C).[43]

TLR4 was the first receptor protein identified in the TLRs family within animal cells. TLR4 recognizes the lipid A component of LPS produced by Gram-negative bacteria. However, the potent toxic side effects of LPS have limited its application in human vaccines. Therefore, the development of natural or synthetic attenuated LPS derivatives is particularly crucial. In 1979, Ribi et al. found that acid hydrolysis of LPS significantly reduced its toxicity without altering its antitumor effects. Subsequent alkaline treatment was discovered to specifically remove a fatty acid chain from Monophosphoryl Lipid A (MLA) to produce 3-O-Desacyl-4'-Monophosphoryl Lipid A (3D-MLA), further reducing its toxicity. Purified via liquid chromatography, MPL (Monophosphoryl Lipid A) was obtained. Natural extracts of MPL are a mixture with varying numbers and lengths of fatty chains. The purified MPL retains its immunostimulatory activity but with substantially reduced toxicity, possessing only 0.1% of the toxicity of LPS. Additionally, with advancements in chemical synthesis technology, chemically synthesized MPL analogs have also been developed, such as Glucopyranosyl Lipid Adjuvant (GLA) and Second-generation Lipid Adjuvant (SLA).[44,45]

The natural ligands for TLR7/8 are single-stranded RNAs (ssRNAs) derived from viruses. Due to the poor drug-like properties of RNA, several small-molecule compounds have been synthesized to activate TLR7/8, such as Resiquimod (R848) and Imiquimod (R837). R837 is a nucleoside analog that primarily activates TLR7, while R848 can activate both TLR7 and TLR8 in humans. Currently, most clinical trials employ R837, although no TLR7/8 agonists have yet been approved for use in vaccine adjuvants. A clinical trial targeting HIV demonstrated that R837 could significantly enhance antigen-specific T cell responses and antibody secretion. Another study found that treating Leishmania infections with R837 could enhance macrophage-dependent killing capabilities and lesion resolution. Additionally, the rapid coupling properties of TLR7/8 agonists with protein or peptide antigens make TLR7/8 agonists promising immunostimulants applicable in various fields.[46]

TLR9 is located intracellularly and can recognize nucleic acid sequences containing specific CpG motifs, primarily expressed in B cells and plasmacytoid dendritic cells (pDCs). Activation of TLR9 can induce the activation of natural killer cells, T cells, B cells, monocytes, and macrophages, as well as the release of pro-inflammatory and Th1 cytokines (e.g., IL-6, IL-1, TNF-α, IFN-γ). CpG-ODN consist of single-stranded oligonucleotides with 20-30 nucleotides containing several CpG motifs, effectively activating TLR9. Based on the structure and immunological mechanisms of CpG-ODN, they are primarily classified into three types: Class A, Class B, and Class C. Currently, dozens of drugs or vaccines containing CpG-ODN have entered clinical trials, with several having completed Phase III trials. Among them, Dynavax's Heplisav was approved by the FDA in November 2017 for use in hepatitis B vaccines. This vaccine enhances the immune response through the non-covalent binding of the hepatitis B surface antigen to the TLR9 agonist.[47]

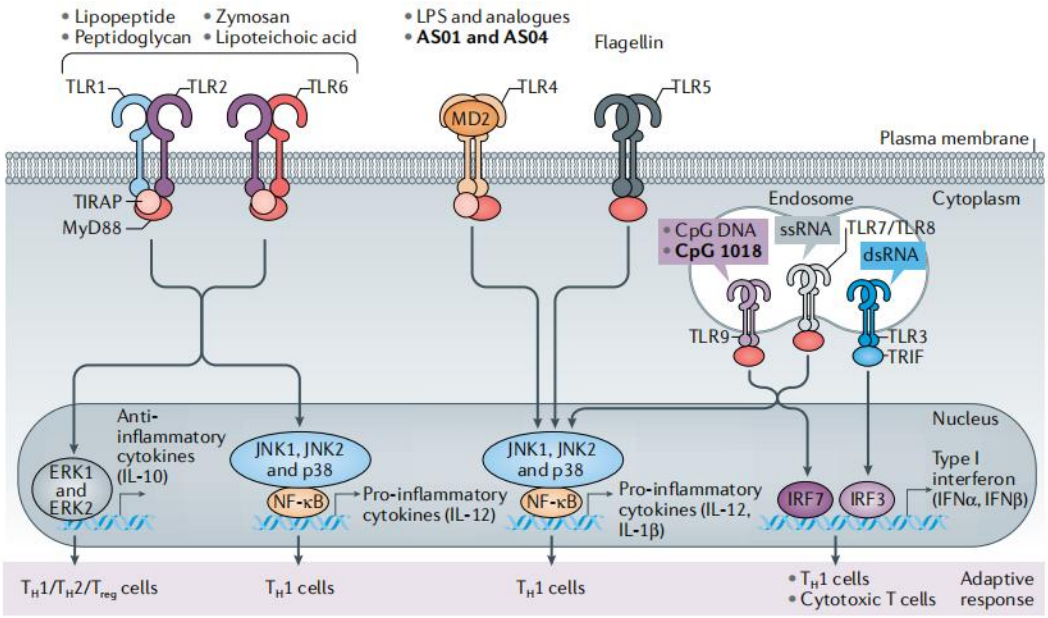

Figure 1-5 Molecular targets of TLRs. TLR1, TLR2, TLR4, TLR5 and TLR6 are expressed on the cell surface, whereas TLR3, TLR7, TLR8 and TLR9 are expressed in endosomes.[48]

1.3 Nanoparticle delivery.

With the continual advancements in nanotechnology, utilizing nanoparticles as vaccine adjuvants has become a focal area of research. Firstly, antigens or immunostimulatory molecules can be efficiently loaded into the particles, protecting them from degradation and prolonging antigen presentation time, thereby enhancing the immune response. Additionally, the intrinsic adjuvant properties can be enhanced by modulating the shape and composition of nanoparticles to mimic the characteristics of pathogens. A variety of nanoparticles have been developed, including carbon nanotubes, metallic particles, hydrogel particles, liposomes, and polymer nanoparticles (Figure 1-6).[49-52] The material composition, size, surface physicochemical properties, and shape of nanoparticles can all influence the interaction between the carrier and antigen-presenting cells, leading to different biological responses. Therefore, nanoparticles with specific properties are selected based on the particular delivery requirements.

Numerous nanoparticles have been successfully used for the delivery of proteins, peptides, nucleic acids, and other biomolecules. Biodegradable particles are particularly advantageous due to their ability to degrade within physiological environments, allowing for the sustained release of loaded drugs within the body. Currently, suitable biodegradable polymers for biological applications mainly include poly (lactic acid) (PLA), poly (lactic-co-glycolic acid) (PLGA), polycaprolactone (PCL), and alginate derivatives. PLGA is the most commonly used due to its excellent biocompatibility and FDA approval, and its degradation rate can be easily controlled by adjusting the ratio of glycolic acid (GA) and lactic acid (LA). There are numerous and well-established techniques for the preparation of PLGA particles, including nanoprecipitation and emulsification methods. Research has shown that PLGA

particles can be used to load various drugs, and the size of PLGA particles can be precisely controlled through adjustments in the oil-to-water ratio or by modifying the type and concentration of surfactants.[53,54] Despite the vast potential for applications, the clinical deployment of nanoparticles faces substantial challenges. One significant hurdle is the low encapsulation efficiency of nanoparticles, necessitating a large initial input of antigens and consequently higher costs. Furthermore, it is challenging to achieve uniform particle sizes across different batches, resulting in considerable variability that adversely affects the reproducibility of outcomes.[55]

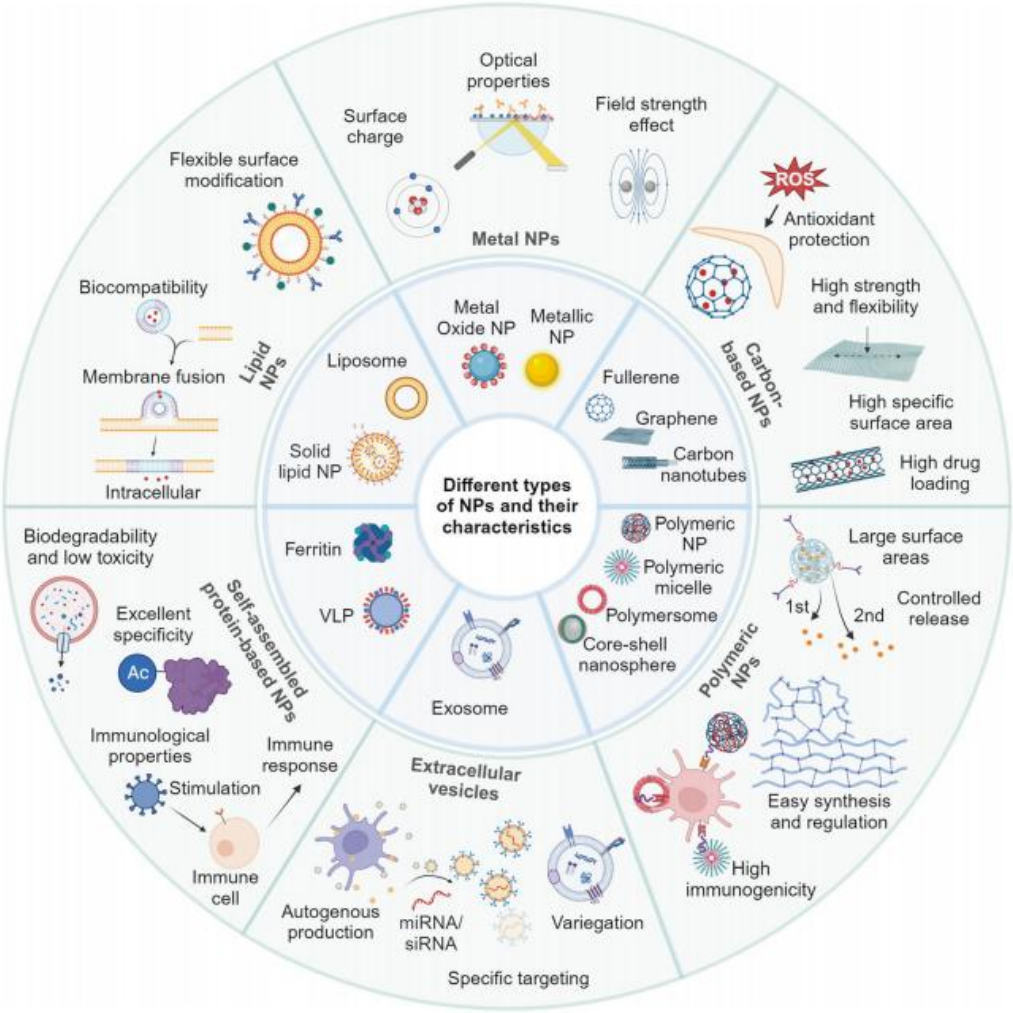

Figure 1-6 Six common nanomaterials and their characteristics.[52]

1.4 Aluminum-based adjuvants.

Aluminum adjuvants have been used in clinical settings for over 90 years and remain the only vaccine adjuvants approved for use in most developing countries. By simply mixing with antigens and immunizing the human body, they can create an antigen depot effect at the injection site, slowly releasing antigens and causing local inflammation. This recruits immune cells to the injection site, enhancing or inducing a humoral immune response. Therefore, aluminum adjuvants are commonly used as immunostimulants added to human vaccine formulations. After long-term and large-scale clinical use, their safety as human vaccine adjuvants have been widely

recognized.[56-62]

Vaccines containing aluminum adjuvants primarily function by promoting the secretion of antigen-specific antibodies, thereby enabling the body to achieve a protective immune response (Figure 1-7). Examples of such vaccines include those against diphtheria, tetanus, hepatitis B, hepatitis A, and rabies. Currently, 25 vaccines that include aluminum salt adjuvants have been approved by the FDA for clinical use in humans. During his research on the diphtheria vaccine, Glenny discovered that adding potassium aluminum sulfate to the vaccine significantly enhances its immunogenicity, eliciting a stronger and more sustained immune response. Since then, aluminum salts have been utilized in vaccines to prevent various infectious diseases. The types of aluminum salt adjuvants approved by the FDA as vaccine additives include aluminum hydroxide, aluminum phosphate, and amorphous aluminum hydroxyphosphate sulfate. Additionally, vaccines like TWINRIX and PEDIARIX incorporate a mixture of aluminum hydroxide and aluminum phosphate as adjuvants.

Different types of aluminum salts exhibit distinct physicochemical properties, which are crucial for their immunomodulatory effects. The commercial aluminum hydroxide adjuvant is actually a crystalline form of aluminum oxyhydroxide (AlOOH). In contrast, aluminum phosphate chemically constitutes an amorphous form of aluminum hydroxyphosphate, denoted as Al (OH)x (PO4) y. Another type of commercially used aluminum salt adjuvant is amorphous aluminum hydroxyphosphate sulfate (AAHS). The surface charges of these aluminum salts also significantly differ; for instance, in physiological solution (pH = 7.4), aluminum hydroxide carries a positive charge, aluminum phosphate carries a negative charge, and AAHS nearly unchanged. The isoelectric points of aluminum phosphate, AAHS, and aluminum hydroxide are respectively 5.0, 7.4, and 11.1.[63]

Extensive research indicates that the cellular immune response to aluminum adjuvants, particularly the Th1-associated adaptive immune response, is suboptimal. In fact, when aluminum adjuvants interact with dendritic cells (DCs), they bind strongly to the DC cell membranes in a manner that does not depend on inflammasomes or membrane proteins, initiating lipid sorting and promoting antigen phagocytosis. However, the aluminum adjuvants themselves do not enter the cells, thus minimally affecting the intracellular presentation of the antigen. As a result, antigens processed via the lysosomal pathway are predominantly presented by MHC-II molecules, inducing a protective humoral immune response. They do not elicit a therapeutic $CD8^+$ T cell immune response through cross-presentation via MHC-I molecules. This limitation could restrict the use of aluminum adjuvants in therapeutic vaccines and cancer immunotherapy applications.[64-67]

Although aluminum adjuvants are widely used as a safe and effective component in various vaccine formulations, the mechanisms by which they enhance immunity remain a subject of considerable debate. The prevailing theories include the "antigen depot effect" and the "immune stimulation effect". Recent studies have also proposed that aluminum adjuvants facilitate local cell apoptosis, which triggers the release of danger signals and inflammatory cytokines, thereby stimulating an immune response. This understanding helps to elucidate the complex interplay between aluminum

adjuvants and the immune system, highlighting their multifaceted role in vaccine efficacy.[68,69]

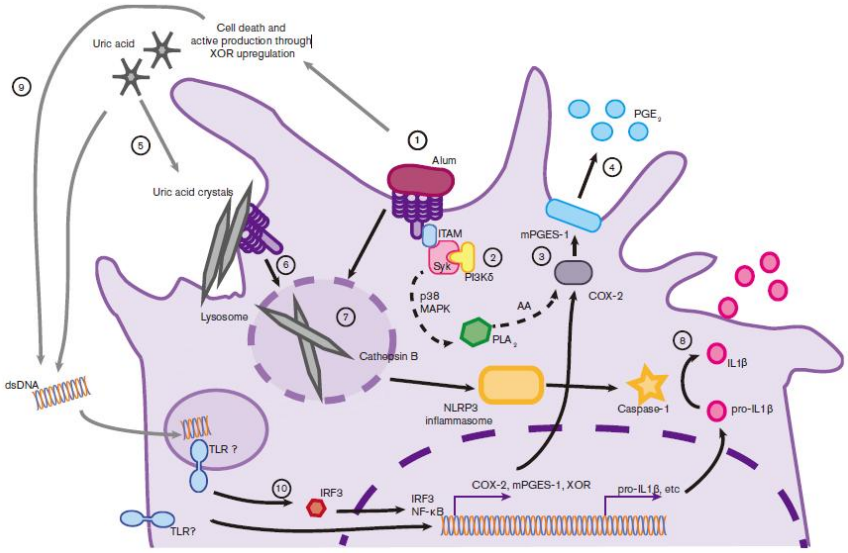

Figure 1-7 Models for the activation mechanism of aluminum salt-based adjuvants.[70]

1.5 Oil emulsion adjuvant delivery.

Oil emulsion adjuvants are one of the widely used commercialized adjuvants in animal vaccines. They can assist single or multiple antigens, stimulating the body to produce a rapid immune response, generating high levels of antigen-specific antibodies that are maintained over a long period within the body, thus offering prolonged protection.[71-73] The mechanisms by which Oil emulsion adjuvants enhance immunity include several key aspects: (1) The oil droplets protect the antigen from enzymatic degradation present in bodily fluids, reducing antigen loss and increasing the likelihood of contact between the antigen and immune cells. (2) The antigens embedded in the oil phase are released slowly, continually inducing specific immune responses. (3) The oil phase of the emulsion adjuvant induces local inflammatory reactions at the injection site, which is beneficial for the recruitment and proliferation of immune cells, enhancing both cellular and humoral immunity. Fourth, oil emulsion adjuvants transport antigens stored at the injection site through the lymphatic system to lymph nodes and the spleen throughout the body, thereby generating a new stimulatory effect for antigen induction.[74-76]

Based on the type of oil used, oil emulsion adjuvants are categorized into mineral oil and non-mineral oil adjuvants. Freund's adjuvant, a classic example of a mineral oil adjuvant, includes both complete and incomplete Freund's adjuvant. However, these adjuvants are known for their significant toxicity and poor stability at room temperature, making long-term storage challenging. Currently, these adjuvants are no longer used in vaccine formulation production and are only utilized for basic research purposes in experimental settings. In contrast, non-mineral oil adjuvants are made from oils that are easier to metabolize, such as squalene. Compared to traditional mineral oil adjuvants, non-mineral oil adjuvants exhibit virtually no significant adverse effects. During their production, surfactants like Tween 80 and Span 85 are

typically added, and then oil emulsion adjuvants are prepared using shear forces such as high-pressure homogenization, ultrasonication, or high-pressure micro-fluidization. The final commercial oil emulsion adjuvants are filtered through a 0.22 μm polysulfone membrane to ensure the uniformity of the particle size of the prepared emulsions. Currently, the FDA-approved oil emulsion adjuvants developed based on squalene include AS03 (by GSK) and MF59 (by Novartis).

MF59 was the first oil-in-water adjuvant approved for use in human vaccines in Italy in 1997. Primarily used in the development of influenza vaccines, researchers have found that incorporating MF59 into influenza vaccine formulations can significantly enhance antigen-specific antibody levels and boost both Th1 and Th2 immune responses. Regarding the mechanism by which MF59 enhances immune responses (Figure 1-8), it is primarily believed to recruit monocytes, macrophages, and dendritic cells at the injection site. These recruited cells internalize the antigen and secrete chemokines, which further attract more antigen-presenting cells to the injection site, forming an immunological microenvironment. This facilitates the uptake of the antigen and the homing of antigen-presenting cells to the lymph nodes, thereby inducing a robust immune response within the lymph nodes.[77]

AS03 is an oil-in-water emulsion adjuvant, and a monovalent H5N1 influenza vaccine based on AS03 was approved by the FDA in 2013. Since then, AS03 has played an increasingly important role in influenza and malaria vaccines. Studies show (Figure 1-8) that AS03 can induce the production of cytokines and chemokines in the muscle at the injection site and the draining lymph nodes (dLNs), promoting the migration of monocytes, dendritic cells, and granulocytes to the dLNs. Additionally, AS03 has been found to stimulate $CD4^+$ T cell-specific immune responses, which likely contributes to the sustained production of neutralizing antibodies and the generation of a higher number of memory B cells (Figure 1-8).[78-81]

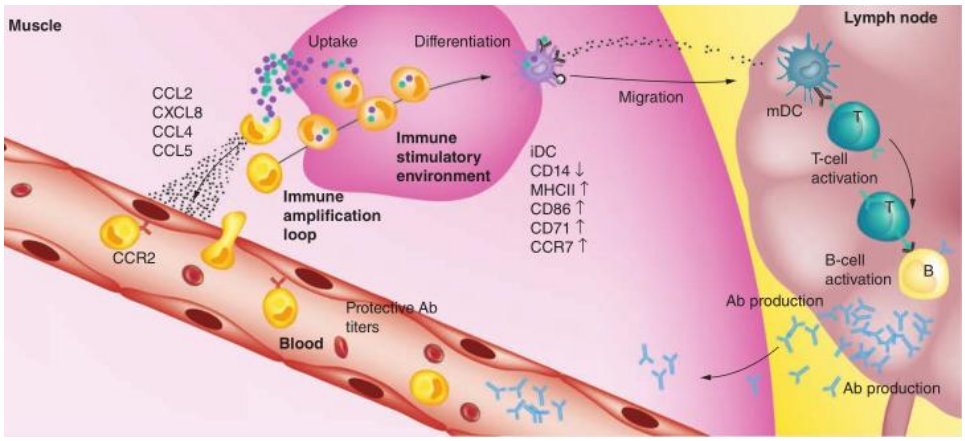

Figure 1-8 Models for the activation mechanism of MF59 and AS03 adjuvants.[82]

1.6 Particle-stabilized emulsion.

In recent years, with in-depth research into Pickering emulsions, the mechanisms of their immunological effects have been progressively elucidated.[83-85] The main perspectives include the following. (1) Pickering emulsions, characterized by their unique surface structure with nanoparticles adsorbed at the oil-water interface,

possess a larger specific surface area, significantly enhancing the antigen loading capacity. For instance, a Pickering emulsion stabilized by PLGA nanoparticles (PLGA nanoparticle-stabilized emulsion, PPAS) shows antigen adsorption rates for OVA antigen and MUC1 peptide antigen that are respectively twice and seven times higher than those of the commercial adjuvant MF59. This demonstrates that the structural configuration of Pickering emulsions is advantageous for antigen loading, potentially leading to a more effective stimulation of the immune response.[86]

1.6.1 Antigen loading efficiency

Pickering emulsions, characterized by their unique surface structure with nanoparticles adsorbed at the oil-water interface, possess a larger specific surface area, significantly enhancing the antigen loading capacity. For instance, a Pickering emulsion stabilized by PLGA nanoparticles showed antigen adsorption rates for OVA antigen and MUC1 peptide antigen that are respectively twice and seven times higher than those of the commercial adjuvant MF59. This demonstrates that the structural configuration of Pickering emulsions is advantageous for antigen loading, potentially leading to a more effective stimulation of the immune response.

1.6.2 Capable of deformability

For O/W (oil-in-water) type Pickering emulsions, which feature an oily core, they are capable of exhibiting mechanical deformation. Xia et al. characterized the flexibility of PPAS using a quartz crystal microbalance. The experiments revealed that these Pickering emulsions mostly adsorbed onto the cell membrane and did not flow out with the moving phase. This suggests that the emulsions can deform on the surface of the membrane, increasing the contact area between the emulsion and the cell membrane, potentially enhancing cellular interactions.

Additionally, compared to surfactant-stabilized emulsions (SSE), the PPAS Pickering emulsions exhibits higher vibration frequency (AF) and dissipation factor (AD), indicating superior viscoelasticity and flexibility. This may be attributed to the uneven surface of PPAS, which facilitates more effective interactions with the cell membrane, thereby enhancing the capture of APCs. In summary, Pickering emulsions demonstrate excellent flexibility, which increases the contact area with immune cells and holds potential for enhancing immune responses. This property positions Pickering emulsions as promising candidates in the field of biomedicine for vaccine and therapeutic applications (Figure 1-9).

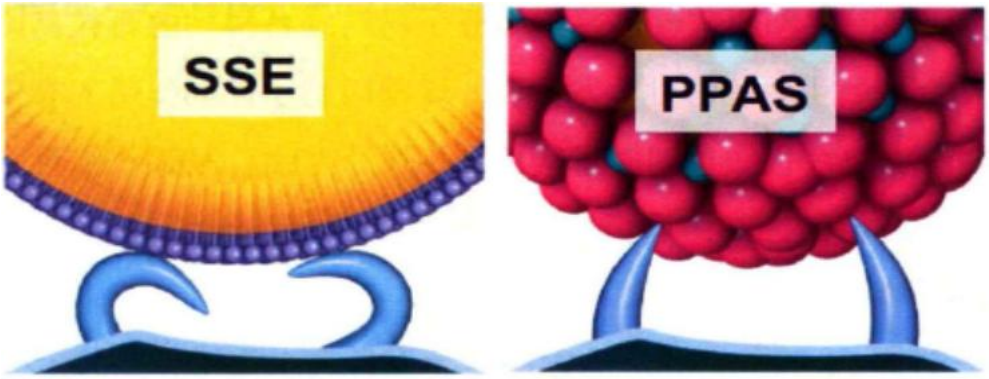

Figure 1-9 Schematic diagram of the interaction between cells and SSE/PPAS[86]

1.6.3 Antigen mobility

Due to the rough and uneven surface of Pickering emulsions, antigens can not only adsorb onto the surface of the particles but also flow within the interstices, thereby dynamically activating the recognition and uptake by immune cells and enhancing the immune response. Xia. and colleagues confirmed this mechanism using fluorescence recovery after photobleaching (FRAP) techniques. After photobleaching, the fluorescence of the antigens was significantly restored over time, whereas the fluorescence of the particles did not show this recovery. This indicates that the unique surface structure of Pickering emulsions enables antigens to flow between the interstices of the particles, which facilitates their recognition and uptake by immune cells, thereby strengthening the immune response. This feature highlights the potential of Pickering emulsions to enhance immunogenicity in vaccine applications within the biomedical field (Figure 1-10).

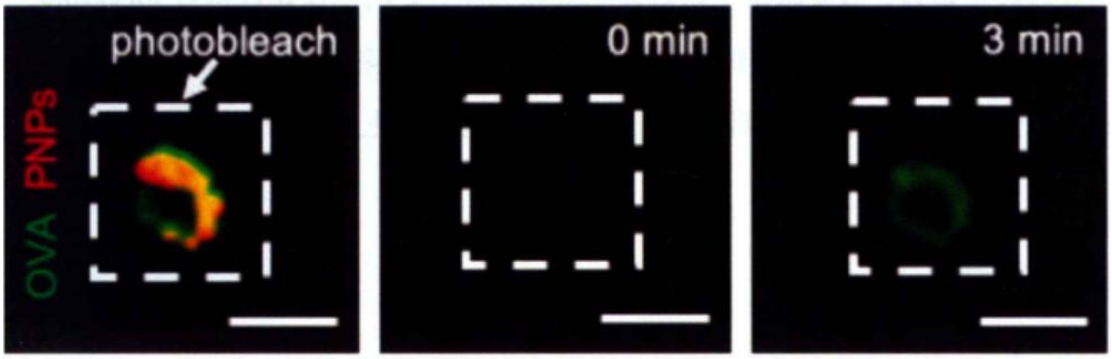

Figure 1-10 Schematic diagram of the interaction between cells and SSE/PPA[86]

Leveraging our prior investigations, alum-stabilized Pickering emulsions exhibit a higher affinity for DCs uptake, and acts as immune stimuli to induce the expression of high levels of co-stimulatory molecules, essential for T cell binding and maturation. Additionally, once internalized by APCs, these droplets can escape from lysosomes due to their positively charged property, thereby facilitating cross-presentation of peptide. Furthermore, due to the hydrophobic core of Pickering emulsion, the release kinetics can be easily tuned by engineering the length of the hydrophobic chain on the lipo-peptide. Finally, when alum is used as stabilizer of droplets, utilizing the positive charge properties of alum, the negatively charged substances can effectively adsorbed on the surface of droplets. Thus, alum-stabilized Pickering emulsions possess properties that enable the efficient, multistage loading of substances, allowing for the sequential release of different agents within cells. This capability facilitates the optimal immune response by regulating the spatio-temporal differential release of these agents.[87]

Based on the aforementioned research, we have selected an alum-stabilized Pickering emulsion as the antigen delivery system. This system facilitates the spatiotemporal sequential loading and release of antigens, allowing us to simultaneously investigate the optimal immunization strategy through the sequential

release of antigens.

In Chapter 2, we evaluated the potential of alum-stabilized Pickering emulsion as a cancer vaccine and optimized the immune strategy. Chicken egg albumin (OVA), composed of 386 amino acids and with a molecular weight of about 45 kD, was selected as the model antigen. We first proved the T cell engagement after intramuscular injection of APE/OVA. Additionally, the effectiveness against tumor regression of two administrations (APE-2), three administrations (APE-3), and four administrations (APE-4) of the vaccine was estimated and compared. A more detailed analysis in tumor draining lymph nodes (TDLNs) and the tumor microenvironment (TME) was undertaken to assess the underlying mode of action of the anti-tumor effect of multiple vaccinations. Finally, we combined the APE-adjuvant vaccine with anti-programmed cell death 1 ligand 1 antibody (anti-PD-1) to further amplify the effector T cell potency and induce potent anti-tumor immune responses.

In Chapter 3, soft particle-stabilized emulsions (SPEs) were developed to modulate the antigen release dynamics and APC activation (Figure 1-12). Leveraging our prior investigations, these droplets exhibited enhanced APC uptake and acted as immune stimuli, promoting robust expression of co-stimulatory molecule, such as CD86 and CD80, essential for T cell binding and maturation. Additionally, once internalized by APCs, the positively charged droplets facilitated escape from lysosomes, enhancing peptide cross-presentation. By adjusting the hydrophobic chain length of the lipopeptides, the antigen release kinetics can be easily tuned, yielding SPEs with varied release profiles but similar immunogenicity, such as C_6-SPE (fast release), C_{10}-SPE (medium release), and C_{16}-SPE (slow release). After intramuscular injection, C_{10}-SPE induced coordinated upregulations of antigen cross-presentation (MHC-I-peptide complex) and the expression of co-stimulatory molecule (CD86), leading to stronger T cell response and anti-tumor effects, contrasting with C_6-SPE and C_{10}-SPE. Additionally, co-delivering CpG with C_6-SPE addressed early deficits in APC activation and was associated with increased antigen cross-presentation, eliciting significantly reduced tumor volumes and prolonged mice survival that comparable to C_{10}-SPE. This indicated that synchronizing the spatiotemporal dynamics of antigen presentation and APC activation may confer an optimal strategy for cancer vaccines.

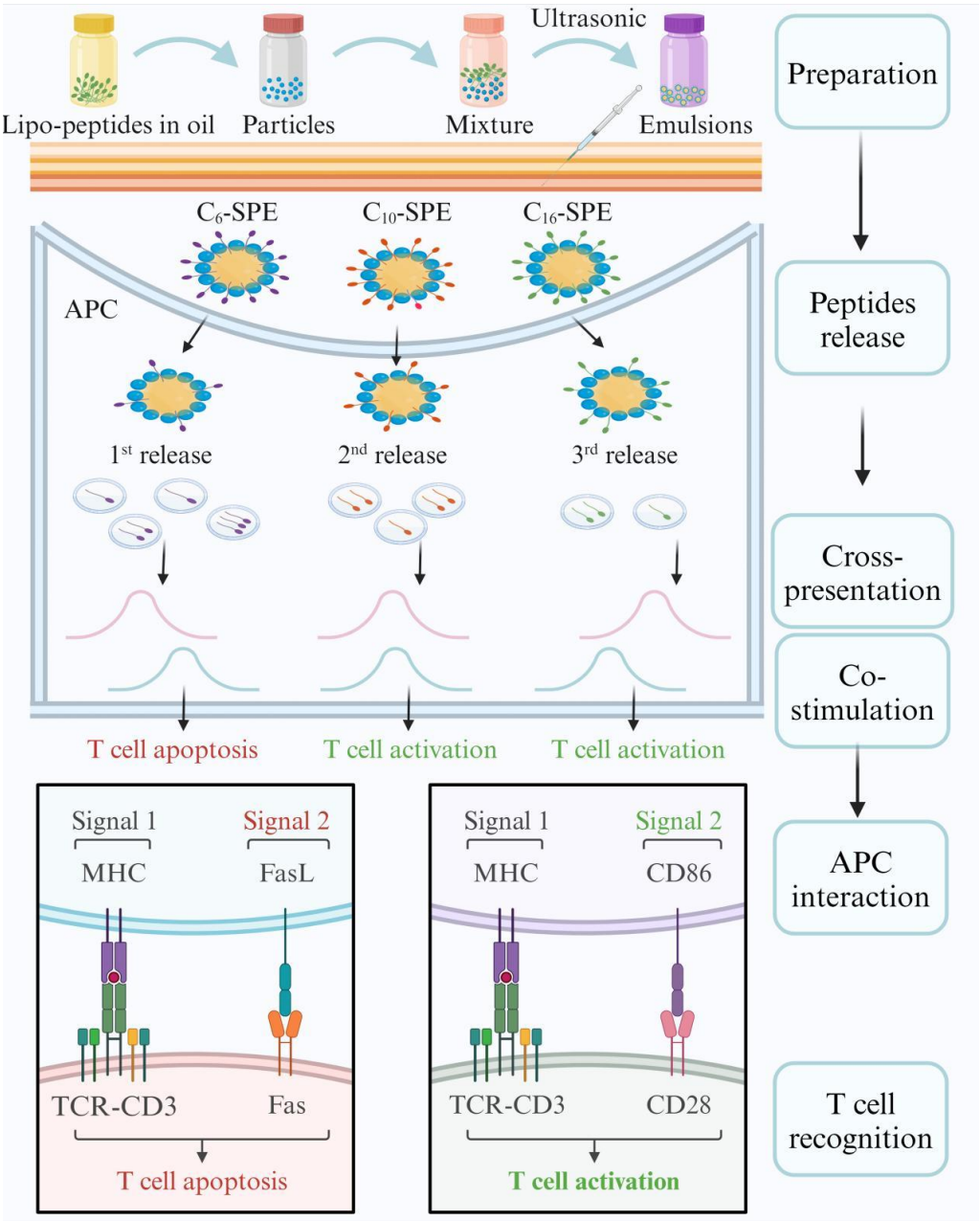

Figure 1-12. Schematic illustration depicting the preparation process and mechanism of emulsions for the sequential release of lipopeptides. This diagram also highlights the synergistic of cross-presentation and the co-stimulatory molecule for regulation T cell apoptosis and activation.

In Chapter 4, Multi-layered aluminum hydroxide-stabilized emulsion (MASE) was designed to optimize the delivery sequence of antigens and enhance immune responses against enveloped RNA viruses (Figure 1-11). Through the co-assembly of alum and antigen at the oil/water (o/w) interface, the core antigen was trapped within the nanocage formed by the alum and o/w interface. Subsequently, another layer of alum was deposited, which further shielded the inner antigen and provided adsorption sites for the outer antigen. As such, the embedded antigen was only released after the detachment of the deposited alum, thus constituting the sequential delivery system.

On the o/w interface, the layer-by-layer assembly may bypass the multiple encapsulation procedures and the involvement of organic reagents, assuring the epitope integrity of the proteins and the consecutive loading of surface antigen and NP in a facile and moderate way. To demonstrate the natural dissemination, surface antigen and NP were assembled consecutively on the outside and inside of the multi-layered droplets (iMASE). In contrast, the inside-out assembly reversed the delivery of surface antigen and NP (rMASE), thereby exposing the "soft spot" of the viruses. Consequently, it is anticipated that the inside-out strategy can cultivate the reversed encounter of the surface and core antigens to the immune system, which may strongly stimulate the anti-viral host immune responses. In this manner, IFN-I-mediated innate immune response may be activated for enhanced adaptive immune responses.

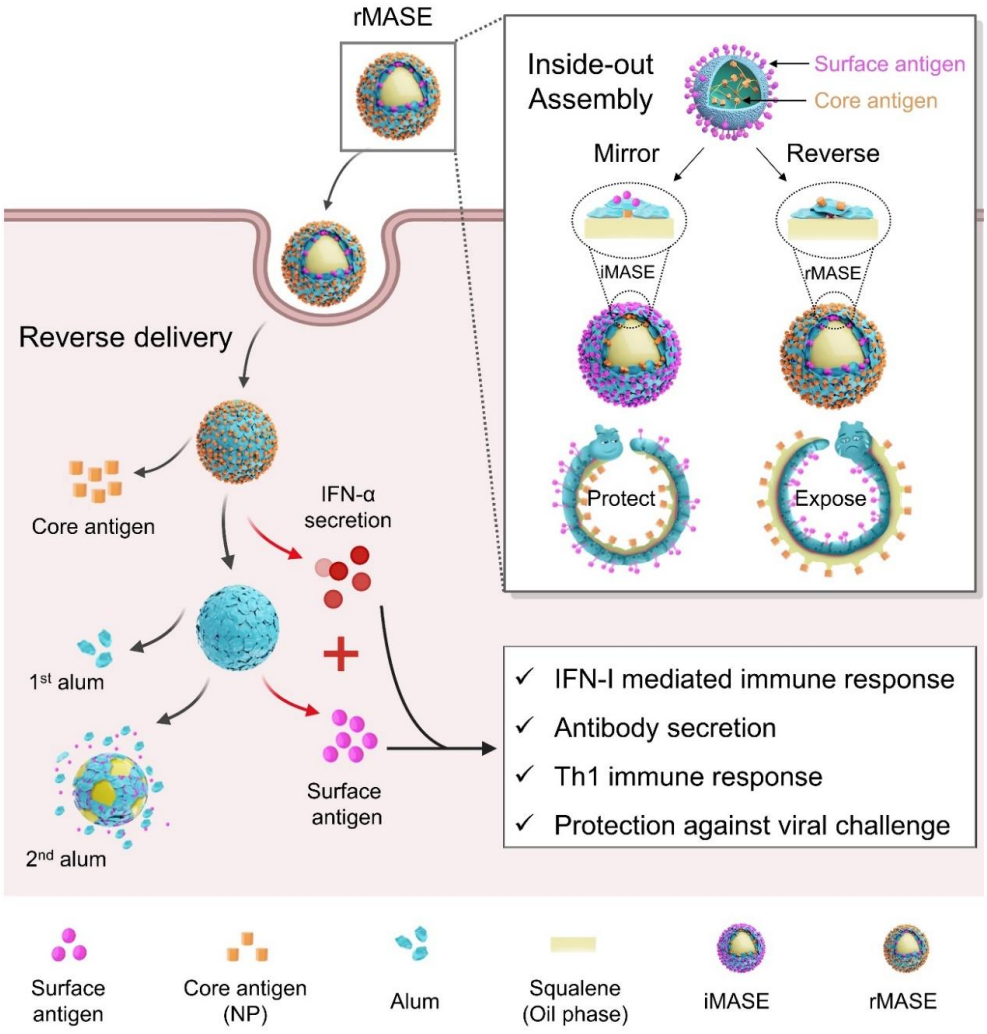

Figure 1-11 **Schematic illustration of the inside-out assembly of the viral antigens.** Compared with the natural dissemination (iMASE, left), the reversed delivery (rMASE, right) allowed for the prior encountering of NP to the immune surveillance, as hidden caterpillars (pathogens) forced to expose their "soft spot" to the predators (immune systems), provoking IFN-I secretion in advance. Along with the delivered surface antigen, rMASE promoted the innate immune response for the enhanced antibody secretion, antigen-specific T cell immune response against viral challenge.

Chapter 2 Development and Optimal Immune Strategy of an Alum-Stabilized Pickering emulsion for Cancer Vaccines

2.1 Abstract

Therapeutic cancer vaccines are considered as one of the most cost-effective ways to eliminate cancer cells. Although many efforts have been invested into improving their therapeutic effect, transient maturation and activations of dendritic cells (DCs) cause weak responses and hamper the subsequent T cell responses. Here, we report on an alum-stabilized Pickering emulsion (APE) that can load a high number of antigens and continue to release them for extensive maturation and activations of antigen-presenting cells (APCs). After two vaccinations, APE/OVA induced both IFN-γ-secreting T cells (Th1) and IL-4-secreting T cells (Th2), generating effector $CD8^+$ T cells against tumor growth. Additionally, although they boosted the cellular immune responses in the spleen, we found that multiple administrations of cancer vaccines (three or four times in 3-day intervals) may increase the immunosuppression with more PD-1^+ $CD8^+$ and LAG-3^+ $CD8^+$ T cells within the tumor environment, leading to the diminished overall anti-tumor efficacy. Combining this with anti-PD-1 antibodies evidently hindered the suppressive effect of multiple vaccine administrations, leading to the amplified tumor regression in B16-OVA-bearing mice.

2.2 Introduction

As a safe and effective therapeutic modality, cancer immunotherapy aims to activate the endogenous immune responsiveness and eliminate malignant cells by eliciting antigen-directed cytotoxicity of functional tumor-specific cytotoxic T cells.[88-90] Cancer immunotherapy approaches are classified into several categories, and tumor vaccination, as one of the most attractive immunotherapy strategies, provokes a persistent T cell activation and acquisition of effector functions, and it displays clear rationale and compelling preclinical data for further development.[91,92] In order to elicit effector T cell for recognition and elimination of tumor cells, the ideal vaccines are expected to deliver antigens to the antigen-presenting cells (APCs), such as dendritic cells (DCs), and allow them to activate with immunogenic signals and process and present the antigens.[93,94] In this step, fluid antigens fail to potently enter the APCs, and there is a demand for delivery vehicles or adjuvants to stimulate the activations of APCs.[95] Next, the primed DCs, with a high expression of activation and/or maturation signals, would further differentiate and migrate to the lymph nodes to present antigens to naive T cells,[96,97] with the robust secretion of a series of immunogenic cytokines, such as IL-12, IFN-α, IL-10, etc.[98] The activations of APCs should lead to the expansion of T cells in sufficient amounts for recognizing and eliminating malignant cells.[99] Accordingly, dynamic APC activations, which capture, process, and present tumor antigens to T cells systematically and act as immunostimulants, are vital for the onset of anti-tumor effects in cancer vaccines.[100]

Based on our previous research, with the ability to efficiently load antigens and enter APCs, and elicit robust and durable activation, particle-stabilized emulsion (Pickering emulsion) composed of oil and nanoparticles is regarded as a potential vaccine candidate for cancer therapies.[101,102] Furthermore, alum-stabilized Pickering emulsion (APE) using a commercialized aluminum adjuvant (termed "alums") and the US Food and Drug Administration (FDA)-approved squalene is regarded as able to achieve safe transfer in the clinic.[103] Simply preparing and long-term preserving of it further promote its clinical translation. Moreover, APE was developed with the following functions. (1) The particle adsorbed interphase offers higher adsorption of antigens, leading to amplified antigen delivery. (2) Hydrophobicity of the APE allows for increased APC uptake and activations. (3) The delivered antigens can escape from lysosomes by APE because of the positive charge of the oil/water interface, facilitating the cross-presentation to T cells for higher cellular immune responses. The abovementioned advantages have led to a mixed Th1 and Th2 activation by APE, which was found to offer comprehensive immune protection against COVID-19.[104] To broaden its clinical applicability, the potential of APE as a tumor vaccine should be investigated. To achieve the optimal therapeutic effect, it is necessary to explore the best immunization strategy, including the use of booster vaccinations. Increasing the number of administrations is frequently employed in clinical tumor vaccines to increase anti-tumor efficacy. However, in many trials, the effectiveness remains limited after frequent vaccinations and with advancing cancer growth.[105] Numerous studies have shown that persistent antigen presentation could lead to amplification of exhausted T cells, thus resulting in a decrease in the effector functions and an increase in the expression of PD-1 in the immunosuppressive microenvironment for the hindered tumor regression.[106-108] Therefore, developing an optimal immune strategy of APE for cancer vaccines is crucial to enhance the anti-tumor efficacy.

Here, we evaluated the potential of alum-stabilized Pickering emulsion as a cancer vaccine and optimized the immune strategy. Chicken egg albumin (OVA),[109] composed of 386 amino acids and with a molecular weight of about 45 kD, was selected as the model antigen. We first proved the T cell engagement after intramuscular injection of APE/OVA. Additionally, the effectiveness against tumor regression of two administrations (APE-2), three administrations (APE-3), and four administrations (APE-4) of the vaccine was estimated and compared. A more detailed analysis in tumor draining lymph nodes (TDLNs) and the tumor microenvironment (TME) was undertaken to assess the underlying mode of action of the anti-tumor effect of multiple vaccinations. Finally, we combined the APE-adjuvant vaccine with anti-programmed cell death 1 ligand 1 antibody (anti-PD-1) to further amplify the effector T cell potency and induce potent anti-tumor immune responses.

2.3 Materials and Methods

2.3.1 Materials

Alum Hydroxide Gel Adjuvant (10 mg/mL) was purchased from invivoGen (San Diego, CA, USA). The micro-BCA kit, ovalbumin (OVA), and FDA-approved squalene were purchased from Sigma (Saint Louis, MI, USA). Penicillin–

streptomycin, Dulbecco's modified Eagle medium (DMEM), Roswell Park Memorial Institute (RPMI) 1640, and fetal bovine serum (FBS) were purchased from GIBCO BRL (Gaithersburg, MD, USA). Mouse IFN-γ and IL-4 ELISpot BASIC kits and BCIP/NBT-plus substrate for ELISpot were purchased from Mabtech (Stockholm, Sweden). Poly vinylidene difluoride-backed plates were received from Merck-Millipore (Burlington, MA, USA). All other reagents used in this study were of analytical grade.

2.3.2 Cell Culture

B16-OVA tumor cells were obtained from ATCC (Manassas, VA, USA) and were cultured in DMEM. The cell lines used in this study were confirmed to be without mycoplasma contamination. All media included both 10% heat-inactivated FBS (v/v) and 1%penicillin–streptomycin (v/v).

2.3.3 Mice

C57BL/6 mice (6- to 8-week-old females) were received from Vital River Animal Laboratories (Beijing, China). All mice were housed in ventilated cages without pathogens and offered suitable humidity, temperature, and light–dark cycles. All animal experiments were reviewed and approved by the Institutional Animal Use Committee of the Institute of Process Engineering (Chinese Academy of Sciences).

2.3.4 Preparation of APE

APE was prepared through a single-step sonication of alum as a colloidal stabilizer and squalene as a dispersion phase. Specifically, alum was dispersed in ultrapure water to form the aqueous phase. Squalene, which served as the oil phase, was further added at an oil/water ratio of 1/9 (v/v). Then, uniform emulsion droplets were prepared by single-step sonication (Branson Digital Sonifier, total time = 120 s, power = 30%, interval time = 4 s). OVA as a model antigen was assembled on the emulsion droplets through electrostatic adsorption, and the loading efficiency was measured by a micro-BCA kit.

2.3.5 Vaccination Study

Female C57BL/6 mice (6–8 weeks old) (n = 6 mice per group) were intramuscularly immunized with 100 µL APE (100 µg alum + 5 µL squalene) containing 10 µg OVA per mouse based on the indicated schedule (Figure 2-1). One week after the final immunization, the mice were sacrificed and their spleens were collected for subsequent immune assessment.

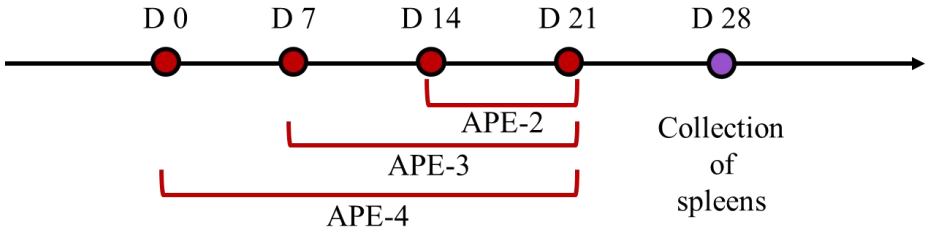

Figure 2-1 Schematic diagram of vaccination regimens. (Red dots: vaccinations of APE on different time points; Purple dot: collection and analyses of splenocyte on day

28).

2.3.6 ELISpot Evaluations

For ELISpot evaluations, 96-well PVDF-packed plates (Millipore) were activated by 35% ethyl alcohol followed by washing 5 times with pure water. Then, the plates were coated with anti-mouse IFN-γ or IL-4 antibodies (5 μg/mL, 100 μL/well) overnight at 4 ℃. The next day, after washing two times, the plates were blocked using culture medium (RPMI 1640 with 10% FBS) in the dark for at least 1 h. Then, splenocytes from vaccinated mice 7 days after the final administration were added (5×10^5 cells/well, 100 μL/well) with OVA model antigen (2 μg/mL) and cultured for 24 h (37 ℃, 5% CO_2) without moving the plates. After removing cells and washing five times, the plates were incubated in the dark using detection antibody (1 μg/mL, 100 μL/well) for more than 2 h, followed by streptavidin-ALP detection antibody (1 μg/mL, 100 μL/well) at 25 ℃. Then, the BCIP/NBT (100 μL/well) was added to the plates and incubated for about 5 min without light. Finally, the plates were washed with pure water and air-dried without light overnight. The spots were scanned and counted via an ELISpot Analyzer (AT-Spot 2100, Antai Yongxin Medical Technology, Beijing, China). Each of the experiments was repeated three times, obtaining similar results each time.

2.3.7 Cytokine Secretion and Immune Cells in the Spleen

The vaccinated mice were sacrificed humanely 7 days after the final administration, and the spleens were isolated for further mechanical disruption for the preparation of cell suspensions. After lysis of the red blood cells, the single-cell suspensions were added to 24-well plates (2×10^6 cells/well) and restimulated with the OVA (2 μg/mL) at 37 ℃, 5% CO_2 for 48 h. Next, the supernatant was collected by centrifugation (10,000 × g, 5 min) for further cytokine secretion assays (IL-2, IL-4, IFN-γ, TNF-α, granular enzyme B) via ELISA kits from Solarbio (Beijing, China). The treated cells were collected (500 × g, 5 min) and stained with fluorescent antibodies stained with Ghost Dye™ Violet 450, APC-Cy7 anti-mouse CD3e antibody, PerCP-Cyanine5.5 anti-mouse CD8 antibody, and PE anti-mouse SIINFEKL-Pentamer antibody and analyzed by flow cytometry. According to the manufacturer's handbook, the antibody dilution was performed for flow cytometry staining. Data were collected by flow cytometry (CytoFlex LX, Beckman Coulter, Brea, CA, USA). Three repetitions of each experiment were carried out.

2.3.8 Cytokine Secretion and Immune Cells in Tumors and TDLNs

For the tumor-bearing mice, 3 days after the last immunization, the mice were sacri-ficed humanely and the tumors and TDLNs were isolated for further mechanical disruption for the preparation of single-cell suspensions. Specifically, TDLNs were mechanically disrupted and resuspended in PBS. Single-cell suspensions obtained from the TDLNs were collected by centrifugation (500 × g, 5 min) and stained with fluorescent antibodies stained with Ghost Dye™ Violet 450, APC-Cy7 anti-mouse CD3e antibody, PerCP-Cyanine5.5 anti-mouse CD8 antibody, APC anti-mouse LAG 3 antibody, and FITC anti-mouse PD-1 antibody.

For immune cell analysis in tumors, the tumors were suspended in whole blood and tissue diluent (100 mg tissue/mL) and mechanically disrupted. Tumor-infiltrating lymphocytes (TILs) were obtained by using a mouse tumor-infiltrating tissue lymphocyte isolation kit (Solarbio, Beijing, China), following the manufacturer's instructions. Firstly, the single cells were collected at 500 × g for 5 min at 4 ℃ and resuspended in 5 mL of whole blood and tissue diluent. Next, the single-cell suspension was slowly dropped into 5 mL of lymphocyte isolation fluid for tumor-infiltrating tissue and centrifuged at 900 × g for 30 min at 4 ℃. Finally, lymphocytes were gently collected, washed three times using washing solution, and stained with fluorescent antibodies stained with Ghost Dye™ Violet 450, APC-Cy7 anti-mouse CD3e antibody, PerCP-Cyanine5.5 anti-mouse CD8 antibody, APC anti-mouse LAG-3 antibody, and FITC anti-mouse PD-1 antibody, before being analyzed by flow cytometry.

According to the manufacturer's handbook, the antibody dilution was performed for flow cytometry staining. Data were collected by flow cytometry (CytoFlex LX, Beckman Coulter, Brea, CA, USA). Three repetitions of each experiment were carried out.

2.3.9 Evaluation of Health

For detection of the serum biochemical parameters, 7 days after final vaccination, blood supernatant samples were collected through the retro-orbital route, and we analyzed the levels of AST, ALT, BUN, ALP, and LDH via an automated analyzer (Hitachi 917, Hitachi Ltd., Tokyo, Japan). To determine the morphological changes in the main visceral organs, the hearts, spleens, livers, kidneys, and lungs were harvested and fixed in 4% (v/v) formaldehyde and sectioned for H&E staining.

2.3.10 Evaluation of tumor growth Inhibition using a B16-OVA-bearing mouse model

Single B16-OVA tumor cells (5×10^5 cells per mouse) were subcutaneously inoculated into the left axillary region of C57BL/6 mice (6-week-old females). APE (100 μg alum + 5 μL squalene) with OVA (10 μg) was injected based on the indicated schedule after random assigning of tumor-bearing mice to different groups (eight mice per group). Mice of the control group were PBS-treated simultaneously. To monitor tumor progression, tumor growth and survival of the mice were measured every two days. The volume of the tumor was calculated using the following formula: (long-axis diameter) × $(\text{short-axis diameter})^2/2$.

2.3.11 Combination with anti-PD-1 antibody using a B16-OVA-bearing mouse model

Six days after of tumor inoculation (5×10^5 cells per mouse), the mice received APE (100 μg alum + 5 μL squalene), with OVA (10 μg), according to the indicated schedule, after random assigning of tumor-bearing mice to different groups (eight mice per group). Anti-PD-1 antibody (clone: RMP1-14, BioXCell, 100 μg) immunizations were performed every 3 days for a total of three times based on the indicated schedule.

2.3.12 Statistical Analysis

All animal studies were performed after randomization. All values were expressed as means ± s.e.m. Data were analyzed by one- or two-way analysis of variance (ANOVA) for comparison of multiple groups with GraphPad Prism 9. Flow cytometry data were analyzed using FlowJo 7.6 and CytExpert. *P* values less than 0.05 were considered statistically significant.

2.4 Result

2.4.1 Alum-Stabilized Pickering Emulsion Preparation and Characterization

We prepared alum-stabilized Pickering emulsion using a previously reported method.[110] After conducting a series of optimizations, alum hydrogel (2 mg/mL), which is a commercially employed adjuvant, was dispersed in sterile deionized water (pH 7) as the aqueous phase, then mixed with the oil phase (squalene) to form the emulsion droplets. The size and zeta potentials of APE and the corresponding alum hydrogel (alum) are shown in Table 2-1.

Table 2-1 The characterization of Alum and APE

	Size (nm)	Zeta potential （mV）	OVA loading efficiency[1] (%)
Alum	847.0 ± 18.9	+ 17.1 ± 0.3	97.9 ± 0.4
APE	2761.0 ± 179.4	+ 30.6 ± 2.4	98.1 ± 0.6

[1] The OVA-antigen loading efficiency was calculated by the proportion of adsorbed OVA and the total amount of the added OVA. OVA-antigen were mixed with the APE or Alum for 1 h at 25 ℃. Data were demonstrated as mean ± s.d. (n = 3).

In this study, ovalbumin (OVA) was selected as the model antigen, which is recognized by the T cell-mediated immune system and activates the T cell immune response.[111] The particle-adsorbed interphase of APE offered a large specific surface area that facilitated the adsorption of OVA. Moreover, the positively charged surface further increased the electrostatic adsorption of negatively charged OVA. Thus, APE adsorbed more than 90% of the OVA antigen (10 μg/per mouse) within 1 h (Table 3-1), indicating that it was equipped to effectively trigger an immune response.

2.4.2 Adjuvant Effects of Alum-Stabilized Pickering Emulsion as a Tumor Vaccination

We postulated that APE could modulate the adaptive immune responses in tumor vaccinations. To test our hypothesis, the adjuvanticity of APE/OVA formulations, which contained 100 μg of alum and 10 μg of OVA antigen per mouse, was investigated. Compared with the control group, in the spleen, over 15-fold more OVA-specific IFN-γ-secreting T cells (Th1 cells) were detected after prime-post intramuscular injection of APE/OVA (APE-2), as illustrated in Figure 2-2a. Furthermore, increasing the administration frequency also further boosted the IFN-γ-mediated T cell responses. As shown in Figure 2-2b, 2-fold and 3-fold more IFN-γ-secreting T cells were detected after three (APE-3) and four (APE-4) intramuscular

injections, compared with two intramuscular injections (APE-2). The amounts of IL-4-secreting cells (Th2 cells) was also 5-fold higher than the control group after two intramuscular injections, and 2-fold and 3-fold more IL-4 spot-forming cells were also detected in APE-3 and APE-4, compared with APE-2 (Figure 2-2c-d).

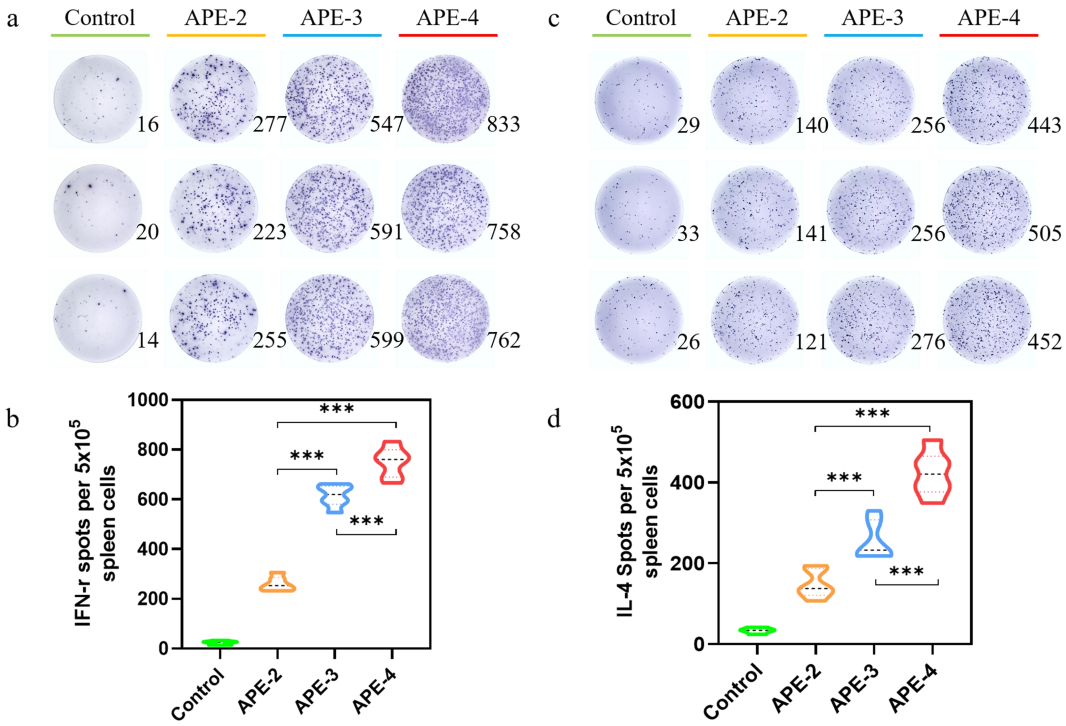

Figure 2-2 Potent adaptive response to APE/OVA tumor vaccinations. (a) ELISpot images of IFN-γ spot-forming cells among splenocytes. (b) Statistical analysis on IFN-γ spot-forming cells among the splenocytes. (c) ELISpot analysis of IL-4 spot-forming cells among splenocytes. (d) Statistical analysis on IL-4 spot-forming cells among the splenocytes. Data in the graphs were presented as arithmetic means ± s.e.m. from 3 independent experiments. $*P < 0.05$, $**P < 0.01$, $***P < 0.001$.

Moreover, the IL-4 and IFN-γ cytokine profile of the splenocyte supernatant showed a similar tendency. In comparison to the control group, APE-2 increased IFN-γ secretion by 1260% (Figure 2-3a) and IL-4 secretion by 200% (Figure 2-3b). With the increase in the frequency of vaccinations, more robust secretion of IFN-γ (~860%) and IL-4 (~370%) was detected in APE-4 compared with APE-2 (Figure 2-3).

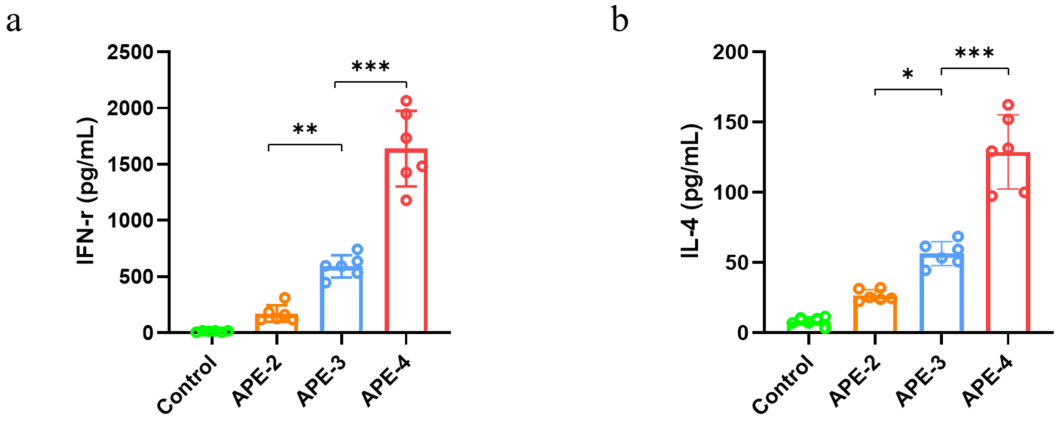

Figure 2-3 Secretion of cytokines. (a) IFN-γ and (b) IL-4 cytokine level in splenocyte supernatant. The data were expressed as mean ± s.e.m. from a representative experiment (n = 6), *$P < 0.05$, **$P < 0.01$, ***$P < 0.001$, analyzed by one-way ANOVA.

Next, the more specific cytokine profile, which was related to tumor immunity, was assessed in the splenocytes. APE triggered significantly enhanced cytokine secretion levels compared with the control. In development, APE-4 increased the concentration of IL-2 secretion by 140% (Figure 2-4a), TNF-α secretion by 70% (Figure 2-4b), and granzyme B secretion (Figure 2-4c) by 230% compared with APE-2-treated mice, indicating potentially robust cellular immune engagement against tumors. As shown in Figure 2-4 d-e, in the spleen of APE-adjuvant mice, the frequency of OVA-specific $CD8^+$ T cells was increased by about 100% after receiving two intramuscular vaccines, and they were further stimulated by 160% after four-dose vaccinations, compared with non-treated mice (control), as shown in Figure 2-5 and Figure 2-4 d-e. These results suggested that APE may harbor the potential to elicit a robust anti-tumor effect. Moreover, boosting administrations of APE (APE-3 and APE-4) may offer a higher cellular immune response.

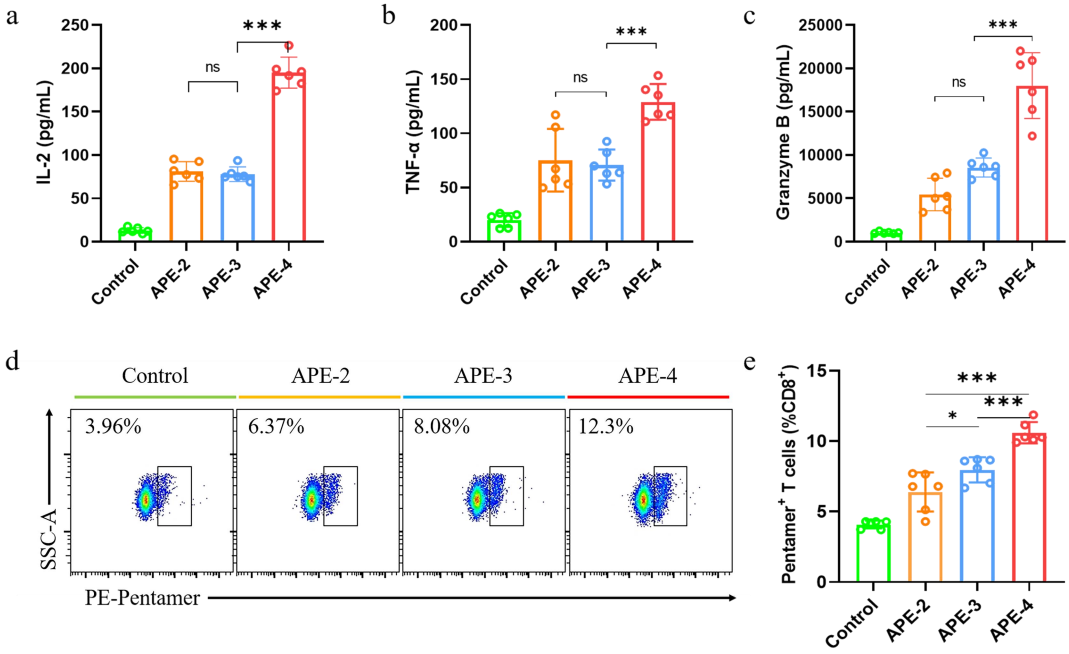

Figure 2-4. Secretion of cytokines. (a) IL-2 cytokine, (b) TNF-α cytokine secretion and (c) granzyme B cytokine secretion among splenocytes. (d) Scatter plots and (e) Statistical analysis of OVA-specific $CD8^+$ T cells in the spleen. The data were expressed as mean ± s.e.m. from a representative experiment (n = 6), $*P < 0.05$, $**P < 0.01$, $***P < 0.001$, analyzed by one-way ANOVA.

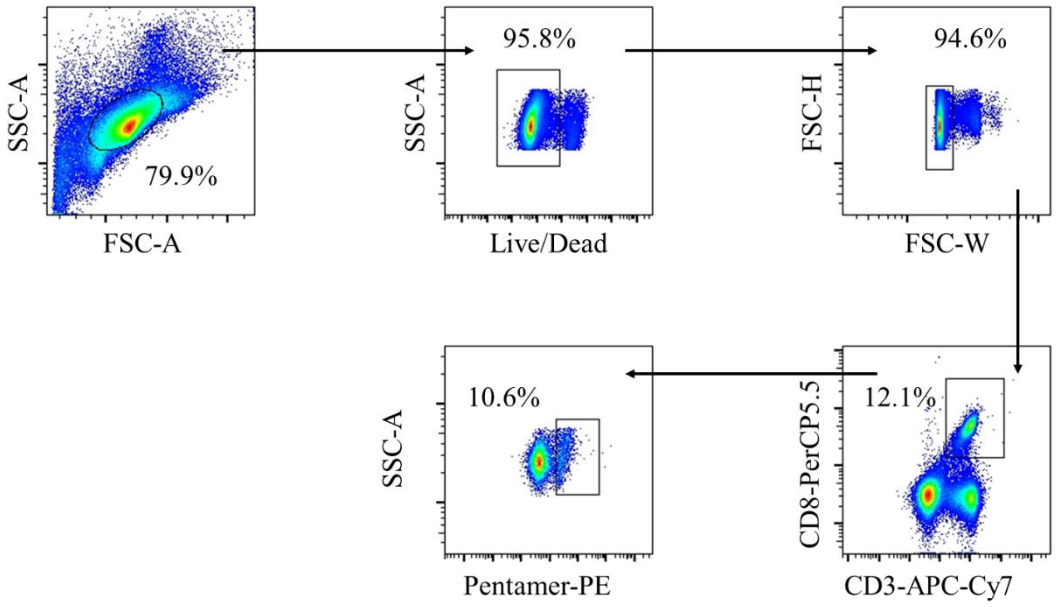

Figure 2-5. Gating strategy of OVA-specific $CD8^+$ T cells in the spleen.

2.4.3 The Safety Profile of APE after Multiple Immunizations

The safety profile of APE after four immunizations (APE-4) was evaluated by histopathology analysis of the major organs and serum biochemical parameters of the

key factors. No noticeable signs of side effects were observed in the heart, liver, spleen, lung, and kidney after four administrations (Figure 2-6), compared with the non-treated group (control). Additionally, the levels of lactate dehydrogenase (LDH), aspartate aminotransferase (AST), alanine aminotransferase (ALT), alkaline phosphatase (ALP), and blood urea nitrogen (BUN) were within a similar range to those of the PBS-treated mice (control), as shown in Figure 2-7.

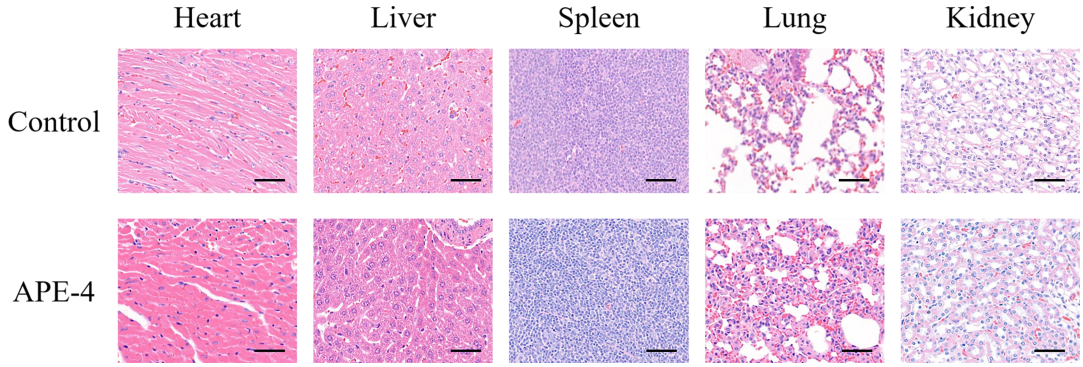

Figure 2-6 Biocompatibility evaluations via hematoxylin and eosin (H&E) staining of the key organ sections from C57BL/6 mice after fourth administration (APE-4). Scale bar = 50 μm.

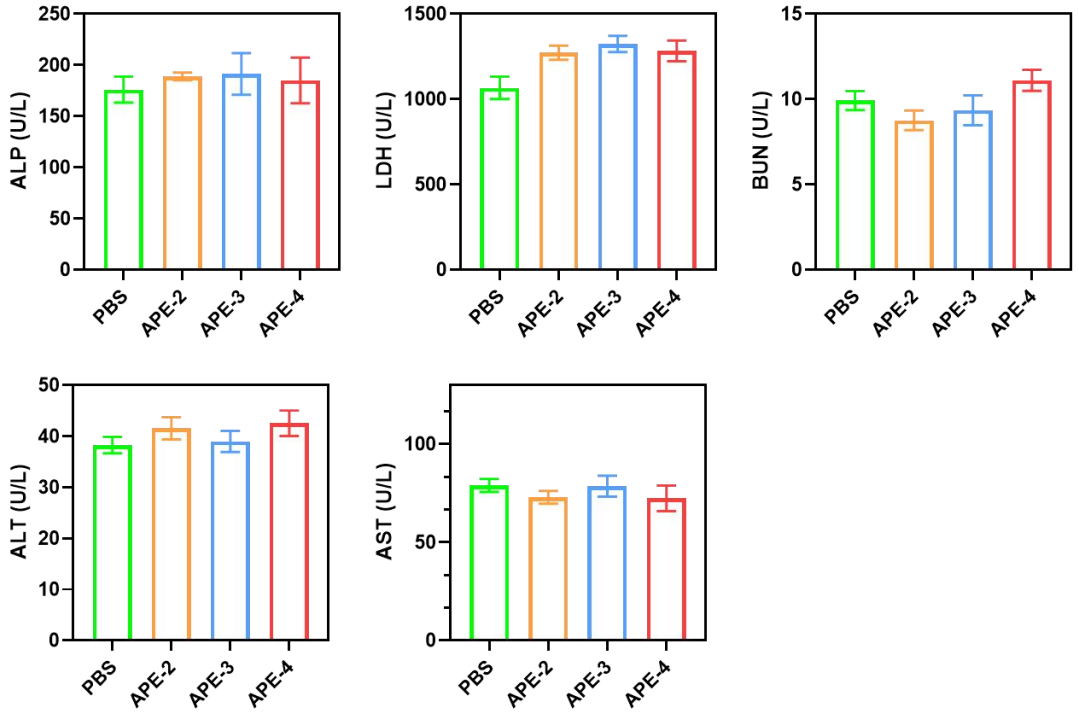

Figure 2-7 Serum chemistry levels in mice. Including lactate dehydrogenase (LDH), alanine aminotransferase (ALT), aspartate aminotransferase (AST) and blood urea nitrogen (BUN). Data are expressed as mean ± SEM (n = 6).

2.4.4 Anti-Tumor Therapeutic Efficacy

The above evaluations encouraged us to conduct a further appraisal of the therapeutic effect in an established B16-OVA cancer model. The C57BL/6 mice were

implanted subcutaneously with B16-OVA cells (5 × 10^5/per mouse) on D + 0 (Day0), and subsequently received the vaccinations of APE at various times (Figure 2-8a, each dose containing 100 μg of alum and 10 μg of OVA). Intramuscular administration with APE/OVA delayed the onset of the B16-OVA tumor model (Figure 2-8b-c) and increased the mouse survival rates (Figure 2-8d), with a stable body weight (Figure 2-9). These results demonstrated that APE functioned as a potent adjuvant to dampen the activity of tumor proliferation. Surprisingly, unlike the results of the cellular immune responses, the intensified tumor regression was not observed after further immunizations (APE-3 and APE-4).

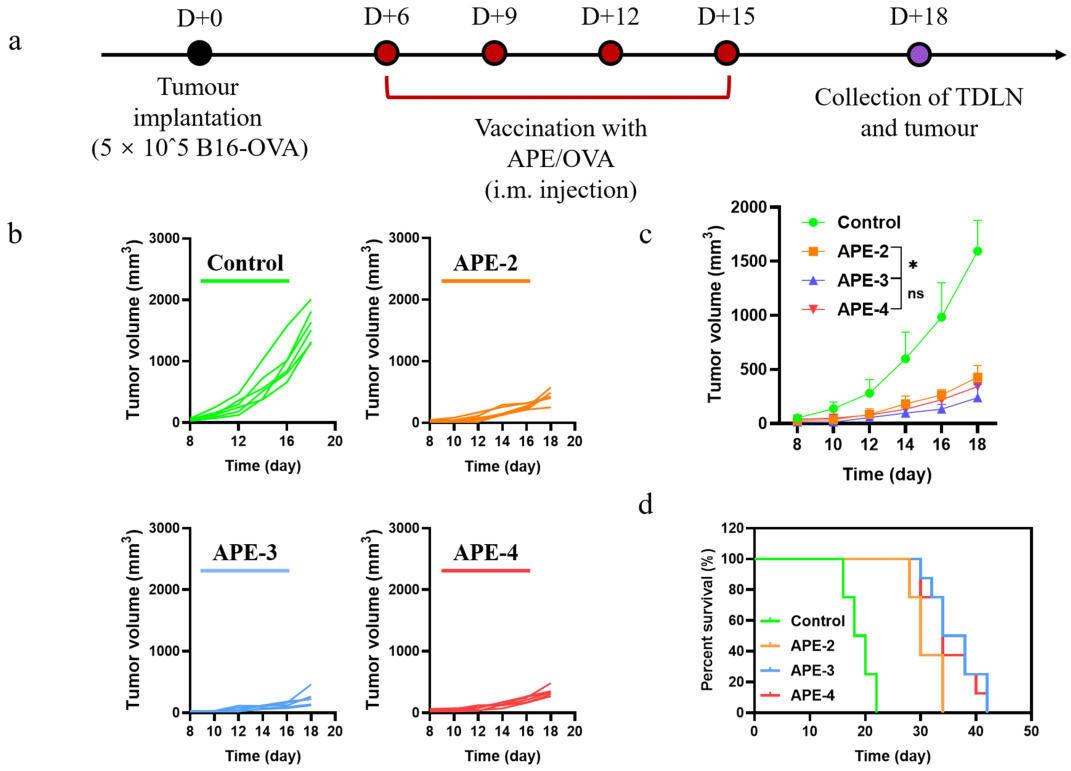

Figure 2-8 In vivo anti-tumor immune responses by APE/OVA in a B16-OVA model. (a) Schedule of vaccination in B16-OVA tumor model. (b) Individual tumor growth kinetics of B16-OVA tumors after different treatments. APE-2: two times vaccination on D + 6 and D + 9; APE-3: three times vaccination on D + 6, D + 9 and D + 12; APE-4: Four times vaccination on D + 6, D + 9, D + 12 and D + 15. (c) Average tumor growth curves (n = 6). (d) Survival curves (n = 8) in the B16-OVA tumor model. The data are shown as the mean ± s.e.m. from a representative experiment (n = 6). NS, not significant, *P < 0.05, **P < 0.01, ***P < 0.005, analyzed by two-way ANOVA.

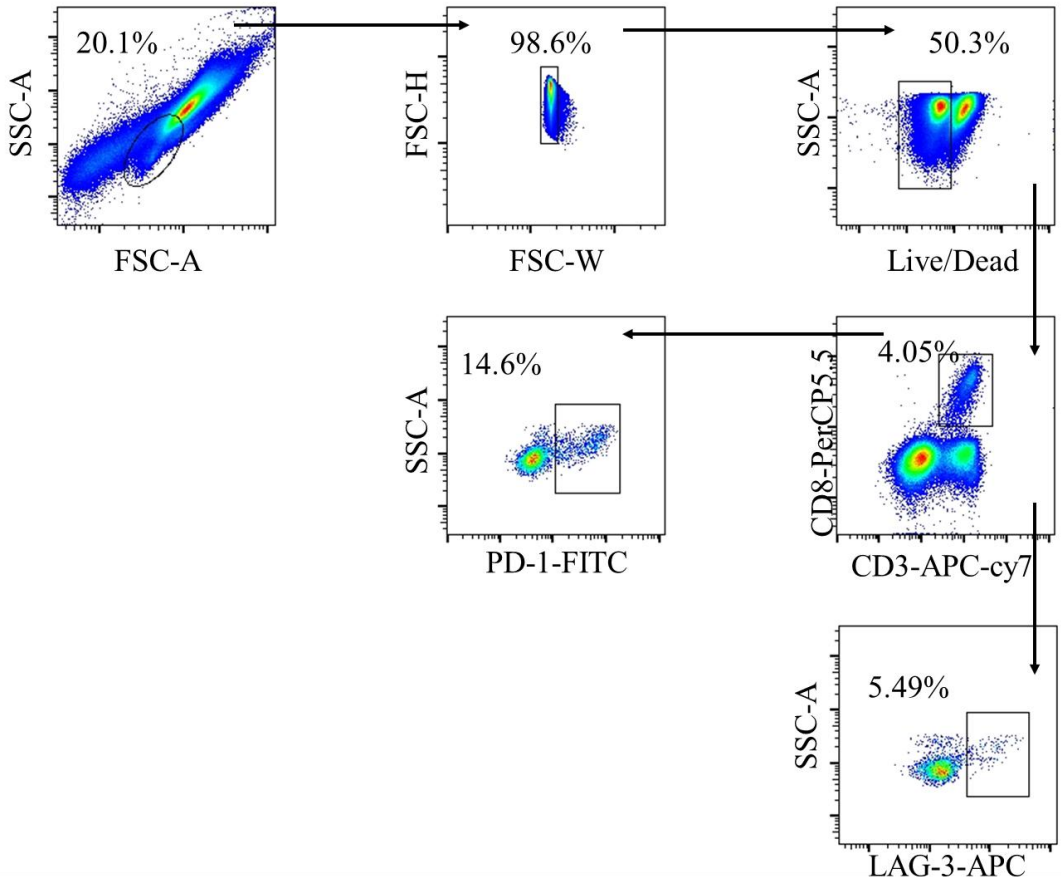

Figure 2-9 Gating strategy of PD-1$^+$ cells or LAG-3$^+$ cells in CD8$^+$ T cells (CD3$^+$ CD8$^+$) in TME.

2.4.5 Immune Responses in TDLNs and TME in the B16-OVA Tumor Model

Considering that the immunosuppressive tumor microenvironment (TME) may hinder the anti-cancer efficacy of the tumor-infiltrating lymphocytes, we subsequently explored the underlying cause of the diminished anti-tumor effect of the frequent administrations, with the aim of determining the optimal strategy. The leading exhaustion marker involved in tumor immune surveillance was evaluated in the TMEand TDLNs. As shown in Figure 2-10, compared with non-treated mice, immunosuppression-related PD-1$^+$ CD8$^+$ T cells were observed, with decreases of 540% and 340% in TDLNs (Figure 2-10a-b) and the TME (Figure 2-10c-d) after two vaccinations, respectively, indicating a potent anti-tumor efficacy. Nevertheless, PD-1$^+$ CD8$^+$ T cells' proportion was evidently elevated after further boosting administrations of APE/OVA. Compared with APE-2, APE-4 increased the intratumoral PD-1$^+$ CD8$^+$ T cells by 220% in TDLNs and 150% in the TME. This indicated that the less potent anti-tumor efficacy of APE-4 may be attributed to the sudden increase in PD-1$^+$ CD8$^+$ T cell populations.

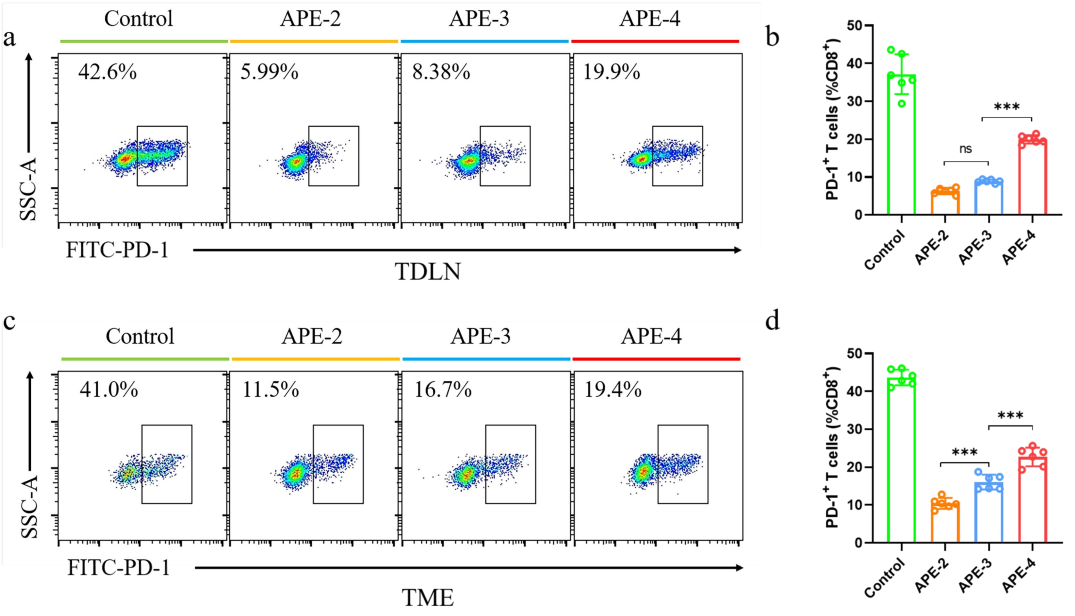

Figure 2-10 Immune cell analysis in a B16-OVA model. (a) Representative flow cytometry dot plots and (b) percentage of PD-1$^+$ cells in CD8$^+$ T cells (CD3$^+$ CD8$^+$) in TDLNs. (c) Representative flow cytometry dot plots and (d) percentage of PD-1$^+$ cells in CD8$^+$ T cells (CD3$^+$ CD8$^+$) in TME. These data are shown as the mean ± s.e.m. from a representative experiment (n = 6). *P < 0.05, **P < 0.01, ***P < 0.005, analyzed by one-way ANOVA.

Lymphocyte activation gene-3 (LAG-3), an inhibitory immune checkpoint molecule comparable to PD-1, was further evaluated as shown in Figure 2-11. Although APE down-regulated the expressions of LAG-3, higher frequencies of LAG-3$^+$ CD8$^+$ T cells were observed with further boosting doses. APE-4 allowed the proportion of LAG-3$^+$ CD8$^+$ T cells to increase by both of ~1-fold in TDLNs and TME, respectively, compared to APE-2 (Figure 2-11a-d). These results suggested that dose-boosting with higher times may induce the engagement of the PD-1$^+$ CD8$^+$ T cells and LAG-3$^+$ CD8$^+$ T cells, triggering the immune-regulatory effects. These results suggested that dose-boosting at later times may induce the engagement of the PD-1$^+$ CD8$^+$ T cells and LAG-3$^+$ CD8$^+$ T cells, triggering the immune-regulatory effects.

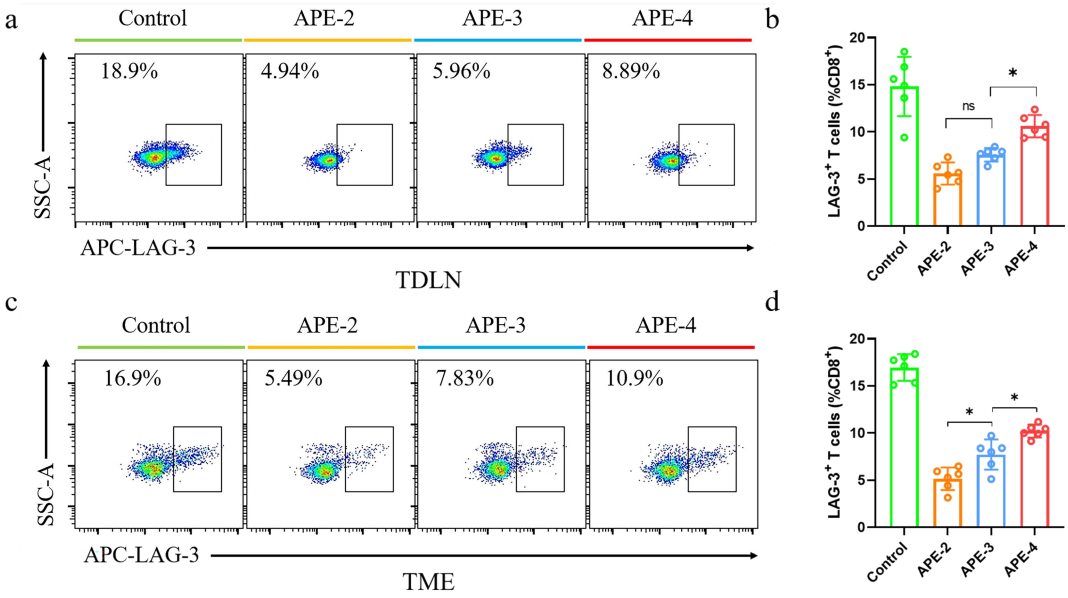

Figure 2-11 Immune cell analysis in a B16-OVA model. (a) Representative flow cytometry dot plots and (b) percentage of LAG-3$^+$ cells in CD8$^+$ T cells (CD3$^+$ CD8$^+$) in TDLNs. (c) Representative flow cytometry dot plots and (d) percentage of LAG-3$^+$ cells in CD8$^+$ T cells (CD3$^+$ CD8$^+$) in TME. These data are shown as the mean ± s.e.m. from a representative experiment (n = 6). *P < 0.05, **P < 0.01, ***P < 0.005, analyzed by one-way ANOVA.

2.4.6 Anti-Tumor Therapeutic Efficacy of APE Combined with Anti-PD-1 Therapy

It is worth noting that the binding between programmed cell death protein 1 (PD-1) and programmed cell death ligand 1 (PD-L1) participate in the process of immune escape during the development and metastasis of tumors. Blocking the immunosuppression-associated protein binding of PD-1 and PD-L1 has been proven to slow progression of a tumor's expansion through regaining suppressed anti-tumor immunity. As aforementioned, frequent dosing of APE cancer vaccines may increase the engagement of PD-1$^+$ CD8$^+$ T cells. We assumed that the co-administration of APE with anti-PD-1 antibody may lessen the immunosuppressive effect and induce higher anti-tumor responses. As shown in Figure 2-12a, combined treatment of anti-PD-1 was given three times at D + 11, D + 14, and D + 17 for each group. In conjunction with anti-PD-1, with a stable body weight, APE-3 and APE-4 were effective in suppressing tumor growth in the B16-OVA subcutaneous tumor model and enhancing mouse survival, while APE-2 showed a suboptimal tumor regression and survival (Figure 2-12b-c). Accordingly, the immunosuppressive TME may be weakened by this cocktail therapy, allowing for the increased cellular immune responses after booster vaccinations.

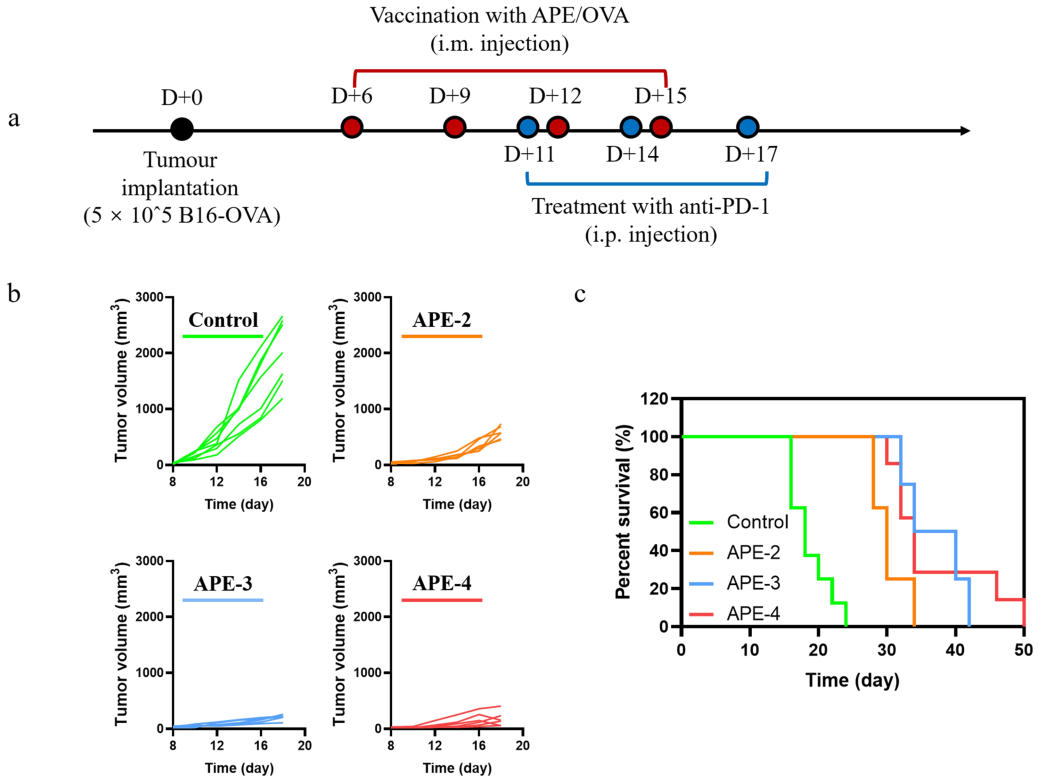

Figure 2-12 In vivo anti-tumor immune responses by APE/OVA combined with anti-PD-1 in a B16-OVA model. (a) Schedule of vaccination in B16-OVA tumor model. (b) Individual tumor growth kinetics of B16-OVA tumors after different treatments. APE-2: two times vaccination on D + 6 and D + 9 combined with thrice anti-PD-1; APE-3: three times vaccination on D + 6, D + 9 and D + 12 combined with thrice anti-PD-1; APE-4: Four times vaccination on D + 6, D + 9, D + 12 and D + 15 combined with thrice anti-PD-1. (c) Survival curves (n = 8) in the B16-OVA tumor model. The data are shown as the mean ± s.e.m. from a representative experiment (n = 6). *$P < 0.05$, **$P < 0.01$, ***$P < 0.005$, analyzed by two-way ANOVA.

2.5 Discussion

The scientifically rigorous standards of safety in clinical vaccines mean alum remains a crucial important benchmark of all adjuvants, effectively augmenting antibody titers and Th2 humoral immunity for protection, yet seldom inducing Th1 or Th17 cellular immunity,[112] which are considered more important for vaccines against diseases such as malaria, tuberculosis, influenza, pertussis, and tumors.[113] Several studies have suggested the potential benefits of nanoscale alum adjuvants, which tend to induce stronger and more persistent antigen-specific IgG levels and augmented immunity, particularly T cell responses, compared to micron-sized aluminum hydroxide particles. However, the small size and large surface area of particles may lead to aggregation and finally affect the immune response.[114] Toll-like receptors (TLRs), which are localized at the cell membrane or in endosomal compartments, can be activated via conjugation with their agonists.[115] Numerous efforts have managed to combine TLRs agonists with aluminum to elicit a T cell response against aggressive

tumors. The combination of CpG oligonucleotides (ODNs), which bind to TLR9, and alum adjuvant elicited antigen-specific antibody production and induced an IFN-γ-secreting T cell response. For CpG–alum, CpG tightly adsorbs to alum via electrostatic interactions that may affect the adsorptive capacity and strength of the antigens. Here, we adsorbed alum on the oil/water interphase to prepare alum-stabilized Pickering emulsion (APE). Besides the electrostatic and coordinate interactions with the alum, the alum-packed oil/water interphase also offered a larger specific surface and more hydrophobic interactions for large quantities of antigens and CpGs with multiple driving forces, which may have diminished the possibility of competitive adsorption. Furthermore, with the aid of the alum-stabilized droplets, antigens or CpG may have the potential to remain at the injection site and cause a robust and durable APC activation at the injection site, which is crucial for T cell activation. Meanwhile, with the positively charged surface, APE may exhibit antigen cross-presentation via lysosomal escape for the Th1-mediated immune response. FDA-approved squalene and alum may confer biosafety to APE after repeat immunizations.

Booster vaccinations have been frequently used to maximize anti-tumor efficacy and have been applied in most cancer vaccine studies.[116] However, incomplete Freund's adjuvant (IFA), in a clinical trial of a melanoma vaccine, demonstrated that 1–3 injections induce accumulation of mature dendritic cells, while 4–6 injections induce $FoxP3^+$ T cells and eosinophils and negative immune regulatory processes in the site.[117] This was in accordance with other recent studies, suggesting that the relative prevalence of T suppressor cells may be responsible for reducing lymphocyte activation and infiltration, causing the suboptimal anti-tumor effect. Here, we put extra emphasis on the connection between frequent vaccinations and the immune efficacy against tumors, and we obtained a similar result. Although more administrations of APE/OVA (APE-3 and APE-4) increased $CD8^+$ T cell activations, a negligible difference in the anti-tumor potency was observed. After the prompted in-depth analysis of immune cells between the tumor microenvironment and tumor-draining lymph nodes, we found that the number of $PD\text{-}1^+$ $CD8^+$ T cells and $LAG\text{-}3^+$ $CD8^+$ T increased, leading to the immunosuppressive microenvironment to diminish the onset of the anti-tumor effect after the further booster injections of APE/OVA.

This indicated that repetitive antigenic stimulations may up-regulate the expression of negative regulatory markers (e.g., PD-1, LAG-3, TIM-3) among the tumor-infiltrating lymphocytes, leading to an elevated immune suppressive microenvironment.[118] Furthermore, the combined injection of anti-PD-1 antibody down-regulated the immune tolerance by binding to PD-1 receptor, bringing back the revitalized T cells. As shown in Figure 2-12, evident tumor regression and higher survival rates were detected after four APE/OVA vaccinations, suggesting that the relative prevalence of T suppressor cells may be responsible for reducing lymphocyte activation and infiltration, causing a suboptimal anti-tumor effect.[119]

Accordingly, to further enhance the anti-tumor efficacy, we employed anti-PD-1 antibody, which can bind to PD-1 receptor to bring back the revitalized T cells. After four APE/OVA vaccinations, suppressed tumor growth was detected in the B16-OVA

subcutaneous tumor model and the mouse survival was increased.

Taken together, APE may serve as a potent adjuvant for cancer vaccines. Moreover, stemming from the above data on APE vaccinations, the tumor regression caused by the cancer vaccines may not be increased by simply increasing the frequency of administrations. Elevated immunocompromised T cells and the microenvironment within the tumor may have major implications for hampered efficacy. Combining cancer vaccines with anti-PD-1 therapy may have greater potential in terms of the anti-tumor effect.

Chapter 3 Spatiotemporal Coordination of Antigen Presentation and Co-stimulatory Signal for Enhanced Anti-tumor Vaccination

3.1 Abstract

Controlled-release systems enhance anti-tumor effects by leveraging local antigen persistence for antigen-presenting cells (APCs) recruitment and T cell engagement. However, constant antigen presentation alone tends to produce the dysfunction of tumor-specific $CD8^+$ T cells, neglecting the synergistic effects of co-stimulatory signal. To address this, we developed a soft particle-stabilized emulsion (SPE) to deliver lipopeptides with controlled release profiles by adjusting their hydrophobic chain lengths: C_6-SPE (fast release), C_{10}-SPE (medium release), and C_{16}-SPE (slow release). Following administration, C_6-SPE release antigen rapidly, inducing early antigen presentation, whereas C_{16}-SPE's slow-release delayed antigen presentation. Both scenarios missed the critical window for coordinating with the expression of CD86, leading to either the T cell apoptosis or suboptimal activations. In contrast, C_{10}-SPE achieved spatiotemporally synergetic effect of MHC-I-peptide complex and co-stimulatory signal (CD86), leading to effective DC activation, enhanced T cell activation and tumor regression in EG7-OVA bearing mice. Additionally, co-delivery of cytosine-phosphate-guanine (CpG) with SPE boosted DC activation at early stage, providing a sustained expression of CD86 window for dendritic cell (DC) activation, improving the immune response and robust anti-tumor effects of C_6-SPE that comparable to C_{10}-SPE. These findings may highlight that synchronizing the spatiotemporal dynamics of antigen presentation and APC activation may confer optimal strategy for the enhanced vaccinations.

3.2 Introduction

Tumor vaccine has emerged as a promising therapeutic strategy, attracting significant interest, and showing potential in the treatment of various malignancies.[26,120,121] Peptide-based antigen, targeting tumor-associated antigens or neoantigens, have particularly revolutionized cancer immunotherapy by promoting antigen-specific CD8+ T cell response for tumor eradication.[122-125] Core to achieving this, is the activation and cross-presentation of (APCs) through the expression of co-stimulatory signal and MHC-I-peptide complex, facilitating potent and durable T cell engagement.[126-128] In fact, the onset of immune response entails a series of spatiotemporal sequences of events, and the underlying mechanisms governing controlled antigens release and APC activation remain to be explored.[129,130]

In tumor vaccine, antigens are expected to release from delivery vehicle and escape lysosomal degradation to reach the cytoplasm. There, they are subsequently processed into peptide, and are presented on cell surface via MHC-I molecule. Then, $CD8^+$ T cells recognize these MHC-I-peptide complex through their T-cell receptors (TCRs), receiving signal that promote their proliferation.[131] Recent research has increasingly focused on optimizing antigen release kinetics to prolong antigen cross-

presentation and enhance T cell-mediated immune response. For instance, mesoporous silica microrod-polyethyleneimine (MSR-PEI) and the self-healing microcapsules have developed to sustain antigen release, promoting APC recruitment, antigen-presentation, activation, and homing to lymph nodes for effective tumor clearance in multiple tumor models.[132-136] Similarly, sponge-like macroporous cryogels, encapsulating immunomodulatory factors and antigens, deliver contents in a controlled manner, consistently eliciting increased T cell response in a melanoma model.[137] These approaches resulted in effective T cell response and tumor regression were observed across various antigens. However, controlled antigen release may yield controversial results. For example, a recent work found that persistent antigen at the injection sites with Incomplete Freund's Adjuvant (IFA) resulted in sequestration, dysfunction, and deletion of tumor-specific $CD8^+$ T cells, leading to limited effective anti-tumor response. This highlights the challenge that antigen persistence and cross-presentation alone may not suffice to induce strong anti-tumor or immunogenic effects.[138] Therefore, it is imperative to synchronize spatiotemporal antigen cross-presentation and co-stimulatory molecule expression to optimize functionalized APC stimuli, facilitating the development of durable, non-exhausted, functional $CD8^+$ T cell response for anti-tumor immunity.

Under these circumstances, we assumed that the spatiotemporal condensate of antigen presentation and co-stimulatory signal may dictate T cell dynamics and the subsequent anti-tumor efficacy. To explore this, we engineered a soft particle-stabilized emulsion (SPE) to modulate the antigen release dynamics and APC activation. Leveraging our prior investigations, these droplets exhibited enhanced APC uptake and acted as immune stimuli, promoting robust expression of co-stimulatory molecule, such as CD86 and CD80, essential for T cell binding and maturation.[86] Additionally, once internalized by APCs, the positively charged droplets facilitated escape from lysosomes, enhancing peptide cross-presentation.[87] By adjusting the hydrophobic chain length of the lipopeptides, the antigen release kinetics can be easily tuned, yielding SPEs with varied release profiles but similar immunogenicity, such as C_6-SPE (fast release), C_{10}-SPE (medium release), and C_{16}-SPE (slow release). After intramuscular injection, C_{10}-SPE induced coordinated upregulations of antigen cross-presentation (MHC-I-peptide complex) and the expression of co-stimulatory molecule (CD86), leading to stronger T cell response and anti-tumor effects, contrasting with C_6-SPE and C_{10}-SPE. Additionally, co-delivering CpG with C_6-SPE addressed early deficits in APC activation and was associated with increased antigen cross-presentation, eliciting significantly reduced tumor volumes and prolonged mice survival that comparable to C_{10}-SPE. This indicated that synchronizing the spatiotemporal dynamics of antigen presentation and APC activation may confer an optimal strategy for cancer vaccines**.**

3.3 Materials and Methods

3.3.1 Materials

Alum Hydroxide Gel Adjuvant was purchased from InvivoGen, and squalene was purchased from Sigma. CpG-ODN 1826 (5’-TCCAT GACGT TCCTG ATGCT-3’)

within a phosphorothioate backbone was synthesized by Sangon Biotech. All antigenic short peptides were synthesized by GenScript Biotech Corporation. Ghost Dye-Violet 450, Ghost Dye-Violet 510, FITC-CD11c, APC-CD86, PE-Cy7-CD86, PE-SIINFEKL/H-2Kb, APC-CCR7, APC-Cy7-CD3e, V450-CD3e, Per-CP5.5-CD8a, and PE-Fas were purchased from Tonbo Biosciences. PE-SIINFEKL pentamer were purchased from MBL. Mouse IFN-γ ELISpot BASIC kits, BCIP/NBT-plus substrate for ELISpot were obtained from Mabtech. Fluorescent hydrophilic dyes Cy5 were purchased from Fanbo Biochemical Co., Ltd. All other reagents used in this study were of analytical grade.

3.3.2 Preparation of lipopeptides binding to SPE.

The epitope peptide of OVA protein, SIINFEKL ($OVA_{257-264}$), served as the model antigen.[139] To ensure efficient peptide loading within the emulsion, characterized by its distinct oil-water interface, the N-terminal amino acid of the peptide was modified with saturated fatty acid carbon chains. This modification facilitated efficient integration into the oil phase squalene at the oil-water interface. Additionally, the presence of aminopeptidase in the cytoplasm ensures the removal of the saturated fatty acid once the lipo-peptides are internalized by cells, thereby preserving the integrity of the antigen presentation. To prevent any impact of the fatty acid chain removal on the antigen sequence and its presentation, an extra amino acid, E, was added to the N-terminus of the original sequence, forming the modified sequence ESIINFEKL. The lipopeptides were synthesized using solid-phase peptide synthesis (SPPS). Variants of the antigens, namely C_6-ESIINFEKL, C_{10}-ESIINFEKL, and C_{16}-ESIINFEKL, were produced by modifying the N-terminal group of ESIINFEKL with different saturated fatty acid chains.

C_6-SPE, C_{10}-SPE, and C_{16}-SPE were formulated using a single-step sonication process (Branson Digital Sonifier; total time = 120 seconds, power = 30%, interval time = 4 seconds). Alum adjuvants were utilized as stabilizers in the water phase, while squalene and the modified peptides C_6-ESIINFEKL, C_{10}-ESIINFEKL, and C_{16}-ESIINFEKL were employed in the dispersion phase, respectively. Following a series of optimizations involving the concentration of alum adjuvant, the characteristics of the continuous phase, and its pH, the final formulations of C_6-SPE, C_{10}-SPE, and C_{16}-SPE were obtained.

3.3.3 Characterization of C_6-SPE, C_{10}-SPE, C_{16}-SPE.

The hydrodynamic size, and zeta potential of all the formulations were measured at 25 ℃ using a Malvern Zetasizer ZS. To determine the lipopeptide antigen loading efficiency, C_6-SPE, C_{10}-SPE, C_{16}-SPE were prepared using Cy5 fluorescent labled lipopeptide, then the fluidic lipopeptide in water phase were separated from the emulsions by the centrifugation at 6000 × g. The concentration of fluidic lipopeptide antigens were determined by detecting the florescent intensity of the water phase. The antigen loading efficiency was calculated by equation: antigen loading efficiency = (total lipopeptide - free lipopeptide)/total lipopeptide × 100%. And the co-localizations of lipopeptide with the formulations were observed by laser scanning confocal microscope (Nikon), where alum (red) and lipopeptide (green) was labeled

by Lumogallion (Sigma) and Cy5 (Thermo Fisher), respectively.

3.3.4 Characterization of antigen release profile of SPE.

Cy5-labeled lipopeptide antigens were encapsulated within SPE and subjected to continuous rotation in a simulated cytoplasmic environment at 37 ℃, using PBS buffer containing 10% FBS, at a dilution of 1:9. To assess the release profile of the lipo-peptides, ESIINFEKL, C_6-ESIINFEKL, C_{10}-ESIINFEKL, and C_{16}-ESIINFEKL were labeled with Cy5, and be prepared as C_0-SPE, C_6-SPE, C_{10}-SPE, and C_{16}-SPE, respectively. To assess the release profile of the CpG, CpG were labeled with Cy3, and be introduced to C_6-SPE, C_{10}-SPE, and C_{16}-SPE, respectively. Each 1 mL of these emulsions was added to 10 mL of PBS (pH 6.5, 10% FBS) and incubated on a vertical rotating mixer at 37 ℃ and 100 rpm. At predetermined intervals, samples were centrifuged (6000 rpm for 10 minutes), and 1 mL of supernatant was extracted for fluorescence-based quantification of the released lipopeptide or CpG, after which an equivalent volume of fresh buffer was added, and the samples were resuspended for further incubation.

3.3.5 Injection site antigen depot effect.

To assess the fluorescence intensity of Cy5-labeled lipopeptides at the injection site (Gene Script), *in vivo* imaging was conducted using the IVIS imaging system (PerkinElmer) following intramuscular administration. Fluorescence signals were captured on Day 0, 1, 3, 7, 10,14, and 21 post-vaccinations to plot the temporal trend of fluorescence intensity at the injection site for each mouse group. Additionally, for histological analysis, sections from the injection sites containing C_6-SPE, C_{10}-SPE, and C_{16}-SPE formulated with Cy5-labeled lipopeptides and lumogallion-labeled alum were prepared. Fourteen days post-vaccination, tissues were excised, dehydrated, and sectioned. Fluorescent images of these sections were acquired using a KFBIO laser scanning confocal microscope and subsequently analyzed using CaseViewer software.

3.3.6 Immune response in the injection sites and the draining lymph nodes.

The Beijing Laboratory Animal Center supplied C57BL/6 mice that were housed in a specific-pathogen-free facility. Groups of six mice (6 - 8 weeks old) were each given a 100 μL suspension containing various formulations and equivalent amounts of antigens intramuscularly on Day 0 and Day 14. Cy5-labeled lipopeptide antigens (Thermo Fisher) were used to prepare SPEs for tracking DC recruitment, antigen uptake, and lipopeptide antigens introduction to SPEs were used to evaluate DC activation and antigen cross-presentation at the injection site, with assessments conducted one day post-injection for uptake and recruitment, and on Day 1, 3, 5, and 7 for DC activation and antigen cross-presentation. Following the injections, muscle tissues were harvested, immersed in PBS with 0.2% collagenase Type II, and incubated at 37 °C for 2 hours to prepare single-cell suspensions. These cells were then stained with anti-CD11c-FITC and Ghost Dye-Violet 450 for evaluate the DC recruitment and antigen uptake. And cells were stained with Ghost Dye-Violet 450, anti-CD11c-FITC, anti-CD86-PE-Cy7, anti-CCR7-APC, anti-MHC-I-SIINFEKL-PE monoclonal antibodies (TONBO Biosciences) for 30 minutes at 4 °C and analyzed for

DC activation and antigen cross-presentation using flow cytometry (CytoFlex LX, Beckman Coulter).

To quantify the level of DC activation and T cell response in the draining lymph nodes (dLNs), identical formulations were administered intramuscularly. dLNs were collected on Day 1, 3, 5, and 7 to prepare single-cell suspensions. These cells were then stained with Ghost Dye-Violet 450, anti-CD11c-FITC, anti-CD86-APC, anti-MHC-I-SIINFEKL-PE monoclonal antibodies (TONBO Biosciences) for 30 minutes at 4 °C and analyzed for DC homing. And cells were stained with Ghost Dye-Violet 510, anti-CD3e-V450, anti-CD8a-PerCP 5.5, anti-Fas-PE monoclonal antibodies (TONBO Biosciences) for 30 minutes at 4 °C and analyzed for T cells apoptosis and using flow cytometry (CytoFlex LX, Beckman Coulter).

3.3.7 Immune response in vivo.

For ELISPOT analysis, frequencies of IFN-γ secreting cells were assessed using the following protocol.[140] 96-well PVDF-based membrane plates (Millipore) were coated overnight with IFN-γ antibody (Mabtech) at 4 °C (15 μg/mL). Post-coating, the plates were washed three times with phosphate balanced solution (PBS) and blocked with 200 μL of RPMI-1640 culture medium containing 10% FBS, 100 U/mL penicillin, and 100 U/mL streptomycin for more than one hour at room temperature. Splenocytes were then added to the blocked plates and stimulated with SIINFEKL peptides, followed by a 24-hour incubation at 37 °C in a humidified 5% CO_2 incubator. Subsequently, the cells were removed and the plates washed five times with PBS. Plates were then incubated with 100 μL of detection antibody (1 μg/mL in PBS-0.5% FCS) for 2 hours, followed by an hour of incubation with streptavidin-ALP (1:1000 dilution), both at room temperature. Following this, plates underwent six washes with PBS and development with BCIP/NBT substrate solution in the dark for 10 minutes, then stopped by extensive washing with tap water. Spots were quantified using an ELISpot Analyzer (AT-Spot 2100, Antai Yongxin Medical Technology) as per the manufacturer's guidelines.

The antigen-specific $CD8^+$ T cells were detected using flow cytometry (CytoFlex LX, Beckman Coulter). Splenocytes were stained with anti-CD3e-APC-Cy7, anti-CD8a-PerCP 5.5, and anti-Pentamer-PE monoclonal antibodies according to the manufacturer's instructions.

To evaluate serum biochemical parameters, blood samples were collected on day 28 to measure levels of aspartate aminotransferase (AST), alanine aminotransferase (ALT), blood urea nitrogen (BUN), alkaline phosphatase (ALP), and lactate dehydrogenase (LDH) using a Hitachi 917 automated analyzer (Hitachi Ltd., Tokyo, Japan). For histological assessment of organ effects, spleens, livers, kidneys, and lungs were harvested and fixed in 4% formaldehyde. These tissues were then processed, stained with Hematoxylin and Eosin (H&E), and examined histologically using the Vectra platform.

3.3.8 Characterization of therapeutic immune effect of C6-SPE, C10-SPE, C16-SPE.

C57BL/6 mice aged 6 - 8 weeks were selected for this study, each inoculated

subcutaneously with 5×10^5 E.G7-OVA tumor cells. Once tumor volumes reached approximately 30 mm^3 to 50 mm^3, mice were randomly assigned into experimental groups. Beginning on Day 7, 12, and 17 post-inoculations, each mouse received 100 μL of the designated vaccine intramuscularly, with a total of three immunizations administered, and the tumor tissue were collected 20 days post-inoculation. Tumor dimensions were measured every other day using an electronic digital caliper, and volumes were calculated using the formula: tumor volume = (length × $width^2$)/2. The progression of tumor growth was continuously monitored. Mice were euthanized upon reaching a tumor volume of 2,000 mm^3 or exhibiting severe clinical signs such as significant weight loss or ulceration.

3.3.9 Ethic statement.

All animals were supplied by Vital River Animal Laboratories and housed under sterile conditions in cages accommodating no more than five individuals each. These cages were maintained in a specific pathogen-free room with a 12-hour light/dark cycle and equipped with laminar airflow hoods. Animals were fed autoclaved chow and water ad libitum. Prior to the experiments, all mice underwent at least one week of acclimation. The animal study protocols received approval from the Committee on the Ethics of Animal Experiments at the Institute of Process Engineering, Chinese Academy of Sciences (approval ID: IPEAECA2024044). This study was performed in strict accordance with the Regulations for the Care and Use of Laboratory Animals and Guideline for Ethical Review of Animals (China, GB/T35892-2018). Efforts were made to optimize all techniques and procedures to ensure maximum comfort and minimal stress for the animals.

3.3.10 Statistics guidelines.

Animal studies were conducted following randomization, with all results presented as means ± s.e.m. Statistical analyses were performed using one-way or two-way ANOVA for comparing multiple groups, utilizing GraphPad Prism 8 software. Flow cytometry data were analyzed by FlowJo 10.0 and CytExpert software 2.3. Statistical significance was set at p value less than 0.05 ($p < 0.05$).

3.4 Result

3.4.1 Engineering SPE for lipopeptides-based tumor vaccine

Due to the oil/water interface of particle-stabilized emulsions, hydrophobic substances can efficiently load at their oil/water interface through hydrophobic interactions. To enhance the incorporation of short peptide (ESIINFEKL) immunogens within these particle-stabilized emulsions, we engineered peptide with site-specific modification of saturated fatty acid carbon chains at the N-terminus to obtain lipopeptides.[141] Furthermore, to regulate the release of lipopeptides, we developed three engineered lipopeptides with varied lipo-chain lengths, each modified at its N-terminus with caproic acid (C_6-ESIINFEKL), capric acid (C_{10}-ESIINFEKL) and palmitic acid (C_{16}-ESIINFEKL), respectively. Due to the hydrophobic interaction, increasing the carbon chain length rises the hydrophobicity of the lipopeptides, resulting in the increased affinity to the oil-water interface of SPE. We postulated that

the longer lipo-chain length may postpone release from the interface, tuning the release dynamics of C_6-ESIINFEKL (fast), C_{10}-SIINFEKL (moderate) and C_{16}-ESIINFEKL (slow). Accumulating evidence demonstrated that intracellular aminopeptidases can cleave the saturated fatty acid chain at the N-terminus within the cytoplasm, releasing the peptide immunogens for the antigen cross-presentation. Therefore, once these lipopeptides are released, the saturated fatty acid chain would be cleaved for the antigen presentation.[142] We prepared SPE using alum as continuous phase and lipopeptides dissolved in squalene as the dispersed phase (Figure 3-1).

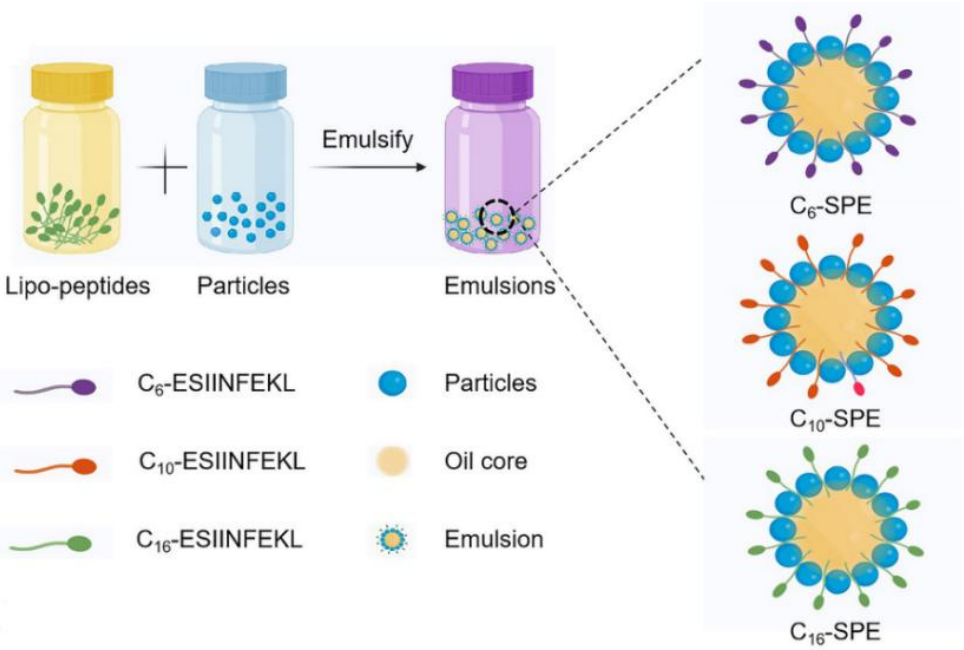

Figure 3-1. Schematic diagram of SPE preparation

After assessing the buffer types (Figure 3-2a), aqueous phase pH (Figure 3-2b) and the particle concentrations (Figure 3-2c) of the continuous phase, we prepared three kinds of emulsions, C_6-SPE, C_{10}-SPE, C_{16}-SPE, respectively.

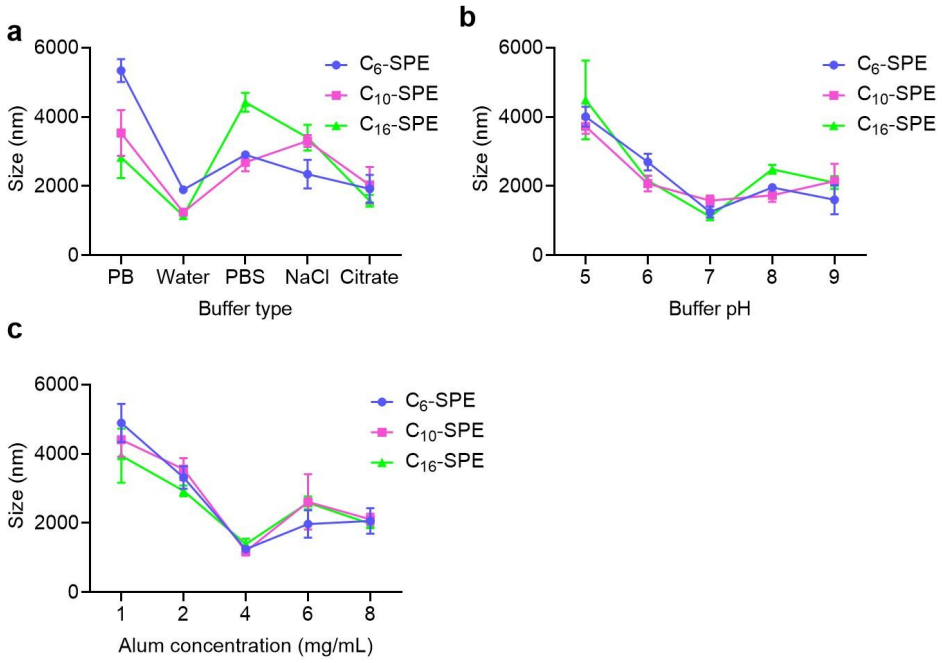

Figure 3-2. Optimizations on the buffer type, pH and particle concentrations of the continuous phase. (a) Optimizations on the buffer type, (b) buffer pH and (c) particle concentrations of the continuous phase. The sizes of emulsion droplets were diluted 100 times determined by dynamic light scattering (DLS) via Nano Zeta Sizer (Malvern) at room temperature (n = 3). By evaluating the size distribution, Citrate, pH 7.0 and 4.0 mg/mL of continuous phase was selected as the optimal pH for the continuous phase.

C_6-SPE, C_{10}-SPE, C_{16}-SPE were prepared within no significant differences of droplets size (~ 1500 nm) (Figure 3-3a) and zeta potential (~ + 48 mV) (Figure 3-3b). The results of antigen loading capacity indicated that all three types of droplets loaded more than 90% of the fluidic antigens, with no significant differences between each group. Furthermore, co-localizations of Alum/Antigen were measured by confocal laser scanning microscope (CLSM), demonstrating that these lipopeptides were loaded at the oil-water interface instead of being encapsulated within the oil core (Figure 3-3c and Figure 3-4).

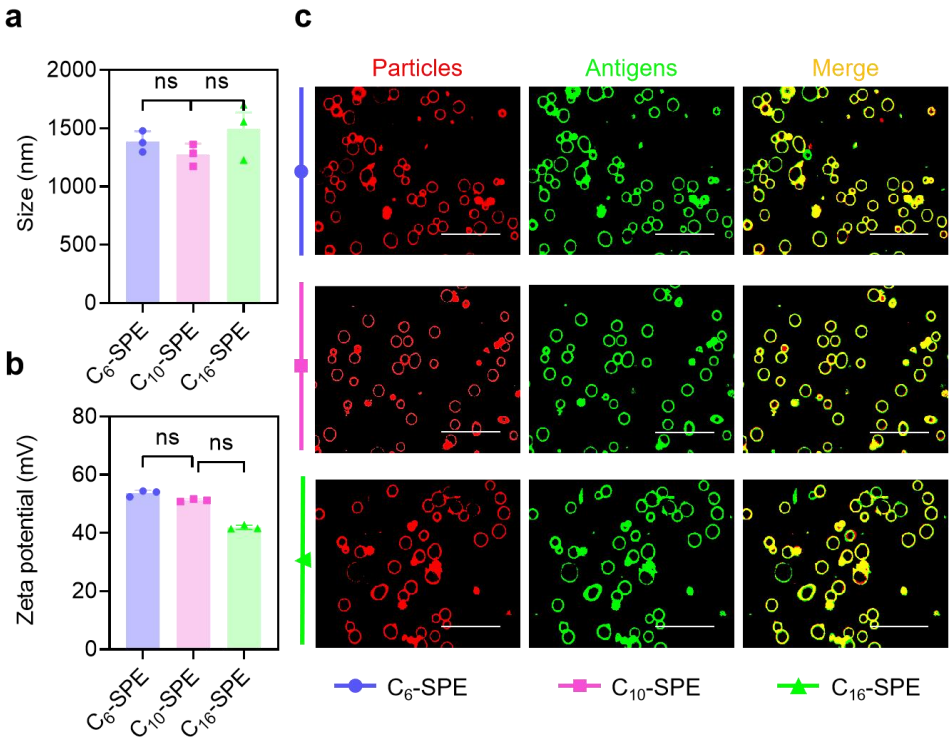

Figure 3-3. Engineered peptide enable tunable binding of immunogens to SPE. (a) The size and (b) Zeta potential of C_6-SPE, C_{10}-SPE and C_{16}-SPE. (c) CLSM images of C_6-SPE, C_{10}-SPE and C_{16}-SPE. Engineered peptide were labelled with Cy5 (green) and alum were labelled with lumogallion (red), respectively. Scale bar, 25 μm. Data were shown as mean ± s.e.m. (n = 3), analyzed by one-way ANOVA. ns, no significant differences.

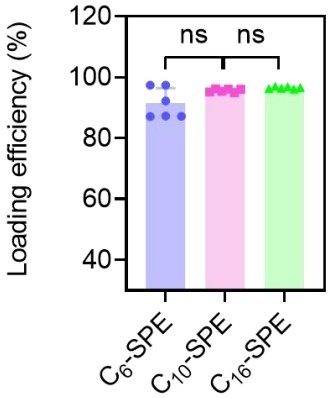

Figure 3-4. Antigen loading efficiency at the oil/water interphase. Data were shown as mean + s.e.m. (n = 3), ns, not significant.

It is known that many antigens rapidly desorb from alum in the presence of serum or interstitial fluid. To evaluate whether these lipopeptides were loaded at the interface of oil/water or adsorbing to the surface alum, we elucidated the *in vitro* release profiles of these lipopeptides in pH 6.5 PBS containing 10% FBS. Comparing with the cumulative release of ESIINFEKL peptides (with no lipo-chain modification),

which exceeded 90%, the limited cumulative release of lipopeptides, less than 20% over 15 days (Figure 3-5) showed that these lipopeptides tightly embedded at the oil/water interface. Accordingly, these results indicated that engineered peptides can be successful loaded at the oil-water interface within no significant differences of size, zeta potential and loading capacity, which is necessary for assessing the lipopeptides release kinetics of different groups.

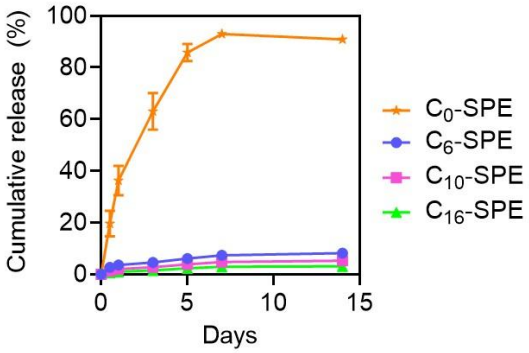

Figure 3-5. The *in vitro* release of lipopeptides and ESIINFEKL short peptides. Accumulation of extracellular release of peptides in simulated the intracellular fluids: 10% FBS in PBS at pH = 6.5.

3.4.2 Dictating antigenic peptide release in vivo

To elucidate the release profile *in vivo*, Cy5-C_6-ESIINFEKL, Cy5-C_{10}-ESIINFEKL and Cy5-C_{16}-ESIINFEKL were used to fabricate Cy5-C_6-SPE, Cy5-C_{10}-SPE, Cy5-C_{16}-SPE, respectively. BALB/c mice (6 - 8 weeks, n = 4/ per group) were injected with the indicated vaccine formulations (Table 3-1) at the injection site. Formulations were intramuscularly injected in a volume of 100 uL per mouse.

Table 3-1 Formulations for antigen metabolism (per mouse)

Group	Alhydrogel®adujvant 0.1% (w/v)	Squalene (5%, v/v)	antigen
Cy5-C_6-SPE	100 μg	5 μL	10 μg
Cy5-C_{10}-SPE	100 μg	5 μL	10 μg
Cy5-C_{10}-SPE	100 μg	5 μL	10 μg

And tracked by *in vivo* imaging system (IVIS). As shown in Figure 3-6a-b, the antigens of Cy5-C_6-SPE cleared by approximately 70% after 3 days, while Cy5-C_{10}-SPE and Cy5-C_{16}-SPE, with about 50% and 30% clearance respectively after 3 days. Additionally, the florescence of Cy5-C_6-SPE were cleared from the injection site within 14 days, whereas those from Cy5-C_{10}-SPE were cleared within 21 days, and antigens from Cy5-C_{16}-SPE persisted for over 21 days. Afterwards, BALB/c mice

were injected with droplets with Lumogallion-labled aluminum and Cy5-labled lipopeptides. Histology of the injection sites 14 days after injection revealed the co-localization of antigens from Cy5-C_{10}-SPE and Cy5-C_{16}-SPE with alum, while antigens from Cy5-C_6-SPE were undetectable (Figure 3-6c). These findings demonstrated that the three engineered peptides were tightly embedded at the oil/water interface, and with distinct clearance rates *in vivo*, with C_6-ESIINFEKL emitting most rapidly, followed by C_{10}-ESIINFEKL, and then C_{16}-ESIINFEKL.

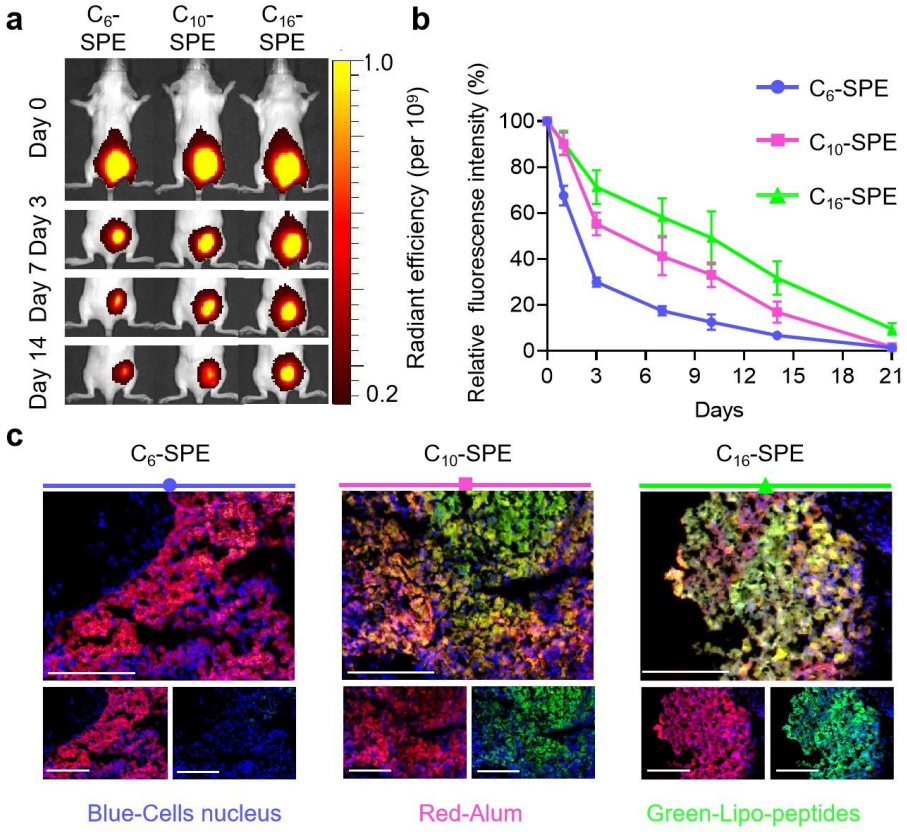

Figure 3-6. The metabolism of lipo-peptides *in vivo*. (a) IVIS images and (b) Mean total radiance from groups of animals over time (n=4/per group). (c) BALB/c mice (n = 3/ per group) injected with C_6-SPE, C_{10}-SPE and C_{16}-SPE (Cy5-labled lipopeptide, Lumogallion-labled alum), and were killed 14 days post-vaccination. Then the tissue from immunization sites were analyzed by histology. Shown are representative injection site cross sections from animals receiving of C_6-SPE, C_{10}-SPE and C_{16}-SPE groups, Scale bar, 200 μm.

3.4.3 Synergetic cross-presentation and co-stimulatory effect for enhanced T cell activation

Considering the vital role of DCs, our research delves into elucidating the effects of sequential lipopeptides delivery on DC dynamics and fate. C57BL/6 mice (6 - 8 weeks, n = 6/ per group) were injected with the indicated vaccine formulations at the injection site. After assessing the recruitment of DCs, which indicated no significant difference among C_6-SPE, C_{10}-SPE and C_{16}-SPE (Figure 3-7a), we next evaluated the antigen uptake of DCs. There were no significant differences among each group until

the 7 days after vaccination (Figure 3-7b-c), possibly due to ample antigen present at the injection site, providing sufficient substrate for cellular uptake. Consequently, endocytosis analysis exhibited no significant difference among the groups. These findings suggested that DC recruitment and antigen uptake did not significant differ during this stage, promoting us to evaluate the activation of DCs *in situ*.

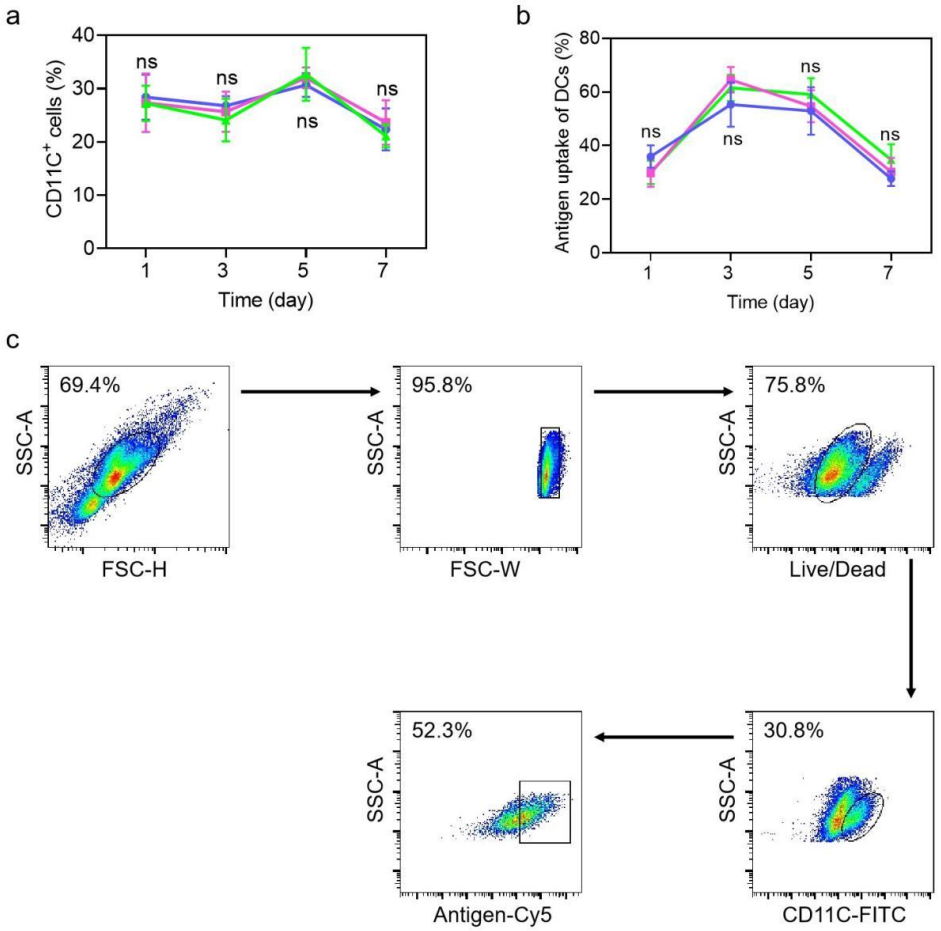

Figure 3-7. DCs recruitment and antigen uptake at the injection site. (a) Flow cytometry analysis on DCs recruitment. (b) C57BL/6 mice (n=6) were intramuscularly administered with the specified formulations containing peptides with Cy5 labels at the N-terminus to assess the uptake of lipo-peptides by DCs at the injection site. The single-cell suspension was prepared to analyze the recruitment and antigen uptake of DCs. (c) Gating strategy of DCs recruitment and antigen uptake at the injection site. All data in the graphs were presented as arithmetic means ± s.e.m. from three independent experiments, ns, not significant.

For tumor peptide vaccines, the activation of tumor-specific $CD8^+$ T cells depends on the recruitment of APCs to injection sites for uptake and subsequent activation, followed by their migration to lymph nodes to prime T cells response. To activate T cells, APCs need to meet three requirements: presenting tumor antigens to TCRs recognition, expressing co-stimulatory molecule to interact with CD28 molecule, and secreting cytokines for providing activation signal (Figure 3-8a).[143] After antigen uptake, DC express co-stimulatory molecule (CD80/CD86) and engage

in antigen cross-presentation (MHC-I-peptide complex), which are crucial for the activation of tumor-specific $CD8^+$ T cells. Interestingly, as illustrated in Figure 3-8b, the frequency of MHC-I-SIINFKEL$^+$ DCs in C_6-SPE rapidly rose to approximately 25% one day post-vaccination, with a 1.8-fold increase compared to C_{10}-SPE and a 3.7-fold increase compared to C_{16}-SPE (Figure 3-9a). This frequency remained elevated for three days, and subsequently showed a significantly decrease. The expression of MHC-I-peptide complex in C_{16}-SPE showed a rising tendency until more than 7 days post-vaccination. In contrast, C_{10}-SPE showed an increasing trend in the populations of MHC-I-SIINFEKL$^+$ DCs, until 5 days post-vaccination, reaching a peak five days post-vaccination, with a 0.9-fold increase compared to C_6-SPE and a 0.8-fold increase compared to C_{16}-SPE (Figure 3-9b).

In addition, the upregulation of co-stimulatory molecule on DCs, in synergy with antigen presentation, is regarded as the key driver of T cells activation. This observation led us to assess the expression level of co-stimulatory molecule on DCs. Surprisingly, although the frequency of MHC-I-SIINFEKL$^+$ DCs in C_6-SPE increased to a high level one day post-vaccination, the optimal expression of $CD86^+$ was delayed until five days post-vaccination, where the amount of MHC-I-SIINFEKL$^+$ DCs in C_{10}-SPE increased to a maximum value of approximately 30%, with no significant difference compared to C_{10}-SPE and C_{16}-SPE. Meanwhile, the frequency of $CD86^+$ DCs showed no significant difference among three groups one day post-vaccination (Figure 3-8c and Figure 3-9c-d).

Moreover, interleukin (IL)-12(p70) and tumor necrosis factor-alpha (TNF-α), are known for inducing effector functions of $CD8^+$ T as well as protecting $CD8^+$ T cells from exhaustion.[144,145] The level of IL-12(p70) in C_{10}-SPE was increased by 100% compared to C_6-SPE and by 42% compared to C_{16}-SPE, while the secretion of TNF-α increased by 204% compared to C_6-SPE and by 53% compared to C_{16}-SPE five days after vaccination, respectively. Conversely, almost no difference was observed between each group one day post-vaccination (Figure 3-9e-h).

In summarize, the preferential antigen release of C_6-SPE led to a significant up-regulated expression of MHC-I-peptide complex one day post-vaccination. Conversely, the slow release of antigen in C_{16}-SPE resulted in a delay in the optimal expression of MHC-I-peptide complex over 7 days post-vaccination. Both missed the peak expression of CD86 and elicited suboptimal secretion of IL-12(p70) and TNF-α five days post-vaccination. Only the C_{10}-SPE induced simultaneous peak expression of MHC-I-peptide complex and CD86, thereby increased secretion of IL-12(p70) and TNF-α five days post-vaccination.

After activation, DC express chemokines and home to lymph node for T cell priming, which promoted us to evaluate the frequency of $CCR7^+$ DCs. As shown in Figure 3-8d, although the expression of $CCR7^+$ on DCs in the C_{16}-SPE group was lower than the C_{10}-SPE group, an increasing tendency of $CCR7^+$ DCs in the group of C_{10}-SPE and C_{16}-SPE over time were observed, indicating potent homing of DCs to lymph nodes. But, C_6-SPE-treated mice demonstrated a rapid decrease in $CCR7^+$ DCs five days post-vaccination, potentially due to DCs exhaustion from high MHC-I interactions with limited co-stimulatory molecule expression (Figure 3-10).

Further examination of CD86$^+$ MHC-I$^+$ DC in draining lymph nodes (dLNs) revealed increased migration in C_{10}-SPE treatment group, peaking on five days post-vaccination (Figure 3-8e and Figure 3-11a-b). This increase was 110 % higher compared to C_6-SPE, and 24 % higher compared to C_{16}-SPE, respectively (Figure 3-11c-d). At the same time, we observed the most robust proliferation of Fas$^+$ CD8$^+$ T cells in C_6-SPE treatment group, increased by 80% compared to C_{10}-SPE and by 20% compared to C_{16}-SPE (Figure 3-8f). This suggested that C_6-SPE-treated group, T cells within the lymph nodes may undergo apoptosis rather than activation into effector T cells, likely due to the binding of Fas receptor to Fas ligand (FasL).

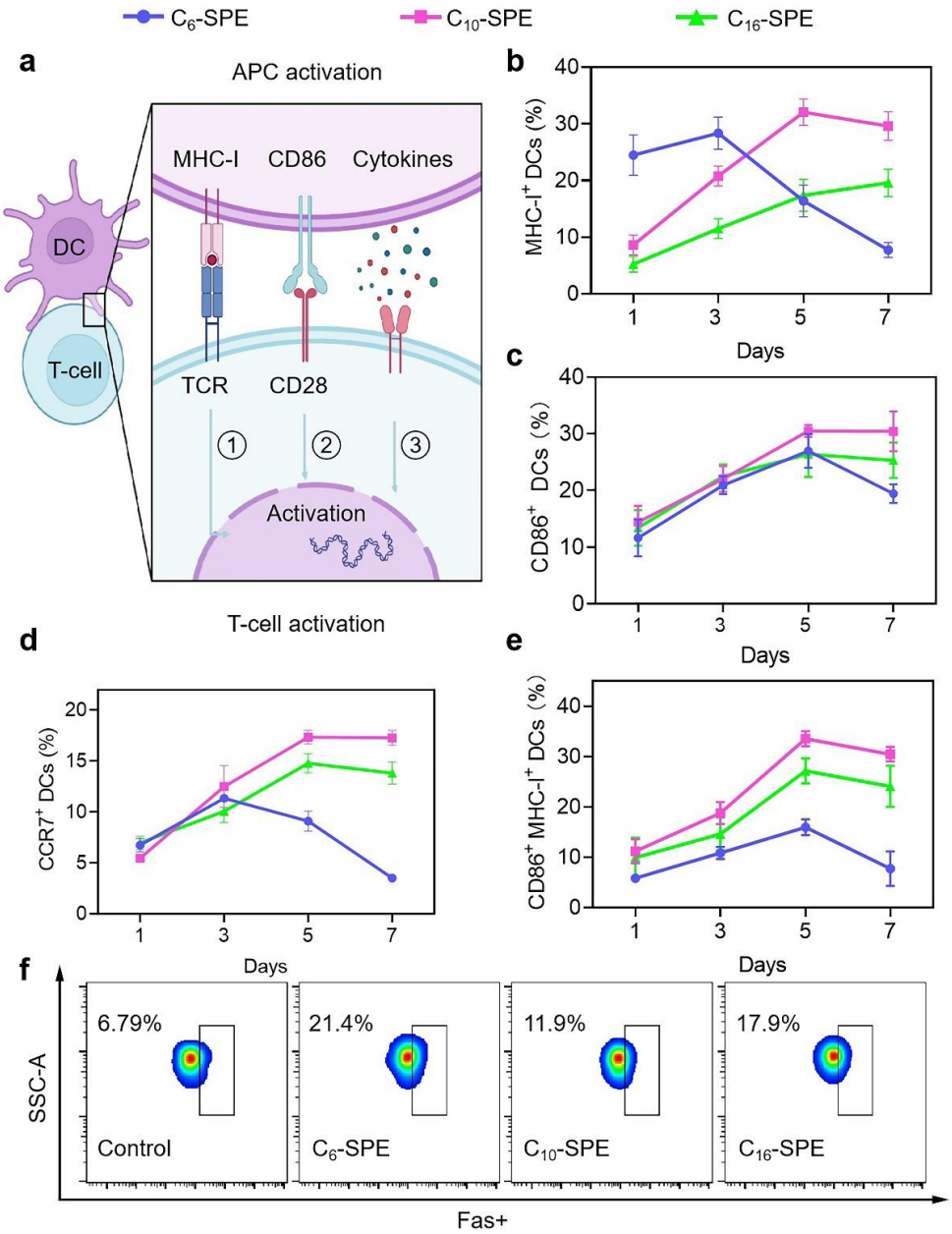

Figure 3-8. Immune activation at the injection sites. (a) Schematic representation of the three key signals for T cell activation. (b) Flow cytometry analysis on the populations of MHC-I-SIINFEKL$^+$ DCs over time *in situ*. (c) Flow cytometry analysis on the populations of CD86$^+$ DCs over time *in situ.* (d) Flow

cytometry analysis on the populations of CCR7$^+$ DCs over time *in situ*. (e) Flow cytometry analysis on the populations of CD86$^+$ MHC-I-SIINFEKL$^+$ DCs over time in dLNs. (f) Flow cytometry images on the populations of Fas$^+$ CD8$^+$ T cells one day post-vaccination in dLNs. Data were shown as mean ± s.e.m. (n = 6).

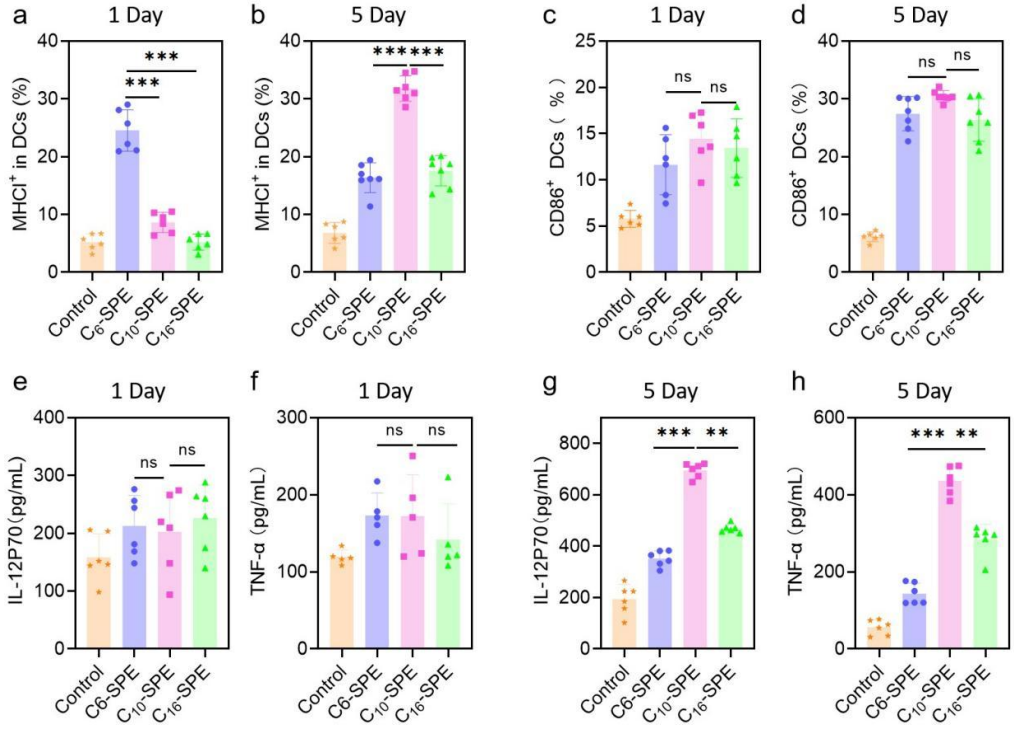

Figure 3-9. Antigen presentation and the number of CD86$^+$ DCs *in vivo*. (a) The number of MHC-I$^+$ DCs one day and (b) five days after vaccination. (c) The number of DC86$^+$ DCs one day and (d) five days after vaccination. The secretion of cytokine (e) IL-12P70 and (f) TNF-α in site one day after vaccination. The secretion of cytokine (g) IL-12P70 and (h) TNF-α in site five days after vaccination. All data in the graphs were presented as the arithmetic mean ± s.e.m. from three independent experiments (n=6). One-way analyses of variance were conducted with Tukey's correction for multiple comparisons. $^{**}P < 0.01$, $^{***}P < 0.001$, ns, not significant.

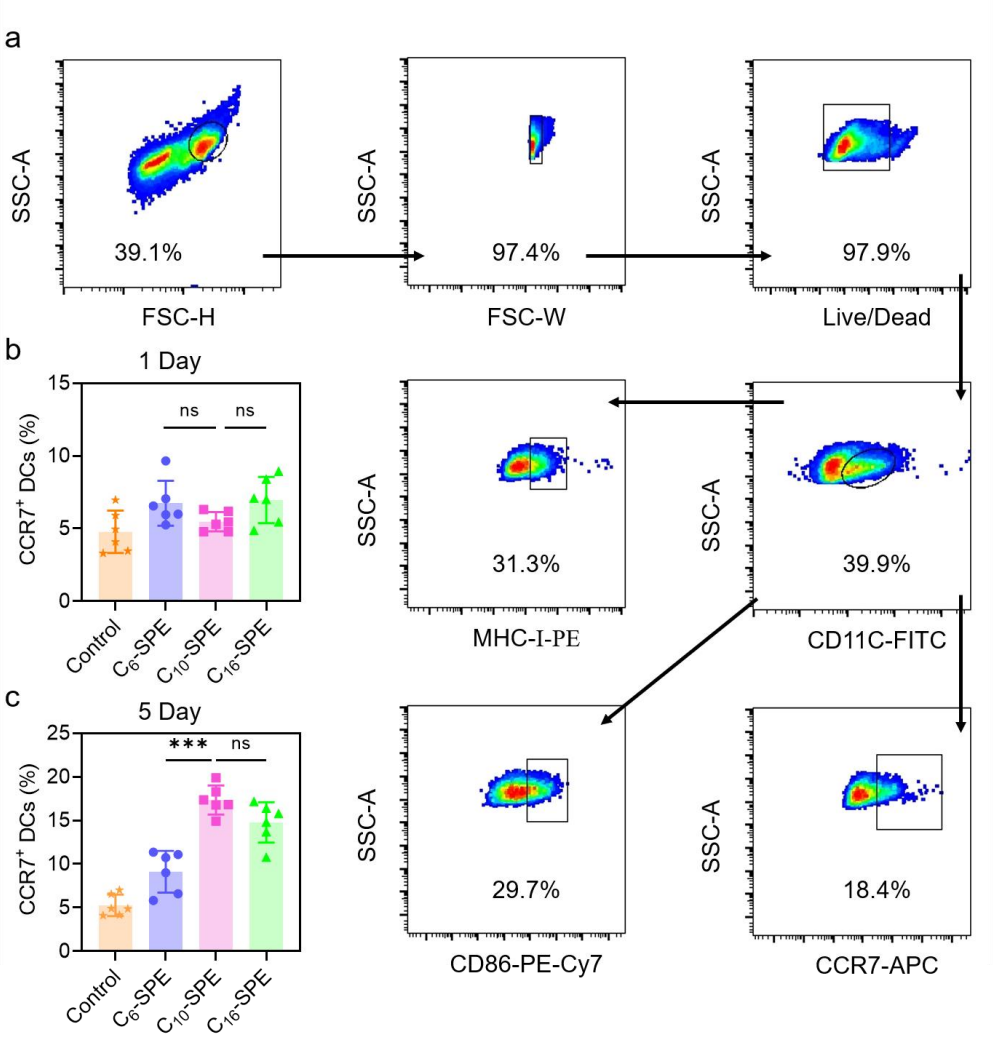

Figure 3-10. Chemokine CCR7$^+$ expression on DCs. (a) Gating strategy of antigen presentation, the expression of CD86 and CCR7 on DCs at the injection site. (b) the expression of CCR7 on DCs (b) one day and (c) five days after vaccination at the injection site. One-way analyses of variance were conducted with Tukey's correction for multiple comparisons. ***$P < 0.001$, ns, not significant.

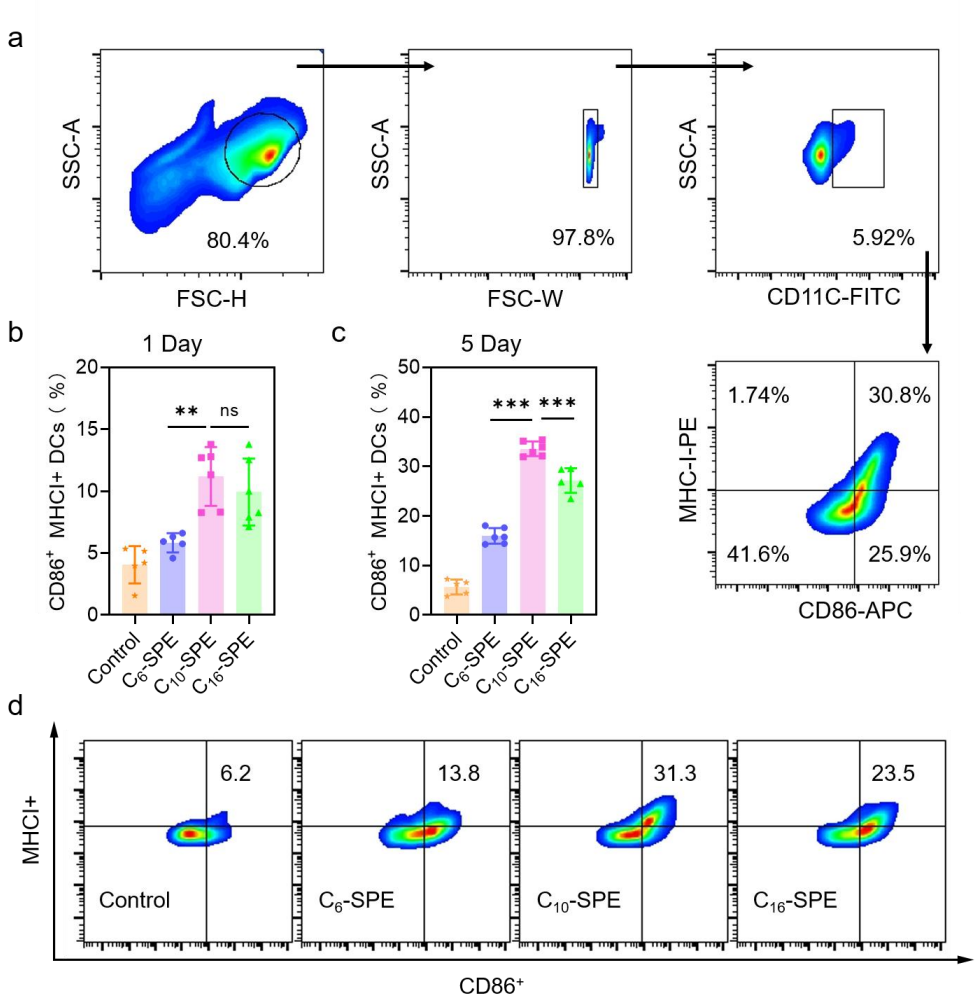

Figure 3-11. The populations of CD86$^+$ MHC-I$^+$ DCs in dLNs. (a) Gating strategy of MHC-I$^+$ CD86$^+$ DCs in dLNs. The populations of MHC-I$^+$ CD86$^+$ DCs (b) one day and (c) five days after vaccination in dLNs. (d) Flow dot plot of MHC-I$^+$ CD86$^+$ DCs five days after vaccination in dLNs. One-way analyses of variance were conducted with Tukey's correction for multiple comparisons. $^{**}P < 0.01$, $^{***}P < 0.001$, ns, not significant.

3.4.4 Regulating T-cell-mediated immune response and anti-tumor effect

Based on the haematoxylin and eosin (H&E) images, there were no observable signs of tissue damage or toxicity in the major organs after SPE treatments (Figure 3-12a). Additionally, there were no significant differences observed between untreated group (Control) and droplets-treated groups in term of biochemical analysis (Figure 3-12b). The results suggested that the three droplets with these lipopeptidess caused no detectable adverse effects on the major organs and possessed safety profile for vaccine applications.

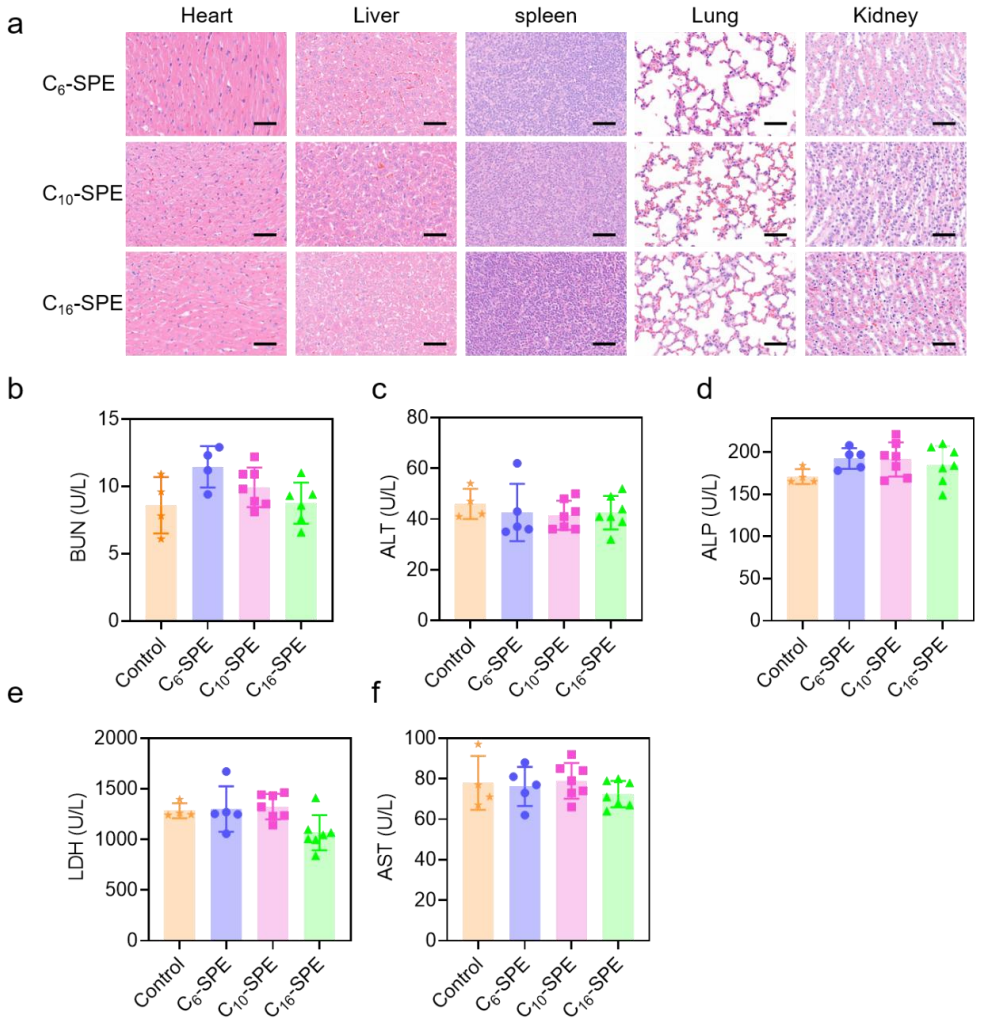

Figure 3-12. The safety profile of droplets. Healthy mice were intramuscularly administered with the indicated formulations, and serum was collected on Day 28 for analysis. (a) Histopathological evaluations of the vital organs from the BALB/c mice. Healthy mice (n=6) were intramuscularly administered with the indicated formulations, 28 days after administration, the heart, live, spleen, lung and kidney were harvested to stained with H&E. Scale bar: 100 μm. Analysis of (b) blood urea nitrogen (BUN), (c) alanine aminotransferase (ALT), (d) alkaline phosphatase (ALP), (e) lactate dehydrogenase (LDH), and (f) aspartate aminotransferase (AST).

Next, we evaluated the T cells response *in vivo* by vaccinating C57BL/6 mice twice with indicated formulations on Day 0 and Day 14. Fourteen days after the final vaccination, splenocytes were collected (Fig. 3-13a). ELISPOT results demonstrated that C_{10}-SPE induced a significant population of IFN-γ secreting cells in spleen, with a 1.8-fold increase compared to C_6-SPE and a 0.7-fold increase relative to C_{16}-SPE (Figure 3-13b, c). Furthermore, the frequency of spleen Pentamer$^+$ CD8$^+$ T cells was significantly elevated in the C_{10}-SPE group, achieving 263% compared to C_6-SPE, and 166 % compared to C_{16}-SPE, respectively (Figure 3-13d). The immune results prompted us to evaluate the therapeutic effects of these droplets.

EG7-OVA tumor-bearing mice were vaccinated three times with PBS, C_6-SPE, C_{10}-SPE and C_{16}-SPE on Day 7, 12, and 17, the tumor tissue of humanely execution tumor-bearing C57BL/6 mice were collected for further immunological analysis, and another tumor-bearing C57BL/6 mice were measured every 2 or 3 days for tumor volumes (Figure 3-13e). We observed a significant reduction in tumor growth and prolonged survival of C_{10}-SPE, compared to C_6-SPE and C_{16}-SPE (Figure 3-13f, g). We also evaluated the infiltration of $CD8^+$ T cells in the tumor microenvironment. Additionally, the infiltration of $CD8^+$ T cells in the tumor microenvironment was evidently higher in the C_{10}-SPE group (Figure 3-13h).

These data collectively demonstrated that by regulating the antigen release kinetics of C_{10}-SPE, a synergistic cross-presentation and co-stimulatory effect were achieved, leading to robust activation of DCs homing to dLNs. This was followed by functional, non-apoptotic activation of $CD8^+$ T cells, resulting in effective tumor regression.

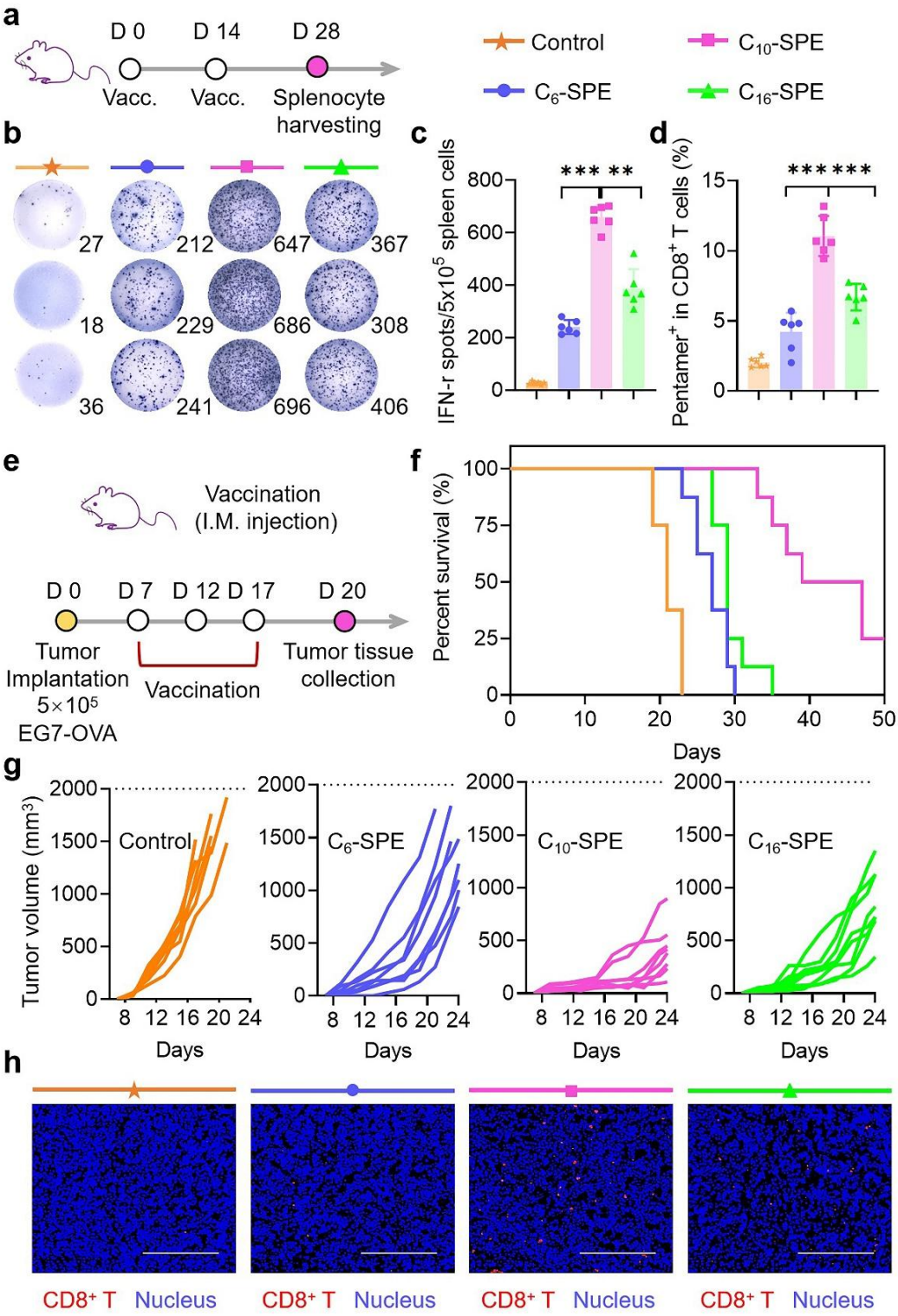

Figure 3-13. Cellular and anti-tumor immune response of C_6-SPE, C_{10}-SPE and C_{16}-SPE groups. (a-c) *In vivo* immune response analysis. C57BL/6 mice (n = 6/per group) were intramuscularly injected with indicated formulations, the splenocytes were collected for analysis at indicated timepoint. (a) Illustration of experimental design. (b-c) ELISPOT assay of IFN-γ secreting cells within the splenocytes. (d) Flow cytometric analysis of pentamer$^+$ CD8$^+$ T cells among splenocytes. (e-h) *In vivo* anti-tumor immune response induced by C_6-SPE, C_{10}-SPE and C_{16}-SPE in the EG7-OVA

model (n = 8/per group). (e) Illustration of experimental design. (f) Survival and (g) Tumor growth of mice (E.G7-OVA tumors) with indicated formulations. (h) Representative immunofluorescence image of tumor sections, corresponding $CD8^+$ T cells distribution in EG7-OVA tumor after injection with indicated formulations, Scale bar, 200 μm. Analyzed by one-way ANOVA. $^{**}p < 0.01$, $^{***}p < 0.001$.

3.4.5 CpG Co-Delivery remedied the immune response of C_6-SPE, inducing comparable anti-tumor effect with C_{10}-SPE

The aforementioned results underscore that SPE vaccines typically induce optimal activation of DCs five days post-vaccination. However, this timing may hinder clinical translation, as in practice, the majority of antigens exhibit rapid release kinetics, typically peaking between one to three days post-injection.[61] To address this, Jin, Seung Mo, and colleagues endeavored to integrate multiple Toll-like receptor (TLR) stimuli within the optimal sequence, duration and time window to induce effector/non-exhausted APCs, there by achieving effective anti-tumor immunity with no evident exhaustion.[146] This inspired us to introduce TLR agonist, specifically, CpG into our SPE formulations to enhance the immunogenicity. We engineered three types of droplets: C_6-SPEC (C_6-SPE/CpG), C_{10}-SPEC (C_{10}-SPE/CpG), and C_{16}-SPEC (C_{16}-SPE/CpG) (Figure 3-14a). These droplets were designed to efficiently incorporate lipopeptides at the oil-water interface, and utilized the positive charge properties of aluminum adjuvants for the effective adsorption of negatively charged CpG. This method has been demonstrated to activate plasmacytoid dendritic cells (pDCs) and express a high level of co-stimulatory molecule for T cell binding and maturation. We presume that the release of CpG from SPE may facilitate the expression of co-stimulatory molecule at the early stage, thereby enhancing T cell response in the C_6-SPEC group. Furthermore, the initially released CpG interacts spatiotemporally with SPE to promote a sustained activation environment for DCs *in situ*, further enhancing the immune response in the C_{10}-SPEC groups.

As shown in Figure 3-14b-c, the results of antigens and CpG loading capacity indicated that all three types of droplets adsorbed more than 90% of the fluidic antigens and CpG, with no significant differences between each group. Following successful loading, we next evaluated the release kinetics of CpG, which have been shown to be strongly correlated with the activation of DCs. As shown in Figure 3-15, the cumulative release of CpG over 72 hours may provide sufficient overlap of co-stimulatory signal with antigen cross-presentation in C6-SPEC, potentially boosting the immunogenic response.

Above results promoted us to evaluate the populations of MHC-I-$SIINFEKL^+$ and $CD86^+$ DCs at injection site. C57BL/6 mice (6 - 8 weeks, n = 6/ per group) were injected with the indicated vaccine formulations at the injection site. As shown in Figure 3-14d, the populations of MHC-I-$SIINFEKL^+$ DCs in each group exhibited a similar trend as without CpG, indicating consistent antigen processing irrespective of CpG inclusion. Simultaneously, the release of CpG facilitated the upregulation of co-stimulatory (CD86) molecule on DCs at early stage (Figure 3-14e), leading to a continuous expression of these molecule till five days following vaccination. This

timing aligns with the maximal antigen cross-presentation, ensuring temporal synchronization between DC activation and antigen presentation in C_6-SPEC and C_{10}-SPEC groups. This coordination is crucial for optimizing the efficacy of the immune response initiated by the vaccine. After immunization, the IFN-γ secreting cells and the antigen-specific $CD8^+$ T cells induced among splenocytes by C_6-SPEC demonstrated a comparable level with that by C_{10}-SPEC. (Figure 3-14f-h). Accordingly, when applied to EG7-OVA tumor vaccine, the observed inhibition of tumor growth (Figure 3-14i) and prolonged survival (Figure 3-14g) in C_6-SPEC were comparable with C_{10}-SPEC, further verified that regulated spatiotemporal synchronization between antigen cross-presentation and co-stimulatory factors enhances the stimulatory function of APCs. This, in turn, facilitates the development of durable, non-exhausted, functional $CD8^+$ T cells, thereby bolstering anti-tumor immunity.

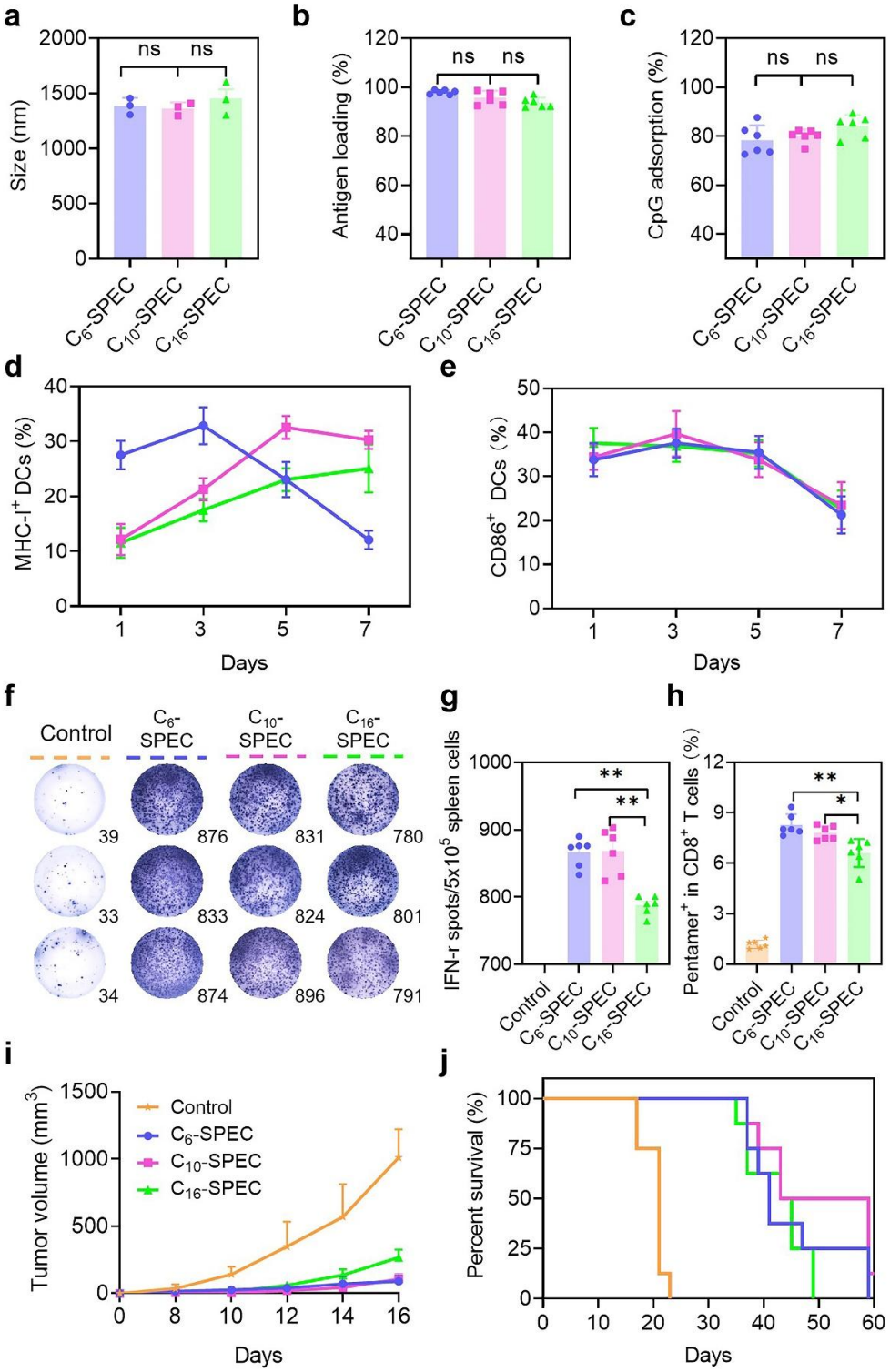

Figure 3-14. Co-delivery of CpG with lipo-peptides via SPE for a robust immune response. (a) The size of C_6-SPEC, C_{10}-SPEC and C_{16}-SPEC. (b) Lipopeptides and (c) CpG loading capacities of SPE. Flow cytometry analysis on the populations of (d) MHC-I-SIINFEKL$^+$ and (e) CD86$^+$ DCs over time *in vivo*. (f-g) ELISPOT assay of IFN-γ secreting cells within the splenocytes. (h) Flow cytometric analysis of pentamer$^+$ CD8$^+$ T cells among splenocytes. (i) Tumor growth and (j) Survival of mice with indicated formulations. Data were shown as mean ± s.e.m. The mouse was

n=6 per group for the immune response assay, and n=8 per group for the anti-tumor assay. Analyzed by one-way ANOVA. *$p < 0.05$, **$p < 0.01$.

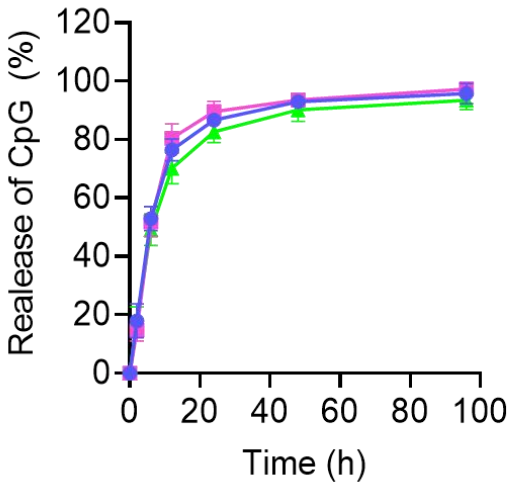

Figure 3-15. Accumulation of extracellular release of CpG in simulated the intracellular fluids: 10% FBS in PBS at pH = 5.0.

3.5 Conclusion

In this study, we developed SPEs to modulate antigen release dynamics and APC activation, investigating the synchronizing effect of antigen presentation and co-stimulatory signal on T cell engagement. By site-specific introducing saturated fatty acids with varied carbon chain length, these lipopeptides achieved high loading efficiency exceeding 90%, but demonstrated distinct release kinetics from the droplets, leading to varied *in vivo* clearance rates, with C_6-ESIINFEKL released most rapidly, followed by C_{10}-ESIINFEKL, and then C_{16}-ESIINFEKL. After intramuscular administration, SPEs loaded with these varied lipopeptide induced comparable recruitment of DCs and the expression of CD86, but exhibited diverse dynamics in the expression of MHC-I-peptide complex. This tuned the spatiotemporal synchronization of antigen cross-presentation and the co-stimulatory signal. Specifically, the rapid antigen release of C_6-SPE led to a significant up-regulated expression of MHC-I-peptide complex one day post-vaccination, Conversely, the slow release of antigen in C_{16}-SPE resulted in a delay in the optimal expression of the MHC-I-peptide complex over 7 days post-vaccination. Both missed the critical window to coordinate with CD86 expression for DC activation, thereby hindering effective T cell activation. This mismatch led to an elevated rate of T cell apoptosis within the lymph nodes, which subsequently reducing the population of tumor-infiltrating T cells, and causing suboptimal tumor regression. C_{10}-SPE, however, induced simultaneous peak expression of MHC-I-peptide complex and CD86 five days post-vaccination, achieving an optimal DC activation. These activated DCs further engaged with T cell, initiating robust T cell activation, resulting in effective tumor regression and prolonged survival in EG7-OVA-bearing mice. Furthermore, when combined with the TLR agonist (CpG), the release of CpG, boosted DC activation at the early stage, providing a sustained expression of CD86 window for DC activation. This not only

prevented T cell apoptosis in the C_6-SPE group, but also enhanced the T cell response observed in the C_{10}-SPE, inducing an enhanced anti-tumor response in the tumor-bearing mice.

Our results underscore the critical of coordinated antigen presentation and co-stimulatory for effective anti-tumor immunity. Despite promising outcomes, several key points warrant our attention. Although the C_{16}-SPE induced a suboptimal T cell response compared to C_{10}-SPE, it still elicited a robust T cell response compared to C_6-SPE. This may be contributed to the temporal delivery, where the maximum expression of co-stimulatory molecule preceding the peak of antigen cross-presentation (C_{16}-SPE) induced a more effective T cell response compared to the reverse order (C_6-SPE). This aligned with the findings using CpG, where its co-delivery with C_6-ESIINFEKL and C_{10}-ESIINFEKL, provided a sustained expression of CD86 window for DC activation, resulting in an enhanced T cell response in both C_6-SPEC and C_{10}-SPEC, though a suboptimal T cell response was observed in C_{16}-SPEC.

Admittedly, Pickering emulsion may not be the only delivery system to dictate the spatiotemporal dynamics. Other vehicles, such as layer-by-layer assemblies, multi-chamber liposomes or hydrogels with hierarchical structures, may also be designed to regulate the release kinetics.[147-149] Herein, through comparing the SPEs with varied antigen release kinetics, we aim to prone upon the importance of the synergetic effects of antigen presentation and APC activation, hoping to encourage a paradigm shift in vaccine design, urging researchers to consider the dynamic interplay between antigen presentation and co-stimulatory signal. This approach may inspire the design of nanoplatforms for the efficient co-delivery and controlled release of multiple therapeutic cargoes, such as mRNA-based neoantigen, STING agonist and more, to achieve coordinated antigen presentation and co-stimulatory signal for effective anti-tumor immunity.

Chapter 4 Inside-out assembly of viral antigens for the enhanced vaccination

4.1 Abstract

Current attempts in vaccine delivery systems concentrate on replicating the natural dissemination of live pathogens, but neglect that pathogens evolve to evade the immune system rather than to provoke it. In the case of enveloped RNA viruses, it is the natural dissemination of nucleocapsid protein (NP, core antigen) and surface antigen that delays NP exposure to immune surveillance. Here, we report a multi-layered aluminum hydroxide-stabilized emulsion (MASE) to dictate the delivery sequence of the antigens. In this manner, the receptor-binding domain (RBD, surface antigen) of the spike protein was trapped inside the nanocavity, while NP was absorbed on the outside of the droplets, enabling the burst release of NP before RBD. Compared with the natural packaging strategy, the inside-out strategy induced potent type I interferon-mediated innate immune responses and triggered an immune-potentiated environment in advance, which subsequently boosted $CD40^+$ DCs activation and the engagement of the lymph nodes. In both H1N1 influenza and SARS-CoV-2 vaccines, rMASE significantly increased antigen-specific antibody secretion, memory T cell engagement, and Th1-biased immune response, which diminished viral loads after lethal challenge. By simply reversing the delivery sequence of the surface antigen and core antigen, the inside-out strategy may offer major implications for enhanced vaccinations against the enveloped RNA virus.

4.2 Introduction

A major challenge in vaccine design is stimulating the potency and duration of the immune responses.[150,151] The immune responses to infection or vaccination are temporal sequences of events, which depend on the ordered exposure of antigenic components to the immune system,[152,153] as well as the coordinated actions of the lymph nodes, immunocytes, cytokines, etc.[154,155] Thus, potent vaccines are expected to harness spatial and temporal control over sequential immune activation.[156]

To address this, nano- and micro-delivery systems with controllable physicochemical properties and multi-level nanostructures are engineered to deliver multiple vaccine components.[157,158] Additionally, since pathogens are the perfect vehicles of natural selection, there is a trend to mimic their structures or physiochemical properties.[159,160] Increased lymph node accumulation of antigen, antigen uptake, and antigen cross-presentation have been witnessed in previous attempts to replicate live pathogens' sizes, shapes, charges, and softness.[161,162] As for the delivery kinetics, it is thought to replicate the natural dissemination of multiple antigenic components, which may dictate the exposure sequence for subsequent immune activation in a biomimetic manner.[163]

Nonetheless, pathogens usually evolve to escape the immune system rather than to provoke it.[164-166] In the case of enveloped RNA viruses, genome replication results

in the accumulation of pathogen-associated molecular patterns, which can lead to a strong host anti-viral response.[167,168] To circumvent this, immunogenic components, such as viral genes and proteins (e.g., nucleocapsid protein, NP), are tightly bound and hidden inside.[169,170] Subsequently, the embedded NP is delayed in its exposure to immune surveillance, leading to suppressed type I interferon (IFN-I) expression, as well as impeded anti-viral effects.[171] Accordingly, the exact replicas of natural dissemination may not be an optimal solution. As a preliminary test, we treated bone marrow-derived dendritic cells (BMDCs) with the surface antigen and NP of H1N1 influenza virus (A/Puerto Rico/8/1934)[172] and SARS-CoV-2 (hCoV-19/China/CAS-B001/2020),[173] respectively. In the presence of the surface antigen, higher doses of NP resulted in the up-regulated expression of IFN-α, suggesting a robust anti-viral effect (Figure 4-1).

Under these circumstances, we anticipated that it would be the natural packaging of NPs on the inside and surface antigens on the outside, which delays the exposure of NPs to immune surveillance. Instead, the inside-out assembly of the viral antigens, which enables the exposure of the core antigens before the surface antigens (reversed delivery), may potentiate the immune responses. Compared to the exact replicas of the natural dissemination, the inside-out strategy may trigger a more robust IFN-I-mediated innate immune response in advance, cultivating an immune stimulatory environment for enhanced potency and duration of the immune responses. To this end, the delivery system is expected to offer a multi-level landing spot for the ordered and inside-out assembly of viral antigens with high loading efficiency, which may offer a tunable release at the specific location and the right time, thus dictating IFN-I signaling. Moreover, to maintain the protein structure and immunogenicity, it is also imperative to provide a facile and mild loading method to avoid the involvement of high-shear stress or organic solvents.

To achieve this, we developed a multi-layered alum-stabilized emulsion (MASE) to harness the delivery kinetics of the surface and core antigens. Through the co-assembly of alum and antigen at the oil/water (o/w) interface, the core antigen was trapped within the nanocage formed by the alum and o/w interface. Subsequently, another layer of alum was deposited, which further shielded the inner antigen and provided adsorption sites for the outer antigen. As such, the embedded antigen was only released after the detachment of the deposited alum, thus constituting the sequential delivery system. On the o/w interface, the layer-by-layer assembly may bypass the multiple encapsulation procedures and the involvement of organic reagents, assuring the epitope integrity of the proteins and the consecutive loading of surface antigen and NP in a facile and moderate way. To demonstrate the natural dissemination, surface antigen and NP were assembled consecutively on the outside and inside of the multi-layered droplets (iMASE). In contrast, the inside-out assembly reversed the delivery of surface antigen and NP (rMASE), thereby exposing the “soft spot” of the viruses. Consequently, it is anticipated that the inside-out strategy can cultivate the reversed encounter of the surface and core antigens to the immune system, which may strongly stimulate the anti-viral host immune responses. In this manner, IFN-I-mediated innate immune response may be activated for enhanced

adaptive immune responses.

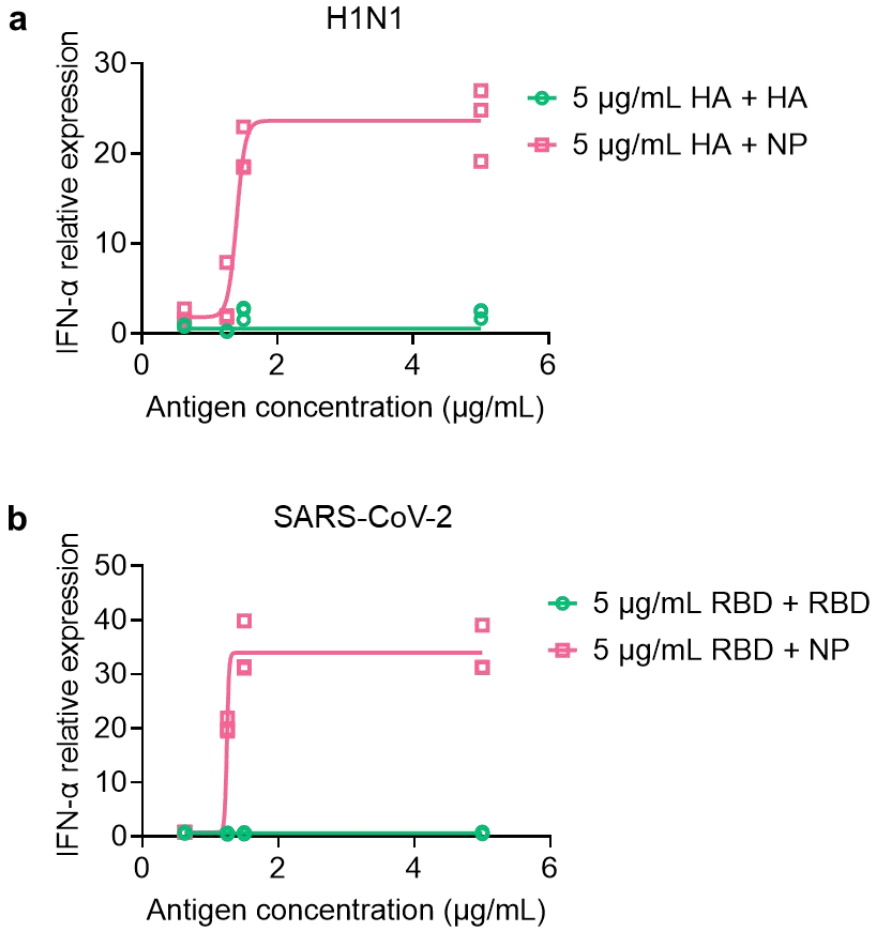

Figure 4-1 The expression of IFN-α by the BMDCs after surface antigen and nucleocapsid protein of (a) H1N1 influenza virus and (b) SARS-CoV-2 treatment. For H1N1, HA and NP were used to treat BMDCs, the mRNA expression of IFN-α was determined using RT-qPCR. These data were analyzed by nonlinear-regression (dose-response-stimulation). Simply increasing the levels of the surface antigens barely boosted the IFN-α expression. However, the IFN-α levels were in accordance with the presence of NP. With 2 μg/mL NP in the system, evident IFN-α-relative gene expression was observed, indicating that the pre-exposure of the NP before the surface ones may confer the enhanced IFN-I-mediated immune response and anti-viral effect.

4.3 Experimental details

4.3.1 Materials

Alum Hydroxide Gel Adjuvant (10 mg/mL) was purchased from InvivoGen, and squalene was purchased from Sigma. HA and NP of H1N1 influenza virus were purchased from Sino Biological. Recombinant RBD-sc-dimers of spike protein were obtained from the Institute of Microbiology, Chinese Academy of Sciences. The NPs were purchased from VACURE and Sino Biological. Roswell Park Memorial Institute

(RPMI) Medium 1640 basic, Dulbecco's modified Eagle's medium (DMEM), fetal bovine serum (FBS), and phosphate-buffered saline (PBS; pH = 7.4) were purchased from GIBCO BRL (Gaithersburg, MD, USA.). Fluorescent hydrophilic dyes Cy3, Cy5, and Cy7 were purchased from Fanbo Biochemical Co., Ltd. (Beijing, China). CCK-8 was purchased from Dojindo (Kumamoto, Japan).

HEK293T cells, Huh7 cells, and Vero cells were obtained from the American Type Culture Collection (ATCC). SARS-CoV-2 pseudovirus was obtained from National Institutes for Food and Drug Control (NIFDC). Luciferase 1000 Assay System was purchased from Promega (Madison, WI, USA).

4.3.2 Animals

All mice were raised in a specific pathogen-free facility, and the Institutional Animal Care and Use Committees at the Institute of Process Engineering, Chinese Academy of Sciences approved all experimental animal protocols (approval ID: IPEAECA2020401 and IPEAECA2021403). This study was performed in strict accordance with the Regulations for the Care and Use of Laboratory Animals and Guideline for Ethical Review of Animals (China, GB/T35892-2018).

4.3.3 Preparation of rMASE and iMASE

rMASE was prepared through layer-by-layer assembly of alum and antigen on the o/w interface. First, the alum/HA-assembled droplets were prepared by ultrasonication (Branson Digital Sonifier, total time = 120 s, power = 25%, interval time = 4 s) of the mixture of HA, alum, water, and squalene (Sigma, Germany). The alum concentration was 0.5 mg/mL, and the o/w ratio was fixed at 1/9. Then, an additional alum (0.5 mg/mL) was added into alum/HA-assembled droplets and mixed for about 30 min, and subsequently adsorbed with NP (0.05 mg/mL) to constitute the multi-layered alum-stabilized emulsion. Similarly, iMASE was prepared with NP entrapped on the inside, and HA absorbed on the outside. As a control, an alum-stabilized emulsion was prepared by single-step sonication (total time = 120 s, power = 30%, interval time = 4 s) of alum as the colloidal stabilizers and squalene as the dispersion phase.

4.3.4 Interactions between outer alum and alum/HA-assembled droplets

QCM-D (Biolin Science/Q-Sense, Sweden) was used to test the interactions between the outer alum and alum/HA-assembled droplets. The chips were modified by spin-coating with alum/HA-assembled droplets, HA and alum stabilized emulsions, respectively. Once the modified chips were installed, alum (0.5 mg/mL) was added to the QCM chamber at a continuous flow rate of 50 μL/min. The vibration frequency (ΔF) was measured to illustrate the adsorption tendency of the outer alum.

4.3.5 Characterization of rMASE and iMASE

To characterize the surface topography, the droplets were solidified and observed using scanning electron microscopy (SEM; JEOL, Japan). Briefly, solid alum/HA-assembled droplets were prepared using paraffin wax as the dispersion phase. The multi-layered solidified droplets were generated by cooling the temperature from 50 °C to 4 °C, and the outer alum (0.5 mg/mL) was added to attach for approximately

30 min. The droplets were observed by SEM after appropriate dilution (1:40). Three-dimensional structured illumination microscopy (3D-SIM; GE Healthcare, Issaquah, USA) and stimulated emission depletion microscopy (STED; Leica, Mannheim, Germany) were used to track the assembly of rMASE. Briefly, the indicated droplets were prepared through the assembly of Cy3-labeled HA, Cy5-labeled NP, and Lumogallion-labeled alum on the droplets. With the diluted droplets (1:50), the assembly steps were observed in detail at ×100 magnification. The surface elemental composition of rMASE was precisely determined using inductively coupled plasma mass spectrometry (ICP-MS; Agilent Technologies, Santa Clara, CA, USA).

4.3.6 Coverage of the inner antigen and the surface display of outer antigen

The specific binding properties of the antigen and antibody were used to analyze whether the attached alum shielded the inner antigens. To eliminate the non-specific interactions of the antibodies, the formulations were blocked with 4% FBS. The treated droplets were then incubated with anti-HA (Sino Biological Scientific) and anti-NP antibodies (Creative Biolabs). After removing the excess antibodies, Alexa Fluor 647-coupled goat anti-Rabbit IgG (H + L) cross-adsorbed secondary antibody (Thermo Fisher Scientific) and Alexa Fluor 488-coupled goat anti-mouse IgG (H + L) cross-adsorbed secondary antibody (Thermo Fisher Scientific) were added to maintain the reaction at 4 °C for 30 min. After washing off the uncombined secondary antibodies, the droplets were observed under a confocal laser scanning microscope (CLSM; Nikon, Japan).

4.3.7 Force tendency of the inner and outer antigen

An X-ray diffractometer (XPert3 MRD, X-ray Stress Analyzer, Malvern, UK) was used to measure the residual stress. Data collection was performed using the side-inclination method (Ψ-goniometer). The analysis was performed with an operating voltage of 45 kV and a current of 0.8 mA. The diffraction patterns were obtained using Cu-Kα radiation of wavelength 1.54 Å and an angle from 50° to 60° in steps of 0.02° intervals in the transverse direction. The least-squares method was used to regress each data point into a straight line.

$$M = \frac{\partial(2\theta)_{\psi}}{\partial \sin^2 \psi}$$

$$K = \frac{E_C}{2(1+v)} tan\,\theta_0 \bullet \frac{\pi}{180}$$

From the above equation, we measured and calculated the modulus of elasticity E and Poisson's ratio υ to calculate K, which was combined with the linear slope M to obtain the residual stress equation:

$$\sigma_{\varphi} = KM$$

Thermal stability was estimated using differential scanning calorimetry (DSC; Netzsch, Germany) to assess the antigens release trend. An empty alum pan was used as the reference. The heating rate of the samples was 10 °C/min in the temperature range of 25–200 °C. The locations of the thermal peaks were determined using GraphPad Prism 9.

4.3.8 Evaluation of antigen release

To analyze the intracellular alum dynamics, BMDCs were co-incubated with rMASE or iMASE for different periods. In the following step, cells were fixed with 2.5% glutaraldehyde overnight in a 0.5 M phosphate solution. Afterward, cells were postfixed in osmium tetroxide, dehydrated in ethanol, and embedded in Epon. To observe the cells, the dishes were broken into pieces and glued onto Epon sticks, and a range of 80–100 nm was selected for each section. Uranyl acetate and lead citrate were used to stain slices. Transmission electron microscopy (TEM; JEOL, Japan) was performed to obtain images at ×10,000 magnification.

The intracellular antigen release profile was evaluated using a high-content live-cell imaging system (Operetta CLS, PerkinElmer, Waltham, MA, USA). rMASE and iMASE were prepared using FITCHA and Cy5-NP, respectively, and were co-incubated with BMDCs for 6 h to allow maximum uptake. Residual droplets were removed from the medium. Subsequently, the fluorescence intensities of HA and NP were measured at the indicated times.

4.3.9 Antigens depot and uptake

To measure antigen retention at the injection site, BALB/c mice (6–8 weeks, female) were intramuscularly administrated the indicated formulations containing 5 μg/dose Cy5-HA conjugate and 5 μg/dose Cy7-NP conjugate (Thermo Fisher). The in vivo imaging system FX Pro (Kodak, Rochester, USA) was used to collect fluorescence signals of the antigens at the injection site after intramuscular administration at the indicated time points.

In addition, we evaluated the uptake in vivo by the intramuscular administration of the indicated formulations to BALB/c mice (6–8 weeks, female). Specifically, muscle tissues at the injection sites were harvested and digested with 0.2% (w/v) collagenase type II for 2 h at 37 °C. Afterward, the cells were collected and blocked with anti-mouse CD16/CD32 antibody. After washing thrice, the cells were stained with Ghost Dye™ Violet 450 Viability, PE dump channel markers (anti-mouse F4/80 and Ly-6C antibodies), and PerCP-Cy5.5 anti-mouse CD11c antibody. Data were collected using flow cytometry (CytoFlex LX; Beckman Coulter).

4.3.10 Antigen-specific antibody secretion

BALB/c mice (6 – 8 weeks, female) were intramuscularly administered then indicated vaccines, and serum was collected to detect antigen-specific antibody titers. Briefly, 100 μL of antigen diluent (2 μg/mL) was added to 96-well plates and stored at 4 °C overnight. On the second day, after washing with PBS–0.5% Tween 20 (PBST) three times, the 96-well plates were blocked with 0.5% bovine serum albumin (BSA) at 37 °C for 1 h. The serum was diluted to the appropriate dilution in the plates and incubated at 37 °C for 40 min. Afterward, the HRP-conjugated goat anti-mouse IgG antibody (1:50000; Abcam) was added to react at 37 °C for another 40 min. After washing six times, TMB substrate (50 μL per well) was added, and the reaction was immediately stopped. OD450 values were measured using an Infinite 200 PRO (TECAN, Mannedorf, Switzerland). Antibody titers were defined as the end-point of dilutions where the OD450 value was greater than or equal to twice that of the

negative control group. Antigen-specific IgG1 and IgG2a titers were detected on day 28 using the same method.

4.3.11 ELISPOT evaluations

For ELISPOT evaluation, polyvinylidene difluoride (PVDF)-based membrane plates (Millipore) were activated with 35% ethyl alcohol. Then the plates were coated with anti-mouse IFN-γ or IL-4 antibodies (5 μg/mL) and stored at 4 °C overnight. The next day, the plates were blocked with the culture medium (RPMI 1640, 10% FBS) for more than 1 h. Splenocytes from vaccinated mice were immediately added to the wells at 5×10^5 cells/well and restimulated with a specific antigen (2 μg/mL). On the third day, the plates were incubated with the detection antibody (1 μg/mL) for 2 h after removing the cells, followed by incubation with the streptavidin-ALP detection antibody (1 μg/mL) at room temperature. BCIP/NBT was then added to the plates and incubated for approximately 10 min in the dark. Each of the above steps requires washing the plates 3–6 times. Finally, the plates were washed with distilled water at the appropriate time points and air-dried overnight in the dark. The spots were scanned and counted using an ELISPOT Analyzer (AT-Spot 2100, China). Each experiment was repeated three times, and similar results were obtained.

4.3.12 Influenza A challenge experiments

For the prophylactic protection assay, BALB/c mice (6 – 8 weeks, female) were randomly divided into different groups and immunized twice by intramuscular injection. After 14 d, the mice were challenged intranasally with influenza A (A/Puerto Rico/8/1934) at a dose of 2 LD50 in 50 μL of PBS. The body weight and survival rate of all mice were monitored daily for 21 d. Mice were euthanized when their body weight loss exceeded 20% of their pre-challenge weight.

BALB/c mice (6 – 8 weeks, female) were euthanized on day 9 post-challenge to dissect the lung tissues for histology and viral load detection. To measure and quantify viral loads, a section of the lung tissue was homogenized and resuspended in 1 mL TRIzol reagent to extract total RNA for RT-qPCR analysis. The primer pair for the mRNA of the influenza virus was F-5′ AAGACCAATCCTGTCACCTCTGA-3′, R-5′-CAAAGCGTCTACGCTGCAGTCC-3′, and that for the internal reference gene (GAPDH) was F-5′-CAATGTGTCCGTCGTGGATCT-3′, R-5′-GT CCTCAGTGTAG CCCAAGATG-3′.

4.3.13 Evaluation of the transcriptome

The total RNA of BMDCs co-cultured with iMASE or rMASE for 24 h was extracted using the TRIzol reagent (Invitrogen). RNA libraries were sequenced on an Illumina sequencing platform (Gene Denovo Biotechnology, Co., Ltd., Guangzhou, China). In order to normalize and standardize the expression level of each gene, each part of the transcript per kilobase of transcript per million mapped reads (FPKM) was used. Differentially expressed genes (DEGs) were filtered using FPKM based on the edgeR's general filtering criteria (log2| fold change | >1, false discovery rate [FDR] < 0.05).

4.3.14 DC activation at the injection sites

To evaluate DC activation, BALB/c mice (6 – 8 weeks, female) were intramuscularly administrated with the indicated formulations and euthanized 1-, 3-, 5-, and 7-d post-administration. The tissues at the injection site were selected and immersed in collagenase type II (0.2%, w/v) for 2 h at 37 °C, allowing for the tissue digestion and isolation of the single-cell suspension. Then, the cells were blocked with anti-mouse CD16/CD32 antibody for 20 min and stained with Ghost Dye™ Violet 450, PE-labeled dump channel markers (anti-mouse F4/80 and Ly-6C antibodies), PerCP-Cyanine5.5 anti-mouse CD11c antibody, APC anti-mouse CD40 antibody, and FITC anti-mouse CD86 antibody at 4 °C for 30 min and then analyzed by flow cytometry. Furthermore, the muscle tissues were removed from the injection sites to test the expression of CCR7 among the recruited DCs. The tissues were then transferred to a grinder and homogenized on ice. Afterward, the cells were collected and blocked with anti-mouse CD16/CD32 (mouse Fc block) antibody at 4 °C for 20 min. After washing three times, the cells were stained with Ghost Dye™ Violet 450 Viability Dye, PE dump channel markers (anti-mouse F4/80 and Ly-6C antibodies), and Brilliant Violet 605™ anti-mouse CCR7 antibody at 4 °C for approximately 30 min and then analyzed by flow cytometry (CytoFlex LX, Beckman Coulter).

To determine cytokine secretion at the injection site, approximately 80 mg of the muscle tissue was ground. After removing cell fragments, the supernatant was collected by centrifugation at 500 × g for 5 min. The cytokine levels of IFN-α, IFN-β, TNF-α, and IL-2 in the supernatants were determined using enzyme-linked immunosorbent assay (ELISA).

4.3.15 DC and Germinal center activations in draining lymph node

To analyze the dLN activation, BALB/c mice (6 – 8 weeks, female) were immunized via intramuscular injection in the calf muscles of the hind limb with 100 μL vaccine that contained 5 μg/dose RBD and 5 μg/dose NP and euthanized at the indicated days. Afterward, the lymph nodes in the popliteal fossa between the biceps femoris and semitendinosus were picked and passed through a 70 μm Cell Strainer (BD Falcon) to obtain single-cell suspensions. In terms of DCs subsets in dLN, the obtained single cells were blocked with anti-mouse CD16/CD32 antibody and stained with Ghost Dye™ Red 780, PerCP-Cyanine5.5 anti-mouse CD11c antibody, FITC anti-mouse CD8α antibody, PE anti-mouse CD11b antibody, and PE-Cy7 anti-mouse CD103 antibody. Data were collected by flow cytometry. To detect DC activation, obtained single cells were blocked with anti-mouse CD16/CD32 antibody and stained with Ghost Dye™ Violet 450 Viability, FITC anti-mouse CD11c antibody, and APC anti-mouse CD40 antibody at 4 °C for approximately 30 min, and then analyzed through flow cytometry. In addition, $CD40L^+$ T-cells were tested. Briefly, cells were labeled with APC-Cy7 anti-mouse CD3e and eFluor 450 anti-mouse CD40L antibodies and analyzed by flow cytometry.

Tfh and GC B cells were then probed. Briefly, mice were injected intramuscularly with the indicated vaccines and euthanized 7 d post-administration. Afterward, the LN cells were prepared and labeled with the Ghost Dye™ Violet 450, PE dump channel markers (anti-mouse B220, CD11b, CD11c, and F4/80 antibodies)

and antibodies against Tfh (PerCP-Cyanine5.5 anti-mouse CD3e, APC-Cy7 anti-mouse CXCR5, and PE-Cy7 anti-mouse ICOS antibodies). To confirm the presence of GC B cells, cells were stained with Ghost Dye™ Violet 450, PE dump channel markers (anti-mouse CD3, CD11c, CD11b, and F4/80 antibodies), and antibodies against GC B cells (FITC anti-human/mouse B220, eFluor™ 660 anti-mouse GL-7, and PerCP-eFlour 710 anti-mouse CD95 antibodies). Antibody dilution was performed for flow cytometry staining according to the manufacturer's handbook. We defined GC B cells as FAS^+ $GL\text{-}7^+$ $B220^+$ and Tfh cells as $CXCR5^+$ $ICOS^+$ $CD3^+$. [174,175] Data were collected by flow cytometry.

Immunofluorescence staining was performed as previously described.[176] LNs were fixed with paraformaldehyde, embedded in paraffin, and sectioned into slices of 5–6 μm thickness. After deparaffinization and hydration, the samples were washed with Tris-buffered saline containing Tween® 20, treated with 3% H_2O_2 for 10 min, and blocked with 2% BSA solution for 30 min. The desired concentration of primary antibody was diluted in 500 μL of 0.1% BSA (CD4, CXCR5, or ICOS), added to the cells, and incubated overnight at 4 °C. The corresponding secondary antibodies were incubated after washing at 1:500 in 2% BSA blocking solution for 1 h at room temperature. After washing, the slides were incubated with 4′-6-diamidino-2-phenylindole in PBS for 5 min. Finally, the autofluorescence was quenched, and the slides were detected using K-Viewer.

Afterward, LN-residing memory B cells were evaluated. Briefly, LNs were collected two weeks after boost immunization. The cells were then stained with Ghost Dye™ Violet 450 Viability, PE dump channel markers (anti-mouse CD3e, CD11c, CD11b, and F4/80 antibodies), FITC anti-mouse B220 antibody, and APC anti-mouse CD27 antibody. Data were collected using flow cytometry.

4.3.16 Binding affinity measurement

To test antibody affinity, serums from immunized mice were purified using protein A antibody affinity chromatography. The binding affinity of antibodies to the RBD antigen was tested by BLI using the Octet® R8 system (Startorius BioAnalytical Instruments Inc.). Briefly, the biotinylated RBD antigen was diluted to 1200 μL and cured for 600 s. Afterward, the RBD antigen was diluted with PBST to 200 nM and then half-diluted for a total of six concentration gradients (200 nM, 100 nM, 50 nM, 25 nM, 12.5 nM, and 6.25 nM). Antibody samples were added to a 96-well plate, and the assay program was set. Ligand-loaded Streptavidin (SA) biosensors were then incubated with different concentrations of RBD antigen in a kinetics buffer. A global fit of the binding curves generated the best fit with the 1:1 model, and kinetic association and dissociation constants were determined. The data were aligned to obtain the kinetic parameters (K_D) using Fortebio data analysis 12.0.

4.3.17 Pseudovirus neutralization assay

A published method was used to evaluate the neutralization of SARS-CoV-2. First, the $TCID_{50}$ was determined by infection of Huh7 cells. Afterward, serial dilutions of heat-inactivated serum collected from immunized mice were incubated with 100 $TCID_{50}$ of pseudovirus at 37 °C for 1 h. The mixture was then added to 96-

well plates that contained Huh7 and incubated for 24 h. Finally, the cells were lysed, and a Luciferase Assay System (Promega, USA) was applied to evaluate luciferase activity. Experiments were performed according to the manufacturer's instructions. A relative light unit (RLU) reduction greater than 90% compared with the virus control well was defined as NT90, the highest reciprocal serum dilution at which RLUs were reduced. To determine half of the limit of detection, an NT90 below that level was considered.

4.3.18 Detection of memory T cells

BALB/c mice (6 – 8 weeks, female) were euthanized 28 d after the first immunization, and splenocytes were isolated and gently passed through a 100 μm cell strainer (BD Falcon). Next, erythrocyte lysis buffer was added, followed by washing three times with RPMI 1640 to obtain single-cell suspensions. Then, the single-cell suspensions (4×10^6 cells/well) were re-stimulated with the antigen (2 μg/mL) at 37 °C in a humidified, 5% CO_2 atmosphere. After 48 h of culture, the splenocytes were collected and stained with memory T cell related-fluorescent antibodies, including Ghost Dye™ Violet 450, PE dump channel markers (anti-mouse B220, CD11c, CD11b, F4/80, and Ly-6C antibodies), PE-Cy7 anti-mouse CD3e antibody, APC-Cy7 anti-mouse CD4 antibody, PerCP-Cyanine5.5 anti-mouse CD8a antibody, APC anti-mouse CD44 antibody, and FITC anti-mouse CD62L antibodies. $CD44^{high}$ $CD62L^{high}$ and $CD44^{high}$ $CD62L^{low}$ are known as the central memory T cells and effector memory T cells, respectively. Data were collected by flow cytometry.

4.3.19 SARS-CoV-2 challenge experiments

For SARS-CoV-2 challenge experiments, BALB/c mice (6–8 weeks, female) were vaccinated with iMASE and rMASE via intramuscular injection on days 28 and 49 before the challenge and compared with the non-immunized mice (term "Sham"). Challenge experiments and immunoassay were performed on the same day under consistent conditions for all the groups. Briefly, mice were intranasally transduced with 8×10^8 vp of Ad5-hACE2 23 or 44 days after the first immunization with iMASE and rMASE to rapidly induce the mouse model of SARS-CoV-2 infection. Five days later, the transduced mice were given 5×10^5 $TCID_{50}$ of SARS-CoV-2 (hCoV-19/China/CAS-B001/2020; GISAID No.EPI_ISL_514256-7) via the intranasal administration,[177] and all mice were euthanized and necropsied 3 d after challenge. Finally, lung tissues were harvested to calculate the viral loads and detect the pathological status. All animal experiments with SARS-CoV-2 the challenge were operated at the Animal Biosafety Level 3 (ABSL3) facility of IMCAS.

4.3.20 Determination of viral loads in the lung

For the determination of viral loads in lung tissue samples, RT-qPCR was used. First, the lung tissues of mice were collected and homogenized. Following homogenization and centrifugation, 50 μL of the supernatant was used to extract RNA from SARS-CoV-2 using a MagMAX™ Express Magnetic Particle Processor (Applied Biosystems, USA). RT-qPCR assays were conducted using the FastKing One Step Probe RT-qPCR kit (Tiangen Biotech, China), according to the

manufacturer's instructions.[178] The N gene of the SARS-CoV-2 genome was detected using the corresponding primers and probes.

4.3.21 Histopathology analysis

Three days after infection, necropsies were performed on six mice per group following a standard protocol. We collected the lungs of challenged mice, fixed them in 10% neutral buffered formaldehyde, and embedded them in paraffin. Tissue sections (5 μm) were stained with H&E to reflect the characteristics of infection, such as interstitial pneumonitis and alveolitis.

4.3.22 Live SARS-CoV-2 neutralization assay

For live SARS-CoV-2 neutralization assay, we inactivated the plasma samples collected from mice at 56 °C for 0.5 h. Following serial dilution with cell culture medium at a concentration of 1: 4 or 50,000 ng/mL, the inactivated diluted serum was mixed with 100 $TCID_{50}$ of the SARS-CoV-2 virus and incubated at 37 °C for 1 h. Next, the mixtures were added to the 96-well plates covered with confluent Vero cells. Next, the mixture was incubated for another 5 d at 37 °C. Three different individuals were observed, and the cytotoxic effect (CPE) of each well was recorded under a microscope. The CPE was then used to calculate neutralizing titers using the Reed Muench method. All experiments were conducted at the biosafety level 3 (BSL3) facility of the SINOVAC.

4.3.23 Statistics

All animal studies were performed after randomization. All values are expressed as the mean ± the standard error of the mean (s.e.m). Data were analyzed by one- or two-way analysis of variance (ANOVA) for comparison of multiple groups using GraphPad Prism 9 and Origin 9 software. Flow cytometry data were analyzed using FlowJo 10.0 and CytExpert Software 2.3. Statistical significance was set at a P-value less than 0.05 ($P < 0.05$).

4.4 Result

4.4.1 Tailoring multi-layer alum-stabilized emulsions for the inside-out assembly of the antigens

By adjusting the pH and type of the continuous phase, alum and HA were co-assembled on the o/w interface, forming alum/HA-assembled droplets (Figure 4-2). Specifically, to harness the delivery kinetics of antigens, surface antigen was trapped within the nanocage through the co-assembly of alum and antigen on the oil/water (o/w) interface. In this research, to meet the requirements of safety and immunization strategies, the 0.5 mg/mL alum was selected as stabilizer. To simulate the formulations of oil emulsion adjuvants, the squalene was selected as the dispersion phase. With similar compositions, smaller droplets may harbor higher interfacial energy for enhanced stability. For the buffer pH, although the smallest emulsion was obtained in buffer with pH 8.0-9.0, evident flocculation of droplets was observed, which was not conducive to the deposition of the outer alum. In comparison, buffer with pH 7.0 could obtain homogeneous droplets, which might be the optimum for a

continuous phase. Furthermore, citrate acid, water, NaCl, and PBS were used as a continuous phase to prepare alum/HA-assembled droplets, respectively. As shown in the results, citrate acid, PBS, and NaCl as continuous phase obtained biggish emulsion droplets, which may be affected by the charge screening effect of saline ions. Only water as a continuous phase met requirements of both smaller size and homogeneity. Therefore, water (pH = 7.0) may be the optimal continuous phase.

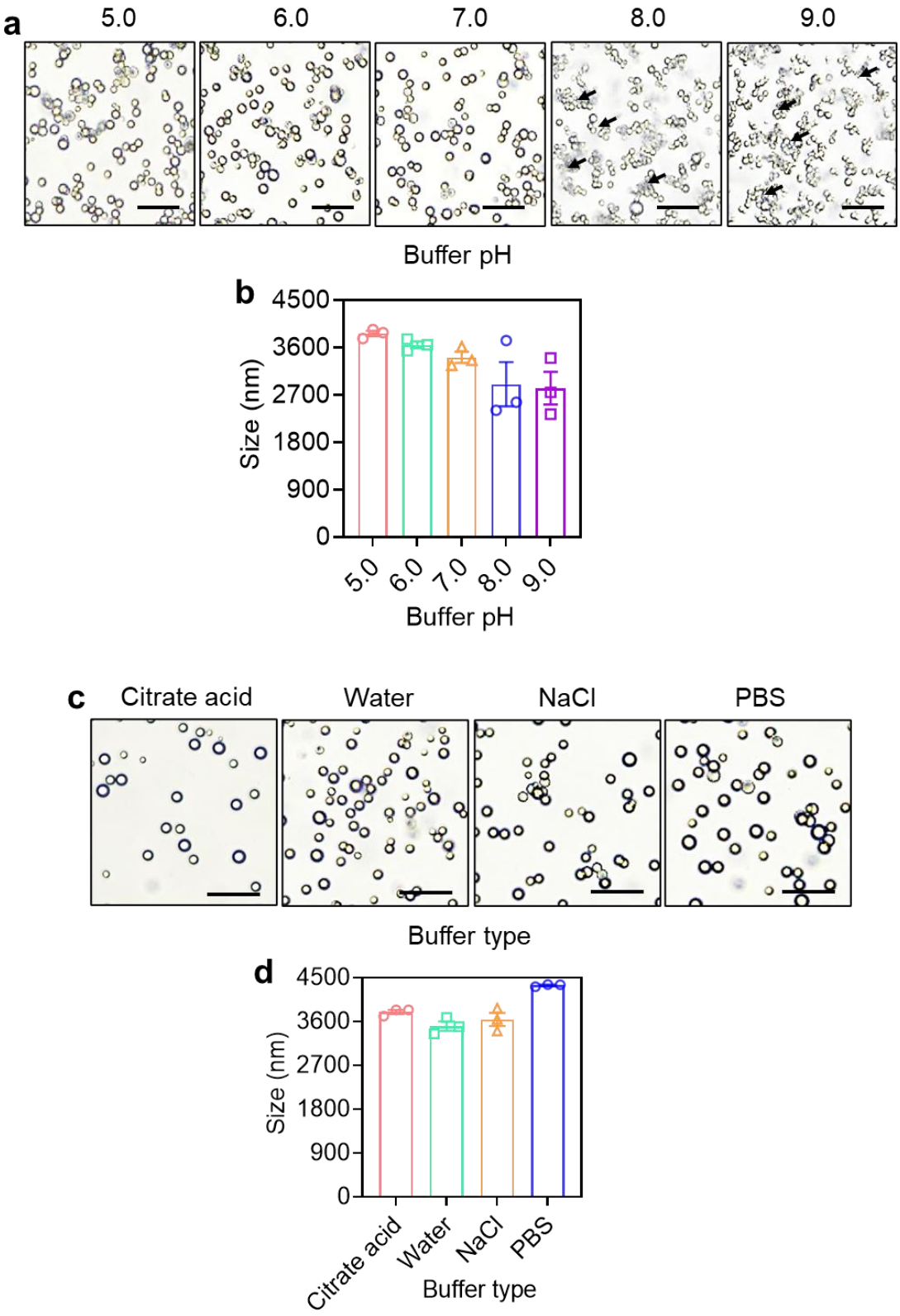

Figure 4-2. Optimization of the buffer pH and buffer type for alum/HA-assembled droplets. (a) Optical micrographs and (b) size distributions of droplets constructed by water with different pH. (c) Optical micrographs and (d) size

distributions of droplets constructed with different buffers. The optical images were acquired with 20 × magnification. Scale bar: 20 μm. The black arrows indicated the flocculation of droplets. The droplet sizes were determined by dynamic light scattering (DLS, Malvern) via nano zeta sizer. Alum/HA-assembled droplets were evaluated after 3 days of preparation. Data were shown as mean ± s.e.m. (n = 3, from 3 independent experiments).

To determine the secondary structure of the antigen after assembly, the droplets were demulsified and the HA was collected by dialysis method (100 kDa MWCO, Millipore). The spectra were detected via a JASCO spectrometer, where the X axis showed wavelength in nm and the Y axis showed molar ellipticity per residue ([θ], deg cm2 dmol-1). Circular dichroism (CD) analysis revealed that the secondary structure of HA remained unchanged after co-assembly with alum. Subsequently, the adsorption of alum on the alum/antigen co-assembled droplets (the 2nd layer of the droplet) was analyzed via quartz crystal micro-balance with dissipation monitoring (QCM-D, Q-SENSE E4). The chips were modified with HA, alum-stabilized emulsions, and alum/HA-assembled droplets, respectively, and then interacted with the fluidic alum in a continuous mode (flow rate = 50 μL/min). The stronger (red line) indicated the increased adsorption of alum on alum/antigen assembled droplets. As evidenced by the quartz crystal micro-balance with dissipation monitoring (QCM-D), another layer of alum was attached via the interaction with the alum/HA-assembled droplets (Figure 4-3).

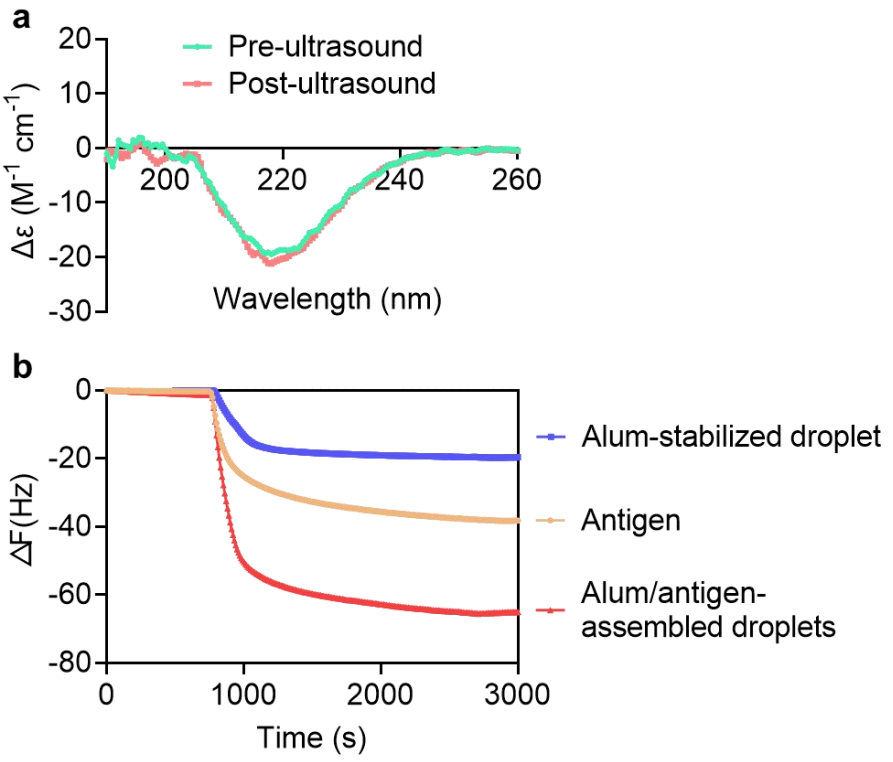

Figure 4-3. The characterization of alum/HA-assembled droplets.
(a) The circular dichroism analysis of the HA before and after the co-assembly with alum on the o/w interface. (b) Adsorption of alum on alum/antigen co-assembled droplets.

After optimization of the outer layer alum concentration, multi-layered droplets were prepared with no excess alum in the continuous phase, but with enough alum to cover the inner antigen (Figure 4-4). As alum/HA-assembled droplets were mixed with 0.5 mg/mL alum, the inner antigens were thoroughly shielded, and there was no redundant alum remained in continuous phase. 0.25 mg/mL alum could not thoroughly cover the inner antigen, while the excess alum remained in a continuous phase when 1 mg/mL alum was added. Therefore, 0.5 mg/mL alum may be suitable as the outer layer on the alum/HA-assembled droplets.

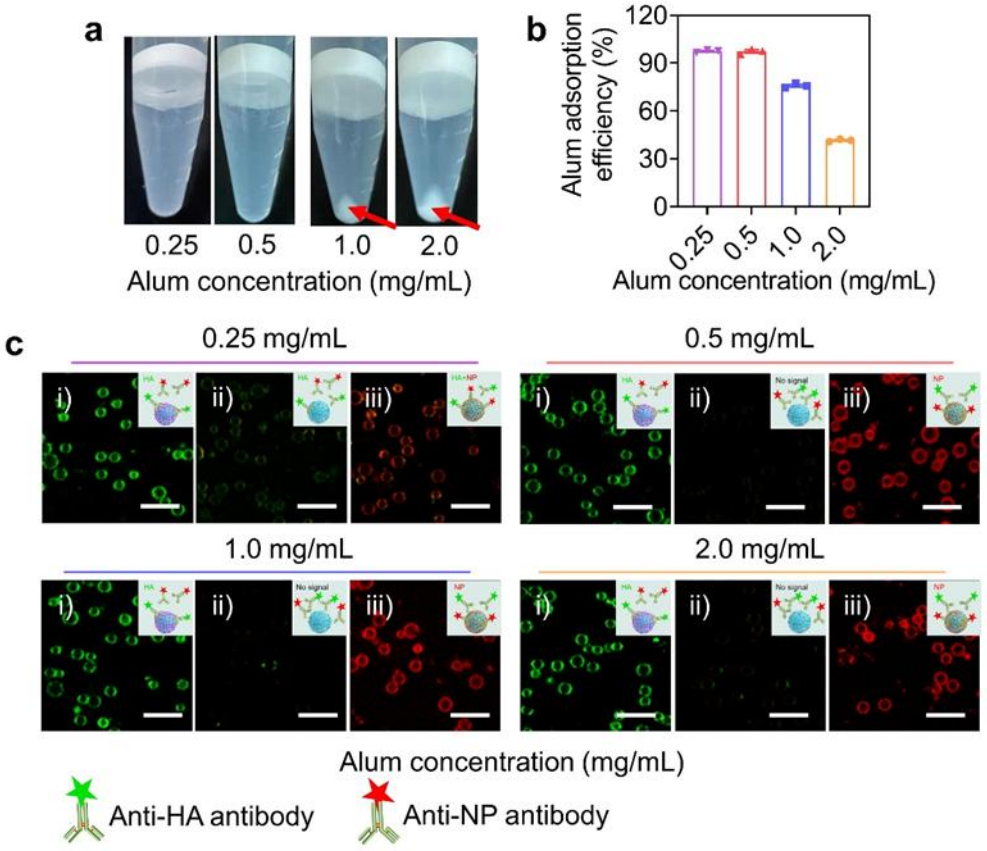

Figure 4-4. Optimization of alum concentrations for the stable multi-layer droplets. To obtain multi-layered droplets, the fluidic alum was added and mixed with the alum/HA-assembled droplets for 0.5 h. (a) Appearance of the droplets adsorbed various concentration of alum after high-speed centrifugation (6000 g, 10 min). (b) Alum adsorption efficiency on the alum/HA-assembled droplets. Alum adsorption efficiency (%) = (Alum input - Fluidic alum after mixing) / Alum input × 100%. (c) Verifying the coverage of the inner HA and the surface display of NP for the inside-out strategy. The droplets were treated with 4% (v/v) FBS solution to avoid non-specific interactions and then treated with a mixture of anti-HA and anti-NP

antibodies, followed by a confocal imaging. Scale bar: 10 μm.

Thus, rMASE was prepared according to the schematic illustration (Figure 4-5a). Unlike the alum/HA-stabilized droplets, scanning electron microscopy (SEM) images demonstrated an increased padding morphology, and stimulated emission depletion microscopy (STED) indicated an additional alum layer (red) on the alum/HA-stabilized droplets, thereby entrapping the inner HA (green) within the layer-by-layer nanostructures (Figure 4-5b). In addition, a large surface area was exposed for NP adsorption. Based on the changes in the zeta potentials and elemental compositions, rMASE was prepared with HA and NP loaded inside and outside, respectively (Figure 4-5c).

To test whether the inner antigen was completely shielded, the droplets were treated with a mixture of monoclonal antibodies against HA and NP. The images illustrated that alum/HA-stabilized droplets were strongly bonded with anti-HA antibodies (green). Subsequently, the addition of outer layer alum showed an evident reduction in the fluorescent intensity, suggesting the covering of the inner HA to avoid pre-exposure during antigen delivery. Additionally, after NP adsorption, the strong signal of a single fluorescence (red) indicated the dense display of NP on the rMASE surface (Figure 4-5d).

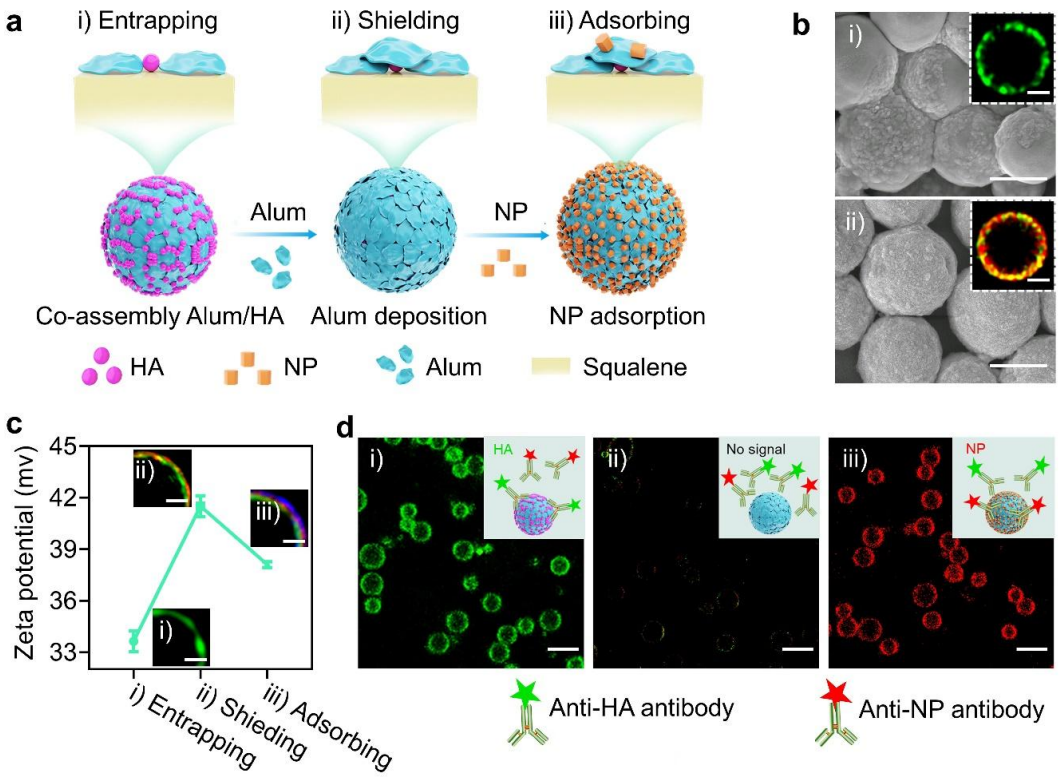

Figure 4-5 Tailoring rMASE for the inside-out strategy. (a) Schematic illustration on rMASE preparation for the inside-out assembly of HA and NP. Stepwise formation of rMASE. i) Co-assembly of alum and HA on the o/w interface; ii) another layer of alum deposition to shield the inner HA; iii) NP adsorption to constitute the sequential

loading of HA and NP to finally obtain rMASE. (b) SEM (scale bar: 2 μm) and STED (scale bar: 1 μm) images of co-assembly alum/HA (i) and alum deposition (ii). (c) Zeta potential and structure illumination microscopy (SIM) images of rMASE. HA, NP and alum were labeled with Cy3 (green), Cy5 (blue) and lumogallion (red), respectively. Scale bar: 1 μm. Data were shown as mean ± s.e.m (n = 3, from 3 independent experiments). (d) Verifying the thorough coverage of the inner HA and the surface display of NP for the inside-out strategy. The droplets were treated with 4% (v/v) FBS solution to avoid non-specific interaction, and then with a mixture of anti-HA antibody (green) and anti-NP antibody (red), followed by confocal imaging. Scale bar: 5 μm.

In a similar fashion, iMASE was prepared to load NP on the inside and adsorb HA on the outside of the droplets, which was determined with similar size and antigen loading efficiency but reversed antigen distribution compared to rMASE. iMASE was prepared to load NP on the inside and adsorb HA on the outside of the droplets, which were determined with similar size and antigen loading efficiency compared with rMASE (Figure 4-6 a-b). The size distributions of droplets were uniform. Tracing by the changes of zeta potentials and element compositions, iMASE demonstrated the natural antigen distributions of HA and NP (Figure 4-6c). Furthermore, there was an evident reduction in the fluorescent intensity of NP after adsorbing the outer alum, suggesting the NP covered by outer alum to avoid pre-exposure during the vaccine delivery. Additionally, after loading with the outer HA, only the fluorescent signal of HA was observed, indicating the surface display of the HA (Figure 4-6e).

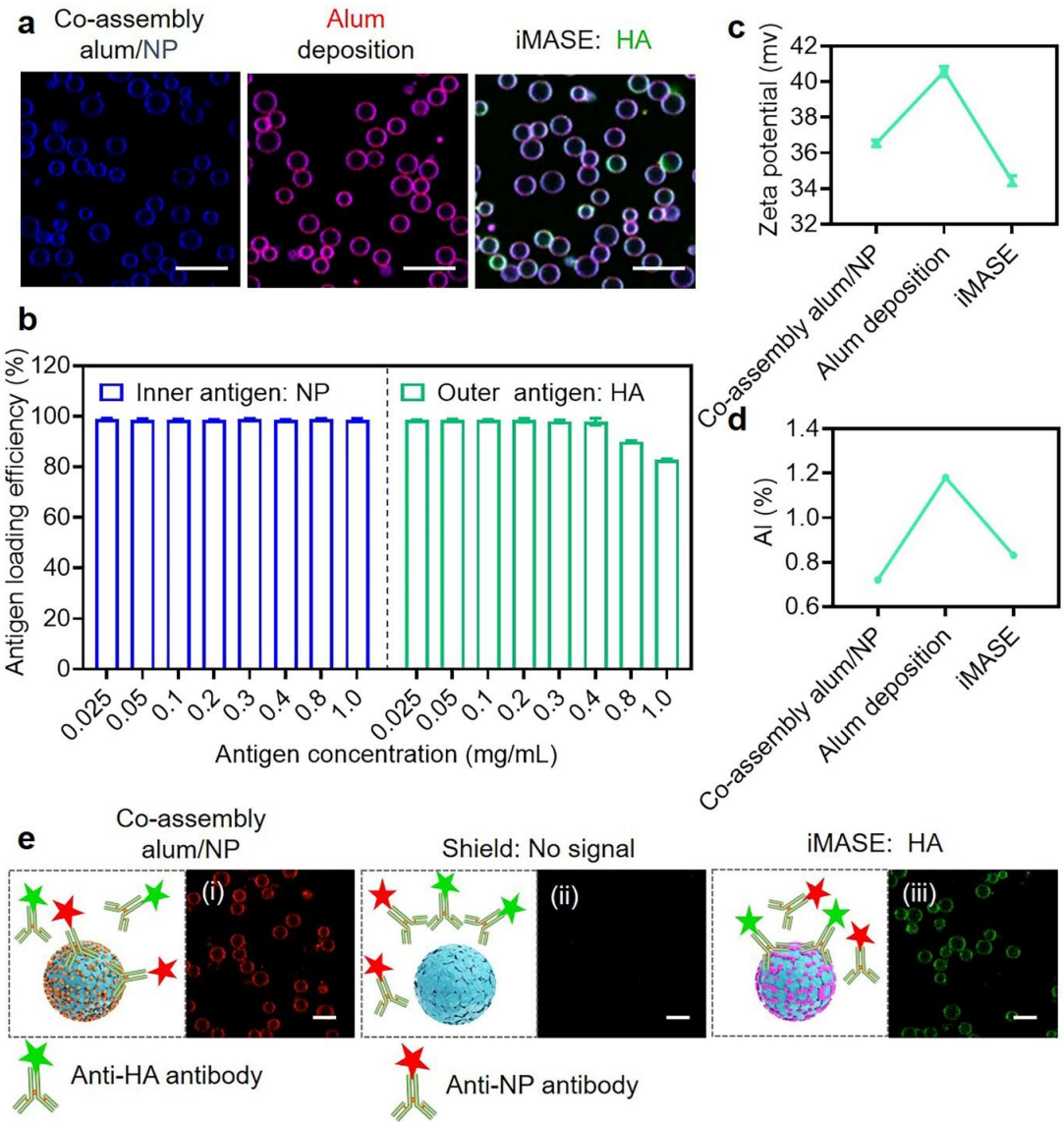

Figure 4-6 Characterization of the optimized iMASE. (a) Confocal image of iMASE. HA, NP, and outer layer of alum were labeled with Cy3 (green), Cy5 (blue), and lumogallion (red), respectively. The images were acquired with 100 × magnification via CLSM. Scale bar: 10 μm. (b) The antigen loading efficiency of HA and NP. The antigen loading efficiency was determined using the equation: Antigen loading efficiency (%) = (Total antigens - Fluidic antigens) / Total antigens × 100%. (c) Zeta potential of iMASE. The zeta potential of droplets was determined by DLS. (d) The atomic percentage of aluminum element on the droplets surface were determined via ICP-MS. (e) Verifying the coverage of the inner NP and the surface display of HA for the iMASE. After treating the droplets with 4% (v/v) FBS solution to avoid non-specific interactions, the droplets were incubated with the mixture of anti-HA antibody (green) and anti-NP antibody (red), followed by confocal imaging. The confocal images were acquired with 100 × magnification. Scale bar: 5 μm. Data of (b) and (c) were shown as mean ± s.e.m. (n = 3, from 3 independent experiments).

Accordingly, the multi-layered alum-stabilized emulsion was developed for the inside-out assembly of NP and surface antigens. Through the layer-by-layer procedure on the o/w interface, iMASE and rMASE achieved consecutive loading of HA and NP in a facile and moderate manner, demonstrating the natural and reversed antigen distributions of the H1N1 influenza virus (Table 4-1).

Table 4-1 Characterization of the multi-layered Pickering emulsions

Group	Size (nm)	Zeta potential (mv)	Antigen loading efficiency (%)	
			HA	NP
iMASE	3504.33 ± 91.34	34.43 ± 0.35	98.63 ± 0.21	98.61 ± 0.26
rMASE	3567.33 ± 184.43	38.10 ± 0.62	98.56 ± 0.30	98.50 ± 0.24

iMASE and rMASE were prepared according to the indicated method. The size distributions and zeta potential were determined by DLS via nano zeta sizer. The loading efficiency was evaluated using the equation: Antigen loading efficiency (%) = (total antigens (mg/mL) - fluidic antigens (mg/mL)) / total antigens (mg/mL) ×100%. Data were demonstrated as mean ± s.e.m. (n = 3).

4.4.2 Dictating the release tendency of the antigens

Next, we investigated whether consecutive loading could affect the release kinetics of the outer and inner antigens. To verify the release tendency, the residual stress was evaluated via X-ray diffraction (XRD) analysis (Figure 4-7a). Compared to their antigen-adsorbed counterparts (pink line), the co-assembled antigen and alum demonstrated decreased tensile stress. Whereas the attachment of the outer alum layer changed the residual stress from tensile stress to compressive stress, suggesting that the inner antigen was more likely to be entrapped within the nanocage formed between the close-binding alum and the o/w interface. Moreover, the right shift of the thermal peak in differential scanning calorimetry (DSC) demonstrated that a high thermal energy was required for the antigen to escape from the alum/HA-assembled droplets. These results indicated that the inner antigen had an impeded release tendency (Figure 4-7b).

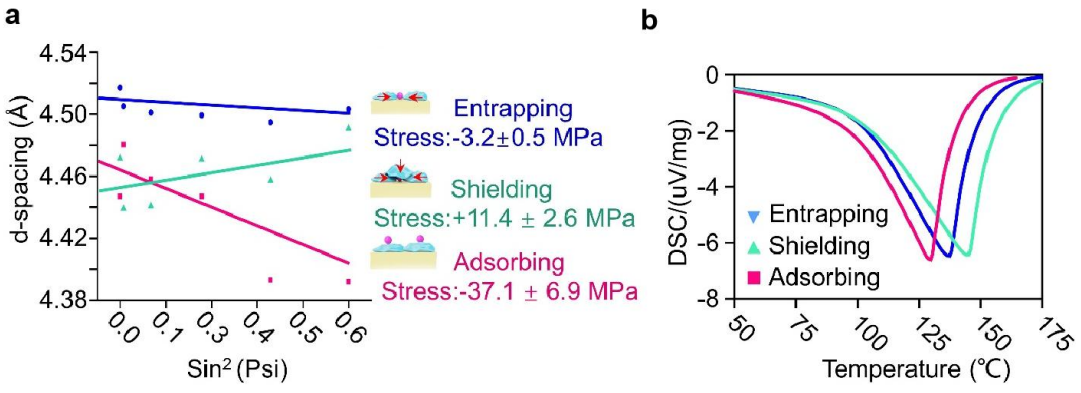

Figure 4-7 XRD analysis on surface residual stress of droplets and DSC studies

on the varied cooperated states of the inner HA. (a) XRD analysis on surface residual stress of droplets. The presence of residual stress (σφ) reflected the force tendency of the inner and outer antigens. The data were analyzed by regressing each data point to a straight line, and the linear slope M was obtained. Measuring and calculating the modulus of elasticity and Poisson's ratio to calculate K, and the stress can be calculated from $\sigma\varphi = KM$. Residual stress (σφ) indicated the tendency of the antigen towards ($\sigma\varphi > 0$, compressive stress) or backwards ($\sigma\varphi < 0$, tensile stress) the o/w interface. (b) DSC studies on the varied cooperated states of the inner HA. The right-shifting of the thermal peak indicated a greater energy for antigen to escape from the droplets, implying a more impeded release tendency.

Then, rMASE was co-incubated with a 10% (v/v) fetal bovine serum (FBS) solution to test the release profile after administration. To better simulate the interstitial fluid, macromolecules larger than 30 kDa were removed using a centrifugal concentrator (30 kDa MWCO).[179,180] As shown in Figure 4-8a, b, a limited amount of antigen was discharged from the droplets, suggesting that the antigens were only released after cellular internalization. With the macromolecules in the system, the outer NP was released before the entrapped HA (Figure 4-8 c-e). In the case of rMASE, the outer antigen (blue) began to release along with the detachment of the outer alum after incubation with the 10% (v/v) FBS in PBS. Approximately 31.0% of the NP were released within 24 h. Over time, an apparent dissociation of alum was observed, and the inner antigen (green) was discharged from the droplets subsequently. With the shielding of the alum on the interface, HA release was quite slow. Additionally, a reversed release trend in iMASE was observed. Therefore, the consecutive loading of HA and NP on the iMASE and rMASE could result in the release of the outer antigen before the inner antigen. Furthermore, the release rates were increased with the climbing of the FBS concentrations, suggesting that antigens were discharged by the ligand exchange of the macromolecular proteins. (Figure 4-8f, g).

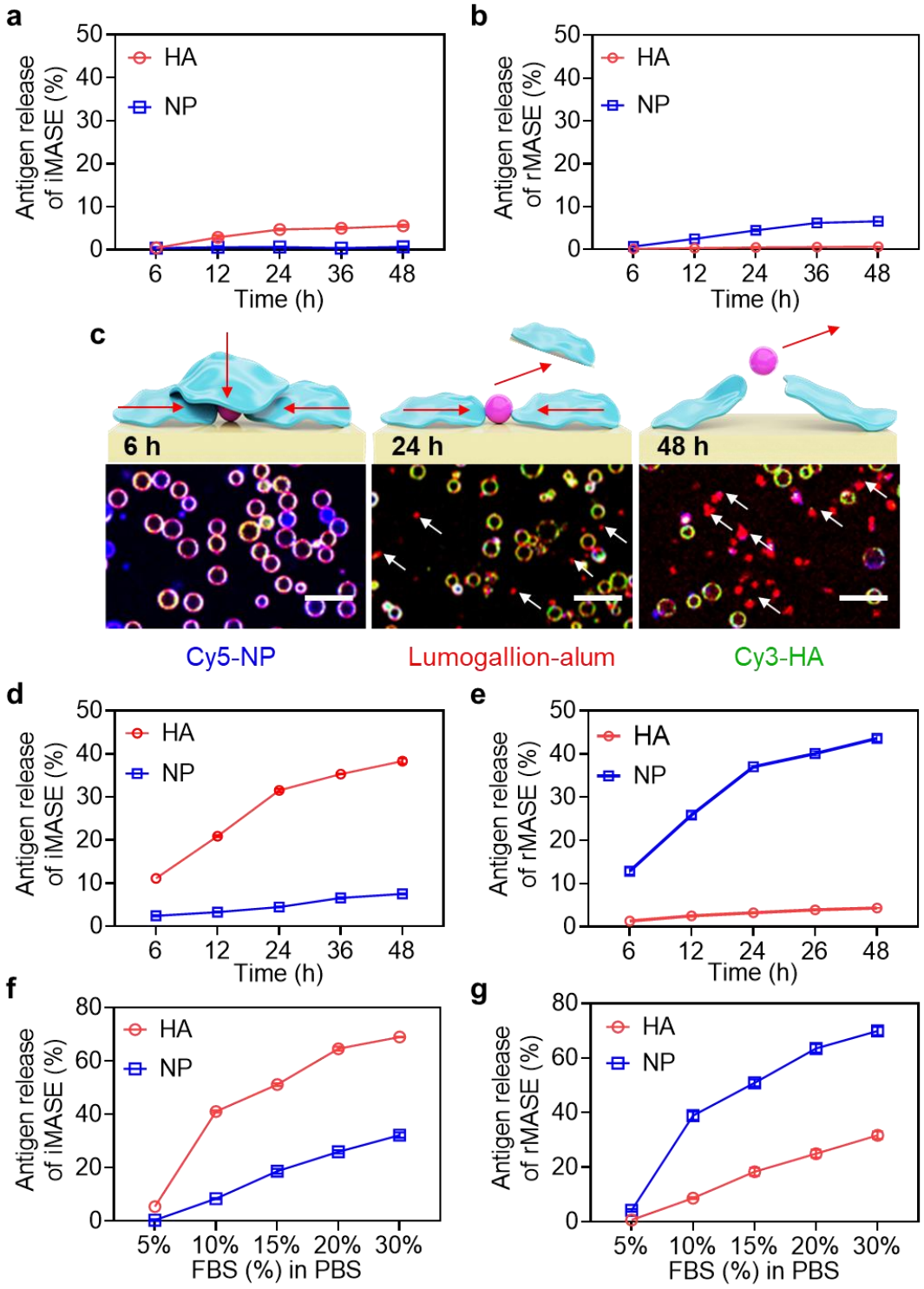

Figure 4-8 The release profiles of iMASE and rMASE.

The release profiles of HA and NP from (a) iMASE or (b) rMASE after incubation in the simulated interstitial fluid for the indicated time periods. The simulated interstitial fluid was prepared by removing the macromolecules that were larger than 30 kDa from 10% (v/v) FBS in PBS. (c) Confocal images of rMASE after incubation with the 10% (v/v) FBS in PBS. HA, NP, and alum were labeled with Cy3 (green), Cy5 (blue), and lumogallion (red), respectively. The white arrow indicated the scattering of alum

that was associated with antigen release. Scale bar: 10 μm. The release profiles of (d) iMASE and (e) rMASE in 10% FBS (v/v) in PBS. The release profiles of (f) iMASE and (g) rMASE in the climbing FBS concentrations at 48h. HA and NP were labeled with FITC and Cy5, respectively. The fluorescence intensity of fluid antigen was determined by fluorescence spectrophotometer. Antigen release was determined by fluorescence intensity of fluid antigen/fluorescence intensity of total antigen × 100%. Data were shown as mean ± s.e.m. (n = 3, from 3 independent experiments).

4.4.3 Reversed delivery of surface and core antigens

To further assess the release profiles, the intracellular distribution of rMASE was evaluated within BMDCs. As illustrated in the transmission electron microscopy (TEM) images, the droplets were first wrapped by the membrane to increase the contact area, triggering phagocytosis (Figure 4-9a, i-ii). With an increase in the specific surface area, the multi-layered droplets stimulated cellular uptake and reached maximum internalization after 6 h (Figure 4-10 a-b). As macromolecular proteins increased within the cytoplasm, the surface alum gradually fell off, along with the release of NP (Figure 4-9a, iii). After 24 h, the apparent dissociation of alum occurred, indicating discharge of the inner antigen (Figure 4-9a, iv).

Subsequently, the intracellular release of the antigen was monitored using a high content imaging system (Operetta CLS, PerkinElmer). First, HA (FITC-labeled, green) and NP (Cy5-labeled, red) were sequentially loaded. The droplets were subsequently co-incubated with BMDCs for 6 h to achieve the maximum uptake. The fluorescence intensities of the fluidic antigens were too weak to be detected, in contrast to the fluorescence enrichment via microsized droplets. Accordingly, the release profile could be assessed by comparing the fluorescence decay of the loaded antigens. In the case of rMASE, a decrease in Cy5 fluorescence intensity demonstrated NP release. After 12 h, the fluorescence intensity of HA started to decline with a primarily constant but gentler slope, representing its subsequent dischargement at a relatively slow rate. Additionally, a reversed trend in iMASE-treated cells suggested the prior release of HA before NP (Figure 4-9b and Figure 4-10 c-d). To further verify this, NP-specific immunoglobulin M (IgM) was evaluated. Serum from mice immunized with rMASE exhibited a decreased level of NP-specific IgM on day 14. However, iMASE induced a higher titer on day 14 than on day 7, implying that the release of the inner antigen was delayed for immune recognition (Figure 4-10e). Thus, by consecutive loading via multi-layered droplets, the inside-out strategy dictated the delivery kinetics of the viral antigens.

To explore the immune effect, the inside-out strategy was tested in BMDCs. Compared with iMASE, rMASE significantly boosted the expression of IFN-α mRNA, with a 138% increase in IFN-α cytokine secretion, indicating the robust activation of IFN-I signaling (Figure 4-9 c-d). Subsequently, rMASE-treated DCs showed elevated expression of CD40, CD80, and CD86 by 174%, 128%, and 180%, respectively (Figure 4-9e).

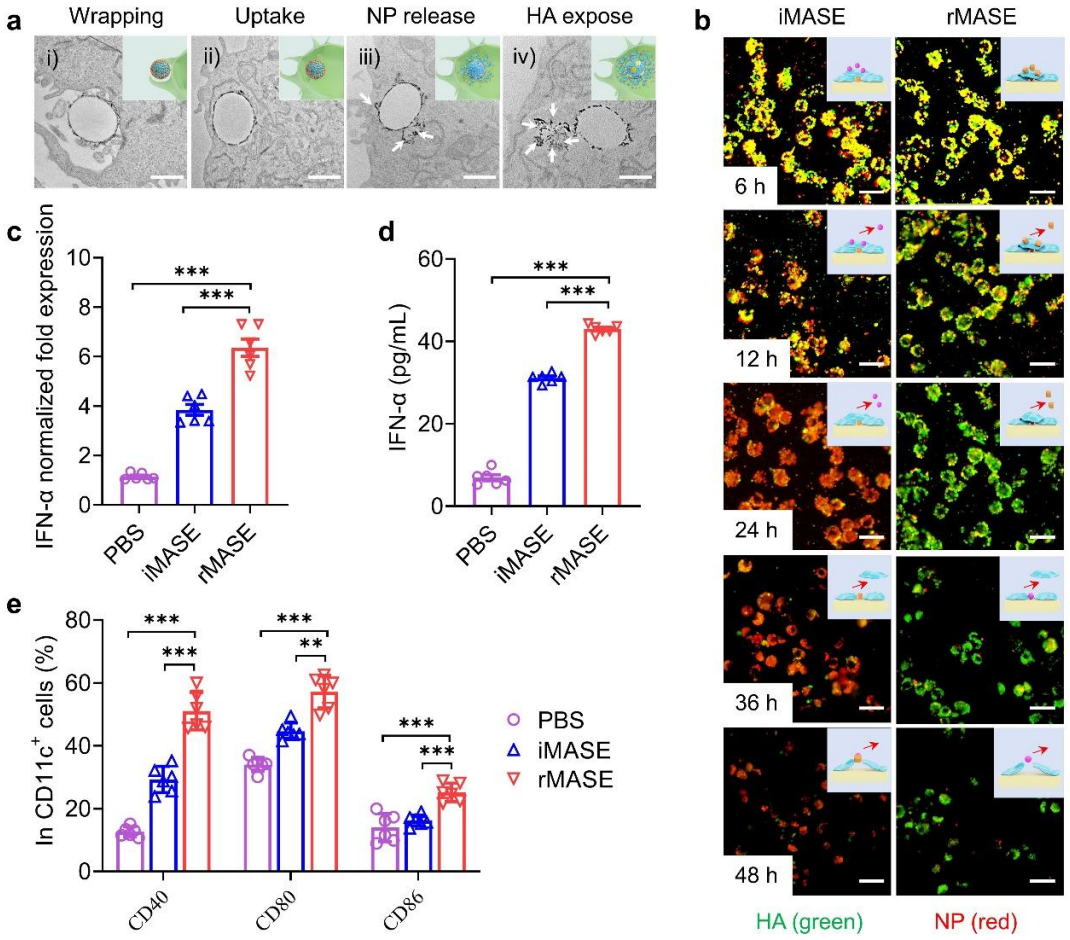

Figure 4-9 Reversed delivery for the potent IFN-I-mediated immune activation in vitro. (a) Intracellular transfer of rMASE traced by TEM. Arrows indicated the dischargement of the alum. Scale bar: 2 μm. (b) Intracellular release of the antigens monitored via high content screen microscopy. HA and NP were labeled with FITC (green) and Cy5 (red), respectively. Scale bar: 20 μm. The release profile could be assessed by the fluorescence decaying of the loaded antigens. (c) IFN-α mRNA expression levels of the treated DCs at 24 h. (d) IFN-α cytokine secretion of the treated DCs at 48 h. (e) The expression of CD40, CD80 and CD86 of the treated DCs at 48 h. All data in the graphs were presented as the arithmetic mean ± s.e.m. from three independent experiments. For statistical analysis, a one-way analysis of variance was conducted with Tukey's correction for multiple comparisons. $*P < 0.05$, $**P < 0.01$, $***P < 0.001$.

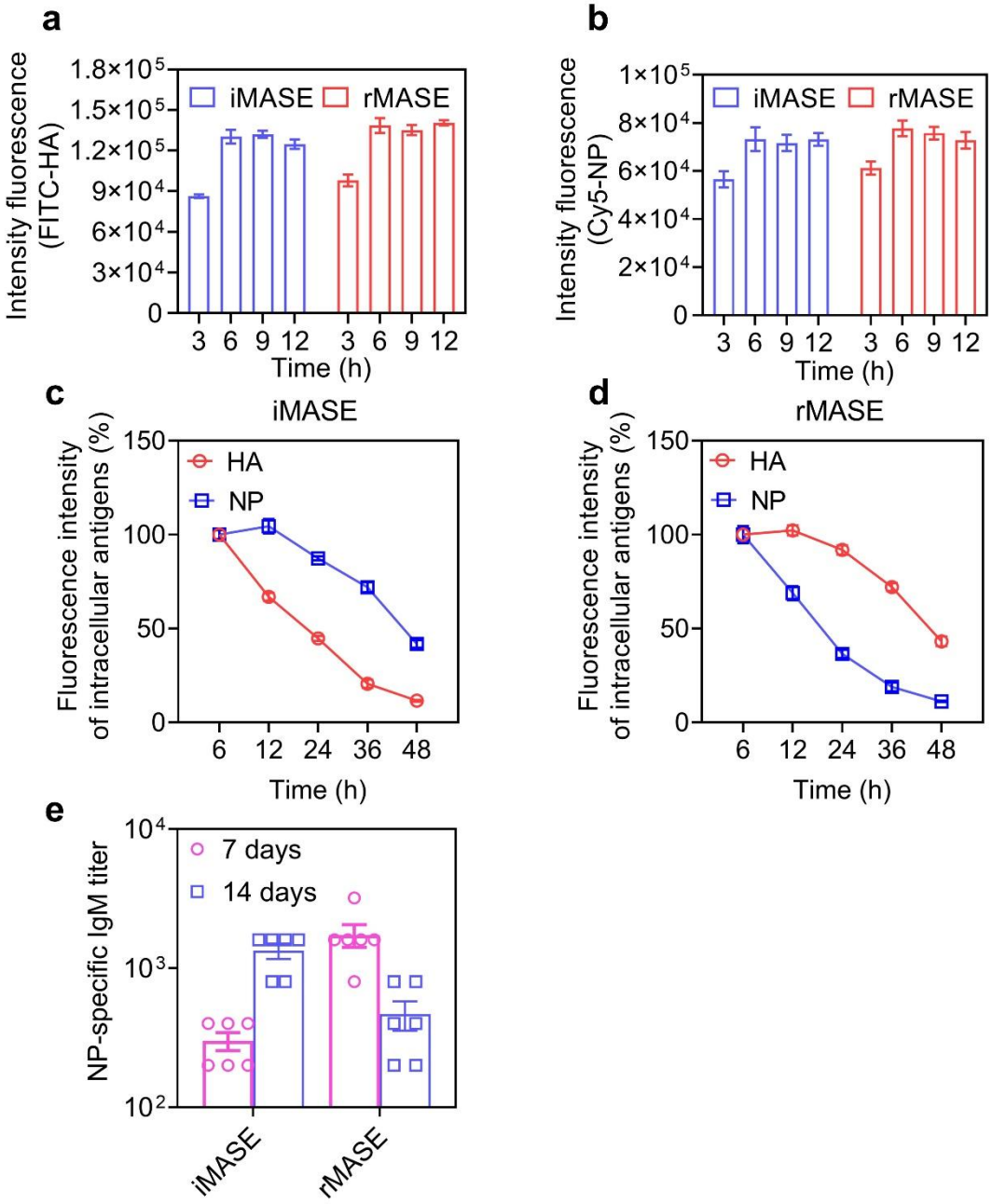

Figure 4-10 The delivery kinetics of antigens in vitro or in vivo. Internalization of (a) HA and (b) NP by BMDCs at indicated time points. Flow cytometry on the uptake of HA and NP after co-incubation with rMASE and iMASE. HA and NP were labeled with FITC and Cy5, respectively. The quantitative analysis of the fluorescent intensity of HA (red line) and NP (blue line) within the (c) iMASE-treated BMDCs and (d) rMASE-treated BMDCs. HA and NP were labeled with FITC and Cy5, respectively. And the average fluorescent intensity of antigens was detected by high content imaging system (Perkin Elmer) at 6 h, 12 h, 24 h, 36 h, and 48 h. Data were calculated by the equation: Fluorescence intensity of intracellular antigen (%) = (Average fluorescence intensity at indicated times/Average fluorescence intensity at 6 h) ×100%. (e) NP-specific IgM titers on day 7 and day 14 post-administration. Data were shown

as mean ± s.e.m. (n = 6, from 3 independent experiments).

Additionally, both iMASE and rMASE were detected with limited endotoxin levels and cytotoxicity, suggesting that the increased DC activation was attributed to the exposure of NP before HA, instead of potential material contamination or cell damage (Figure 4-11). Consequently, simply reversing the delivery of HA and NP can promote IFN-I-mediated immune responses.

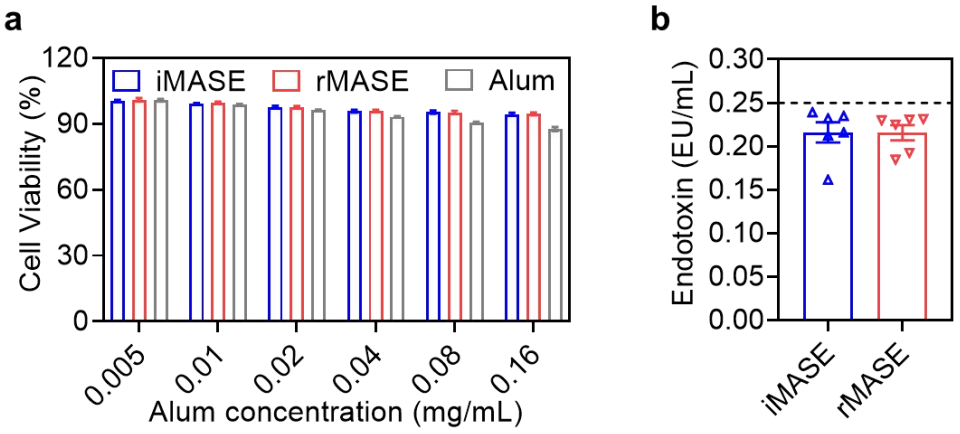

Figure 4-11 Cytotoxicity and endotoxin levels of the testing groups.
(a) Cytotoxicity performed on BMDCs. The dose effect of iMASE and rMASE were demonstrated by the alum concentrations in the system. Cell viability was assessed using the colorimetric cell counting kit-8 (CCK-8) from Dojindo Laboratories (Kyoto, Japan) at 48 h. (b) Endotoxin level of the formulations. Endotoxin levels were detected via the chromogenic LAL endotoxin assay kit (GenScript, USA). Data were shown as mean ± s.e.m. (n = 6, from 3 independent experiments).

4.4.4 Boosting humoral and cellular immune responses against H1N1 influenza

We postulated that rMASE may improve the immune response to H1N1 influenza infection. BALB/c mice were intramuscularly injected once with the formulations indicated in Table 4-2. For the in vivo analysis, all formulations were administered with the same number of antigens, regardless of the different antigen loading efficiency. Formulations were intramuscularly injected in a volume of 100 uL per mouse for a total of two injections.

Table 4-2. Formulations of the treated groups for H1N1 influenza

Group	Alhydrogel®adjuvant 0.1% (w/v)	Squalene (5%, v/v)	HA	NP
Antigen	0 μg	0 μL	5 μg	5 μg
Alum	100 μg	0 μL	5 μg	5 μg
iMASE	100 μg	5 μL	5 μg	5 μg

rMASE	100 μg	5 μL	5 μg	5 μg

Then, the antigen depot was traced over time using an in vivo imaging system. As shown in Figure 4-12a, an evident antigen depot was observed, comparable with the HA and NP co-adsorbed alum (term “Alum”), and persisted for longer than 3 d. In contrast, the fluidic mixture of HA and NP (term “Antigen”) was cleared from the injection site within 12 h. With the elevated antigen repertoire, DCs were evidently attracted to the injection site for higher antigen uptake (Figure 4-12 b-e). Notably, both iMASE and rMASE demonstrated similar trends in the antigen depot and DC internalization, indicating that the sequential release of viral antigens occurred intracellularly.

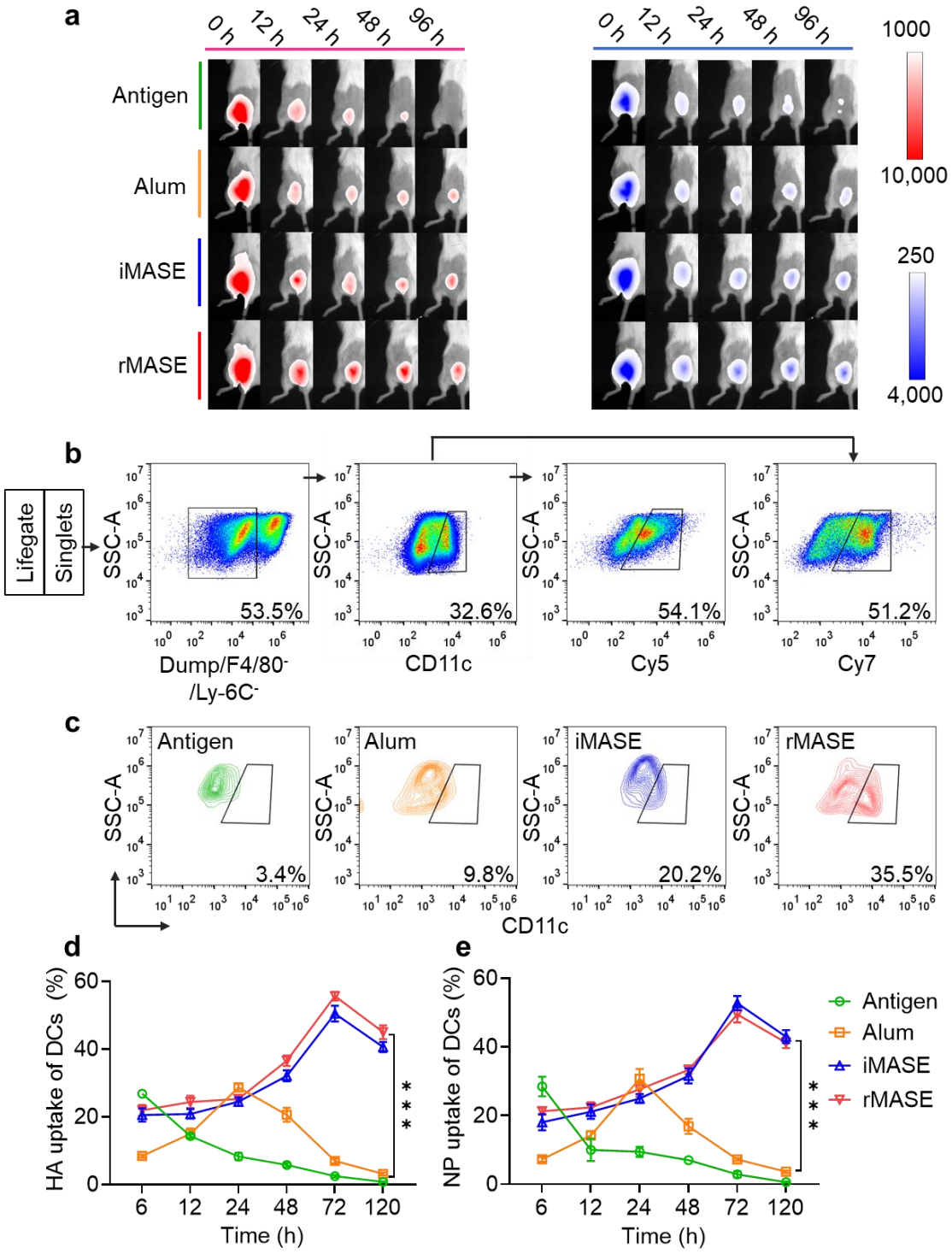

Figure 4-12. Antigen depot and uptake at the injection site. (a) Fluorescent intensity of antigen persistence over time. HA (left, red) and NP (right, blue) were labeled with Cy5 (ex: 648 nm; em: 662 nm) and Cy7 (ex: 743 nm; em: 767 nm), respectively. BALB/c mice (n = 6) were intramuscularly administrated with the indicated formulations (5 μg HA and 5 μg NP in 100 μL per mouse). Antigen persistence at the injection site was measured by in vivo imaging system FX Pro (Kodak) at the indicated time points. (b) Gate strategy for antigen uptake at the injection site. (c) Flow cytometry analysis on DC recruitment. Flow cytometry

analysis on (d) HA and (e) NP uptake by DCs at the injection site. HA and NP were labeled with Cy5 and Cy7, respectively. BALB/c mice (n = 6) were intramuscularly administrated with the indicated formulations. The single-cell suspension was prepared to analyze the recruitment and antigen uptake of DCs. All data in the graphs were presented as arithmetic means ± s.e.m. from three independent experiments. For statistical analysis, a two-way analysis of variance was carried out with Tukey's correction for multiple comparisons. *$P < 0.05$, **$P < 0.01$, ***$P < 0.001$.

After immunizing BALB/c mice intramuscularly twice (three weeks apart), rMASE-induced antigen-specific immune responses were investigated. Notably, rMASE-induced significantly higher HA-specific IgG titers compared with Alum (10-fold increase, $P < 0.001$) and iMASE (3-fold increase, $P < 0.001$) after 28 d (Figure 4-13a). Additionally, elicitation of a potent serum antibody was also observed after 49 d. To test the cross-reactivity, the serum was also tested on other strains, including A/California/07/2009 (H1N1), A/Hong Kong/3039/2011 (H3N2), and A/Shanghai/4664 T/2013 (H7N9). As shown in Figure 4-13b, compared with H1N1 (1934), the antibody titers of iMASE-treated mice showed 220%, 340%, and 800% decreases in H1N1 (2009), H3N2 (2011), and H7N9 (2013) subtypes, respectively. As for rMASE, the reductions were alleviated, with 110%, 210%, and 350% decreases in H1N1 (2009), H3N2 (2011), and H7N9 (2013) subtypes, respectively, suggesting the increased humoral immune responses.

Moreover, reversed delivery of HA and NP promoted cellular immune responses. Compared to iMASE, rMASE increased the presence of IFN-γ-secreting T cells by 162% among splenocytes ($P < 0.001$, Figure 4-13c). However, no significant differences were observed in IL-4 secreted cells (Figure 4-14a). Meanwhile, rMASE elicited a more than 6-fold higher HA-specific IgG2a titer ($P < 0.001$) than iMASE (Figure 4-13d). With potent secretion of IL-2, IL-12, and TNF-α, the cytokine profiles further demonstrated that the inside-out strategy stimulated a Th1-biased immune response (Figure 4-14b). Furthermore, among the rMASE-treated splenocytes, IFN-γ-secreting T cells demonstrated increased cross-reactivity against H1N1 (2009), H3N2 (2011), and H7N9 (2013) subtypes, indicating the enhanced cross-protection against viral mutations (Figure 4-14c).

To further test immune protection in mice, we challenged the animals with H1N1 strain A/PR/8/34/1934. Weight loss and survival of the animals were monitored for 21 d post-challenge. rMASE-treated mice experienced a slight decrease in mean body weight on day 10, but quickly increased back to normal weight in less than 7 d. All mice in the Antigen- and Alum-treated groups experienced ≥ 20% weight loss within 13 d. Comparatively, the mean weight loss in the rMASE-treated group was approximately 15.7% of the original weight 10 days post-challenge (Figure 4-13e). Notably, the survival rate in the rMASE-treated group was 100%. In contrast, the survival rate was only 50% in the iMASE-treated group, indicating that the reversed delivery of HA and NP increased immune protection against the H1N1 influenza viruses (Figure 4-13f). Moreover, reverse transcription quantitative real-time polymerase chain reaction (RT-qPCR) analysis revealed that rMASE-immunized mice

had significantly lower amounts of viral RNA in the lung tissues than those immunized with iMASE on day 9 (Figure 4-13g). To evaluate pulmonary inflammatory damage, pathological examination was performed using Hematoxylin and Eosin (H&E) staining. As shown in Figuge 2-14h, no significant infiltration was observed in rMASE-immunized mice. However, iMASE-treated mice developed perivascular and interstitial infiltrates. Next, inflammatory cytokines in the lung were tested. Compared with iMASE, rMASE significantly decreased the levels of MCP-1, IL-8, IL-1β, and IL-6, indicating the alleviation of inflammation (Figure 4-14 d-g). Collectively, the delivery of NP before HA provoked antigen-specific adaptive immune responses against viral infection.

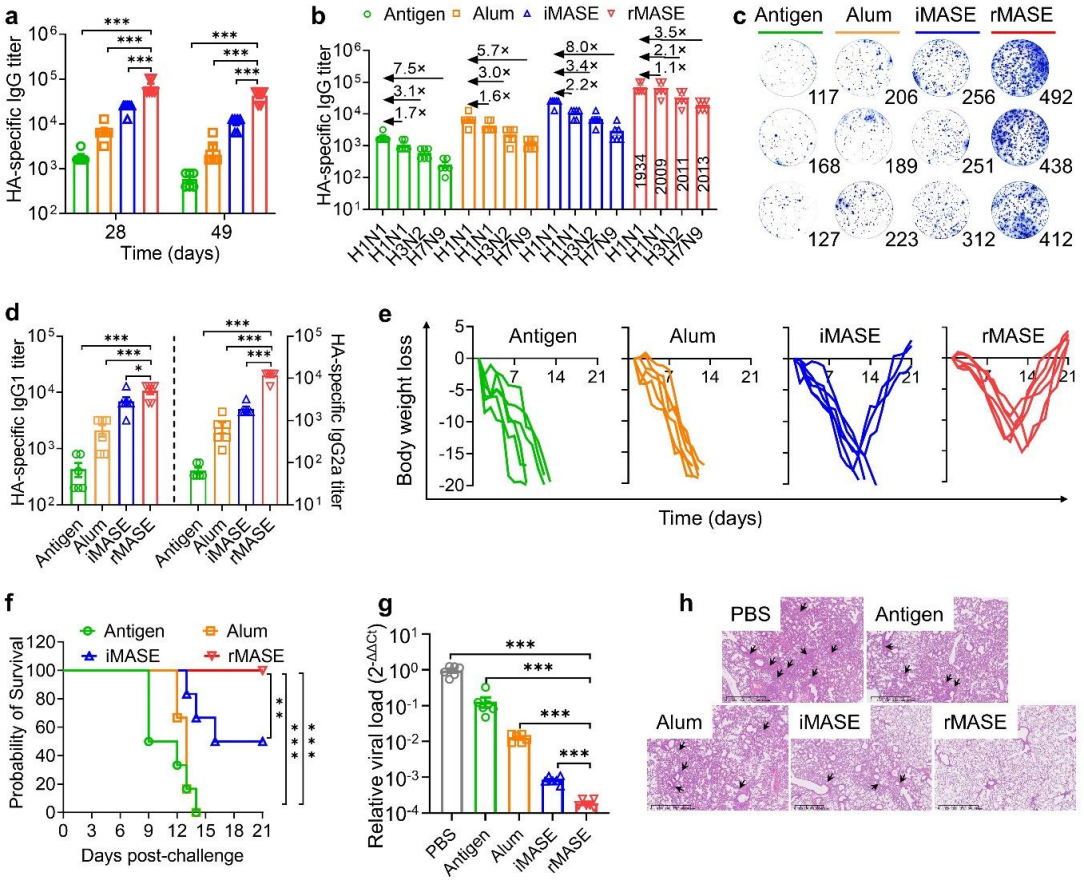

Figure 4-13 Provoking IFN-I activation in advance for the robust local reaction and lymph node activation. (a) GO term enrichment of the differentially expressed genes between iMASE and rMASE. GO analysis of differentially expressed genes within clusters identified the top associated enriched GO terms with corresponding enrichment P values. (b) Transcriptome analysis of DCs after co-culture with iMASE and rMASE. Representative heatmap showed differentially expressed genes relevant to IFN-I signaling pathway. (c) IFN-α concentrations at the injection site over time. (d) Frequencies of CD40 expressions among the recruited DCs. (e) CCR-7 expressions among the recruited DCs, indicating the LN tropism. (f) The DC subsets within lymph nodes. (g) The bubble plot displays the engagement of the CD40L, germinal center: follicular T helper cells and GC B cells in LN. (h) Representative images of ICOS and

CXCR5 immunofluorescence staining in Tfh cells in LN. Sections were stained for anti-mouse CD4 antibody (green), anti-mouse ICOS (red), cells in yellow indicate the co expression of CD4 and ICOS. The other sections were stained for anti-mouse CD4 antibody (green), anti-mouse CXCR5 (red), cells in yellow indicate the co expression of CD4 and CXCR5. The scale bar indicated 100 μm. (i) Memory B cells populations within the LN. All data in the graphs were presented as the arithmetic mean ± s.e.m. from three independent experiments. One-way and two-way analyses of variance were conducted with Tukey's correction for multiple comparisons. $*P < 0.05$, $**P < 0.01$, $***P < 0.001$.

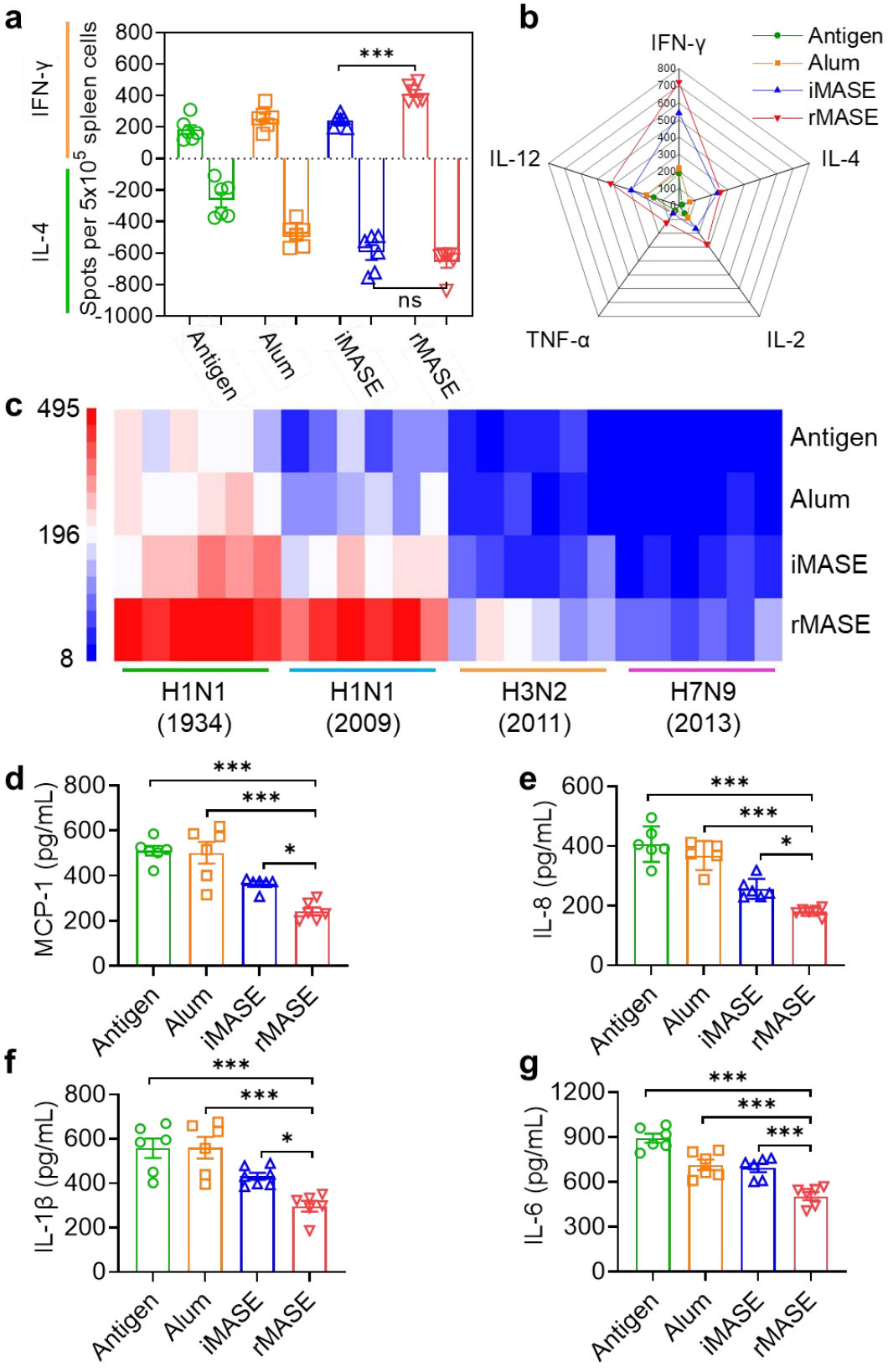

Figure 4-14 The enhanced immune response against the H1N1 influenza virus. (a) Frequency of IFN-γ and IL4-secreting cells among splenocytes via ELISPOT assay. ELISPOT analysis of IFN-γ and IL-4 spot-forming cells among the splenocytes after

ex vivo restimulation with HA on day 28. (b) Comparison of the secretion of cytokine (IL-2, IFN-γ, TNF-α, IL-4, and IL-12) in the supernatant of the ex vivo stimulated splenocytes. ELISA analysis of the cytokines from the splenocytes after ex vivo restimulation with HA on day 28. (c) Heatmap representing the frequency of IFN-γ-producing cells responding to different HA antigens. ELISPOT analysis of IFN-γ spot-forming cells among the splenocytes after ex vivo restimulation with different HA on day 28. Blue boxes correlate with lower cytokine present and red boxes with higher cytokine present (see scale). The levels of (d) monocyte chemoattractant protein 1 (MCP-1), (e) interleukin-8 (IL-8), (f) interleukin-1β (IL-1β), and (g) interleukin-6 (IL-6) in lung homogenates were detected by ELISA after viral challenge. All data in the graphs were presented as arithmetic means ± s.e.m. from three independent experiments. For statistical analysis, a one-way analysis of variance was carried out with Tukey's correction for multiple comparisons. $*P < 0.05$, $**P < 0.01$, $***P < 0.001$.

4.4.5 Robust IFN-I-mediated immune response and lymph node activation

It remains challenging to enhance the long-term immune response and neutralization capabilities against the prevailing mutant strains of SARS-CoV-2. After finding an increase in adaptive immune response and cross-reactivity in H1N1 influenza vaccines, we postulated that the inside-out strategy may also improve the immune potency and duration of SARS-CoV-2 vaccination. Here, the multi-layer alum-stabilized emulsion shielded the surface antigen (RBD) on the o/w interface and adsorbed the core antigen (NP) on the outside (rMASE), allowing for the prior release of NP before RBD (Figure 4-15 a-c). By successive loading of the viral antigens, iMASE achieved higher release concentrations of RBD before NP (Figure 4-15 d-e).

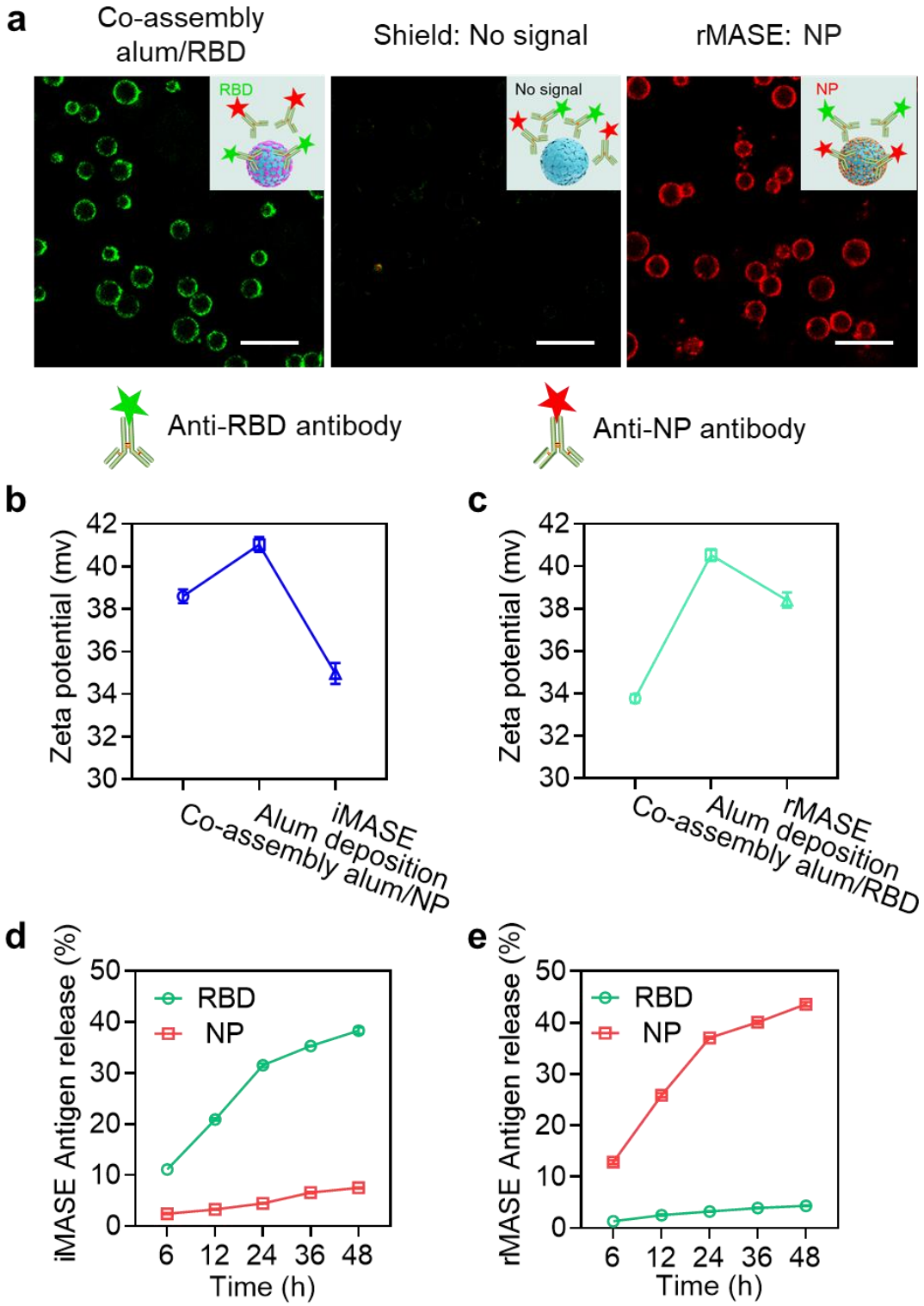

Figure 4-15 Inside-out assembly of RBD and NP. (a) Verifying the coverage of the inner RBD and the surface display of NP for the inside-out strategy. The droplets were treated with 4% (v/v) FBS solution to avoid the non-specific interactions and then treated with a mixture of anti-RBD and anti-NP antibodies, followed by confocal imaging. Scale bar: 10 μm. Zeta potential of (b) iMASE and (c) rMASE. (d) The release profile of iMASE in FBS (10% v/v in PBS). (e) The release profile of rMASE

in FBS (10% v/v in PBS). Data were shown as mean ± s.e.m. (n = 3, from 3 independent experiments).

To test whether the inside-out assembly of RBD and NP also provoked IFN-I-mediated immune responses, their impact on the transcriptome profile was assessed. The gene ontology (GO) term enrichment analysis revealed that rMASE significantly increased the IFN-I-related signaling pathway (under the criteria of $P \leq 0.05$; Figure 4-16a). Furthermore, comparative gene signature analysis revealed that interferon regulatory factor 7 (Irf7) was differentially expressed among rMASE-treated DCs, triggering the activation of a series of IFN-stimulated genes (Jak1, Stat1, Stat2, Irf9, and Isg15; Figure 4-16b).

After intramuscular administration, rMASE significantly boosted the secretion of IFN-α ($P < 0.001$) and IFN-β ($P < 0.001$) at the injection site compared with iMASE (Figure 4-16c and Figure 4-17a). As a consequence of IFN-I-mediated innate immune responses, higher levels of IL-2 ($P < 0.001$, Figure 4-17b) and TNF-α ($P < 0.001$; Figure 4-17c) secretions were observed in the early stage after administration, cultivating a more robust immunogenic microenvironment.[181,182] In response to this, the expression of CD40 and CD86 in the recruited DCs was evidently increased, suggesting enhanced DC activation (Figure 4-16d and Figure 4-17 d-e). Notably, no evident inflammation or abnormal levels of IL-6, IL-17A, or MPC-1 were observed, indicating acceptable biosafety and well-controlled immunogenicity (Figure 4-18). Thus, the inside-out strategy stimulated IFN-I-mediated pathways, which cultivated an immune-stimulatory environment for the onset of an anti-viral state.[183,184]

Then, the activation of the draining lymph nodes (LNs) was probed.[185] At the injection site, rMASE increased the expression of CCR-7 on the recruited DCs by 195% after 7 d post-administration compared to iMASE, indicating that the recruited DCs have a high potential for migration to LNs (Figure 4-16e).[186] Accordingly, rMASE showed a lower elevated LN-resident DCs proportion ($CD8\alpha^+$ $CD11c^+$), but a more noticeable increase in the number of migrated DCs ($CD103^+$ $CD11c^+$ and $CD11b^+$ $CD11c^+$) within the LNs (Figure 4-16f and Figure 4-19 a-b). This indicated that rMASE promoted potent DCs migration from the injection site to the LN to achieve higher LN-accumulation of the antigens, rather than the direct delivery of antigens. Regarding DC activation within the LNs, $CD40^+$ DCs were boosted by 150% on the 7th day after the administration of rMASE, compared with the iMASE-treated mice (Figure 4-19 c-d). Furthermore, a significantly higher CD40L expression ($P < 0.001$) among the LN-residing $CD3^+$ T cells suggested the increased interactions between DCs and T cells.[187] Consequently, the rMASE-treated group exhibited a notable expansion of $CXCR5^+$ $ICOS^+$ $CD3^+$ T cells and FAS^+ $GL\text{-}7^+$ $B220^+$ B cells with an approximate 150% and 200% elevation, respectively (Figure 4-16g and Figure 4-20 a-d). Meanwhile, the LN immunofluorescence staining also demonstrated a similar trend, suggesting robust activation of the germinal center (GC; Figure 4-16h). Furthermore, we also found that rMASE induced 140% more $CD27^+$ $B220^+$ cells, compared to iMASE, demonstrating an increase in memory B cells (Figure 4-16i and Figure 4-20e). Thus, the inside-out strategy induced a higher IFN-I-mediated immune

response at the early stage of vaccination, which subsequently led to potent LN activation for the onset of a strengthened adaptive immune response.

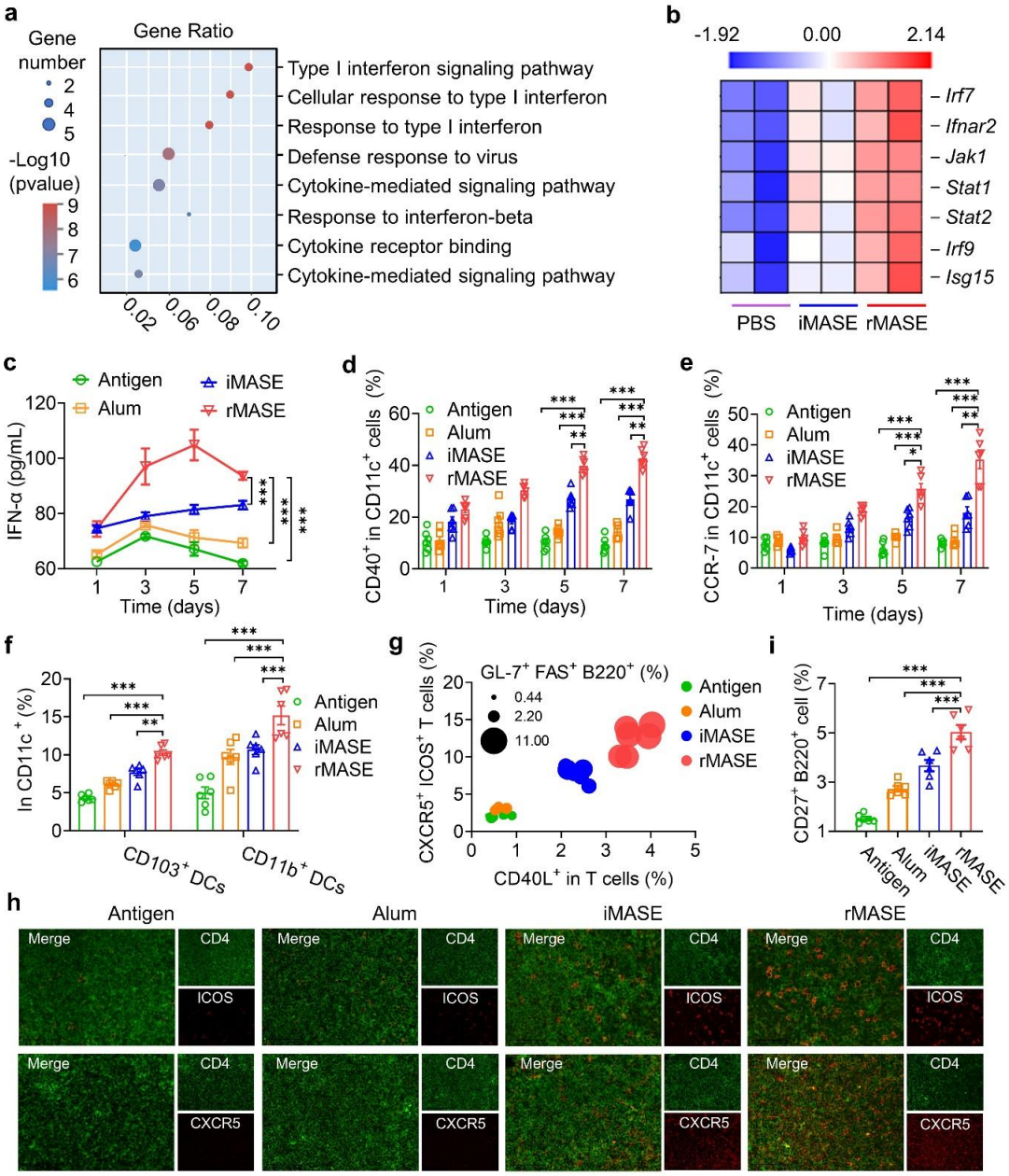

Figure 4-16 Provoking IFN-I activation in advance for the robust local reaction and lymph node activation. (a) GO term enrichment of the differentially expressed genes between iMASE and rMASE. GO analysis of differentially expressed genes within clusters identified the top associated enriched GO terms with corresponding enrichment P values. (b) Transcriptome analysis of DCs after co-culture with iMASE and rMASE. Representative heatmap showed differentially expressed genes relevant to IFN-I signaling pathway. (c) IFN-α concentrations at the injection site over time. (d) Frequencies of CD40 expressions among the recruited DCs. (e) CCR-7 expressions among the recruited DCs, indicating the LN tropism. (f) The DC subsets within lymph nodes. (g) The bubble plot displays the engagement of the CD40L, germinal center: follicular T helper cells and GC B cells in LN. (h) Representative images of ICOS and

CXCR5 immunofluorescence staining in Tfh cells in LN. Sections were stained for anti-mouse CD4 antibody (green), anti-mouse ICOS (red), cells in yellow indicate the co expression of CD4 and ICOS. The other sections were stained for anti-mouse CD4 antibody (green), anti-mouse CXCR5 (red), cells in yellow indicate the co expression of CD4 and CXCR5. The scale bar indicated 100 μm. (i) Memory B cells populations within the LN. All data in the graphs were presented as the arithmetic mean ± s.e.m. from three independent experiments. One-way and two-way analyses of variance were conducted with Tukey's correction for multiple comparisons. $*P < 0.05$, $**P < 0.01$, $***P < 0.001$.

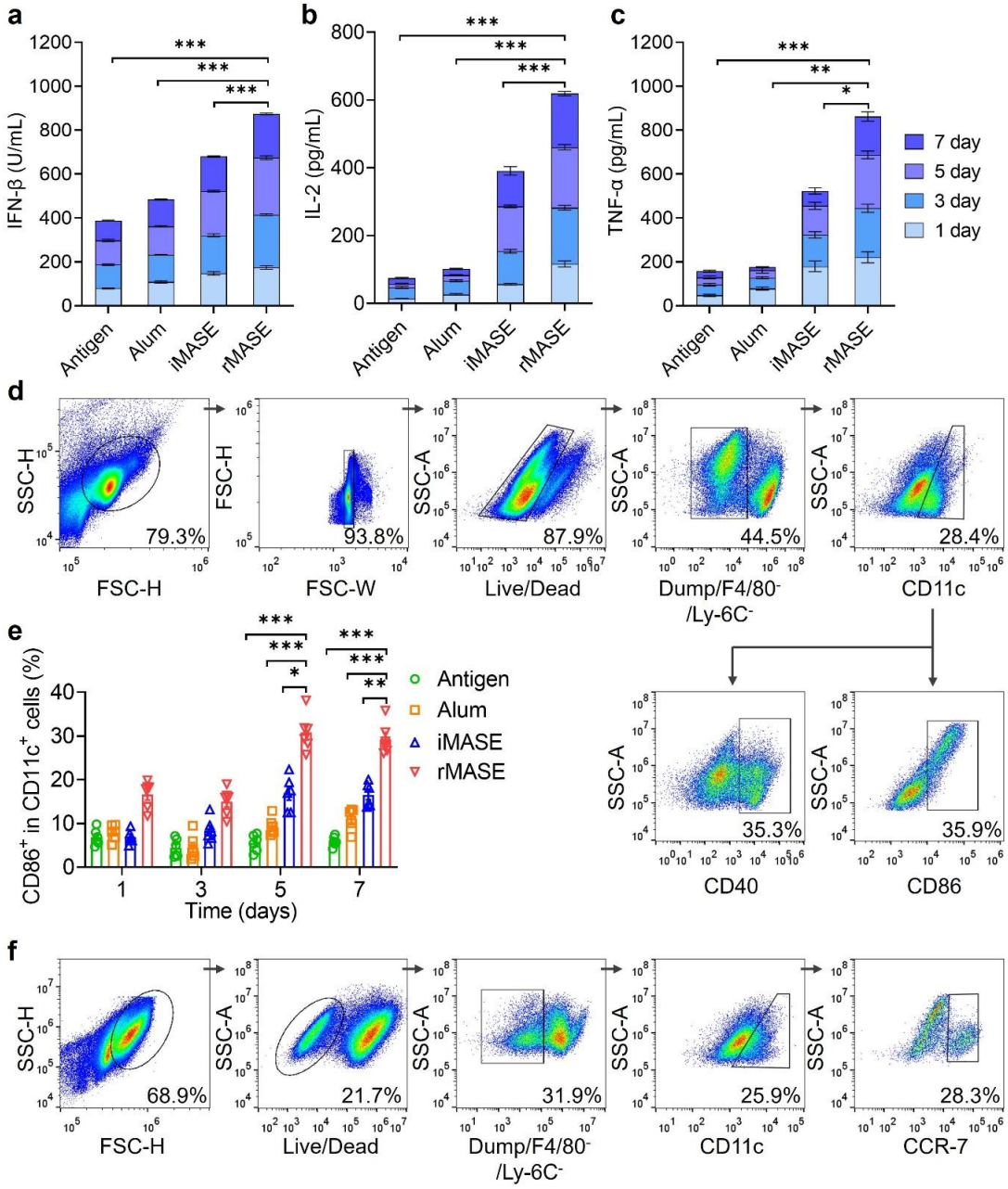

Figure 4-17 The local immune reactions at the injection site. The secretions of (a) IFN-β, (b) IL-2, and (c) TNF-α at the injection site. (d) Gate strategy for CD86 and CD40 subsets among the recruited DCs. (e) Flow cytometry on the expression of

CD86. (f) Gate strategy for CCR-7 subsets among the recruited DCs. All data in the graphs were presented as arithmetic means ± s.e.m. A two-way analysis of variance was carried out with Tukey's correction for multiple comparisons. $*P < 0.05$, $**P < 0.01$, $***P < 0.001$.

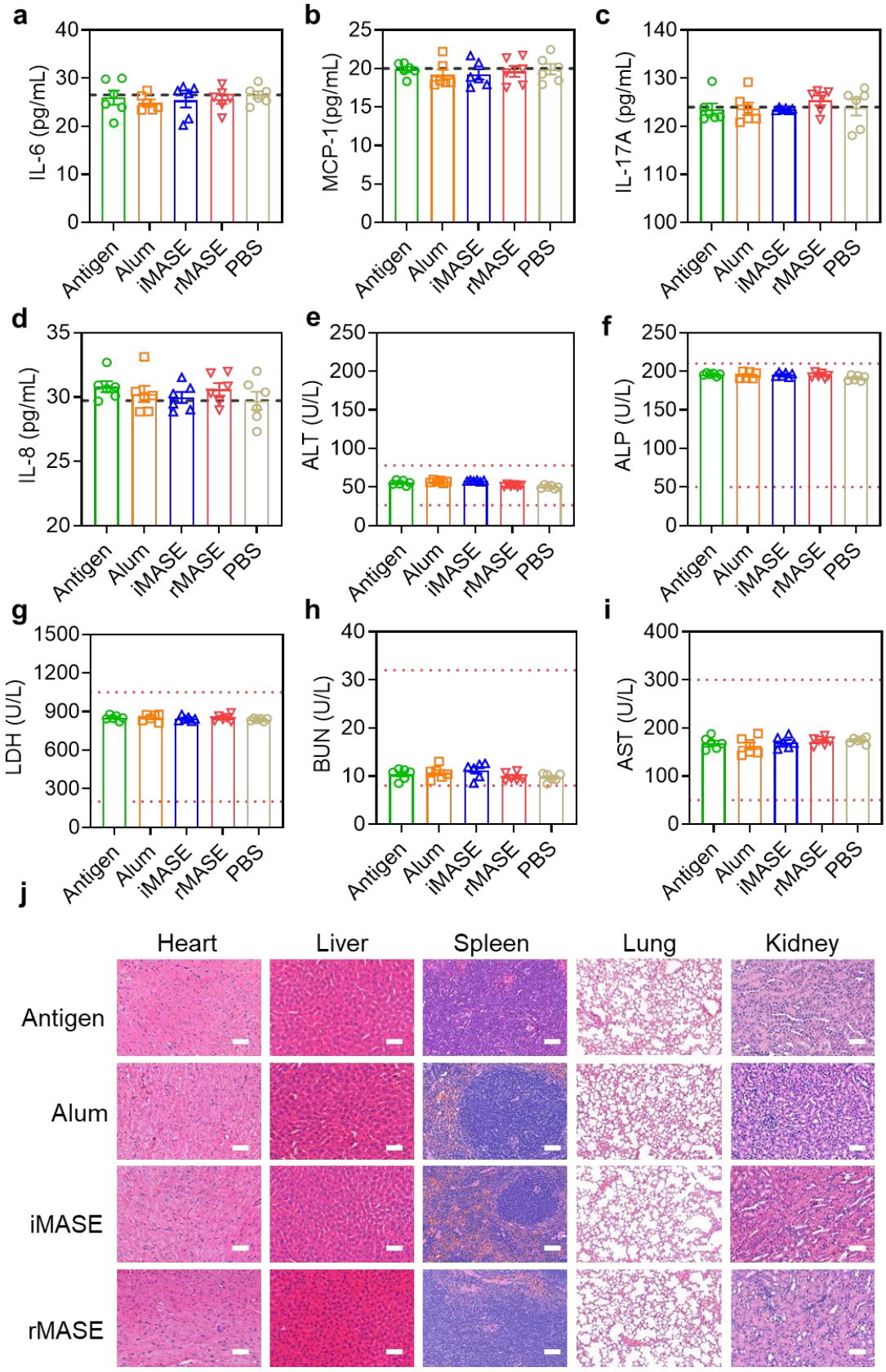

Figure 4-18 The safety profile of rMASE. (a) IL-6, (b) MCP-1, (c) IL-17A, and (d) IL-8 levels in serum on day 28. The dotted line indicated the average concentrations of the untreated group (PBS). Healthy mice were intramuscularly administered with

the indicated formulations, and serum was collected on day 28 for analysis. Analysis of (e) alanine aminotransferase (ALT), (f) alkaline phosphatase (ALP), (g) lactate dehydrogenase (LDH), (h) blood urea nitrogen (BUN), and (i) aspartate aminotransferase (AST). Healthy mice were intramuscularly administered with the indicated formulations, and serum was collected on day 28 for biochemical analysis. The value between the two lines represented the normal level. (j) Histopathological evaluations of the vital organs from the BALB/c mice. Healthy mice (n = 6) were intramuscularly administered with the indicated formulations, 28 days after administration, the heart, liver, spleen, lung, and kidney were harvested to stain with H&E. Scale bar: 100 μm. All data in the graphs were presented as arithmetic means ± s.e.m. from three independent experiments. For statistical analysis, a one-way analysis of variance was carried out with Tukey's correction for multiple comparisons. $*P < 0.05$, $**P < 0.01$, $***P < 0.001$.

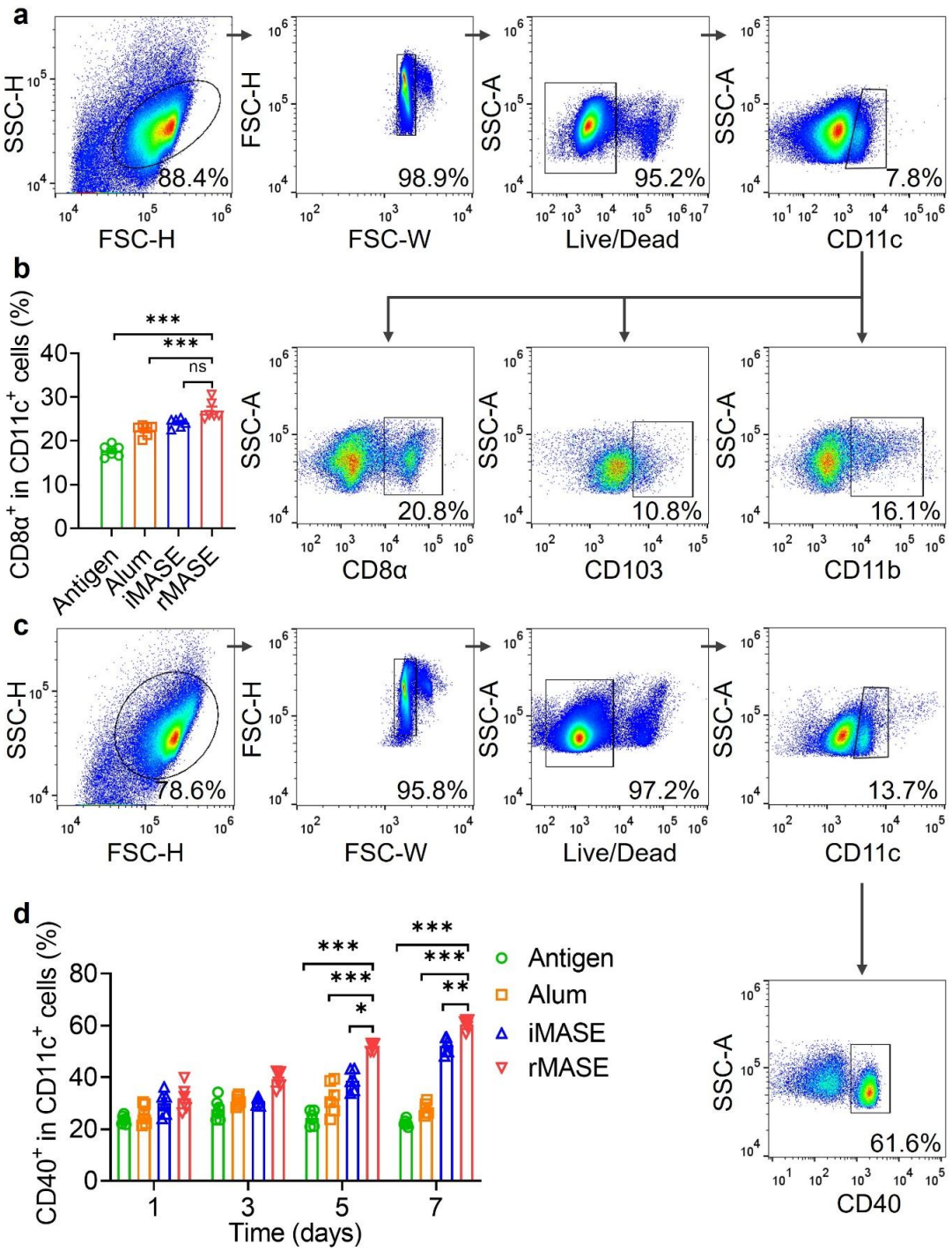

Figure 4-19 DC subsets and activation in lymph nodes. (a) Gate strategy and (b) frequencies of DC subsets in lymph nodes (LNs). (c) Gate strategy and (d) population of CD40-expressing DCs in LNs. All data were presented as arithmetic means ± s.e.m. from three independent experiments. One-way or two-way analysis of variance was carried out with Tukey's correction for multiple comparisons. *$P < 0.05$, **$P < 0.01$, ***$P < 0.001$.

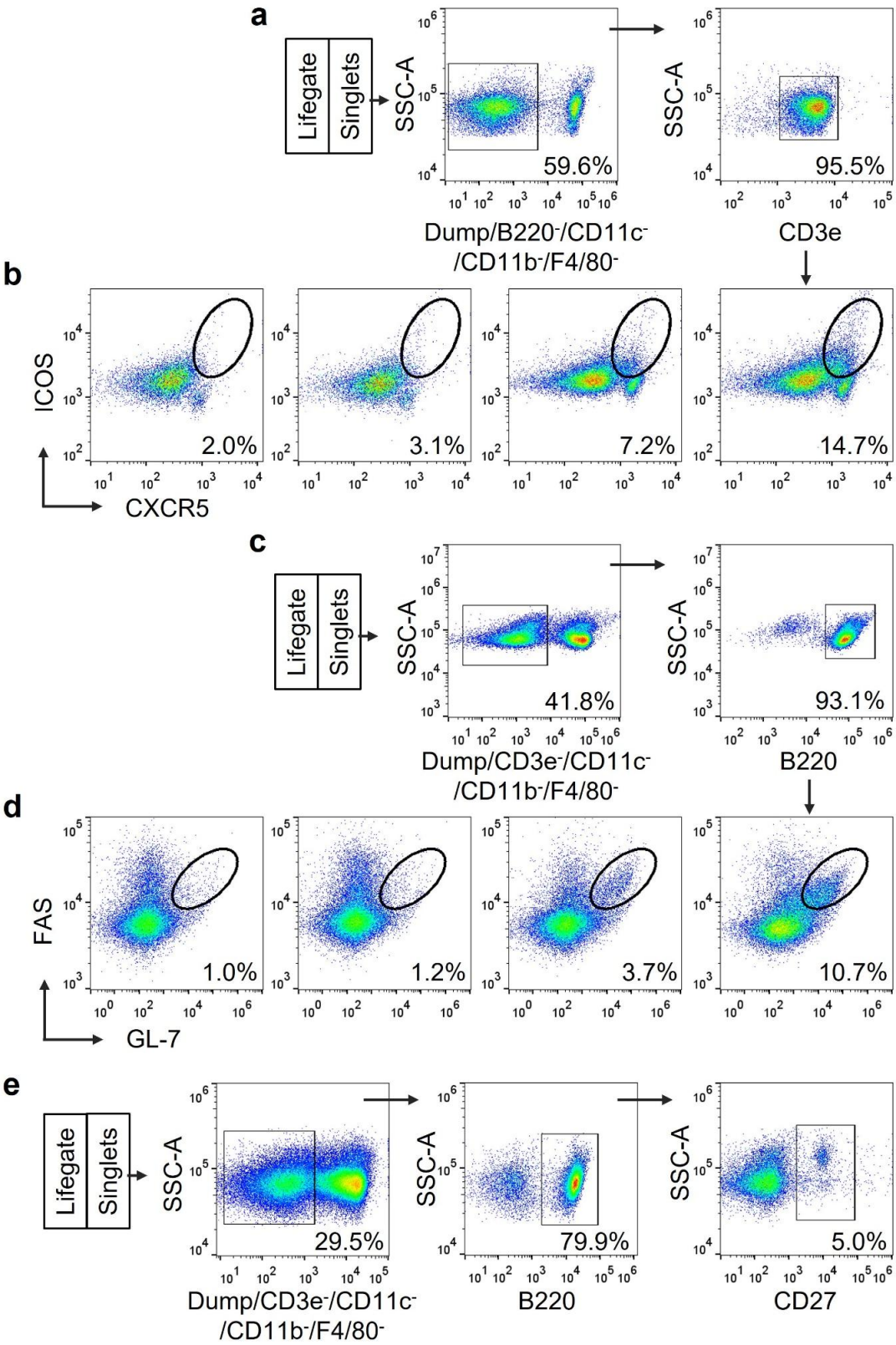

Figure 4-20 Representative flow cytometry analysis of the germinal center and memory response. (a) Gate strategy and (b) population of ICOS$^+$ CXCR5$^+$ CD3$^+$ T cell. (c) Gate strategy and (d) population of FAS$^+$ GL-7$^+$ B220$^+$ cells. (e) Gate strategy of CD27$^+$ B220$^+$ cells.

4.4.6 Activations on the long-term immune protection against SARS-CoV-2

Next, RBD-specific humoral response was evaluated (Figure 4-21a). rMASE adjuvanted formulations induced significantly higher RBD-specific IgG titers than Alum (16-fold increase, $P < 0.001$) and iMASE (2-fold increase, $P < 0.001$) after 35 days, and this persisted for longer than 3 months. Then, antibody affinity to the RBD antigen was determined using bio-layer interferometry (BLI). As shown in Figure 4-21b, the association rate constant of rMASE (Kon = 3.63×10^4 Ms^{-1}) was significantly higher than that of iMASE (Kon = 1.06×10^4 Ms^{-1}). Additionally, rMASE elicited a lower value of equilibrium dissociation constant ($K_D = 0.26 \pm 0.03$ nM) compared with iMASE ($K_D = 22.4 \pm 4.7$ nM), indicating that reversed delivery of RBD and NP may enhance the antibody affinity against the viral infections. Neutralizing activity against the pseudovirus was subsequently probed. Compared with iMASE, rMASE elicited ~180% and ~275% higher neutralization titers (NT90) on days 28 and 49, respectively (Figure 4-21c), which suggested efficient binding capabilities against viral infections. Notably, no differences in NP-specific antibody secretion were observed in either iMASE or rMASE, implying a limited effect of NP on the enhanced neutralizing capability (Figure 4-22a). The prior delivery of NP was further validated by the elevated cytokine profiles of IL-2, IL-12, TNF-α, and granzyme B (Figure 4-22b). Furthermore, central memory T cells ($CD3^+$ $CD8^+$ $CD44^{high}$ $CD62L^{high}$) and effector memory T cells ($CD3^+$ $CD8^+$ $CD44^{high}$ $CD62L^{low}$) in response to rMASE were significantly increased by 150% ($P < 0.001$) and 148% ($P < 0.001$), respectively (Figure 4-22 c-e), suggesting an increased long-term immune response.[188]

To explore the protective efficacy, a SARS-CoV-2-sensitive animal model was constructed using intranasal transduction of Ad5-hACE2-expressing adenovirus. After 5 d, the transduced mice were intranasally challenged with 5×10^5 $TCID_{50}$ of SARS-CoV-2 (Figure 4-21d).[189,190] With high serological neutralizing antibody (NAb) titer, rMASE significantly reduced the viral loads in the lung compared with iMASE, with an approximate 1000-fold decrease compared with the sham group (Figure 4-21e). No detectable subgenomic RNA (sgRNA) was observed in the rMASE-treated group, indicating that the rMASE vaccine was able to inhibit viral replication in lung tissue (Figure 4-22f). Furthermore, lung sections from the sham group exhibited thickened alveolar walls, vascular congestion, and inflammatory cell infiltration, which was consistent with viral pneumonia. In addition, iMASE-vaccinated mice exhibited moderate vascular congestion and inflammatory cell infiltration. In the case of rMASE, milder lesions were observed with substantially less infiltration of inflammatory cells (Figure 4-21f). Furthermore, pulmonary histopathology was scored based on thickening of the alveolar septa, pulmonary alveolar congestion and inflammatory cell infiltration in the alveoli and trachea. As shown in Figure 4-22g, high lung lesion scores were found in the control animals, and the scores of lung lesions were reduced in the rMASE-vaccinated animals compared to the iMASE-treated groups. In particular, all six control animals (Sham) showed severe pulmonary alveolar congestion. In contrast, the rMASE-vaccinated group demonstrated almost no signs of alveolar congestion. These results indicated that rMASE can cultivate

protective immune responses to diminish SARS-CoV-2- induced infections and lung injuries in mice.

To evaluate the efficacy of rMASE against the prevailing variants, we tested its neutralizing abilities against the live wild-type (WT) and variants of concern Delta (B.1.617.2) and Omicron (B.1.1.529). As shown in Figure 4-21g, iMASE experienced a 230% decrease in Delta and a 1710% decrease in Omicron in the NAb titers compared with WT. In the case of rMASE, NAb titers decreased by approximately 2-fold and 8-fold against Delta and Omicron variants, which was less evident than that of iMASE, indicating the enhanced immune protection against the variant infections.

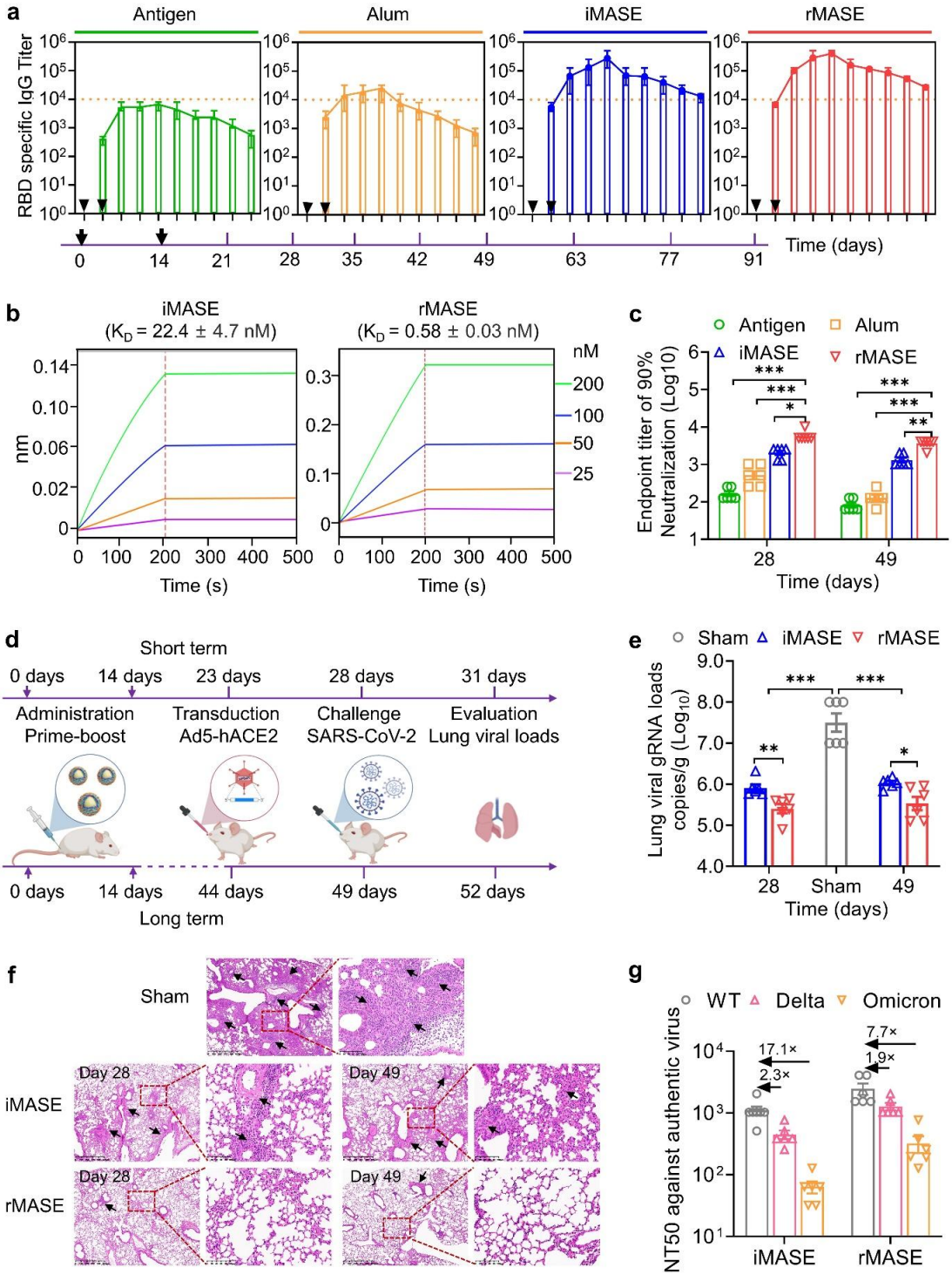

Figure 4-21 Boosting humoral and cellular response for the persistent protection against SARS-CoV-2. (a) Serum RBD-specific IgG titer over time. Arrows illustrated the time points for vaccinations. The red line indicted the highest level of RBD-specific IgG titer induced by Alum. (b) The binding affinity of antibodies with RBD antigen measured by BLI. Post-administration, the antibodies were purified from the mouse serum collected on day 28. The association signals at different concentrations of RBD were monitored and fitted to obtain the kinetic parameters. (c) Measurement of SARS-CoV-2 pseudotyped virus 90% neutralizing titer (NT90) of serum samples from mice) on the 28th and 49th day after the first immunization. The SARS-CoV-2 pseudoviruses were developed by inserting full-length S protein (Wuhan-Hu-1) into vesicular stomatitis virus (VSV) G pseudotyped virus (G*ΔG-VSV). (d) Schematic illustration of the experimental design. BALB/c mice (n = 6) were administrated with the indicated formulations at two-week intervals. To assess the short-term immune protection, mice were transduced with 2.5×10^8 pfu of Ad5-hACE2 via i.n. route on day 23. For long-term evaluations, mice were transduced on day 44. On day 5, the transduced mice were challenged with 5×10^5 $TCID_{50}$ of SARS-CoV-2 (hCoV-19/China/CAS-B001/2020, GISAID No. EPI_ISL_514256-7) via the i.n. route, following the harvest of lung tissues to test the viral load and pathology 3 d later. (e) Virus titers in lung. SARS-CoV-2 titration from lung tissue by RT-qPCR probing virus gRNA. (f) Histopathology analysis of the harvested lung tissue. Tissue sections were stained with H&E. The black arrows indicated the infection-related symptoms, including the thickened alveolar walls, vascular congestion, and inflammatory cell infiltration. Scale bar: 625 μm (left) and 100 μm (right), respectively. (g) Serum neutralizing activity evaluated by authentic SARS-CoV-2 mutants, illustrated by the serum half-maximal neutralizing titer (NT50) against live SARS-CoV-2 WT, Delta and Omicron. The serum was collected on day 28 post-administration. The number represented the fold decrease in neutralizing antibody titer. All data in the graphs were presented as the arithmetic mean ± s.e.m. from three independent experiments. For statistical analysis, a one-way analysis of variance was conducted with Tukey's correction for multiple comparisons. $*P < 0.05$, $**P < 0.01$, $***P < 0.001$.

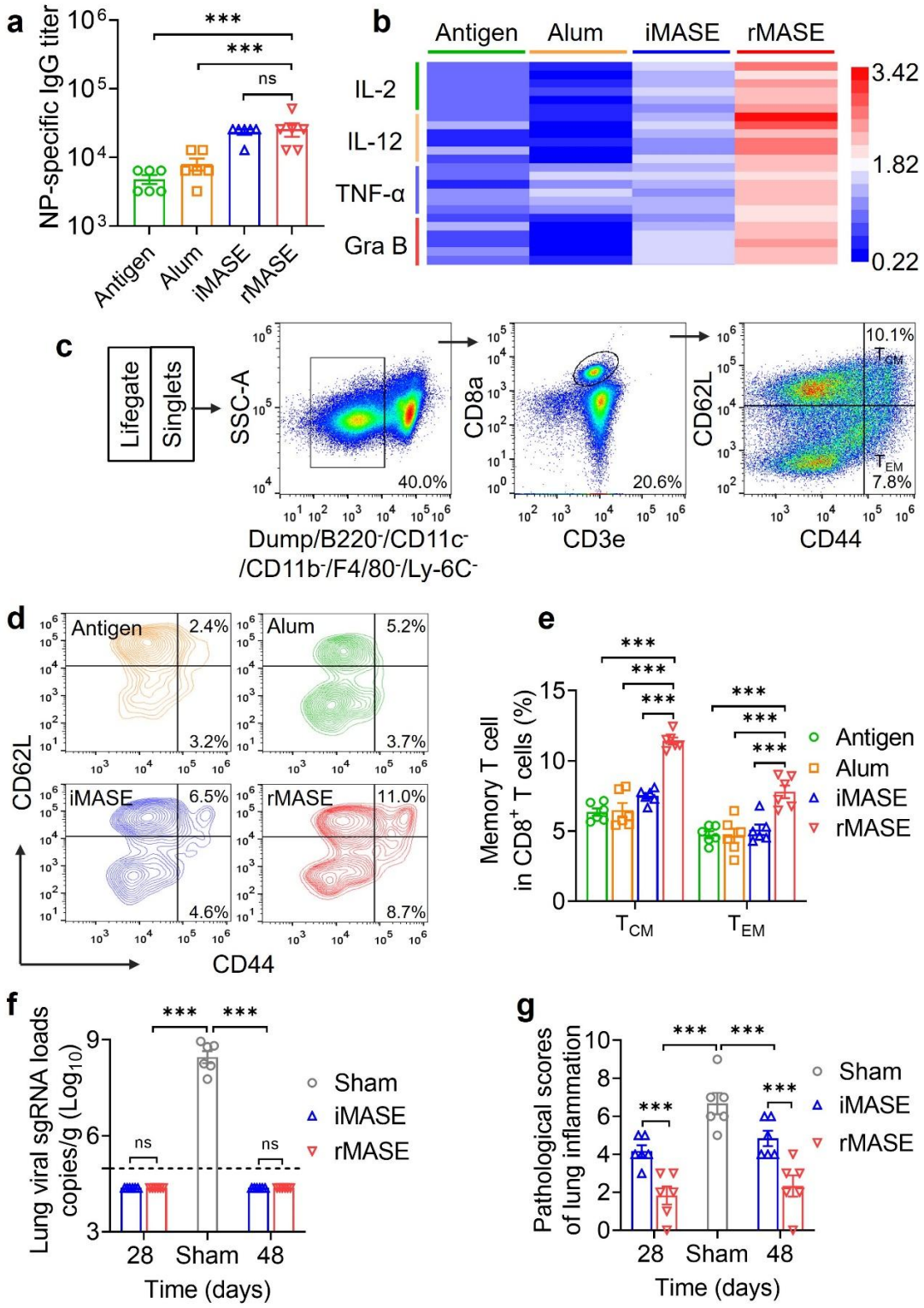

Figure 4-22 rMASE induced potent immune response against SARS-CoV-2. (a) NP-specific IgG titer. Healthy mice were intramuscularly administered with the indicated formulations, and serums were collected on day 28 for antigen-specific antibody analysis. (b) Heatmap of the cytokines array. Comparison of the secretion profile of cytokines (IL-2, IL-12, TNF-α, and granzyme B) in the supernatant of the ex vivo stimulated splenocytes. ELISA analysis of cytokines from the splenocytes

after ex vivo restimulation with RBD on day 28. The red color indicated the upregulation of the cytokines. (c) Gate strategy and (d) Representative data of the effector memory T cells ($CD44^{high}$ $CD62L^{low}$) and central memory T cells ($CD44^{high}$ $CD62L^{high}$) among $CD3^+$ $CD8^+$ splenocytes. (e) Frequency of TCM and TEM in $CD8^+$ T cells on day 28. TCM and TEM were identified by $CD3^+$ $CD8^+$ $CD44^{high}$ $CD62L^{high}$ and $CD3^+$ $CD8^+$ $CD44^{high}$ $CD62L^{low}$, respectively. (f) SARS-CoV-2 titration from lung tissues. SARS-CoV-2 titration from lung tissues was evaluated by probing virus subgenomic RNA (sgRNA) using RT-qPCR. (g) Histopathology scores of overall lung lesions and pulmonary alveolar congestion. All data in the graphs were presented as arithmetic means ± s.e.m. from three independent experiments. For statistical analysis, a one-way analysis of variance was carried out with Tukey's correction for multiple comparisons. *$P < 0.05$, **$P < 0.01$, ***$P < 0.001$.

4.5 Discussion

In summary, we developed a multi-layer alum-stabilized emulsion for the inside-out assembly of viral antigens, which led to a higher concentration of NP before the release of the surface antigen. In this manner, rMASE reversed the delivery of the surface antigen and NP and stimulated increased IFN-I-mediated innate immunity, in contrast to the natural package (iMASE). Furthermore, prior engagement of IFN-I signaling boosted adaptive immune responses against the influenza A (H1N1) and SARS-CoV-2 viruses. Thus, without any additional adjuvant components, simply altering the delivery sequence of the surface antigen and NP significantly increased the immune potency and duration against enveloped RNA viruses. Through multi-layer alum-stabilized emulsion, the inside-out strategy may offer a facile and efficient platform to elicit potent vaccine efficiency and broad immune protection.

In addition, the increased immune activations were attributed to the reversed delivery of the core and surface antigens, instead of the positive charges on NP. To test it, RBD and protamine, a commonly employed cationic protein, were loaded sequentially via MASE. As a result, the co-delivery of protamine and RBD failed to increase the immune activations by changing the release sequence of the cargos, which indicated that the inherent positive charges of NP scarcely contributed to the enhanced immune response (Figure 4-23). Moreover, the adjuvant effect of the inside-out strategy was not restrained by the source or sequence of the NP and surface antigens. Through the sequential delivery with NP, SARS-CoV-2 S1 protein or RBD-monomer as surface antigens also elicited a similar trend via MASE. Additionally, the prior release of NPs from *Escherichia coli* (*E. coli*) and eukaryotic cell lines (baculovirus-insect cells) also induced increased antibody secretion and T cell-mediated immune response (Figure 4-24).

To further demonstrate the efficacy, rMASE was compared with the commercial adjuvant (AddaVax™), a surfactant-stabilized emulsion in a formulation similar to that of MF59®.[191] As shown in Figure 4-25, the AddaVax™-adjuvanted formulation failed to elicit comparable IgG titers ($P < 0.001$) and cellular immune responses, indicating increased immune potentiation against the commercial emulsion adjuvant.

Subsequently, rMASE was compared with SARS-CoV-2 RBD-mRNA@ lipid nanoparticle (LNP), which shared a similar antigen sequence with the protein RBD antigen employed in this manuscript and formulated with SM-102 as the ionizable lipid, 1,2-distearoyl-sn-glycero-3-phosphocholine (DSPC) as the phosphate lipid, 1,2-dimyristoyl-racglycero-3-methoxypolyethylene glycol-2000 (DMG-PEG2000) as the PEGylated lipid, along with the cholesterol.[192] As shown in Figure 4-26, rMASE induced slightly lower antigen-specific antibody titers and neutralizing antibody titers against WT than RBD-encoded mRNA@LNP. Additionally, rMASE showed comparable responses to Delta (B.1.617.2) and Omicron (B.1.1.529) variants, and a similar level in the engagement of the IFN-γ-producing T cells. Interestingly, rMASE elicited a higher frequency of central memory T cells ($CD3^+$ $CD8^+$ $CD44^{high}$ $CD62L^{high}$; $P < 0.001$), suggesting the higher immune memory may be activated by the reversed delivery of the core antigens and surface antigens. By contracting the mRNA-based strategy, rMASE induced comparable immune responses, which were evidently higher than the natural exposure of the antigens (iMASE), indicating that the reversed delivery of antigens may offer an enhanced strategy for recombinant protein vaccinations.

Notably, we do not imply that the inside-out strategy can be applied to all viral vaccines. As a preliminary attempt, we employed the multi-layer alum-stabilized emulsion to deliver the surface antigen (HBsAg) and core antigen (HBcAg) of the hepatitis B virus (HBV, a type of DNA virus). Intriguingly, the inside-out assembly failed to elicit higher immune potency. Instead, it is the natural distribution pattern that entrapped the core antigen inside, but displayed the surface antigen on the outmost layer, which significantly boosted the antigen-specific IgG titers, induced higher levels of IFN-γ^+ T cells, and increased populations of the central memory T cells ($CD44^{high}$ $CD62L^{high}$) among the $CD8^+$ T and $CD4^+$ T cells (Figure 4-27 a-d). This may be attributed to the more advanced potency of HBsAg to induce IFN-α expression compared with HBcAg (Figure 4-27e), which may subsequently potentiate the adaptive immune engagement. Presumptively, for the rational delivery of multi-component vaccines, prior delivery of immunogenic ingredients may result in the enhanced immune effect. As such, the prior delivery of adjuvants, such as Toll-like-receptor agonists and STING activators, before the co-delivered antigens may better boost the immune responses for enhanced vaccinations.

Collectively, the exact replication of live virus may not always offer an optimal solution. In the case of vaccines against H1N1 and SARS-CoV-2, reversed delivery of surface antigens and NPs (core antigens) were proved to potentiate the anti-viral effects. Besides modeling the steric structures of pathogens, it is also imperative to dictate the delivery kinetics of the vaccines, in view of spatiotemporal dynamics during immune activation.

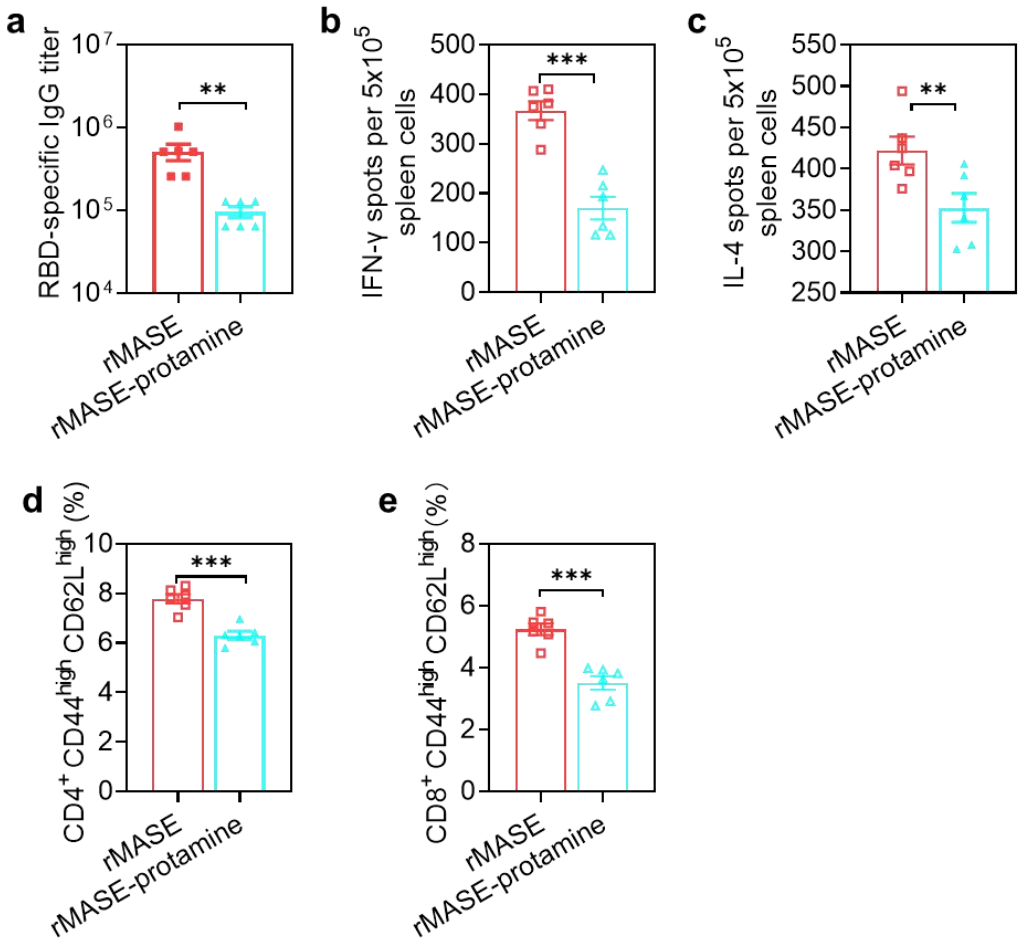

Figure 4-23 Evaluation of the charge effect on inside-out strategy via the comparison with the protamine-delivered formulation. (a) Serum RBD-specific IgG titer. ELISPOT analysis of (b) IFN-γ and (c) IL-4 spot-forming cells among splenocytes. Flow cytometry of central memory T cells ($CD44^{high}$ $CD62L^{high}$) among (d) $CD4^+$ T cells and (e) $CD8^+$ T cells. All data in the graphs were presented as arithmetic means ± s.e.m. from three independent experiments. Unpaired Student's t was carried out for statistical analysis. $^*P < 0.05$, $^{**}P < 0.01$, $^{***}P < 0.001$.

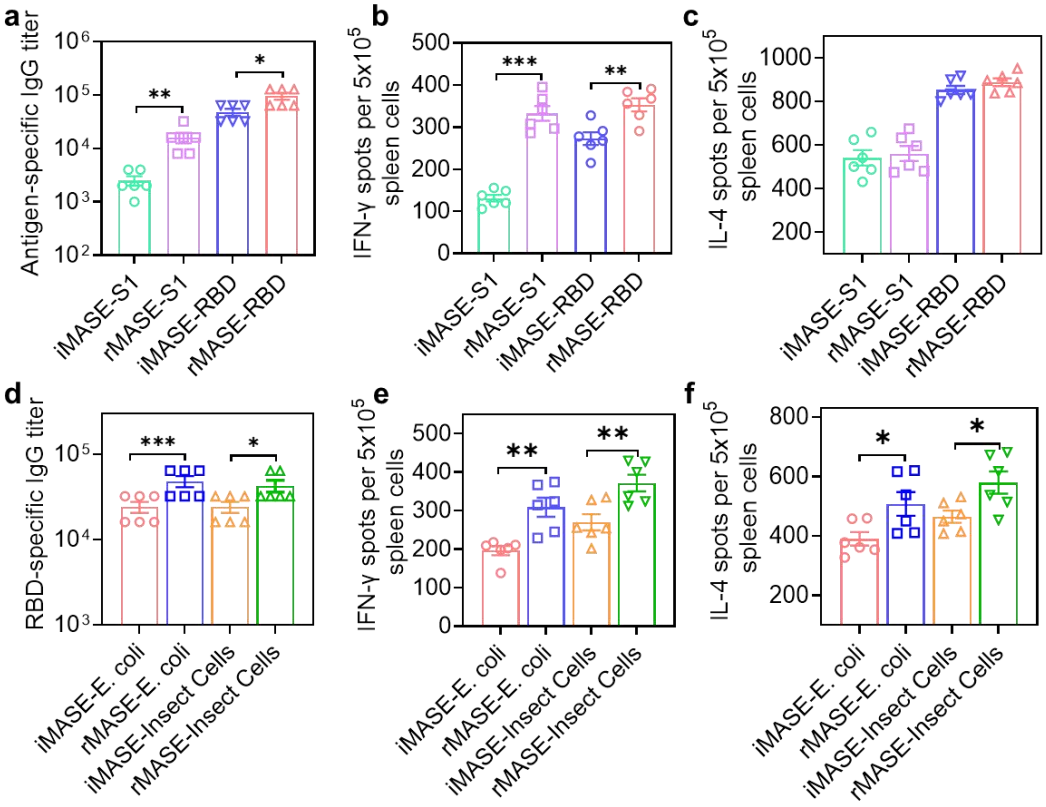

Figure 4-24 rMASE assembled from different types of surface antigens and NPs for enhanced immune responses. (a-c) Both S1 protein- and monomer-RBD-formulated rMASE induced enhanced immune responses. (a) Serum antigen-specific IgG titer. ELISPOT analysis of (b) IFN-γ and (c) IL-4 spot-forming cells among splenocytes. (d-f) rMASE, combined with NP from both *Escherichia coli* (*E. coli*) and the eukaryotic cell lines, increased the immune responses. (d) Serum RBD-specific IgG titer. ELISPOT analysis of (e) IFN-γ and (f) IL-4 spot-forming cells among splenocytes. Mice were administrated intramuscularly with indicated formulations, and the immune responses were detected on day 28. All data in the graphs were presented as arithmetic means ± s.e.m. from three independent experiments. Unpaired Student's t was carried out for statistical analysis. *$P < 0.05$, **$P < 0.01$, ***$P < 0.001$.

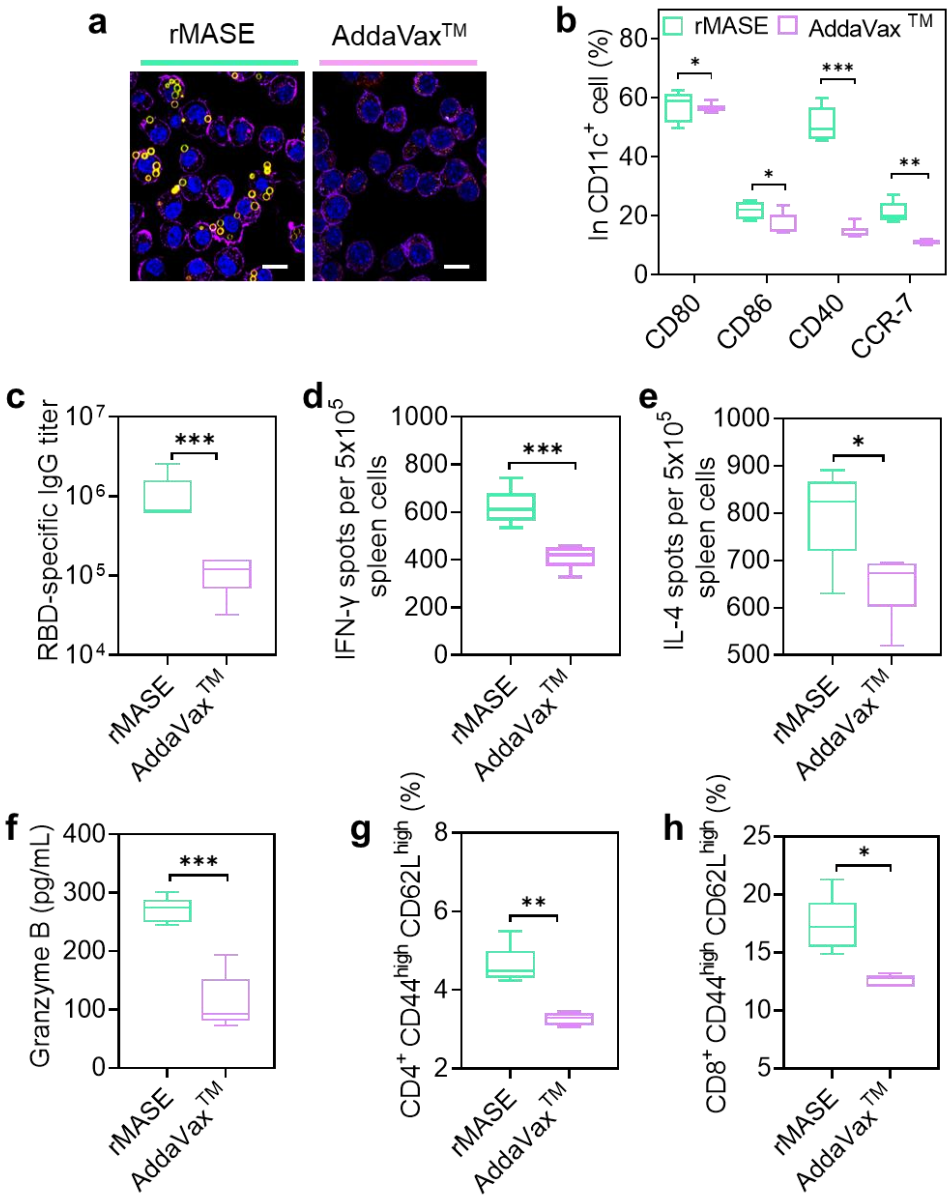

Figure 4-25 A comparison of the immune response to rMASE and AddaVax™. (a) Confocal images of the antigen uptake. DCs membrane, RBD, and NP were labeled with FITC-phalloidin (purple), Cy3 (red), and Cy5 (green), respectively. Scale bar: 10 μm. (b) DC activation after treating with the formulations in vitro. (c) Serum RBD-specific IgG titer. ELISPOT analysis of (d) IFN-γ and (e) IL-4 spot-forming cells among splenocytes. (f) The secretion of Granzyme B among the splenocytes. Flow cytometry of central memory T cells ($CD44^{high}$ $CD62L^{high}$) among (g) $CD4^+$ T cells and (h) $CD8^+$ T cells. All data in the graphs were presented as arithmetic means ± s.e.m. from three independent experiments. Unpaired Student's t was carried out for statistical analysis. *$P < 0.05$, **$P < 0.01$, ***$P < 0.001$.

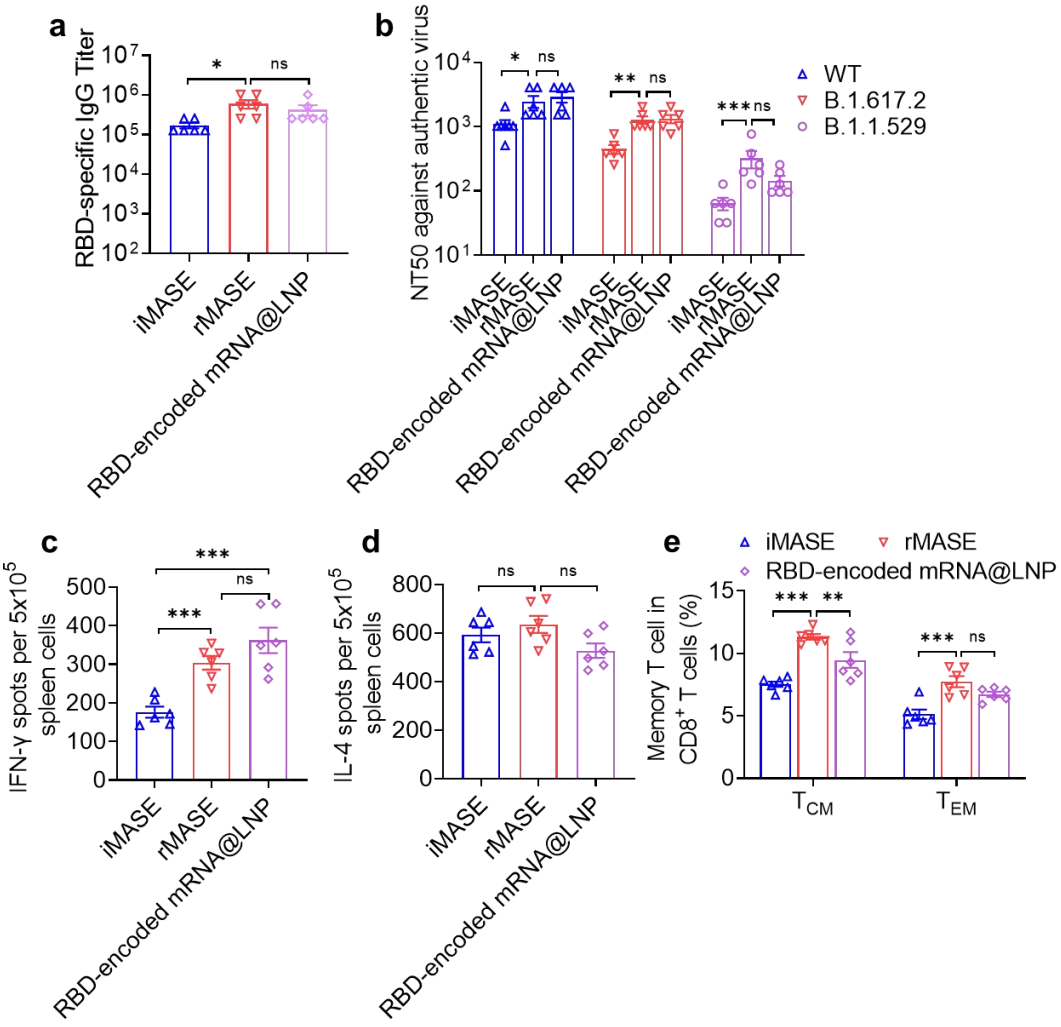

Figure 4-26 A comparison of RBD-encoded mRNA@LNP with rMASE in terms of immune effectiveness. (a) Serum RBD-specific IgG titer on day 28. (b) Serum neutralizing activity was evaluated by authentic SARS-CoV-2 mutants, illustrated by the serum half-maximal neutralizing titer (NT50) against live SARS-CoV-2 WT, B.1.617.2 and B.1.1.529. The number represented the fold decrease in neutralizing antibody titer. ELISPOT assay on (c) IFN-γ and (d) IL-4 spot-forming cells among the splenocytes, following stimulation with RBD. (e) Flow cytometry on the effector memory T cells ($CD44^{high}$ $CD62L^{low}$) and central memory T cells ($CD44^{high}$ $CD62L^{high}$) among $CD3^+$ $CD8^+$ splenocytes. All data in the graphs were presented as arithmetic means ± s.e.m. from three independent experiments. For statistical analysis, a one-way analysis of variance was carried out with Tukey's correction for multiple comparisons. $*P < 0.05$, $**P < 0.01$, $***P < 0.001$.

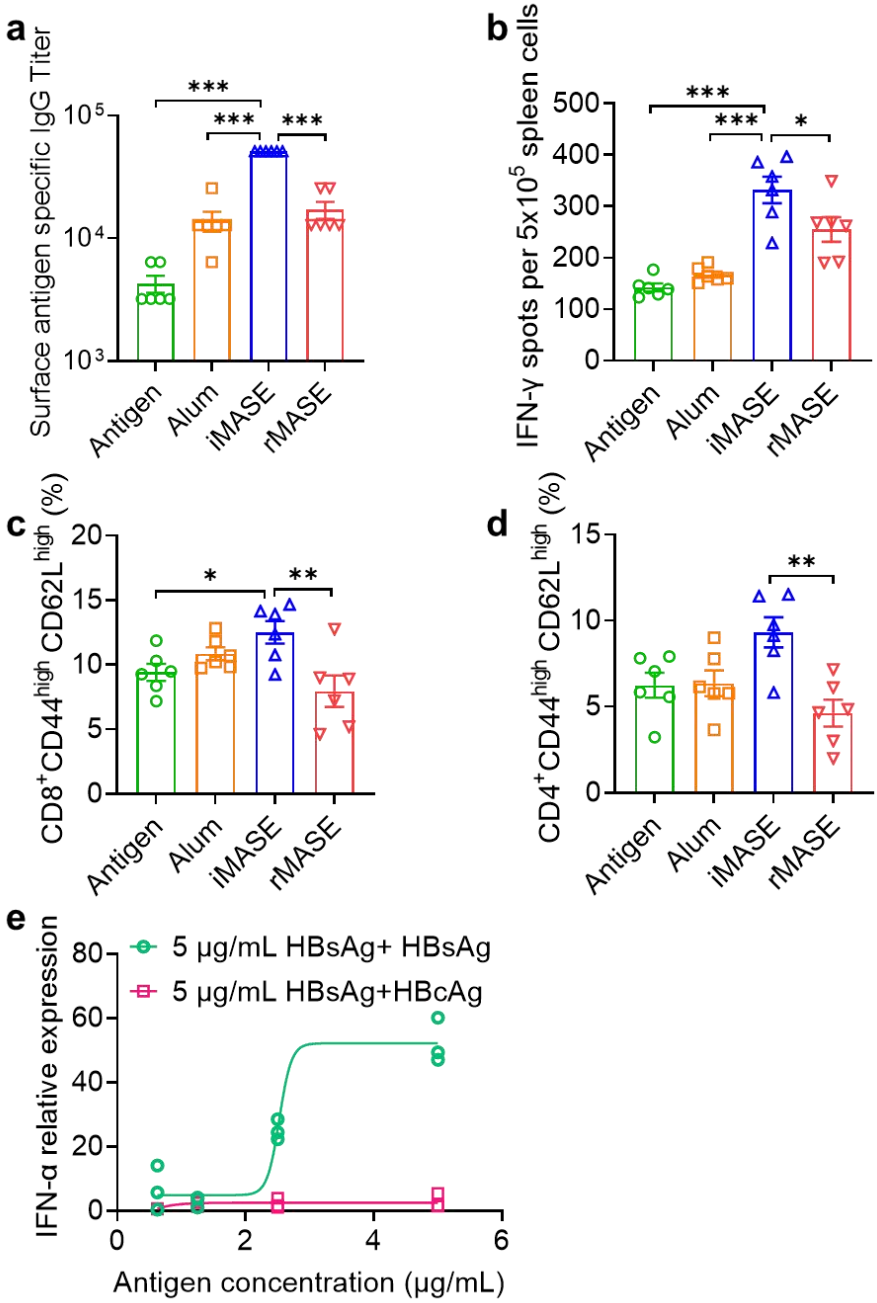

Figure 4-27 The sequential delivery of the core and surface antigen of Hepatitis B virus via MASE system. (a) Serum HBsAg-specific IgG titer. (b) ELISPOT analysis of HBsAg-specific IFN-γ^+ T cell. Flow cytometry of central memory T cells ($CD44^{high}$ $CD62L^{high}$) among (c) $CD8^+$ T cells and (d) $CD4^+$ T cells. (e) The expression of IFN-α among the BMDCs after treatment with the surface antigen (HBsAg) and core antigen (HBcAg) of HBV. For HBV, HBsAg and HBcAg were used to treat BMDCs, and the mRNA expression of IFN-α was determined using RT-qPCR. (a-d) These data in the graphs were presented as arithmetic means ± s.e.m. from three independent experiments. For statistical analysis, a one-way analysis of variance was carried out with Tukey's correction for multiple comparisons. *$P < 0.05$, **$P < 0.01$, ***$P < 0.001$. (e) These data were analyzed by nonlinear-regression (dose-response-stimulation).

Chapter 5 Concluding remarks

In this chapter, the author summarizes this thesis. In chapter 1, we extensively discussed the advancements and mechanisms of modern vaccine technologies with a specific focus on the components and actions of various vaccine adjuvants. The summary explains how traditional vaccines work, their limitations, and the evolution towards using novel adjuvants and delivery systems like nanoparticle carriers, aluminum-based adjuvants, and oil emulsion adjuvants to enhance the efficacy, safety, and stability of vaccines. Particular attention is given to describing how these adjuvants facilitate a more robust and targeted immune response by modifying the antigen presentation and activation pathways. The description of Toll-like receptors (TLRs) and their role in recognizing pathogen-associated molecular patterns to activate immune responses highlights the intersection of innate and adaptive immunity in vaccine function. Furthermore, the use of alum-stabilized Pickering emulsions as advanced carriers demonstrates the integration of material science and immunology to optimize vaccine delivery and efficacy through controlled release and enhanced antigen presentation. This comprehensive review underscores the critical role of innovative vaccine formulations and adjuvants in overcoming the limitations of traditional vaccines and enhancing global public health measures against infectious diseases.

In chapter 2, in this study, we assumed that frequent vaccination may cause immune suppression within the tumor. Herein, the tumor-bearing mice were vaccinated with APE for two (APE-2), three (APE-3) and four doses (APE-4). We found that APE-4 increased the IFN-γ responses among the splenocytes, but also induced the engagement of the immunosuppressive related PD-1^+ $CD8^+$ and LAG-3^+CD8^+ T cells within the TME and TDLNs, hampering the subsequent antitumor immunity. Furthermore, the co-administering with anti-PD-1 antibody evidently lessened this effect. Under these circumstances, APE-4 elicited more potent tumor regression, compared with APE-2, indicating that the anti-PD-1 therapy may serve as a cure for the vaccination-induced immunosuppression within the tumor microenvironment.

In chapter 2, we developed soft particle-stabilized emulsions (SPEs) to deliver lipopeptides with controlled release profiles by adjusting their hydrophobic chain lengths: C_6-SPE (fast release), C_{10}-SPE (medium release), and C_{16}-SPE (slow release). After intramuscular administration, the rapid release of antigen in C_6-SPE led to a significant up-regulated expression of MHC-I-peptide complex one day post-vaccination. And the slow release of antigen in C_{16}-SPE resulted in the delay of the optimal expression of MHC-I-peptide complex over 7 days post-vaccination. Both scenarios missed the critical window to coordinate with CD86 expression for DC activation, thereby hindering effective T cell activation. C_{10}-SPE, however, with a medium release of antigen, induced simultaneous peak expression of MHC-I-peptide

complex and CD86 five days post-vaccination, achieving an optimal DC activation, resulting in effective tumor regression and prolonged survival in EG7-OVA-bearing mice. Additionally, co-delivery of CpG with SPEs boosted DC activation at early stage, providing a sustained expression of CD86 window for dendritic cells (DCs) activation, improving the anti-tumor effects of C_6-SPE that comparable to C_{10}-SPE. These findings may highlight the importance of synchronizing the spatiotemporal dynamics of antigen presentation and antigen-presenting cells (APC) activation for the enhanced vaccinations. Our findings indicate that synchronizing spatiotemporal co-stimulatory signal and antigen delivery is essential to avoid T cell exhaustion and apoptosis, thereby ensuring a sustained and effective immune response. These insights could inform the development of strategies for sequential content delivery, potentially enhancing the efficacy of immunization against complex diseases like malignant tumors. Additionally, we aim to draw the research attention of tumor vaccine to cultivate a spatiotemporally coordinated approach to enhance the efficacy of treatments through the strategic management of antigen presentation and APC activation.

In chapter 4, a multi-layer Pickering emulsion based on alum adjuvant was heralded to dictate the delivery kinetics of the antigenic components. Using this method, RBD was trapped inside the nanocage, and NP was absorbed on the outside of the droplets, which enabled NP to be released before RBD. Furthermore, we also employed cross-disciplinary approaches to detail the sequential assembly and release of RBD and NP, including the combination of XRD and DSC to illustrate the release kinetics of the entrapped and adsorbed antigens, and the high content imaging systems to trace the intracellular release profile of the antigens and etc. and IFN-I signaling was significantly boosted by simply reversing the exposure of RBD and NP to the immune system. These data may gain a delivery insight on the spatial-temporal control over the sequential immune activations for the enhanced vaccination. rMASE boosted antigen-specific antibody, neutralizing antibody, immune memory and Th1-biased cellular responses. Furthermore, we also detected the evident decrease in SARS-CoV-2 viral loads in the infected lungs and the improved neutralizing capabilities against the prevailing mutated variants (P.1 and B.1.617.2). Here, through the inside-out assembly and the reversed delivery of SARS-CoV-2, we aimed to demonstrate that, instead of the exact replication of the live pathogens, it is more important to induce the ordered exposure of antigenic components, triggering the coordinated actions of the lymph nodes, immunocytes, and the cytokines for the enhanced vaccination.

Reference

1 Proceedings of the National Academy of Sciences of the United States of America. Annual subject and author indexes. *Proc Natl Acad Sci U S A* **87 Suppl**, 10069-10240 (1990).

2 Irvine, D. J., Swartz, M. A. & Szeto, G. L. Engineering synthetic vaccines using cues from natural immunity. *Nat Mater* **12**, 978-990, doi:10.1038/nmat3775 (2013).

3 Garçon, N., Chomez, P. & Van Mechelen, M. GlaxoSmithKline Adjuvant Systems in vaccines: concepts, achievements and perspectives. *Expert Rev Vaccines* **6**, 723-739, doi:10.1586/14760584.6.5.723 (2007).

4 Lee, S. & Nguyen, M. T. Recent advances of vaccine adjuvants for infectious diseases. *Immune Netw* **15**, 51-57, doi:10.4110/in.2015.15.2.51 (2015).

5 Dowling, J. K. & Mansell, A. Toll-like receptors: the swiss army knife of immunity and vaccine development. *Clin Transl Immunology* **5**, e85, doi:10.1038/cti.2016.22 (2016).

6 Pulendran, B. & Ahmed, R. Immunological mechanisms of vaccination. *Nat. Immunol.* **12**, 509-517, doi:10.1038/ni.2039 (2011).

7 Kieny, M. P. & Girard, M. P. Human vaccine research and development: an overview. *Vaccine* **23**, 5705-5707, doi:10.1016/j.vaccine.2005.07.077 (2005).

8 Newman, M. J. & Powell, M. F. Immunological and formulation design considerations for subunit vaccines. *Pharm Biotechnol* **6**, 1-42, doi:10.1007/978-1-4615-1823-5_1 (1995).

9 Shah, R. R., Hassett, K. J. & Brito, L. A. Overview of Vaccine Adjuvants: Introduction, History, and Current Status. *Methods Mol Biol* **1494**, 1-13, doi:10.1007/978-1-4939-6445-1_1 (2017).

10 Coffman, R. L., Sher, A. & Seder, R. A. Vaccine adjuvants: putting innate immunity to work. *Immunity* **33**, 492-503, doi:10.1016/j.immuni.2010.10.002 (2010).

11 Rappuoli, R., Mandl, C. W., Black, S. & De Gregorio, E. Vaccines for the twenty-first century society. *Nat. Rev. Immunol.* **11**, 865-872, doi:10.1038/nri3085 (2011).

12 Brito, L. A. & O'Hagan, D. T. Designing and building the next generation of improved vaccine adjuvants. *J Control Release* **190**, 563-579, doi:10.1016/j.jconrel.2014.06.027 (2014).

13 Hafner, A. M., Corthésy, B. & Merkle, H. P. Particulate formulations for the delivery of poly(I:C) as vaccine adjuvant. *Adv Drug Deliv Rev* **65**, 1386-1399, doi:10.1016/j.addr.2013.05.013 (2013).

14 Sahin, U. & Türeci, Ö. Personalized vaccines for cancer immunotherapy. *Science* **359**, 1355-1360, doi:10.1126/science.aar7112 (2018).

15 Yin, N. *et al.* Development of pharmacological immunoregulatory anti-cancer therapeutics: current mechanistic studies and clinical opportunities. *Signal Transduct Target Ther* **9**, 126, doi:10.1038/s41392-024-01826-z (2024).

16 Hu, A. *et al.* Harnessing innate immune pathways for therapeutic advancement in cancer. *Signal Transduct Target Ther* **9**, 68, doi:10.1038/s41392-024-01765-9 (2024).

17 Lionakis, M. S., Drummond, R. A. & Hohl, T. M. Immune responses to human fungal pathogens and therapeutic prospects. *Nat. Rev. Immunol.* **23**, 433-452, doi:10.1038/s41577-022-00826-w (2023).

18 Roth, G. A. *et al.* Designing spatial and temporal control of vaccine responses. *Nat Rev Mater* **7**, 174-195, doi:10.1038/s41578-021-00372-2 (2022).
19 Guy, B. The perfect mix: recent progress in adjuvant research. *Nat. Rev. Microbiol.* **5**, 505-517, doi:10.1038/nrmicro1681 (2007).
20 Reed, S. G., Orr, M. T. & Fox, C. B. Key roles of adjuvants in modern vaccines. *Nat. Med.* **19**, 1597-1608, doi:10.1038/nm.3409 (2013).
21 Buonsanti, C. & D'Oro, U. in *Immunopotentiators in modern vaccines* 85-104 (Elsevier, 2017).
22 Kawai, T. & Akira, S. Innate immune recognition of viral infection. *Nat. Immunol.* **7**, 131-137, doi:10.1038/ni1303 (2006).
23 Iwasaki, A. & Medzhitov, R. Control of adaptive immunity by the innate immune system. *Nat. Immunol.* **16**, 343-353, doi:10.1038/ni.3123 (2015).
24 Shaw, A. C., Joshi, S., Greenwood, H., Panda, A. & Lord, J. M. Aging of the innate immune system. *Curr. Opin. Immunol.* **22**, 507-513, doi:10.1016/j.coi.2010.05.003 (2010).
25 Anderson, K. V. Toll signaling pathways in the innate immune response. *Curr. Opin. Immunol.* **12**, 13-19 (2000).
26 Zhao, T. *et al.* Vaccine adjuvants: mechanisms and platforms. *Signal Transduct Target Ther* **8**, 283, doi:10.1038/s41392-023-01557-7 (2023).
27 Carroll, M. C. The complement system in regulation of adaptive immunity. *Nat. Immunol.* **5**, 981-986, doi:10.1038/ni1113 (2004).
28 Medzhitov, R. & Janeway, C., Jr. Innate immune recognition: mechanisms and pathways. *Immunol. Rev.* **173**, 89-97, doi:10.1034/j.1600-065x.2000.917309.x (2000).
29 Felício, M. R., Silva, O. N., Gonçalves, S., Santos, N. C. & Franco, O. L. Peptides with Dual Antimicrobial and Anticancer Activities. *Front Chem* **5**, 5, doi:10.3389/fchem.2017.00005 (2017).
30 Medzhitov, R. & Janeway, C. A., Jr. Innate immunity: impact on the adaptive immune response. *Curr. Opin. Immunol.* **9**, 4-9, doi:10.1016/s0952-7915(97)80152-5 (1997).
31 Banchereau, J. & Steinman, R. M. Dendritic cells and the control of immunity. *Nature* **392**, 245-252, doi:10.1038/32588 (1998).
32 Heath, W. R. & Carbone, F. R. Cross-presentation, dendritic cells, tolerance and immunity. *Annu. Rev. Immunol.* **19**, 47-64, doi:10.1146/annurev.immunol.19.1.47 (2001).
33 Mutwiri, G. K., Nichani, A. K., Babiuk, S. & Babiuk, L. A. Strategies for enhancing the immunostimulatory effects of CpG oligodeoxynucleotides. *J Control Release* **97**, 1-17, doi:10.1016/j.jconrel.2004.02.022 (2004).
34 Montomoli, E. *et al.* Current adjuvants and new perspectives in vaccine formulation. *Expert Rev Vaccines* **10**, 1053-1061, doi:10.1586/erv.11.48 (2011).
35 Temizoz, B., Kuroda, E. & Ishii, K. J. Vaccine adjuvants as potential cancer immunotherapeutics. *Int. Immunol.* **28**, 329-338, doi:10.1093/intimm/dxw015 (2016).
36 Pashine, A., Valiante, N. M. & Ulmer, J. B. Targeting the innate immune response with improved vaccine adjuvants. *Nat. Med.* **11**, S63-68, doi:10.1038/nm1210 (2005).
37 Zhou, J., Kroll, A. V., Holay, M., Fang, R. H. & Zhang, L. Biomimetic Nanotechnology toward Personalized Vaccines. *Adv. Mater.* **32**, e1901255, doi:10.1002/adma.201901255 (2020).
38 Pifferi, C., Fuentes, R. & Fernández-Tejada, A. Natural and synthetic carbohydrate-based

vaccine adjuvants and their mechanisms of action. *Nat Rev Chem* **5**, 197-216, doi:10.1038/s41570-020-00244-3 (2021).

39 Xiao, Y. *et al.* Immunoregulatory nanomedicine for respiratory infections. *Nature Reviews Bioengineering* **2**, 244-259 (2024).

40 Eshaghi, B. *et al.* The role of engineered materials in mucosal vaccination strategies. *Nature Reviews Materials* **9**, 29-45 (2024).

41 Shetab Boushehri, M. A. & Lamprecht, A. TLR4-Based Immunotherapeutics in Cancer: A Review of the Achievements and Shortcomings. *Mol. Pharm.* **15**, 4777-4800, doi:10.1021/acs.molpharmaceut.8b00691 (2018).

42 Didierlaurent, A. M. *et al.* AS04, an aluminum salt- and TLR4 agonist-based adjuvant system, induces a transient localized innate immune response leading to enhanced adaptive immunity. *J. Immunol.* **183**, 6186-6197, doi:10.4049/jimmunol.0901474 (2009).

43 Boland, G. *et al.* Safety and immunogenicity profile of an experimental hepatitis B vaccine adjuvanted with AS04. *Vaccine* **23**, 316-320, doi:10.1016/j.vaccine.2004.06.006 (2004).

44 Naud, P. S. *et al.* Sustained efficacy, immunogenicity, and safety of the HPV-16/18 AS04-adjuvanted vaccine: final analysis of a long-term follow-up study up to 9.4 years post-vaccination. *Hum Vaccin Immunother* **10**, 2147-2162, doi:10.4161/hv.29532 (2014).

45 Han, J. E. *et al.* Comparison of the immune responses to the CIA06-adjuvanted human papillomavirus L1 VLP vaccine with those against the licensed HPV vaccine Cervarix™ in mice. *Vaccine* **30**, 4127-4134, doi:10.1016/j.vaccine.2012.04.079 (2012).

46 Heil, F. *et al.* Species-specific recognition of single-stranded RNA via toll-like receptor 7 and 8. *Science* **303**, 1526-1529, doi:10.1126/science.1093620 (2004).

47 Ignacio, B. J., Albin, T. J., Esser-Kahn, A. P. & Verdoes, M. Toll-like Receptor Agonist Conjugation: A Chemical Perspective. *Bioconjug Chem* **29**, 587-603, doi:10.1021/acs.bioconjchem.7b00808 (2018).

48 Pulendran, B., P, S. A. & O'Hagan, D. T. Emerging concepts in the science of vaccine adjuvants. *Nat. Rev. Drug Discov.* **20**, 454-475, doi:10.1038/s41573-021-00163-y (2021).

49 Akagi, T., Baba, M. & Akashi, M. Biodegradable nanoparticles as vaccine adjuvants and delivery systems: regulation of immune responses by nanoparticle-based vaccine. *Polymers in nanomedicine*, 31-64 (2012).

50 Skwarczynski, M. *et al.* Polyacrylate dendrimer nanoparticles: a self-adjuvanting vaccine delivery system. *Angew. Chem. Int. Ed. Engl.* **49**, 5742-5745, doi:10.1002/anie.201002221 (2010).

51 Oyewumi, M. O., Kumar, A. & Cui, Z. Nano-microparticles as immune adjuvants: correlating particle sizes and the resultant immune responses. *Expert Rev Vaccines* **9**, 1095-1107, doi:10.1586/erv.10.89 (2010).

52 Huang, Y. *et al.* Nanotechnology's frontier in combatting infectious and inflammatory diseases: prevention and treatment. *Signal Transduct Target Ther* **9**, 34, doi:10.1038/s41392-024-01745-z (2024).

53 Sun, T. *et al.* Engineered nanoparticles for drug delivery in cancer therapy. *Angew. Chem. Int. Ed. Engl.* **53**, 12320-12364, doi:10.1002/anie.201403036 (2014).

54 Hamdy, S., Haddadi, A., Hung, R. W. & Lavasanifar, A. Targeting dendritic cells with nano-particulate PLGA cancer vaccine formulations. *Adv Drug Deliv Rev* **63**, 943-955,

doi:10.1016/j.addr.2011.05.021 (2011).

55 Hameedat, F. *et al.* Engineering nanomaterials for glioblastoma nanovaccination. *Nature Reviews Materials*, 1-15 (2024).

56 Kool, M. *et al.* Alum adjuvant boosts adaptive immunity by inducing uric acid and activating inflammatory dendritic cells. *J. Exp. Med.* **205**, 869-882, doi:10.1084/jem.20071087 (2008).

57 Lebre, F., Pedroso de Lima, M. C., Lavelle, E. C. & Borges, O. Mechanistic study of the adjuvant effect of chitosan-aluminum nanoparticles. *Int J Pharm* **552**, 7-15, doi:10.1016/j.ijpharm.2018.09.044 (2018).

58 Régnier, M. *et al.* Structural perturbation of diphtheria toxoid upon adsorption to aluminium hydroxide adjuvant. *Vaccine* **30**, 6783-6788, doi:10.1016/j.vaccine.2012.09.020 (2012).

59 Moon, S. H., Shin, E. C., Noh, Y. W. & Lim, Y. T. Evaluation of hyaluronic acid-based combination adjuvant containing monophosphoryl lipid A and aluminum salt for hepatitis B vaccine. *Vaccine* **33**, 4762-4769, doi:10.1016/j.vaccine.2015.08.006 (2015).

60 Rimaniol, A. C. *et al.* Aluminum hydroxide adjuvant induces macrophage differentiation towards a specialized antigen-presenting cell type. *Vaccine* **22**, 3127-3135, doi:10.1016/j.vaccine.2004.01.061 (2004).

61 Moyer, T. J. *et al.* Engineered immunogen binding to alum adjuvant enhances humoral immunity. *Nat. Med.* **26**, 430-440, doi:10.1038/s41591-020-0753-3 (2020).

62 Marrack, P., McKee, A. S. & Munks, M. W. Towards an understanding of the adjuvant action of aluminium. *Nat. Rev. Immunol.* **9**, 287-293, doi:10.1038/nri2510 (2009).

63 Jimenez, H. R., Hallit, R. R., Debari, V. A. & Slim, J. Hepatitis A vaccine response in HIV-infected patients: are TWINRIX and HAVRIX interchangeable? *Vaccine* **31**, 1328-1333, doi:10.1016/j.vaccine.2012.12.045 (2013).

64 Greub, G., Genton, B., Safary, A., Thoelen, S. & Frei, P. C. Comparison of the reactogenicity and immunogenicity of a two injection combined high-dose hepatitis A and hepatitis B vaccine to those of Twinrix. *Vaccine* **19**, 1113-1117, doi:10.1016/s0264-410x(00)00332-7 (2000).

65 Mbow, M. L., De Gregorio, E. & Ulmer, J. B. Alum's adjuvant action: grease is the word. *Nat. Med.* **17**, 415-416, doi:10.1038/nm0411-415 (2011).

66 Yoshida, S. *et al.* The CD153 vaccine is a senotherapeutic option for preventing the accumulation of senescent T cells in mice. *Nat Commun* **11**, 2482, doi:10.1038/s41467-020-16347-w (2020).

67 Hu, Y. *et al.* Alum as an adjuvant for nanoparticle based vaccines: A case study with a hybrid nanoparticle-based nicotine vaccine. *Nanomedicine* **20**, 102023, doi:10.1016/j.nano.2019.102023 (2019).

68 Oleszycka, E. *et al.* The vaccine adjuvant alum promotes IL-10 production that suppresses Th1 responses. *Eur. J. Immunol.* **48**, 705-715, doi:10.1002/eji.201747150 (2018).

69 Bovier, P. A. Epaxal: a virosomal vaccine to prevent hepatitis A infection. *Expert Rev Vaccines* **7**, 1141-1150, doi:10.1586/14760584.7.8.1141 (2008).

70 Kool, M., Fierens, K. & Lambrecht, B. N. Alum adjuvant: some of the tricks of the oldest adjuvant. *J. Med. Microbiol.* **61**, 927-934, doi:10.1099/jmm.0.038943-0 (2012).

71 Lin, Y. J. *et al.* Oil-in-water emulsion adjuvants for pediatric influenza vaccines: a systematic review and meta-analysis. *Nat Commun* **11**, 315, doi:10.1038/s41467-019-14230-x (2020).

72 Schetters, S. T. T. *et al.* Immunological dynamics after subcutaneous immunization with a squalene-based oil-in-water adjuvant. *FASEB J.* **34**, 12406-12418, doi:10.1096/fj.202000848R (2020).

73 Schultze, V. *et al.* Safety of MF59 adjuvant. *Vaccine* **26**, 3209-3222, doi:10.1016/j.vaccine.2008.03.093 (2008).

74 O'Hagan, D. T., Ott, G. S., De Gregorio, E. & Seubert, A. The mechanism of action of MF59 - an innately attractive adjuvant formulation. *Vaccine* **30**, 4341-4348, doi:10.1016/j.vaccine.2011.09.061 (2012).

75 Calabro, S. *et al.* Vaccine adjuvants alum and MF59 induce rapid recruitment of neutrophils and monocytes that participate in antigen transport to draining lymph nodes. *Vaccine* **29**, 1812-1823, doi:10.1016/j.vaccine.2010.12.090 (2011).

76 Song, J. Y. *et al.* Comparison of the long-term immunogenicity of two pandemic influenza A/H1N1 2009 vaccines, the MF59-adjuvanted and unadjuvanted vaccines, in adults. *Clin Vaccine Immunol* **19**, 638-641, doi:10.1128/cvi.00026-12 (2012).

77 O'Hagan, D. T. MF59 is a safe and potent vaccine adjuvant that enhances protection against influenza virus infection. *Expert Rev Vaccines* **6**, 699-710, doi:10.1586/14760584.6.5.699 (2007).

78 Tsai, T. F. MF59 adjuvanted seasonal and pandemic influenza vaccines. *Yakugaku Zasshi* **131**, 1733-1741, doi:10.1248/yakushi.131.1733 (2011).

79 Hauser, M. I., Muscatello, D. J., Soh, A. C. Y., Dwyer, D. E. & Turner, R. M. An indirect comparison meta-analysis of AS03 and MF59 adjuvants in pandemic influenza A(H1N1)pdm09 vaccines. *Vaccine* **37**, 4246-4255, doi:10.1016/j.vaccine.2019.06.039 (2019).

80 Garcia-Sicilia, J. *et al.* Immunogenicity and safety of AS03-adjuvanted H1N1 pandemic vaccines in children and adolescents. *Vaccine* **29**, 4353-4361, doi:10.1016/j.vaccine.2011.04.011 (2011).

81 Madan, A. *et al.* Evaluation of a primary course of H9N2 vaccine with or without AS03 adjuvant in adults: A phase I/II randomized trial. *Vaccine* **35**, 4621-4628, doi:10.1016/j.vaccine.2017.07.013 (2017).

82 O'Hagan, D. T., Ott, G. S., Nest, G. V., Rappuoli, R. & Giudice, G. D. The history of MF59® adjuvant: a phoenix that arose from the ashes. *Expert review of vaccines* **12**, 13-30 (2013).

83 Wu, S., Xia, Y., Hu, Y. & Ma, G. Bio-mimic particles for the enhanced vaccinations: Lessons learnt from the natural traits and pathogenic invasion. *Adv Drug Deliv Rev* **176**, 113871, doi:10.1016/j.addr.2021.113871 (2021).

84 Du, Y. *et al.* Engineering mannosylated pickering emulsions for the targeted delivery of multicomponent vaccines. *Biomaterials* **280**, 121313, doi:10.1016/j.biomaterials.2021.121313 (2022).

85 Song, T. *et al.* Engineering the Deformability of Albumin-Stabilized Emulsions for Lymph-Node Vaccine Delivery. *Adv. Mater.* **33**, e2100106, doi:10.1002/adma.202100106 (2021).

86 Xia, Y. *et al.* Exploiting the pliability and lateral mobility of Pickering emulsion for enhanced vaccination. *Nat Mater* **17**, 187-194, doi:10.1038/nmat5057 (2018).

87 Peng, S. *et al.* Particulate Alum via Pickering Emulsion for an Enhanced COVID-19 Vaccine Adjuvant. *Adv. Mater.* **32**, e2004210, doi:10.1002/adma.202004210 (2020).

88 Stäger, S. *et al.* Natural antibodies and complement are endogenous adjuvants for vaccine-induced CD8⁺ T-cell responses. *Nat. Med.* **9**, 1287-1292, doi:10.1038/nm933 (2003).

89 Xi, X. *et al.* Self-healing microcapsules synergetically modulate immunization microenvironments for potent cancer vaccination. *Science Advances* **6**, doi:10.1126/sciadv.aay7735 (2020).

90 Fan, Y. & Moon, J. J. Nanoparticle Drug Delivery Systems Designed to Improve Cancer Vaccines and Immunotherapy. *Vaccines* **3**, 662-685, doi:10.3390/vaccines3030662 (2015).

91 Mizukoshi, E. *et al.* Peptide vaccine-treated, long-term surviving cancer patients harbor self-renewing tumor-specific CD8⁺ T cells. *Nature Communications* **13**, doi:10.1038/s41467-022-30861-z (2022).

92 Rastogi, I., Muralidhar, A. & McNeel, D. G. Vaccines as treatments for prostate cancer. *Nature Reviews Urology* **20**, 544-559, doi:10.1038/s41585-023-00739-w (2023).

93 Liu, S. *et al.* A DNA nanodevice-based vaccine for cancer immunotherapy. *Nature Materials* **20**, 421-+, doi:10.1038/s41563-020-0793-6 (2021).

94 Macagno, A., Napolitani, G., Lanzavecchia, A. & Sallusto, F. Duration, combination and timing: the signal integration model of dendritic cell activation. *Trends Immunol.* **28**, 227-233, doi:10.1016/j.it.2007.03.008 (2007).

95 Irvine, D. J., Swartz, M. A. & Szeto, G. L. Engineering synthetic vaccines using cues from natural immunity. *Nature Materials* **12**, 978-990, doi:10.1038/nmat3775 (2013).

96 von Andrian, U. H. & Mempel, T. R. Homing and cellular traffic in lymph nodes. *Nature Reviews Immunology* **3**, 867-878, doi:10.1038/nri1222 (2003).

97 Xia, Y. *et al.* Chitosan-based mucosal adjuvants: Sunrise on the ocean. *Vaccine* **33**, 5997-6010, doi:10.1016/j.vaccine.2015.07.101 (2015).

98 Pulendran, B. in *Annual Review of Immunology Vol 33* Vol. 33 *Annual Review of Immunology* (eds D. R. Littman & W. M. Yokoyama) 563-606 (2015).

99 Rosalia, R. A. *et al.* CD40-targeted dendritic cell delivery of PLGA-nanoparticle vaccines induce potent anti-tumor responses. *Biomaterials* **40**, 88-97, doi:10.1016/j.biomaterials.2014.10.053 (2015).

100 Green, J. J. & Elisseeff, J. H. Mimicking biological functionality with polymers for biomedical applications. *Nature* **540**, 386-394, doi:10.1038/nature21005 (2016).

101 Xia, Y. *et al.* Exploiting the pliability and lateral mobility of Pickering emulsion for enhanced vaccination. *Nature Materials* **17**, 187-+, doi:10.1038/nmat5057 (2018).

102 Du, Y. *et al.* Engineering mannosylated pickering emulsions for the targeted delivery of multicomponent vaccines. *Biomaterials* **280**, doi:10.1016/j.biomaterials.2021.121313 (2022).

103 Chen, Q. *et al.* Alum Pickering Emulsion as Effective Adjuvant to Improve Malaria Vaccine Efficacy. *Vaccines* **9**, doi:10.3390/vaccines9111244 (2021).

104 Cao, F. *et al.* Inside-out assembly of viral antigens for the enhanced vaccination. *Signal Transduction and Targeted Therapy* **8**, doi:10.1038/s41392-023-01414-7 (2023).

105 van der Burg, S. H., Arens, R., Ossendorp, F., van Hall, T. & Melief, C. J. M. Vaccines for established cancer: overcoming the challenges posed by immune evasion. *Nature Reviews Cancer* **16**, 219-233, doi:10.1038/nrc.2016.16 (2016).

106 Watkins, E. A. *et al.* Persistent antigen exposure via the eryptotic pathway drives terminal T cell dysfunction. *Science Immunology* **6**, doi:10.1126/sciimmunol.abe1801 (2021).

107 Wherry, E. J. & Kurachi, M. Molecular and cellular insights into T cell exhaustion. *Nature Reviews Immunology* **15**, 486-499, doi:10.1038/nri3862 (2015).

108 Wherry, E. J. T cell exhaustion. *Nat. Immunol.* **12**, 492-499, doi:10.1038/ni.2035 (2011).

109 Fuc, E., Zlotkowska, D., Wasilewska, E. & Wroblewska, B. OVA-Experienced CD4⁺ T Cell Transfer and Chicken Protein Challenge Affect the Immune Response to OVA in a Murine Model. *International Journal of Molecular Sciences* **22**, doi:10.3390/ijms22126573 (2021).

110 Peng, S. *et al.* Particulate Alum via Pickering Emulsion for an Enhanced COVID-19 Vaccine Adjuvant. *Adv. Mater.* **32**, doi:10.1002/adma.202004210 (2020).

111 Pang, G. *et al.* Endotoxin contamination in ovalbumin as viewed from a nano-immunotherapy perspective. *Wiley Interdisciplinary Reviews-Nanomedicine and Nanobiotechnology* **14**, doi:10.1002/wnan.1747 (2022).

112 Orr, M. T. *et al.* Reprogramming the adjuvant properties of aluminum oxyhydroxide with nanoparticle technology. *Npj Vaccines* **4**, doi:10.1038/s41541-018-0094-0 (2019).

113 Moyer, T. J. *et al.* Engineered immunogen binding to alum adjuvant enhances humoral immunity. *Nat. Med.* **26**, 430-+, doi:10.1038/s41591-020-0753-3 (2020).

114 Liu, J., Guo, S., Jin, Z. & Zhao, K. Adjuvanted quaternized chitosan composite aluminum nanoparticles-based vaccine formulation promotes immune responses in chickens. *Vaccine* **41**, 2982-2989, doi:10.1016/j.vaccine.2023.03.067 (2023).

115 HogenEsch, H., O'Hagan, D. T. & Fox, C. B. Optimizing the utilization of aluminum adjuvants in vaccines: you might just get what you want. *Npj Vaccines* **3**, doi:10.1038/s41541-018-0089-x (2018).

116 Teplensky, M. H. *et al.* Multi-antigen spherical nucleic acid cancer vaccines. *Nature Biomedical Engineering* **7**, 911-+, doi:10.1038/s41551-022-01000-2 (2023).

117 Schaefer, J. T. *et al.* Dynamic changes in cellular infiltrates with repeated cutaneous vaccination: a histologic and immunophenotypic analysis. *Journal of Translational Medicine* **8**, doi:10.1186/1479-5876-8-79 (2010).

118 Beatty, G. L. & Gladney, W. L. Immune Escape Mechanisms as a Guide for Cancer Immunotherapy. *Clin. Cancer. Res.* **21**, 687-692, doi:10.1158/1078-0432.Ccr-14-1860 (2015).

119 Wang, J., Mamuti, M. & Wang, H. Therapeutic Vaccines for Cancer Immunotherapy. *Acs Biomaterials Science & Engineering* **6**, 6036-6052, doi:10.1021/acsbiomaterials.0c01201 (2020).

120 Badrinath, S. *et al.* A vaccine targeting resistant tumours by dual T cell plus NK cell attack. *Nature* **606**, 992-998, doi:10.1038/s41586-022-04772-4 (2022).

121 Melief, C. J. & van der Burg, S. H. Immunotherapy of established (pre)malignant disease by synthetic long peptide vaccines. *Nat. Rev. Cancer* **8**, 351-360, doi:10.1038/nrc2373 (2008).

122 Shin, A. R. *et al.* An effective peptide vaccine strategy circumventing clonal MHC

heterogeneity of murine myeloid leukaemia. *Br. J. Cancer* **123**, 919-931, doi:10.1038/s41416-020-0955-y (2020).

123 Purcell, A. W., McCluskey, J. & Rossjohn, J. More than one reason to rethink the use of peptides in vaccine design. *Nat. Rev. Drug Discov.* **6**, 404-414, doi:10.1038/nrd2224 (2007).

124 Kuai, R., Ochyl, L. J., Bahjat, K. S., Schwendeman, A. & Moon, J. J. Designer vaccine nanodiscs for personalized cancer immunotherapy. *Nat Mater* **16**, 489-496, doi:10.1038/nmat4822 (2017).

125 Arbelaez, C. A. *et al.* A nanoparticle vaccine that targets neoantigen peptides to lymphoid tissues elicits robust antitumor T cell responses. *NPJ Vaccines* **5**, 106, doi:10.1038/s41541-020-00253-9 (2020).

126 Teplensky, M. H. *et al.* Multi-antigen spherical nucleic acid cancer vaccines. *Nat Biomed Eng* **7**, 911-927, doi:10.1038/s41551-022-01000-2 (2023).

127 van der Burg, S. H., Arens, R., Ossendorp, F., van Hall, T. & Melief, C. J. Vaccines for established cancer: overcoming the challenges posed by immune evasion. *Nat. Rev. Cancer* **16**, 219-233, doi:10.1038/nrc.2016.16 (2016).

128 Griffiths, K. L. *et al.* Targeting dendritic cells to accelerate T-cell activation overcomes a bottleneck in tuberculosis vaccine efficacy. *Nat Commun* **7**, 13894, doi:10.1038/ncomms13894 (2016).

129 Macagno, A., Napolitani, G., Lanzavecchia, A. & Sallusto, F. Duration, combination and timing: the signal integration model of dendritic cell activation. *Trends Immunol.* **28**, 227-233, doi:10.1016/j.it.2007.03.008 (2007).

130 Irvine, D. J. & Dane, E. L. Enhancing cancer immunotherapy with nanomedicine. *Nat. Rev. Immunol.* **20**, 321-334, doi:10.1038/s41577-019-0269-6 (2020).

131 Kapadia, C. H. *et al.* Extending antigen release from particulate vaccines results in enhanced antitumor immune response. *J Control Release* **269**, 393-404, doi:10.1016/j.jconrel.2017.11.020 (2018).

132 Najibi, A. J. *et al.* Durable lymph-node expansion is associated with the efficacy of therapeutic vaccination. *Nat Biomed Eng*, doi:10.1038/s41551-024-01209-3 (2024).

133 Super, M. *et al.* Biomaterial vaccines capturing pathogen-associated molecular patterns protect against bacterial infections and septic shock. *Nat Biomed Eng* **6**, 8-18, doi:10.1038/s41551-021-00756-3 (2022).

134 Kim, J. *et al.* Injectable, spontaneously assembling, inorganic scaffolds modulate immune cells in vivo and increase vaccine efficacy. *Nat. Biotechnol.* **33**, 64-72, doi:10.1038/nbt.3071 (2015).

135 Li, A. W. *et al.* A facile approach to enhance antigen response for personalized cancer vaccination. *Nat Mater* **17**, 528-534, doi:10.1038/s41563-018-0028-2 (2018).

136 Xi, X. *et al.* Self-healing microcapsules synergetically modulate immunization microenvironments for potent cancer vaccination. *Sci Adv* **6**, eaay7735, doi:10.1126/sciadv.aay7735 (2020).

137 Bencherif, S. A. *et al.* Injectable cryogel-based whole-cell cancer vaccines. *Nat Commun* **6**, 7556, doi:10.1038/ncomms8556 (2015).

138 Hailemichael, Y. *et al.* Persistent antigen at vaccination sites induces tumor-specific $CD8^+$ T cell sequestration, dysfunction and deletion. *Nat. Med.* **19**, 465-472,

doi:10.1038/nm.3105 (2013).

139 Yang, J. *et al.* Asymmetric Assembly and Self-Adjuvanted Antigen Delivery Platform for Improved Antigen Uptake and Antitumor Effect. *Bioconjug Chem* **34**, 856-865, doi:10.1021/acs.bioconjchem.3c00060 (2023).

140 Cao, F. *et al.* Inside-out assembly of viral antigens for the enhanced vaccination. *Signal Transduct Target Ther* **8**, 189, doi:10.1038/s41392-023-01414-7 (2023).

141 Islam, M. A. *et al.* Adjuvant-pulsed mRNA vaccine nanoparticle for immunoprophylactic and therapeutic tumor suppression in mice. *Biomaterials* **266**, 120431, doi:10.1016/j.biomaterials.2020.120431 (2021).

142 Tan, T. G. *et al.* Identification of T. gondii epitopes, adjuvants, and host genetic factors that influence protection of mice and humans. *Vaccine* **28**, 3977-3989, doi:10.1016/j.vaccine.2010.03.028 (2010).

143 Lee, C. Y. C. *et al.* Tumour-retained activated CCR7(+) dendritic cells are heterogeneous and regulate local anti-tumour cytolytic activity. *Nat Commun* **15**, 682, doi:10.1038/s41467-024-44787-1 (2024).

144 Berk, E., Muthuswamy, R. & Kalinski, P. Lymphocyte-polarized dendritic cells are highly effective in inducing tumor-specific CTLs. *Vaccine* **30**, 6216-6224, doi:10.1016/j.vaccine.2012.04.077 (2012).

145 Blanco, P., Palucka, A. K., Pascual, V. & Banchereau, J. Dendritic cells and cytokines in human inflammatory and autoimmune diseases. *Cytokine Growth Factor Rev.* **19**, 41-52, doi:10.1016/j.cytogfr.2007.10.004 (2008).

146 Jin, S. M. *et al.* A nanoadjuvant that dynamically coordinates innate immune stimuli activation enhances cancer immunotherapy and reduces immune cell exhaustion. *Nat Nanotechnol* **18**, 390-402, doi:10.1038/s41565-022-01296-w (2023).

147 Fu, S. *et al.* Temperature sensitive liposome based cancer nanomedicine enables tumour lymph node immune microenvironment remodelling. *Nat Commun* **14**, 2248, doi:10.1038/s41467-023-38014-6 (2023).

148 Wang, Y. *et al.* Engineered exosomes with enhanced stability and delivery efficiency for glioblastoma therapy. *J Control Release* **368**, 170-183, doi:10.1016/j.jconrel.2024.02.015 (2024).

149 Yao, M. *et al.* Microgel reinforced zwitterionic hydrogel coating for blood-contacting biomedical devices. *Nat Commun* **13**, 5339, doi:10.1038/s41467-022-33081-7 (2022).

150 Koff, W. C. *et al.* Accelerating Next-Generation Vaccine Development for Global Disease Prevention. *Science* **340**, doi:10.1126/science.1232910 (2013).

151 Li, S. *et al.* Molecular signatures of antibody responses derived from a systems biology study of five human vaccines. *Nat. Immunol.* **15**, 195-204, doi:10.1038/ni.2789 (2014).

152 Roth, G. A. *et al.* Designing spatial and temporal control of vaccine responses. *Nature Reviews Materials* **7**, 174-195, doi:10.1038/s41578-021-00372-2 (2022).

153 Kaplonek, P. *et al.* Early cross-coronavirus reactive signatures of humoral immunity against COVID-19. *Science Immunology* **6**, doi:10.1126/sciimmunol.abj2901 (2021).

154 Pollard, A. J. & Bijker, E. M. A guide to vaccinology: from basic principles to new developments. *Nature Reviews Immunology* **21**, 83-100, doi:10.1038/s41577-020-00479-7 (2021).

155 Cao, M. *et al.* Molybdenum derived from nanomaterials incorporates into molybdenum

enzymes and affects their activities in vivo. *Nature Nanotechnology* **16**, 708-+, doi:10.1038/s41565-021-00856-w (2021).

156 Desai, N. *et al.* Temporal and Spatial Heterogeneity of Host Response to SARS-CoV-2 Pulmonary Infection. *medRxiv : the preprint server for health sciences*, doi:10.1101/2020.07.30.20165241 (2020).

157 Deng, L. *et al.* Double-layered protein nanoparticles induce broad protection against divergent influenza A viruses. *Nature Communications* **9**, doi:10.1038/s41467-017-02725-4 (2018).

158 Pulendran, B., Arunachalam, P. S. & O'Hagan, D. T. Emerging concepts in the science of vaccine adjuvants. *Nature Reviews Drug Discovery* **20**, 454-475, doi:10.1038/s41573-021-00163-y (2021).

159 Wu, S. *et al.* A single dose of an adenovirus-vectored vaccine provides protection against SARS-CoV-2 challenge. *Nature Communications* **11**, doi:10.1038/s41467-020-17972-1 (2020).

160 Wang, Z., Cui, K., Costabel, U. & Zhang, X. Nanotechnology-facilitated vaccine development during the coronavirus disease 2019 (COVID-19) pandemic. *Exploration* **2**, 20210082, doi:https://doi.org/10.1002/EXP.20210082 (2022).

161 Bachmann, M. F. & Jennings, G. T. Vaccine delivery: a matter of size, geometry, kinetics and molecular patterns. *Nature Reviews Immunology* **10**, 787-796, doi:10.1038/nri2868 (2010).

162 Wu, S., Xia, Y., Hu, Y. & Ma, G. Bio-mimic particles for the enhanced vaccinations: Lessons learnt from the natural traits and pathogenic invasion. *Adv. Drug Del. Rev.* **176**, doi:10.1016/j.addr.2021.113871 (2021).

163 Zheng, B. *et al.* Inhalable nanovaccine with biomimetic coronavirus structure to trigger mucosal immunity of respiratory tract against COVID-19. *Chem. Eng. J.* **418**, doi:10.1016/j.cej.2021.129392 (2021).

164 Bushman, M., Kahn, R., Taylor, B. P., Lipsitch, M. & Hanage, W. P. Population impact of SARS-CoV-2 variants with enhanced transmissibility and/or partial immune escape. *Cell* **184**, 6229-+, doi:10.1016/j.cell.2021.11.026 (2021).

165 Oidtman, R. J. *et al.* Influenza immune escape under heterogeneous host immune histories. *Trends Microbiol.* **29**, 1072-1082, doi:10.1016/j.tim.2021.05.009 (2021).

166 Garcia-Sastre, A. Ten Strategies of Interferon Evasion by Viruses. *Cell Host & Microbe* **22**, 176-184, doi:10.1016/j.chom.2017.07.012 (2017).

167 Fischer, W. *et al.* HIV-1 and SARS-CoV-2: Patterns in the evolution of two pandemic pathogens. *Cell Host & Microbe* **29**, 1093-1110, doi:10.1016/j.chom.2021.05.012 (2021).

168 Artika, I. M., Dewantari, A. K. & Wiyatno, A. Molecular biology of coronaviruses: current knowledge. *Heliyon* **6**, e04743-e04743, doi:10.1016/j.heliyon.2020.e04743 (2020).

169 Caruso, I. P., Sanches, K., Da Poian, A. T., Pinheiro, A. S. & Almeida, F. C. L. Dynamics of the SARS-CoV-2 nucleoprotein N-terminal domain triggers RNA duplex destabilization. *Biophys. J.* **120**, 2814-2827, doi:10.1016/j.bpj.2021.06.003 (2021).

170 Fujita-Fujiharu, Y. *et al.* Structural insight into Marburg virus nucleoprotein-RNA complex formation. *Nature Communications* **13**, doi:10.1038/s41467-022-28802-x (2022).

171 Mu, J. *et al.* SARS-CoV-2 N protein antagonizes type I interferon signaling by suppressing phosphorylation and nuclear translocation of STAT1 and STAT2. *Cell*

Discovery **6**, doi:10.1038/s41421-020-00208-3 (2020).

172 Wang, Y.-T. *et al.* Select autophagy genes maintain quiescence of tissue-resident macrophages and increase susceptibility to Listeria monocytogenes. *Nature Microbiology* **5**, 272-+, doi:10.1038/s41564-019-0633-0 (2020).

173 Li, T. *et al.* A synthetic nanobody targeting RBD protects hamsters from SARS-CoV-2 infection. *Nature Communications* **12**, doi:10.1038/s41467-021-24905-z (2021).

174 Choi, J. *et al.* Bcl-6 is the nexus transcription factor of T follicular helper cells via repressor-of-repressor circuits. *Nat. Immunol.* **21**, 777-+, doi:10.1038/s41590-020-0706-5 (2020).

175 Park, S. *et al.* Capicua deficiency induces autoimmunity and promotes follicular helper T cell differentiation via derepression of ETV5. *Nature Communications* **8**, doi:10.1038/ncomms16037 (2017).

176 Yao, Y. *et al.* METTL3-dependent m⁶A modification programs T follicular helper cell differentiation. *Nature Communications* **12**, doi:10.1038/s41467-021-21594-6 (2021).

177 Xu, K. *et al.* Recombinant chimpanzee adenovirus AdC7 expressing dimeric tandem-repeat spike protein RBD protects mice against COVID-19. *Emerging Microbes & Infections* **10**, 1574-1588, doi:10.1080/22221751.2021.1959270 (2021).

178 Chandrashekar, A. *et al.* SARS-CoV-2 infection protects against rechallenge in rhesus macaques. *Science* **369**, 812-+, doi:10.1126/science.abc4776 (2020).

179 Foghandersen, N., Altura, B. M., Altura, B. T. & Siggaardandersen, O. COMPOSITION OF INTERSTITIAL FLUID. *Clin. Chem.* **41**, 1522-1525 (1995).

180 Brinkman, J. E., Dorius, B. & Sharma, S. *Physiology, Body Fluids*. (StatPearls Publishing, Treasure Island (FL), 2023).

181 Ivashkiv, L. B. & Donlin, L. T. Regulation of type I interferon responses. *Nature Reviews Immunology* **14**, 36-49, doi:10.1038/nri3581 (2014).

182 Theofilopoulos, A. N., Baccala, R., Beutler, B. & Kono, D. H. Type I interferons (α/β) in immunity and autoimmunity. *Annu. Rev. Immunol.* **23**, 307-336, doi:10.1146/annurev.immunol.23.021704.115843 (2005).

183 Hassanzadeh-Kiabi, N. *et al.* Autocrine Type I IFN Signaling in Dendritic Cells Stimulated with Fungal β-Glucans or Lipopolysaccharide Promotes CD8 T Cell Activation. *J. Immunol.* **198**, 375-382, doi:10.4049/jimmunol.1601143 (2017).

184 Le Bon, A. & Tough, D. F. Type I interferon as a stimulus for cross-priming. *Cytokine Growth Factor Rev.* **19**, 33-40, doi:10.1016/j.cytogfr.2007.10.007 (2008).

185 Duan, X. *et al.* ¹IFN-α Modulates Memory Tfh Cells and Memory B Cells in Mice, Following Recombinant FMDV Adenoviral Challenge. *Frontiers in Immunology* **11**, doi:10.3389/fimmu.2020.00701 (2020).

186 Parlato, S. *et al.* Expression of CCR-7, MIP-3β, and Th-1 chemokines in type IIFN-induced monocyte-derived dendritic cells:: importance for the rapid acquisition of potent migratory and functional activities. *Blood* **98**, 3022-3029, doi:10.1182/blood.V98.10.3022 (2001).

187 Luft, T. *et al.* IFN-α enhances CD40 ligand-mediated activation of immature monocyte-derived dendritic cells. *Int. Immunol.* **14**, 367-380, doi:10.1093/intimm/14.4.367 (2002).

188 O'Connor, B. P., Gleeson, M. W., Noelle, R. J. & Erickson, L. D. The rise and fall of long-

lived humoral immunity: terminal differentiation of plasma cells in health and disease. *Immunol. Rev.* **194**, 61-76, doi:10.1034/j.1600-065X.2003.00055.x (2003).

189 Dai, L. *et al.* A Universal Design of Betacoronavirus Vaccines against COVID-19, MERS, and SARS. *Cell* **182**, 722-+, doi:10.1016/j.cell.2020.06.035 (2020).

190 Bao, L. *et al.* The pathogenicity of SARS-CoV-2 in hACE2 transgenic mice. *Nature* **583**, 830-+, doi:10.1038/s41586-020-2312-y (2020).

191 Kang, Y.-F. *et al.* Rapid Development of SARS-CoV-2 Spike Protein Receptor-Binding Domain Self-Assembled Nanoparticle Vaccine Candidates. *ACS Nano.* **15**, 2738-2752, doi:10.1021/acsnano.0c08379 (2021).

192 Ying, B. *et al.* Protective activity of mRNA vaccines against ancestral and variant SARS-CoV-2 strains. *Science Translational Medicine* **14**, doi:10.1126/scitranslmed.abm3302 (2022).

Acknowledgments

This thesis encapsulated the research efforts undertaken during the period of 2021-2023. Throughout the trials of this period, I have been fortunate to receive guidance and support from lots of people around me, each of whom has contributed uniquely towards the fruition of my research and life.

I am profoundly grateful to my supervisor, Professor Ogino, for his significant efforts in facilitating my smooth arrival in Japan. An unforgettable incident that deeply impressed me occurred when I carelessly lost my Certificate of Eligibility (COE). Feeling helpless and frightened, I was met not with blame but with patience from Professor Ogino. He diligently helped me resolve the issue, offering immense comfort and encouragement. I still want to express my gratitude to Professor Ogino for all the support he has provided during my year in Japan. He is exceptionally attentive to students' emotions. Whenever I speak with him, even if I initially fail to understand his points, he patiently switches his methods of explanation until I fully comprehend, which makes me feel warmly cared for in every detail. Finally, I would like to thank Professor Ogino for all his assistance in helping me successfully graduate.

I extend special thanks to Professor Guanghui Ma, whose expertise and insightful guidance have profoundly enriched my research. Professor Ma's extensive knowledge and strategic vision in biomedicine have not only inspired me but also significantly enhanced the quality and breadth of my dissertation. Professor Ma has provided me with boundless academic support and personal care. I am grateful to have had such a nurturing research environment and living conditions over the past five years. I will forever remember our group's motto: "Enjoy science! Enjoy work! Enjoy life!"

I am also immensely thankful to Professor Yufei Xia for his continuous support and expert advice throughout my research. From the inception of the project through to its completion, Professor Yufei Xia's assistance has been a beacon of support, helping me to steer my project to its successful completion. Without the help and guidance of Professor Yufei Xia, there would not be the complete of this thesis. Sometimes words seem pale and powerless in the face of true emotions. Memories of these five years in Professor Yufei Xia's group flood my mind, each moment feeling incredibly precious. Especially during the COVID-19 pandemic, Professor Yufei Xia devotedly revised my papers and stayed up late with us during the revision period. These have all become unforgettable memories in my mind.

I also want to express my gratitude to all the peers in the laboratories of Ma and Ogino. Their generous sharing of expertise greatly aided me in various areas, including daily life, academic discussions, operating instruments, conducting experiments, and more.

Finally, I must convey my profound gratitude to my family. Their unwavering support and faith in my abilities have consistently inspired and strengthened me throughout this journey."

Achievements

1. Peng S#， Yan Y#, Nagi T, Ogino K*, Xia Y*. Development and Optimal Immune Strategy of an Alum-Stabilized Pickering emulsion for Cancer Vaccines. *Vaccines,* 2023;11, 1169.

2. Peng S#, Yan Y#, Kenji Ogino K*, Ma G*, Xia Y* . Spatiotemporal Coordination of Antigen Presentation and Co-stimulatory Signal for Enhanced Anti-tumor Vaccination. *Journal of controlled release* (Under Review)

3. Cao F#, Peng S#, An Y#, Xu K, Zheng T, Dai L, Ogino K*, Nagi T, Xia Y*, Ma G*. Inside-out assembly of viral antigens for the enhanced vaccination. *Signal Transduction and Targeted Therapy*, 2023, 8, 189. (#Co first-author)